Numerical and modeling methods for multi-level large eddy simulations of turbulent flows in complex geometries

Nicolas Legrand

To cite this version:

Nicolas Legrand. Numerical and modeling methods for multi-level large eddy simulations of turbulent flows in complex geometries. Fluid mechanics [physics.class-ph]. Normandie Université, 2017. English. NNT : 2017NORMIR16 . tel-01716423

HAL Id: tel-01716423
https://theses.hal.science/tel-01716423v1

Submitted on 23 Feb 2018

Normandie Université

THÈSE

Pour obtenir le diplôme de doctorat

Spécialité Energétique

Préparée au sein de l'INSA de Rouen Normandie

Numerical and modeling methods for multi-level Large Eddy Simulations of turbulent flows in complex geometries

présentée et soutenue par

Nicolas LEGRAND

Thèse soutenue publiquement le 13 Décembre 2017 devant le jury composé de		
Y. Dubief	Professeur associé à l'Université du Vermont USA	Rapporteur
F. Nicoud	Professeur à l'Université de Montpellier, IMAG	Rapporteur
L. Danaila	Professeur à l'université de Rouen	Examinateur
G. Balarac	Maître de conférence, LEGI	Examinateur
A. Larat	Chargé de recherche CNRS, EM2C	Examinateur
V. Brunet	Chef du département CFD, Safran	Examinateur
A. Berlemont	Directeur de recherche CNRS, CORIA	Directeur de thèse
V. Moureau	Chargé de recherche CNRS , CORIA	Co-encadrant de thèse

■ Thèse dirigée par Alain Berlemont et Vincent Moureau, laboratoire CORIA (UMR 6614 CNRS)

INSA INSTITUT NATIONAL DES SCIENCES APPLIQUÉES ROUEN NORMANDIE

ED PSIME

UMR 6614 CORIA COMPLEXE DE RECHERCHE INTERPROFESSIONNEL EN AEROTHERMOCHIMIE

Abstract : Numerical and modeling methods for multi-level Large-Eddy Simulations of turbulent flows in complex geometries

Large-Eddy Simulation (LES) has become a major tool for the analysis of highly turbulent flows in complex geometries. However, due to the steadily increase of computational resources, the amount of data generated by well-resolved numerical simulations is such that it has become very challenging to manage them with traditional data processing tools. In Computational Fluid Dynamics (CFD), this emerging problematic leads to the same "Big Data" challenges as in the computer science field. Some techniques have already been developed such as data partitioning and ordering or parallel processing but still remain insufficient for modern numerical simulations. Hence, the objective of this work is to propose new processing formalisms to circumvent the data volume issue for the future 2020 exa-scale computing objectives. To this aim, a massively parallel co-processing method, suited for complex geometries, was developed in order to extract large-scale features in turbulent flows. The principle of the method is to introduce a series of coarser nested grids to reduce the amount of data while keeping the large scales of interest. Data is transferred from one grid level to another using high-order filters and accurate interpolation techniques. This method enabled to apply modal decomposition techniques to a billion-cell LES of a 3D turbulent turbine blade, thus demonstrating its effectiveness. The capability of performing calculations on several embedded grid levels was then used to devise the multi-resolution LES (MR-LES). The aim of the method is to evaluate the modeling and numerical errors during an LES by conducting the same simulation on two different mesh resolutions, simultaneously. This error estimation is highly valuable as it allows to generate optimal grids through the building of an objective grid quality measure. MR-LES intents to limit the computational cost of the simulation while minimizing the sub-grid scale modeling errors. This novel framework was applied successfully to the simulation of a turbulent flow around a 3D cylinder.

Keywords : LES - Unstructured grid - Multi-level approach - High-order filters - Dynamic Mode Decomposition

Résumé : Modélisation et méthodes numériques pour la simulation aux grandes échelles multi-niveaux des écoulements turbulents dans des géométries complexes

La simulation aux grandes échelles est devenue un outil d'analyse incontournable pour l'étude des écoulements turbulents dans des géométries complexes. Cependant, à cause de l'augmentation constante des ressources de calcul, le traitement des grandes quantités de données générées par les simulations hautement résolues est devenu un véritable défi qu'il n'est plus possible de relever avec des outils traditionnels. En mécanique des fluides numérique, cette problématique émergente soulève les mêmes questions que celles communément rencontrées en informatique avec des données massives. A ce sujet, certaines méthodes ont déjà été développées telles que le partitionnement et l'ordonnancement des données ou bien encore le traitement en parallèle mais restent insuffisantes pour les simulations numériques modernes. Ainsi, l'objectif de cette thèse est de proposer de nouveaux formalismes permettant de contourner le problème de volume de données en vue des futurs calculs exaflopiques que l'informatique devrait atteindre en 2020. A cette fin, une méthode massivement parallèle de co-traitement, adaptée au formalisme non-structuré, a été développée afin d'extraire les grandes structures des écoulements turbulents. Son principe consiste à introduire une série de grilles de plus en plus grossières réduisant ainsi la quantité de données à traiter tout en gardant intactes les structures cohérentes d'intérêt. Les données sont transférées d'une grille à une autre grâce à l'utilisation de filtres et de méthodes d'interpolation d'ordre élevé. L'efficacité de cette méthodologie a pu être démontrée en appliquant des techniques de décomposition modale lors de la simulation 3D d'une pale de turbine turbulente sur une grille de plusieurs milliards d'éléments. En outre, cette capacité à pouvoir gérer plusieurs niveaux de grilles au sein d'une simulation a été utilisée par la suite pour la mise en place de calculs basés sur une stratégie multi-niveaux. L'objectif de cette méthode est d'évaluer au cours du calcul les erreurs numériques et celles liées à la modélisation en simulant simultanément la même configuration pour deux résolutions différentes. Cette estimation de l'erreur est précieuse car elle permet de générer des grilles optimisées à travers la construction d'une mesure objective de la qualité des grilles. Ainsi, cette méthodologie de multi-résolution tente de limiter le coût de calcul de la simulation en minimisant les erreurs de modélisation en sous-maille, et a été appliquée avec succès à la simulation d'un écoulement turbulent autour d'un cylindre.

Mots-clés : Simulation aux grandes échelles - Grille non structurée - Approche Multi-niveau - Filtres d'ordre élevé - Décomposition en modes dynamiques

Acknowledgments (remerciements)

Ce manuscrit vient clôturer trois années de travaux de recherche au sein du laboratoire CORIA. Par conséquent, c'est pour moi l'occasion de remercier les personnes qui ont fait partie de cette aventure.

Mes remerciements vont en premier lieu à Messieurs Yves Dubief et Franck Nicoud pour avoir accepté de rapporter ce manuscript, ainsi qu'à l'ensemble des membres du jury pour leur participation mais surtout pour la qualité et la pertinence de leurs remarques et questions.

Je souhaite également adresser mes remerciements appuyés à Messieurs Vincent Moureau et Ghislain Lartigue qui m'ont formé et accompagné avec bienveillance et exigence tout au long de ces trois longues et intenses années. Lors de la signature de ce contrat de thèse, n'ayant aucune idée de l'aventure dans laquelle je m'embarquais, j'ai eu la chance immense d'intégrer l'équipe YALES2 dans laquelle règnent excellence scientifique et franche camaraderie dont vous êtes bien évidemment les garants. Par la suite, j'ai eu l'agréable surprise de constater que le sujet de thèse que vous m'aviez proposé était passionnant et qu'il, je pense, me ressemblait. Je vous remercie donc encore une fois pour la qualité de votre encadrement, votre écoute ainsi que vos conseils qui ont été pour moi extrêmement précieux. Enfin, je vous suis d'autant plus reconnaissant que vous m'avez laissé une grande liberté dans l'organisation de mon emploi du temps pour mon récurrent va-et-vient entre Rouen et Bordeaux. Sans cela, ce manuscript n'aurait assurément jamais vu le jour.

Bien évidemment, une thèse reste un projet personnel. Néanmoins, cette aventure n'en est pas pour autant dénuée de rencontres, essentiellement belles et enrichissantes pour ma part. À ce titre, je souhaite remercier mes chères et chers collègues de bureau : Francesco, Hakim, Lancelot, Patricia, Pierre et Yann avec qui j'ai passé trois années intenses dans une ambiance chaleureuse. De cette période, je ne pourrai oublier les blagues douteuses, les affiches et décors du bureau, les onomatopées fulgurantes, les flèches et balles en mousses voltigeantes, les bruits numériques en tout genre, les chants grégoriens, sans oublier le lent mais inéluctable déclin de productivité du vendredi après-midi se terminant en apothéose vers dix-huit heures dans une ambiance complètement "zinzin", ponctuée d'imitations très peu fidèles de Bourvil, de Funès, Astérix et autres en tout genre. Je vous souhaite donc, chers collègues, tous mes voeux de réussite et de soutenir très prochainement.

À ceux que j'ai vu soutenir avec panache et brio - Emeline, Léa, Dorian, Nicolas, Bastien - et à ceux qui le feront, je n'en doute pas, très prochainement - Pierre, Benjamin, Kevin, Umut, Andréa, Alex, Loic - je souhaite également vous adresser de sincères remerciements pour avoir fait partie, de proche ou de loin, de mon aventure Rouennaise.

Comment oublier mon fidèle acolyte, ce troubadour de l'extrême dont l'humour n'a d'égal que la puissance sonore de son rire et qui n'a pas hésité un seul instant à être le cobaye de mes imitations musicales, rarement de qualité, depuis presque cinq années. Messire Yann Dufresne, champion incontesté du karaté serviette, je pense que tu as bien mérité ton titre de major de promo de la "High School of Dynamite Fishing" du Saint Empire Romain Germanique pour m'avoir supporté en collocation pendant quasiment quatre années et demie, ce qui semble être humainement impossible.

Enfin, je souhaite clore cette parenthèse de remerciements en exprimant ma gratitude à l'égard de ceux, qui sont pour moi assurément les plus chers à mes yeux, mes proches bien évidemment. À mes parents, mon frère, ma grand-mère et bien entendu à vous tous, chers autres membres de ma famille, je vous fais part de ma profonde reconnaissance. Vous m'avez apporté un cadre idyllique pour grandir, un soutien sans faille, une grande source de motivation ainsi que de merveilleux moments partagés. Pour cela et bien d'autres choses, je vous adresse mes remerciements les plus sincères et chaleureux.

À ma très chère Audrey...

Contents

Nomenclature

Dimensionless numbers

Symbol	Description
M	Mach number
Re	Reynolds number
Re_t	Turbulent Reynolds number
St	Strouhal number
Sw	Swirl number

Roman letters

Symbol	Description	Unit
a_k	Real scalar temporal evolution of the k^{th} mode	[-]
$\mathbf{A}$	Koopman operator	[-]
c	Sound velocity characteristic scale	[m.s^{-1}]
C_p	Specific heat capacity	[J.kg^{-1}.K^{-1}]
C_s	Smagorinsky constant	[-]
C_ω	Wale constant	[-]
$\mathbf{D}$	Laplacian operator	[m^{-2}]
$\mathbf{D}'$	Weighted Laplacian operator	[-]
$\mathbf{D}_{\boldsymbol{\alpha}}$	Complex square diagonal matrix of the mode amplitude	[-]
$\mathcal{E}$	Enstrophy or energy spectrum	[m.s^{-2}] / [m^{2}.s^{-2}]
$\mathbf{f}$	Real vector function	[-]
$\mathcal{F}_{k,i}$	Diffusive fluxes of the species k in the i direction	[kg.m^{-2}·s^{-1}]
G	Convolution kernel	
G_Δ	Convolution kernel function associated to the filter size Δ	
$\mathcal{G}$	Green function	
$\mathcal{G}_\theta$	Axial flux of the azimuthal momentum	[N.m^{3}]
$\mathcal{G}_z$	Axial flux of the axial momentum	[N.m^{2}]
h_s	Sensible enthalpy	[J.kg^{-1}]

$\mathcal{I}$	Interpolant	
$\mathbf{I}$	Identity matrix	[-]
J	Functional	
k	Wavenumber	[m^{-1}]
k_c	Cut-off wave number	[m^{-1}]
$\mathcal{K}$	Kinetic energy	[$\text{m}^2.\text{s}^{-2}$]
K	Kinetic energy of the mean flow	[$\text{m}^2.\text{s}^{-2}$]
k_t	Turbulent local kinetic energy	[$\text{m}^2.\text{s}^{-2}$]
$l,$	Microscopic characteristic length scale	[m]
$l_0, l_{EI}, l_{DI}, l_t, l_d$	Turbulent characteristic length scales	[m]
l_m	Mean free path	[m]
L	Macroscopic characteristic length scale	[m]
$\mathbf{L}$	Resolved turbulent stress tensor	[$\text{kg}.\text{m}^{-1}.\text{s}^{-2}$]
$\mathcal{L}_2$	Euclidian norm	
$\mathcal{M}_q$	Statistical moment of order q	
$\mathbf{M}$	Matrix	
N	Real or integer number Number	[-]
p_{tot}, p, p_2, p_0	Total, static, dynamic and thermodynamic pressure	[Pa]
$\mathcal{P}$	Probability density function or production energy spectrum	[-] / [$\text{m}^2.\text{s}^{-3}$]
$\mathbb{P}$	Probability	
Q	Q-criterion	[s^{-2}]
Qc	Mesh quality criterion	
$\mathcal{Q}_i$	Diffusive fluxes in the i direction	[$\text{J}.\text{m}^{-2}.\text{s}^{-1}$]
$\dot{\mathcal{Q}}$	Heat source term	[$\text{J}.\text{m}^{-3}.\text{s}^{-1}$]
$\mathbf{R}$	Reynolds tensor	[$\text{m}^2.\text{s}^{-2}$]
$\mathbf{S}$	The viscous stress tensor or Companion matrix	[s^{-1}]
$\mathbf{S}^D$	Deviation part of the viscous stress tensor	[s^{-1}]
$\tilde{\mathbf{S}}$	Schmid modified time shifted operator	[-]
t	Time	[s]
T	Temperature	[K]
$\mathcal{T}, \mathcal{T}_{EI}, \mathcal{T}_{DI}$	Turbulent energy transfer rate	[$\text{m}^2.\text{s}^{-3}$]
u	Characteristic velocity scale	[$\text{m}.\text{s}^{-1}$]
u_θ	Tangential velocity	[$\text{m}.\text{s}^{-1}$]
u_0, u_t, u_d, u_K	Turbulent characteristic velocity scales	[$\text{m}.\text{s}^{-1}$]
$\mathbf{u}$	Velocity field or left eigenvector	[$\text{m}.\text{s}^{-1}$] / [$\text{m}.\text{s}^{-1}$]
$\mathbf{U}$	Matrix of the right Singular Value Decomposition eigenvectors	[$\text{m}.\text{s}^{-1}$]

$\mathbf{v}$	Velocity field or right eigenvector	[m.s^{-1}]
$\mathbf{V}, \mathbf{V}_1^n, \mathbf{V}_2^{n+1}$	Data snapshots matrix	[m.s^{-1}]
$\mathbf{V}_{\text{and}}$	Vandermonde matrix	
x_p	Mesh node	[-]
Y_k	The mass fraction of the species k	[-]
$\mathbf{w}$	Right eigenvector	[-]
$\mathbf{W}$	Matrix of the left Singular Value Decomposition eigenvectors	[-]
$\mathbf{Z}$	Orthogonal square matrix	[-]

Greek letters

Symbol	**Description**	**Unit**
α	Thermal diffusivity, length scale ratio or mode amplitude	[m^2.s^{-1}] / [-] / [-]
Δ	Filter size	[m]
δ_{ij}	Kronecker symbol	
δ_m	Size of the molecules	[m]
Δx	Local mesh size	[m]
ϵ	Dissipation rate or error measurement	[m^2.s^{-3}] / [-]
η_K	Kolmogorov length scale	[m]
η_k	Complex roots	
γ	Isentropic coefficient	[-]
$\Gamma, \Gamma_1, \Gamma_2$	Circulation and metrics	[m^2.s^{-1}] / [-]
λ_k	Eigenvalues	
λ^{ln}	Amplitude growth rate	[s^{-1}]
$\mathbf{\Lambda}$	Square diagonal matrix of the eigenvalues	[-]
μ	Dynamic viscosity	[kg.m^{-1}.s^{-1}]
μ_q	Centered statistical moments	
ν	Kinematic viscosity	[m^2.s^{-1}]
ν_e, ν_t	Effective and turbulent kinematic viscosity	[m^2.s^{-1}]
ω	Pulsation or modulus of the rotational vector	[rad] / [s^{-1}]
$\dot{\omega}_k$	Chemical source term of the species k	[kg.m^{-3}.s^{-1}]
$\dot{\omega}_T$	Chemical source term for energy-enthalpy	[J.m^{-3}.s^{-1}]
$\mathbf{\Omega}$	Rotation rate tensor	[s^{-1}]
$\boldsymbol{\omega}$	Vorticity vector	[s^{-1}]
ϕ	Scalar function	
$\phi_{M_i}^{d_i}$	Discrete representation of ϕ on mesh M_i	

φ	Scalar function	
$\boldsymbol{\phi}_k$	Spatial DMD/POD mode	
$\mathbf{\Phi}$	Fourier transform of the Reynolds tensor or spatial matrix modes	$[\mathrm{m}^2.\mathrm{s}^{-2}]$ /
κ	Condition number	
σ	Singular value or standard deviation	
$\boldsymbol{\sigma}$	Constraint tensor or covariance matrix	$[\mathrm{kg}.\mathrm{m}^{-1}.\mathrm{s}^{-2}]$ /
$\mathbf{\Sigma}$	Singular Values matrix	
τ	Characteristic time scale of local refinement ratio	[s] / [-]
$\tau_0, \tau_t, \tau_d, \tau_K$	Turbulent vortex turnover time scales	[s]
$\boldsymbol{\tau}$	Viscous tensor	$[\mathrm{kg}.\mathrm{m}^{-1}.\mathrm{s}^{-2}]$
$\dot{\theta}$	Angular velocity	$[\mathrm{s}^{-1}]$
ρ	Density	$[\mathrm{kg}.\mathrm{m}^{-3}]$

Mathematical operators

Symbol	**Description**
$\mathcal{F}$	Filtering operator
$\mathcal{I}$	interpolation operator
$(,)$	Canonical scalar product
$\|\|\cdot\|\|_2, \|\|\cdot\|\|_F$	$\mathcal{L}_2$ and Frobenius norms
$\langle\phi\rangle$	Statistical averaging
$\langle\phi\rangle_\mathbf{x}$	Spatial averaging
$\langle\phi\rangle_t$	Temporal averaging
$\overline{\phi}$	Spatial filtering operator
$\widetilde{\phi}$	Estimation operator
$\widehat{\phi}$	Fourier transform operator
ϕ'	Deviation from the mean $\phi' = \phi - \langle\phi\rangle$
ϕ''	Fluctuations $\phi'' = \phi - \overline{\phi}$
$\phi^\star$	Dimensionless variable defined as $\phi^\star = \phi/\phi_r$
ϕ^*	Conjugate operator
$\boldsymbol{\phi}^T$	Transpose operator
$\boldsymbol{\phi}^H$	Adjoint operator
$\boldsymbol{\phi}^{-1}$	Inverse operator
$\boldsymbol{\phi}^+$	Pseudo inverse operator
∇	Gradient operator

$\nabla\cdot$	Divergence operator
$\nabla\times$	Curl operator
Δ	Laplacian operator
$\otimes$	Tensorial product
$(*)$	Convolution product

Abbreviations

Symbol	**Description**
API	Application Programming Interface
CFD	Computational Fluid Dynamics
CFL	Courant Friedrichs Lewy
CPU	Central Processing Unit
DMD	Dynamic Mode Decomposition
DNS	Direct Numerical Simulation
GMRES	Generalized Minimum Residual Method
HOF	High Order Filtering
LES	Large Eddy Simulation
MGHOF	Multi-Grid High Order Filtering
MPI	Message Passing Interface
MR-LES	Multi Resolution LES
OpenMP	Open-Multi-Processing
PCG	Preconditioned Conjugated Gradient
PDE	Partial Differential Equation
PDF	Probability Density Function
POD	Proper Orthogonal Decomposition
PVC	Precessing Vortex Core
RANS	Reynolds-Averaged Navier-Stokes
RCT	Reduced Computational Time
RHS	Right-Hand Side
RMS	Root Mean Square
SGS	Sub-Grid Scale
SVD	Singular Value Decomposition
TKE	Turbulent Kinetic Energy
WCT	Wall Clock Time
YALES2	Yet Another LES Solver : LES/DNS solver developed at CORIA laboratory

Chapter 1

General Introduction

Contents

1.1 Thesis context

1.1.1 Massively parallel Computational Fluid Dynamic

Computational Fluid Dynamics (CFD) refers to one branch of fluid mechanics that uses numerical methods in order to solve and study fluid flow configurations. It is a very common approach that has become a major design tool in a large variety of industrial fields such as aeronautics and aerospace, naval and rail transportation, automobile, energy and meteorology and so on... Furthermore, depending on the computational resources but also on the chosen resolution, CFD enables to access to the three dimensional instantaneous fields everywhere in the computational domain for all computed variables. Under the assumption that the physical processes are correctly captured, this approach enables to minimize the number of necessary experimental studies that are complementary approaches and difficult to set up. Moreover, thanks to this approach, the time and cost of the development processes and the design of high technology products have been reduced over the past decades. Therefore, CFD overcomes both the constraints on the design time and also on the search of new efficient solutions in a context where the objectives can be contradictory. Nowadays, one of the major challenge of CFD is to be able to improve the predictivity of the simulation at a limited Central Processing Unit (CPU) cost. This may be achieved with numerical and modeling improvements and with better understanding of the physical processes.

Moreover, thanks to the exponential growth of the computational power through the improvement of computer performances, the fidelity of CFD simulations has been drastically enhanced by increasing the mesh resolution or the physical time simulated but also by adding more physical phenomena. Nowadays, CFD simulations with meshes up to several billion cells are currently performed, in research laboratories and even in some industrial groups, on massively parallel machines using thousands of processors. Hence, the analysis of these billion-cell simulations is very challenging as it requires to handle a large amount of computed data that cannot be achieved using traditional data processing tools. Therefore, "Big Data" post-processing tools and methods such as data partitioning, data ordering, parallel processing are strongly related to the algorithms implemented in parallel Navier-Stokes solvers. However, the constant increase of data volume necessitates to develop new formalisms to efficiently post-process and analyze these billion-cell CFD simulations.

1.1.2 The "Big Data" challenge

Since the beginning of the new millennium, a new in vogue word called "Big Data" has emerged in the daily life but also in science. This notion refers to the vast amount of data generated and available that can no longer be stored on computer hard drive. Indeed, from genome sequencing machines, that enable to read a human's chromosomal DNA in half an hour leading to 1.5 Gigabytes of data, to the particle accelerator Large Hadron Collider at CERN that produces close to 100 Terabytes every day, the advent of the data age has become a reality in modern science.

In the field of computer science, the "Big Data" concept is closely related to the impressive increase of computational power that may be highlighted thanks to the the well-known Moore's law illustrated in Fig. 1.1. Gordon Moore, co-founder of Fairchild Semiconductor and of Intel, [143], observed in 1965 that the number of components per integrated circuit doubles every year, then he predicted that this rate would continue over at least one decade. In 1975, Moore revised his prediction to every two years [142]. However, David House took into account both the increase of transistors and their efficiency and thus predicted the widely known period of 18 months.

However, even if the availability of a large amount of data may open some new interesting scientific horizons and possibilities, which seems in appearance seductive, "Big Data" concept also has downsides. Indeed, scientists may be saturated with available data and then have to face an endless ocean of information that cannot be straightforwardly processed and may become therefore useless. As a matter of fact, large amount of data may contain "bad data" as outliers, irrelevant or useless data and, as a consequence, having intelligent insights on these dataset generate new challenges for the entire computer science field. Moreover, due to the high dimensionality of the datasets, the understanding of the underlying phenomena may thus become more challenging and tougher. The main "Big Data" challenges can thus be defined as: analysis, sharing, storage, transfer, and visualization.

Finally, the Big Data problematic and challenges may be alleviated through the development of new statistical and computational methods, especially in the field of computer science. These new methods and frameworks have to post-process in a efficient manner the large amount of data but also to extract the relevant information from the mass.

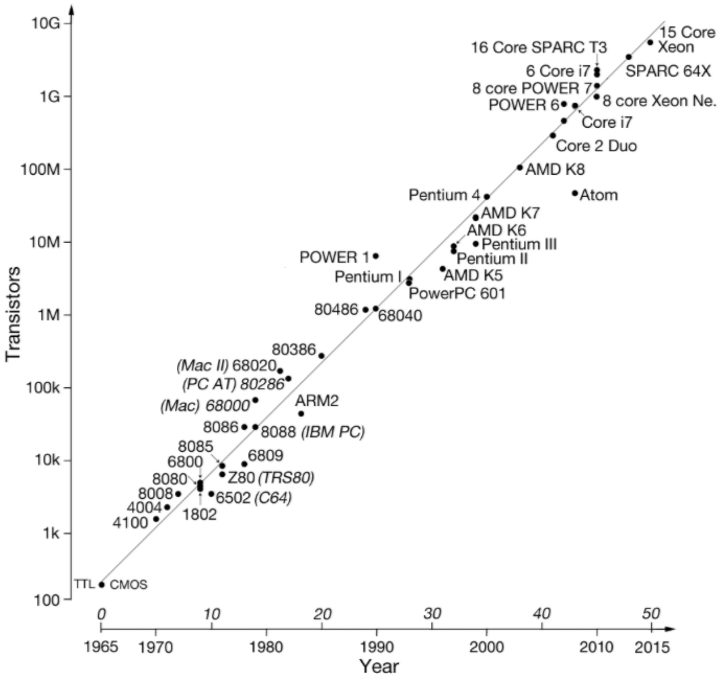

FIGURE 1.1: 50 years of Moore's law: Plot of CPU transistor counts against dates of introduction

1.2 Industrial and scientific context

1.2.1 The ELCI project

This thesis is supported by the ELCI project (Environnement Logiciel pour le Calcul Intensif) and is part of the PIA (Plan d'Investissement d'Avenir), a research investment program of the French State for research and innovative projects. Hence, ELCI is a French software project that brings together academic and industrial partners in order to design and provide a software environment for the next generation of HPC systems but also to improve numerical simulations and computer science methods for the 2020 exascale computing objectives. These challenges can be sum-up as follows : larger scalability, higher resiliency, greater security, improved modularity, with better abstraction and interactivity for application cases. For this purpose, this project will work along four work packages:

1 Execution environment : Future supercomputers will offer heterogeneous architectures, a growing number of computing cores, an increasingly complex memory hierarchy, denser packaging, more integrated high-speed networks. Then, software also has to evolve by incorporating new features such as optimizing the computer topology, maximizing the memory capacity, improving communications between the system and the middleware components, and also to benefit from equipment performance.

2 Libraries and research simulation codes : This work package deals with the design of a pre-, co-, and post-treatment tool chain for well refined high-order CFD calculations over the next few years. First, modern computing platforms and algorithms will be further developed to fully exploit all the available computational power, to leverage CPU and memory costs and to enhance parallel efficiency for both shared and distributed memories. At the solver level, solutions to extract and visualize quantities on-the-fly during code execution will be evaluated. Also, in order to obtain a high fidelity representation of all the physics of a phenomenon, efficient scalable

parallel methods to couple different simulation codes will be sought.

3 Programming environment (models and tools) : Due to the evolution of hardware architectures, it is becoming mandatory to implement multiple levels of parallelism to fully exploit computing resources. This work package studies multiple parallel programming models (hybrid MPI + OpenMP, PGAS) with different abstraction layers but also standard programming and emerging models.
4 Numerical simulation use cases : The last work package intents to validate the tools developed in the previous work packages using industrial test cases within massive computing environments. Grid adaptation, co-processing, multi-physics performance will all be validated on the following configurations : 1) Realistic compressor with the objective to perform co-processing, grid adaptation on a multi-stage compressor that includes technological effects. 2) A single jet for aero-acoustic studies to directly perform the post-processing during the simulation in co-processing mode. 3) A multi-physics test case represented by a cooled turbine with multi-physics coupling, grid adaptation, co-post-processing and performance efficiency.

Finally, this project gathers some industrial and academic partners summarized as follows : ALGO'TECH, BULL, CEA, CENAERO, CERFACS, CORIA, INRIA, KITWARE, ONERA, SAFRAN, UNIVERSITE de VERSAILLES. The present thesis attempts to overcome some of the previous challenges presented in work-packages two and four.

1.2.2 Thesis objectives

As presented above in the ELCI project, this thesis aims at developing new numerical tools and methodologies in order to manage future well-resolved simulations for the next generation of HPC systems. This task has been decomposed into two main objectives that are presented hereafter :

- The first objective deals with the development of new efficient and massively parallel co-processing algorithms. Indeed, as large amount of data produced by current CFD simulations cannot be written and stored on hard drives, one solution to circumvent this issue may be to apply several processings on the data while the simulation is running and after that, to only dump small quantities of interest. Some important and useful applications such as the large-scale extraction and coherent features visualization may benefit of some improvements through the application of these methods. In order to achieve this, the framework proposed in this study is based on a multi-level strategy using selective high-order filters with interpolation steps. This work will attempt to open the way to new processing formalisms for CFD simulations.
- The second objective refers to prospective attempts to hierarchical CFD simulations. This new approach deals with taking advantage of running several simulations at the same time on different levels of grid and then to compare the computed fields. Hence, from these fields, a local error measurement that includes all errors - both modeling and numerical errors - can be built and therefore allows to compute a criterion that characterizes the quality of the mesh. Finally, thanks to this objective metric, the application of mesh adaptation can be achieved in order to optimize the cell size of the grid for the considered flow configurations.

1.3 Manuscript content

During this thesis, a multi-grid framework for the large-scale features has been developed leading to the extraction and visualization of coherent structures on coarse levels of grid. Some challenging applications such as a 3D turbulent plane jet and a 3D turbulent low-Mach turbine blade have been on-the-fly processed thanks to this framework. Moreover, modal decomposition methods have also been developed and applied, leading to the identification of the most dominant modes of turbulent flows configurations. These methods could not have been used on such refined simulations without the application of the previous large-scale features extraction framework that drastically reduces the amount of data. Finally, based on this multi-grid framework, a multi-resolution approach has been developed in order to perform at the same time several simulations with different levels of grid. Thanks to this formalism an objective mesh adaptation criterion has been built leading to the application of the mesh adaptation formalism so that to optimize the CFD meshes. The content of this study is presented hereafter.

Chapter 1: Introduction This chapter introduces the global scientific context with the associated challenges that have to be overcome. A description of the thesis objectives is then provided.

Chapter 2: Coherent structure identification in turbulent flows The second part is dedicated to the state-of-art and literature survey of coherent structures identification in turbulent flows. Some definitions and the most widely used properties will first be presented with a short overview of classical identification technics. Then the restricted notion of vortical coherent structures will be also defined.

Chapter 3: Governing equations and modeling of turbulent incompressible flows In this chapter, some mathematical background on the incompressible flows and on the turbulence modeling is presented. Moreover, the CFD code YALES2 used during this thesis is also introduced with an overview of the most noticeable tools and the presentation of some of the main numerical methods and solvers.

Chapter 4: The Multi-Grid High-Order Filtering framework (MGHOF) for extracting large-scale structures in turbulent flows The fourth chapter of this study deals with the design and implementation of the Multi-Grid High-Order Filtering framework (MGHOF) that enables to on-the-fly extract coherent structures from billion-cells LES. This formalism uses several steps of both high-order filtering and interpolation methods in order to transfer these data on coarse levels of grid. After being introduced, this framework will be applied to a 3D turbulent jet plan with the extraction of the well-known Kelvin-Helmholtz vortex shedding but also on a much more challenging configuration that corresponds to a billion-cells LES of a 3D turbulent flow over a turbine blade.

Chapter 5: Application of the MGHOF framework to modal decomposition methods This chapter uses the previous MGHOF framework to generate a large amount of snapshots that are required for the application of the Dynamic Mode Decomposition (DMD) formalism on the billion-cells LES of the 3D turbulent turbine blade. Identifying the most dynamically dominant features in such configuration is particularly challenging due to the large amount of data that have to be analyzed but also due to the flow complexity of this configuration.

Chapter 6 : Multi-Resolution LES framework (MR-LES) This final chapter presents the Multi-Resolution LES framework that is based on performing several LES at the same time with information exchanges through the application of the MGHOF formalism. Thanks to this approach, both modeling and numerical errors can be estimated, leading to build an objective grid quality criterion that enables to locally determine if the grid has to be refined or coarsened. Then, optimization of the LES grid can be achieved by performing several steps of mesh adaptation.

Chapter 7 : Conclusions and perspectives Finally, this chapter provides a general conclusion for the developed processing methods and suggests perspectives in regards to the improvement of co-processing methodologies for future exascale computing simulations.

1.4 Publications

1.4.1 Peer-Reviewed international journals

- N. Legrand, G. Lartigue, V. Moureau, *A multi-grid framework for the extraction of large-scale vortices in Large-Eddy Simulation*, Journal of Computational Physics, Volume 349, Pages 528-560 (15 November 2017).

1.4.2 International conferences

- N. Legrand, G. Lartigue, V. Moureau, *A geometric multi-grid framework for the extraction of large-scale vortices in turbulent flows. Application to the massively parallel LES of a low-Mach number turbine blade*, in 11^{th} International ERCOFTAC Symposium on Engineering Turbulence Modelling and Measurements, Italy (2016).
- N. Legrand, G. Lartigue, V. Moureau, *Multi-grid framework and Dynamic Mode Decomposition for the extraction of large-scale vortices in turbulent flows. Application to the massively parallel LES of a low-mach turbine blade*, in 11^{th} International ERCOFTAC Workshop on Direct and Large-Eddy Simulation, Italy (2017).
- N. Legrand, G. Lartigue, V. Moureau, *Adaptative multi-resolution Large-Eddy Simulation with control of modeling and numerical errors*, in the American Institute of Aeronautics and Astronautics SciTech Forum, USA (2018).

Chapter 2

Coherent structures identification in turbulent flows

This section attempts to present a global overview of the concept of coherent structures in turbulent flows. This notion has been widely studied during the last decades and still appears to be one of the foundation stone to gain insight into the understanding of turbulent mechanisms. After being introduced, some common definitions for coherent structures are recalled followed by some information about their topology and morphology in canonical flow configurations. Then, among the broad diversity of methodologies that have been developed, some classical methods are briefly introduced. Particular highlights are dedicated to methods based on vorticity and velocity gradient tensor formalism. Moreover, the restriction of the concept of coherent features to vortical structures is exposed followed by the presentation of various identification criteria. Finally, the last section introduces new large-scale extraction frameworks that enable to circumvent the difficulties and limitations in CFD due to the modern computer science.

Contents

2.1 Introduction

Turbulent flows have always fascinated physicists, engineers and mathematicians because of the beauty of their manifestations but also as they are ubiquitous chaotically features present in Nature. Indeed, turbulence is a very widespread phenomenon that can be commonly observed in daily situations such as in atmospheric circulation, oceanic mixing layer, fast flowing rivers, billowing clouds in storms, smoke and many other examples. Contrary to the laminar flow regime, that deals with fluid flowing in parallel layers without disruption between them as Batchelor [11] mentioned, turbulent flows are characterized by sudden changes in the pressure and velocity fields.

In the early years 1508-1513, Leonardo da Vinci was very interested by this subject and he illustrated the fluid patterns produced by flowing water behind obstacles as the sketch presented in Fig. 2.1 refers. Here, the velocity streamlines have been drawn representing wakes that are formed, referring to counter-rotating vortices. Almost four centuries later, the Irish pioneer Osborne Reynolds experimentally studied the pipe transition from laminar to turbulent leading to the creation of the Reynolds number defined as $Re = \frac{ul}{\nu}$, with u the characteristic velocity of the fluid, l the characteristic length scale of the configuration and ν referring to the kinematic viscosity of the fluid. Important insights have emerged in the first part of the twentieth century notably with the concept of energy transfer from the large scales of the turbulence to the smallest ones as Richardson [163] first introduced in 1920, but also thanks to the isotropy and similarity hypotheses of Kolmogorov [110, 111] in 1941 that models the wavenumber spectrum in the turbulence inertial subrange. These concepts will be presented in the next chapter, where some mathematical background on turbulence will be further developed.

FIGURE 2.1: Seated man and studies and notes on the movement of water from [47]

Over the last decades, turbulent flows have been widely studied leading to the emergence of performant industrial applications such as aircraft engines, energy production processes, automobiles, wind turbines... Indeed, turbulence enables to improve all transfer types - momentum, mass and energy - compared to a laminar situation and may lead to an increase of the efficiency of the application. Moreover, Fig. 2.2 presents another practical example that highlights the knowledge of turbulent flows still remains primordial. Here, turbulent structures are generated in the wake of a landing plane. As these features can disturb other planes on the ground, it is thus mandatory to wait until they have been dissipated before another plane lands off.

FIGURE 2.2: Vortices produced by plane take-off from [31]

Despite turbulent flows are extremely complex - as they are characterized by the interaction of many degrees of freedom over a large range of spatial structures with heterogeneous turnover time scales - they can be modeled thanks to the Navier–Stokes formalism assuming certain fluid continuum conditions. Some mathematical background is still missing concerning the existence and the uniqueness of three dimensional solutions [190, 59], but practical applications by solving these equations associated to boundary and initial conditions enable to access detailed solutions with a large amount of data concerning the physics of the flow. However, despite the amount of information, numerical simulations sometimes do not really bring deep understanding of the underlying processes as they may be hidden by the chaotically smallest scales of the flow.

The analysis of turbulence can thus be considered by reducing its degrees of complexity through a simplistic and lower dimensional representation in order to access to its fundamental mechanisms. This can be achieved with the recent discovery by experimental fluid mechanicians of coherent features in some fully developed turbulent flows that paved the way to a better understanding of the underlying turbulent physical phenomena. Indeed, Métais and Lesieur [119] noted in 1991 that the emergence of coherent structures in turbulent flows is one of the most important insight in fluid mechanism over the last 25 years. Even if this discovery is difficult to attribute, the article of Brown et Roshko [24] in 1974, dealing with the large-scales organization in mixing zones, appears to be a truly breakthrough in the scientific community. The previous sketch of Leonard da Vinci in Fig. 2.1, highlighting an example of counter-rotating vortices, can thus be seen in term of coherent structures as they are steady in space and time with approximately constant characteristic length scale.

In this chapter, the presentation of coherent structures is first introduced attempting to define them in a proper manner through the characterization of their origins and their topological/morphological aspects in several canonical flows configurations. In a second time, the notion of vortical coherent structures is developed with the presentation of several extraction methods based on the vortical and velocity gradient tensor formalism. Finally, the presentation of the difficulties and limitations in the large-scale features extraction and visualization due to the modern computer sciences are presented with some examples of novel coherent features extraction frameworks.

2.2 Zoology of coherent structures in turbulent flows

2.2.1 Definition of coherent structures

The concept of coherent structures in turbulent flows has been first introduced by Prandtl in 1925 [158], who experimentally tried to describe turbulent motions with his mixing-length theory by introducing the concept of "Flüssigkeitballen" entities. The underlying hypothesis was that these "Ballen" were responsible of the transport of momentum across the flow and appear thus to be the first coherent features of the history of turbulence. Few decades later, in 1974 and 1984, Bradshaw [22] and Landahl [114] tried respectively to explain and justify Prandtl's coherent features concept.

However, the notion of coherent structure is very difficult to define. The infinite number of turbulent flow configurations leads to an impressive variety of coherent structures and identifying them with a general and mathematical definition is not straightforward. Furthermore, as coherent features are embedded and hidden inside the large range of chaotically structures generated by turbulence, it is therefore very challenging to identify and extract them. Moreover, this identification strongly depends on the choice of the coherent structures characteristics, of the identification method and of the selected criteria. All these difficulties lead to a very challenging tasks.

First, the notion of coherence can appear as being in contradiction to its classical meaning in physics. Indeed, this term was historically introduced in connection with Thomas Young's double-slit experiment in optics but is now used in various fields that involve waves, for instance acoustic or electro-dynamics, neuroscience or quantum mechanics. In physics, coherence is an ideal property of waves - constant phase difference, same frequency and waveform - that enables stationary interference. According to the Funk and Wagnalls Standard Dictionary, coherence is defined as a ". . . *relation of coincidence between two sets of waves, which will produce interference phenomena...* ". Then, spatial coherence describes the correlation between lateral or longitudinal waves at different points in space while temporal coherence describes correlation between waves at different instants in time. More generally, coherence refers to all properties of the correlation between physical quantities of a single wave, or between several waves or wave packets.

In the case of coherent structures in turbulence, this notion refers to a discernible correlation, in other words an element of turbulent motion that sets apart from the stochastic background of turbulence with recurrent and quasi-periodic behaviors associated to a preferential size and frequency for a given spatial location. Fiedler [64] derived some criteria that help to define what coherent structures are:

(a) Their largest scale can be compared to the lateral flow dimension
(b) They are indirectly related to the boundary conditions
(c) They refer to a recurrent pattern with a life span at least the average flow-through time of a structure
(d) They are at best quasi-periodic and their structure possesses high degree of organization

(e) They have similarities with laminar-turbulent transition structures.

Various complementary definitions of coherent structures have been proposed in the previous decades. Delville et al. [57] proposed a comprehensive overview of this concept, from which some of them are recalled hereafter:

Definition from Lesieur et al. [119]:
"*Suppose that, at a given time* t_0 *there exists a vorticity concentration within a domain* $D_{t_0} \subset R^3$. *Let* D_t *be the image of* D_{t_0} *at* $t \geq t_0$. D_t *is a Coherent Structure (coherent vortex) if : i)* D_t *retains a recognizable pattern for time delays greater (typically 5 times) than the turnover time* (τ_0)*. ii)* D_t *is unpredictable (i.e. extremely sensitive to small perturbations of initial conditions).*"

Definition from Hussain et al. [90, 91]:
"*A Coherent Structure is defined as a flow module with instantaneous phase-correlated vorticity*"

Definition from Berkooz et al. [17]:
Coherent structures are defined as "*organized spatial features which repeatedly appear (often in flows dominated by local shear) and undergo a characteristic temporal life cycle.*"

The choice of the coherent structure definition may also depend on the type of available data. On the one hand, unsteady numerical approaches - such as LES or DNS - give access to a large amount of data leading to sufficiently resolved information in both time and space dimensions. Hence, this do not affect the retained choice of the coherent structure definition and also the selection of the detection method. However, in that case the huge quantity of generated data may turn out to be a drawback concerning the analysis and understanding of coherent features behavior. On the other hand, available information generated from experiments is poorly resolved in time and space - unless high-speed diagnostics are used -, the definition choice depends thus on the available and accessible data.

2.2.2 Origins and morphological/topological description

The origin of coherent structures is related to a general phenomenon called synergetics that can be observed in inorganic as well as in organic Nature and which constitutes a scientific discipline of the theoretical physics field [83]. Indeed, the birth of coherent features comes from the spontaneous formation of organized fluid structures out of the turbulence chaos. Hence, Chaos Theory, referring as one specific ramification of the synergetics field, enables to explain the formation of coherent structures as a self-organization phenomenon and is one possible basis in order to describe turbulent flows [139].

According to Ruelle and Takens [168], turbulence might be the manifestation in the physical space of a strange attractor in the phase space and thus coherent structures might be interpreted in a same way as Sreenivasan and Meneveau [185] showed. In the study of dynamical systems, a strange attractor refers to an attractor with a fractal structure corresponding to a space where the dynamical system irreversibly evolutes without perturbations. This formalism is commonly used to study the behavior of large chaotic dynamical systems. However, this theory is beyond the scope of this work, more details can be found in the previous reference papers.

Moreover, due to the strong similarities with the flow transitions from laminar to turbulent state, coherent features can also be seen as flow instabilities and then as unstable modes of a basic laminar mean flow as Gaster et al. [71] showed with the linear inviscid stability theory applied to a turbulent mixing layer configuration. However, even if the results are significant, Fiedler [64] noticed that applying inviscid stability theory on mean profiles does not have physical significance for turbulent flows.

Concerning simple flow configurations, the morphology of coherent structures can be reduced to a combination of elementary elements that are presented in Fig. 2.3 as:

- **Line vortex:** A vortex line or vorticity line is a line which is everywhere tangent to the local vorticity vector. Vortex lines are defined by the relation:

$$\frac{\mathrm{dx}}{\omega_x} = \frac{\mathrm{dy}}{\omega_y} = \frac{\mathrm{dz}}{\omega_z}, \tag{2.1}$$

  where $\boldsymbol{\omega} = (\omega_x, \omega_y, \omega_z)$ is the vorticity vector in cartesian coordinates.
- **Ring vortex:** A : vortex ring, also called a toroidal vortex, is a torus-shaped vortex, that is a region where the fluid mostly spins around an imaginary axis line that forms a closed loop.
- **Hairpin vortex:** Hairpin vortices are found on top of bulges on wall bounded turbulent flows, wrapping along the wall in hairpin shaped loops.
- **Helical vortex:** Vortex with helical streamlines.

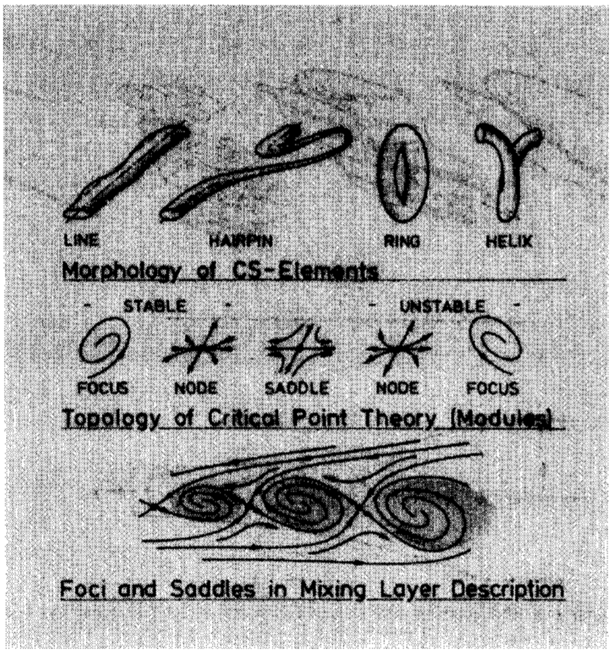

FIGURE 2.3: Morphological and topological elements for the description of coherent structures [64]

Using the theory of critical points of Poincaré [155], Perry and Fairly [152] and others [153, 40] introduced tools that enable to describe the topology of coherent structures. Indeed, Fig. 2.3 shows that coherent structures can be characterized as combinations of stable or unstable nodes, saddles and foci elements. The next sub-section attempts to briefly present some well-known coherent structures in canonical flow configurations.

2.2.3 Coherent structures identification methods

Before trying to detect coherent features from turbulent flows, it is mandatory to understand how to access to their physical behaviors. Indeed, all detection methods necessitate relevant data that have to characterize the underlying physical phenomena and thus the properties of coherent features. The following sub-section aims at presenting three classical approaches for gathering the needed flow information.

2.2.3.1 How to access to coherent structures relevant informations

Visualizations method First, the most simple method in order to access to coherent structures deals with the visualization of events using tracers with negligible molecular viscosity and same density for incompressible flows and Schlieren for compressible flows as the one obtained by Brown and Roshko [24]. On the one hand, tracers as dye or smoke strongly depend on the location of the seeding so that the tracer follows the vorticity, leading therefore to the visualization of streak-lines pictures. Moreover, those streak-lines have been shown to be equivalent to lines of constant vorticity for negligible fluid viscosity as Michalke [138] presented for transition region of a laminar mixing layer. However, some studies have demonstrated that the interpretation of these results is not always straightforward as the dynamics of coherent structures temporally changes [84] or if the seeding location is changed [39]. On the other hand, Schlieren technique, based on the deflection of light by a refractive index gradient that may directly be linked to the flow density gradient, provides integrated information that blot out small scale features while emphasizing two-dimensional coherent structures, contrarily to the smoke visualization which provides more local small-scale informations.

Velocity measurements The detection of coherent structures can also be experimentally managed with quantitative methods that enable to determine the velocity field.

Hot Wire Anemometry is based on the measurement of the heat transfer from a heated wire to the relatively cold surrounding fluid. Then, as the heat transfer is a function of the velocity field, a relationship between the velocity and the electrical output of the system can be established. This intrusive low cost method enables to access to a time-continuous signal with the chosen time sampling. However, this approach is very sensitive to external perturbations encountered in non-ideal applications such as dust or noise.

The Particle Image Velocimetry (PIV) is an optical method of flow visualization. It enables to access to instantaneous velocity measurements with fluid properties. The basic principle deals with the seeding of small particles with very low Stokes number. Then a laser illuminates these particles leading to two-dimensional or even three-dimensional velocity field measurements. This method can be combined with other detection methods that will be presented hereafter.

Scalar measurements such as temperature or pressure can also be considered as relevant. Antonia et al [4] successfully demonstrated the use of the temperature as a passive scalar in order to detect coherent features. Moreover, the pressure field have turned useful for most flow control in aeroacoustic configurations.

Numerical simulations (RANS, LES & DNS) Finally, Reynolds-Averaged Navier-Stokes, Large-Eddy Simulations or Direct Numerical Simulation enable to access to the three-dimensional fields of all variables of interest leading to a good spatial and time discretization of the information. Some attempts in a turbulent jet configuration has been made by Long et al. [126].

2.2.3.2 Detection methods

One of the major difficulties, when attempting to detect coherent structures in turbulent flows, comes from the scale separation that cannot easily be achieved with variables such as pressure or velocity fields and its derivates.

In the years 1945-1960, most of the studies about coherent structures were experimental and based on local Eulerian measures with hot wire anemometry techniques associated to classical probabilistic approaches of the turbulent agitation. Then, as explained Townsend [194], from those experimental information and properties, the structure and the location of coherent structures were deducted in order to validate the observation.

Since the 1960s, the developments in the optical, electronic and computer science fields allowed to extract from the turbulent chaos structural organized elements. A complete overview of those methodologies has been proposed by Bonnet and Delville [19]. Furthermore, contrarily to the previous case, the structure and location of coherent features are available leading to attempt to deduct their physical properties and their impact on the turbulent flows.

Moreover, from Delville et al. [57] overview, such detection methods can be classified into two categories presented in Fig. 2.4. All these methods, combined with morphological information, enable to understand the dynamics of coherent structures and their contributions and interactions with the turbulent transport processes. First, conditional approaches enable to access to the main characteristics of coherent features by detecting their presence when a chosen condition/criterion is fulfilled. This methodology is quite subjective as it requires some information on the flow characteristics in order to define a relevant threshold condition. Second, non-conditional approaches are more objective as they deal with the determination of statistical information, as space-time correlations, in order to access to the characteristics of the coherent structures. Some of these detection methods are briefly introduced in the following paragraphs.

After 1980, the signal processing and the time-frequency analysis of the fluid information from both experiments and numerical simulations appeared, leading to more selective analysis of the available data. Some of those methods are presented hereafter.

The Fourier transform : The Fourier transform has been introduced by Joseph Fourier in his study of heat transfer [65], where Gaussian functions appear to be solutions of the heat equation. This tool represents an original signal in the frequency domain and is called spectrum for physical phenomena. Moreover, the Fourier decomposition can be seen as being the natural tool in order to provide optimal flow representation for homogeneous or periodic flow fields [131]. For time-varying signals, a low-pass filtering procedure should be applied to avoid aliasing effects due to Shannon-Nyquist's sampling

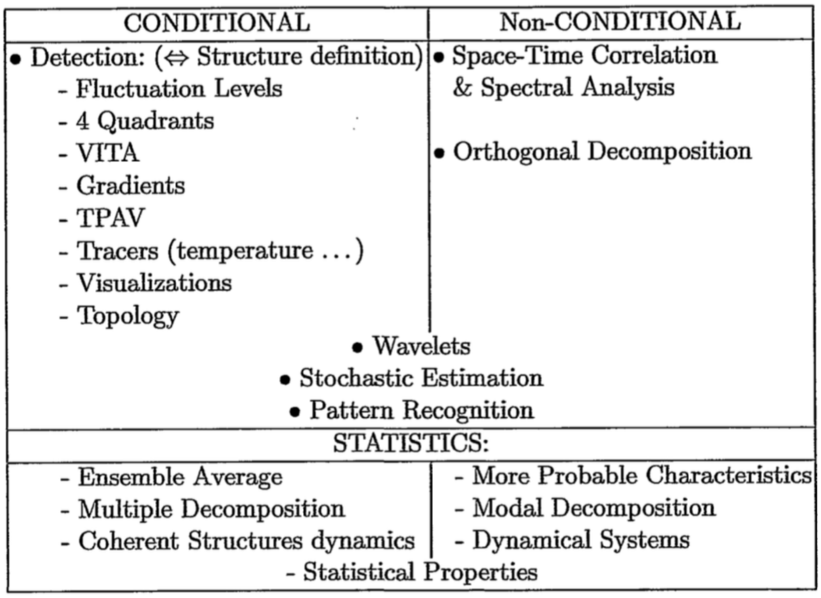

CONDITIONAL	Non-CONDITIONAL
• Detection: (⇔ Structure definition) - Fluctuation Levels - 4 Quadrants - VITA - Gradients - TPAV - Tracers (temperature ...) - Visualizations - Topology	• Space-Time Correlation & Spectral Analysis • Orthogonal Decomposition
• Wavelets • Stochastic Estimation • Pattern Recognition	
STATISTICS:	
- Ensemble Average - Multiple Decomposition - Coherent Structures dynamics	- More Probable Characteristics - Modal Decomposition - Dynamical Systems
- Statistical Properties	

FIGURE 2.4: Classification of detection methods from Delville et al. [57]

theorem. However, homogeneous or periodic conditions is rarely fulfilled in turbulent flows which shows the limitation of this method.

The wavelet transform: The wavelet transform method, described in details by Farge [62] and Vasilyev [179] is based on a time-frequency analysis. Wavelet decomposition aims at finding, in a signal, structures that resemble a reference function (mother wavelet), and a set of functions (child wavelets) obtained by shifting and scaling this mother wavelet. The data resulting of the correlation of these functions with the signal (wavelet coefficients) provides spatial and temporal information. The advantage of wavelet transform over classical Fourier transform is its ability to represent functions that have discontinuities and sharp peaks, and to accurately reconstruct non-periodic signals. Orthogonal wavelet decomposition has been used to process turbulent flows and only keep the Gaussian part of the turbulent flow field [63, 178].

The Adjoint method: Adjoint methods are linear approaches that have been designed in order to perform sensitivity analysis for Partial Derivative Equation (PDE) for a wide range of application domains including hydrodynamic stability. It enables to identify regions of the flow that produce oscillations or instabilities and regions that are most sensitive to external forcing. This can be achieved by linearizing the Navier–Stokes equations around a base flow, enabling to build an operator that characterizes the evolution of small perturbations in the flow. Then, computing the eigenvalues of this operator gives access to the frequency and the growth rate of the perturbations and the eigenfunctions give their spatial shapes. More information and some applications can be found in [33] and [187].

Filtering approach: Spatial filters are based on the extraction of turbulent scales at a given size [146, 120]. Performing the scale separation may not be straightforward for numerical simulations as it requires to extract features from a large amount of data that can be shared across a large number of processors in a parallel environment. Moreover, filters necessitate a sharp cutoff frequency - that means a good selectivity behavior - in order to keep untouched the useful information while removing the other part.

Various high-order filters have been proposed in the past as explicit filters up to order 16 derived by Shapiro [182, 181] in the 70s. These low pass non-recursive filters have been used in the meteorological field and enable to remove small scale features without affecting physical structures. Recursive filters with high selectivity have also been widely studied [26, 87, 151]. In the 90s, Raymond et al. [160, 159] designed implicit high-order filters for the analysis of weather data. Their implicit formulation is particularly interesting as it enables to obtain high-order filters from low-order finite-difference schemes on compact stencils and also enables to overcome the boundary conditions issues.

Chapter 4 will present in details the key concepts and the mathematical background of spatial low-pass filters through the development of a multi-grid framework based on several steps of high-order filtering and interpolation methods in order to extract large-scale features from highly turbulent flows.

Modal decomposition methods The visualization of coherent structures can be achieved thanks to modal decomposition methods that enable to extract the dominant modes of the flow. These methods are particularly interesting when attempting to analyze the dynamics of the large-scale features. However, they require the storage of a large amount of data and thus cannot be applied on billion cells LES simulations without sub-sampling. Moreover, it is generally mandatory to apply some temporal or spatial filtering before applying modal decomposition methods in order to remove high-frequency motions and aliasing issues.

Chapter 5 will present in details the mathematical background of modal decomposition methods such as Proper Orthogonal Decomposition (POD) [17] and Dynamic Mode Decomposition (DMD) [167] with applications in LES of flows over 2D laminar cylinder and 3D turbulent turbine blade.

Vortex identification in turbulent flows: Finally, considering the definition of Hussain et al. [90, 91], coherent structures are strongly related to regions of high vorticity in the flow. Even if there is no universal threshold defining a high level of vorticity, this criterion seems to be relevant and is commonly used in various applications. However, some shortcomings have to be highlighted : in shear zones close to the boundary, the strain due to the viscosity locally produces high level of vorticity without the presence of vortices. In that particular case, other criteria can be used such as the Q-criterion.

The next section presents with more detail the concepts and methods associated to that class of identification methods, which are based on vortical property and on velocity gradient tensor formalism.

2.3 Vortical coherent structures in turbulent flows

Coherent structures are usually identified and located by considering the core of vortices. Strawn et al. [186] defined the vortex core as the local maximum of the vorticity modulus which therefore links coherent structures to vortical features. In this section, the definition of vortical coherent structures is first presented using the vorticity concept that is introduced in a second time. Finally, some vortex detection criteria are briefly exposed.

2.3.1 Vortical coherent structures

Based on the definitions of Lesieur [117] and Hussain [91], vortical coherent structures have been defined by Chassaing [34] considering three main properties that are presented hereafter:

(i) **Physical structure property:** Vortical coherent structures correspond to a mass of fluid which is located in a connected fluid domain D_0 at time t_0.

(ii) **Vorticity intensity property :** Vortical coherent structures correspond to a zone where the local concentration of vorticity is higher compared to the narrowing fluid. This intensity can be measured thanks to a characteristic vorticity scale or with the modulus of the rotational vector noted ω.

(iii) **Physical coherence property:** Vortical coherent structures are able to keep those two previous properties for long time scales compared to their turnover time scales. Indeed, due to the viscosity effects, the structural coherence of the vortices tends to be dissipated. This property can be expressed with to the following inequality:

$$\frac{\omega l^2}{\nu_e} \gg 1\,, \tag{2.2}$$

where l refers to the characteristic length scale of the vortex, ν_e to the effective kinematic viscosity scale in the fluid and $\tau = l^2/\nu_e$ the vortex turnover time scale.

2.3.2 Vortex definition and classification

Vortices can be defined as fluid zones where the flow is principally considered as being rotating around an axis. Here, a vortex on the z-axis that evolves in the plane (r, θ) is considered, then the velocity can be decomposed into axial, tangential and azimuthal components. However, most of the time the radial component can be neglected leading to $u_r = 0$. The description of vortices in term of radial profile for the tangential velocity enables to distinguish two main classical models for eddy flows that will be presented just after the notion of vorticity.

The vorticity: Usually noted $\boldsymbol{\omega}$, the vorticity vector is a main concept in the description of the dynamics of vortices. The vorticity field is defined as the curl of the fluid velocity which is mathematically formulated as follows:

$$\boldsymbol{\omega} = \nabla \times \mathbf{u}\,, \tag{2.3}$$

where ∇ is the vectorial differential operator defined as $\nabla = \left(\frac{\partial}{\partial x}, \frac{\partial}{\partial y}, \frac{\partial}{\partial z}\right)$ and $\mathbf{u}$ the velocity field of the fluid.

This physical quantity measures the local rotation rate in the fluid and can therefore be interpreted as the angular velocity seen by a rough ball at that particular point. Moreover, zero values of vorticity modulus refer to fluid zones without vortices, while positive values are located in the center of vortices.

Even if the dynamics of stream-wise vortices can accurately be represented - through their high vorticity modulus - in free shear flows [41], for wall-bounded flows however, the no-slip boundary conditions at the wall produce a mean shear that is generally much higher than the vorticity modulus of the near-wall vortices. In this case, other criteria that circumvent this issue should be used instead. In addition, the realistic behavior of the velocity field in vortices can be a function of the radius r - distance to the vortex core -, the two main classical models of vortex dynamics are presented below:

Rotational vortices: The term "rotational vortices" characterizes the rigid rotation behavior. Indeed, if the angular velocity $\dot{\theta}$ around the z axis is constant in the vortex plane, then the tangential velocity linearly increases with the axis distance:

$$u_\theta(r) = \dot{\theta} r \,. \tag{2.4}$$

The vector field associated to the solid rotation cancels in the center of vortices, leading to a constant vorticity oriented along the z axis with a norm twice equal to $\dot{\theta}$. The circulation Γ of a circle along radius r, that corresponds to the curvilinear integral of the velocity, can therefore be written as

$$\Gamma(r) = \oint_{\mathcal{C}(r)} \mathbf{u}.d\mathbf{l} = 2\pi\dot{\theta} r^2 \,. \tag{2.5}$$

Irrotational vortices: When no external forces are applied, vortices naturally evolve toward an irrotational flow configuration that refers to fluid zones where the tangential velocity is inversely proportional to the radius r. These irrotational vortices are also called free vortices. In that case, the angular velocity is not equal to zero around the vortex axis but the vorticity cancels for each point. Moreover, the circulation Γ of a circle of radius r is constant and independent of the axis distance. The tangential velocity can thus be written as

$$u_\theta(r) = \frac{\Gamma}{2\pi r} \,. \tag{2.6}$$

More realistic models: The velocity fields of both previous vortex models have been plotted in Fig. 2.5 where the dimensionless velocity $u^\star$ is plotted as a function of the radius r of the vortex:

$$u^\star(r) = \frac{u_\theta(r)}{u_m} \quad u_m = \frac{\Gamma}{2\pi R} \tag{2.7}$$

However, in the case of irrotational vortices, the velocity profile increases toward infinity for points located close to the vortex core. This asymptotical behavior does not allow to model and describe in a realistic manner vortices and therefore, this model can not be used in practice. Most of the time, the area in the center of irrotational vortices is characterized by a rotational zone with a velocity profile that decreases toward zero on the z axis.

More complex vortex models have been proposed by Rankine and Lamb-Oseen and are presented hereafter:

- ***Rankine vortices:*** Rankine vortex modeling, plotted in Fig. 2.5, deals with a combination of the two vortex models previously presented. The velocity profile is defined as follows:

$$u_\theta(r) = u_m \frac{r}{R} \quad \text{if} \quad r \leq R \tag{2.8}$$

$$u_\theta(r) = u_m \frac{R}{r} \quad \text{if} \quad r > R \,, \tag{2.9}$$

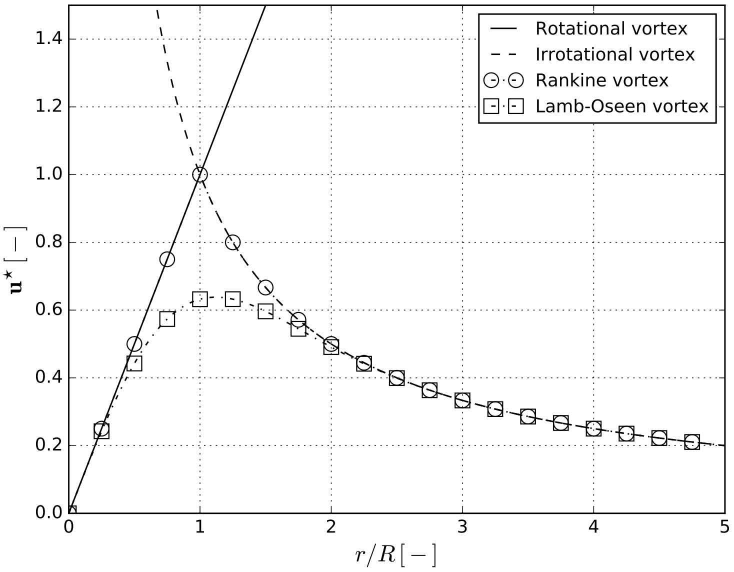

FIGURE 2.5: Tangential velocity models in a vortex

where R refers to the radius of the vortex core. The flow is associated to a rigid rotation in the core ($r < R$) and irrotational out of the core ($r > R$).

- ***Lamb-Oseen vortices:*** Lamb-Oseen vortex modeling, plotted in Fig. 2.5, deals with a rotational vortex associated to viscous effects. The velocity profile is defined as follows:

$$u_\theta(r,t) = u_m \frac{R}{r}\left[1 - \exp\left(-\frac{r^2}{4\nu t}\right)\right]. \tag{2.10}$$

This model assumes cylindrical symmetry and refers to an exact solution of the governing Navier–Stokes equations. It converges to rotational vortices for low radius r and to irrotational vortices for very large radius.

Relation with the pressure As explained in Guedot thesis [81], the velocity field generates a variation of the dynamic pressure in a vortex. Then, under certain hypothesis and using the formula derived by Galley [69], the axial momentum conservation in the plane (r,θ) can be expressed as

$$\rho\frac{u_\theta^2}{r} = \frac{\mathrm{d}p}{\mathrm{d}r}. \tag{2.11}$$

This relation can be combined with the velocity profiles of the Rankine vortex model in order to study the variations of the pressure. Then, the radial profile of pressure in a Rankine vortex can be written as follows:

$$p(r) = p_\infty - \frac{\rho u_m^2}{2}\left(2 - \frac{r^2}{R^2}\right) \quad \text{for} \quad r \le R \tag{2.12}$$

$$p(r) = p_\infty - \frac{\rho u_m^2}{2}\frac{R^2}{r^2} \quad \text{for} \quad r > R. \tag{2.13}$$

First, in the vortex core, the pressure evolves with the square of the axial distance r, moreover, around the vortex core where zones are irrotational, the pressure is inversely proportional to the square of the radius r. In the vortex core, the depression profile, defined as $\Delta p = p(r) - p_\infty$, is represented on the Fig. 2.6. Various vortex detection methods in turbulent flows are based on the pressure difference in the vortex core.

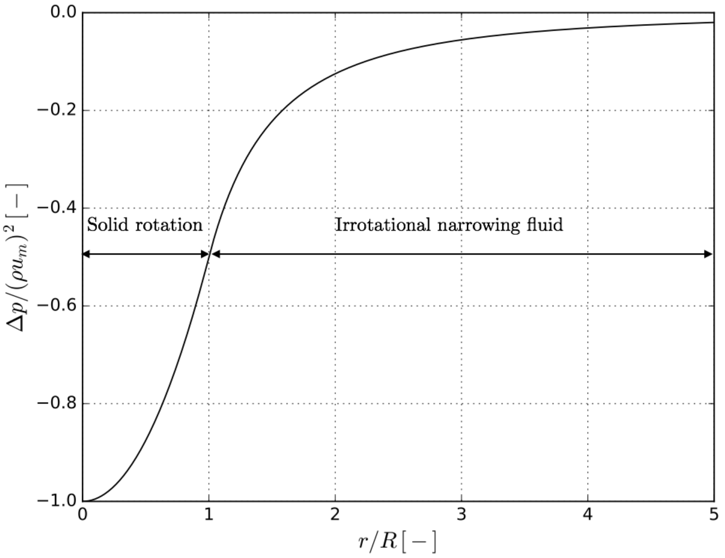

FIGURE 2.6: Analytical radial profile of low pressure region in a Rankine vortex

In a similar manner, the axial variation of the pressure for a Rankine vortex can be characterized with the following expression [127]:

$$\frac{\mathrm{d}p}{\mathrm{d}z} \propto \frac{2\rho}{R^3}\frac{\Gamma^2}{(2\pi)^2}\frac{\mathrm{d}R}{\mathrm{d}z} = 2\rho u_m^2 \frac{1}{R}\frac{\mathrm{d}R}{\mathrm{d}z}\,. \tag{2.14}$$

The vortex contribution to the variation of pressure is positive when the radius of the vortex increases along the z axis. In that case, the pressure grows up along this axis and its gradient can handle a break point in the flow, leading to the creation of a recirculation zone in the vortex core. This well-known phenomenon is called vortex breakdown and appears when the Swirl number reaches critical values. This dimensionless number compares the axial and tangential components of the flows [82] and is defined as

$$Sw = \frac{\mathcal{G}_\theta}{R\mathcal{G}_z}\,, \tag{2.15}$$

where R refers to a characteristic radial dimension of the flow, $\mathcal{G}_\theta$ and $\mathcal{G}_z$ the axial flux of the azimuthal momentum and the axial flux of the axial momentum respectively, that are defined as follows:

$$\mathcal{G}_\theta = \int_0^R \rho u_\theta u_z 2\pi r^2 dr\,, \tag{2.16}$$

$$\mathcal{G}_z = \int_0^R (\rho u_z^2 + p) 2\pi r dr\,. \tag{2.17}$$

Swirl flows are characterized by high tangential velocities that generate radial acceleration leading to a pressure drop at the rotation axis and a radial expansion of the flow - that also decreases the tangential velocity in the axial direction - which generate an opposite pressure gradient in the axial direction. When this pressure gradient becomes too important, then the kinetic energy in the axial direction is no more sufficient and recirculation zones appear. This coupling phenomenon between the axial and radial components of the velocity field has been widely experimentally, theoretically and numerically studied.

2.3.3 Vortex identifiers

Vorticity analysis has been for a long time the only available vortex detection method. As previously mentioned, this simple criterion is based on the gradient of the velocity field and thus does not distinguish vortices from shear layers. Then, other more sophisticated criteria have been developed, some of them are presented hereafter.

The minimum of pressure

Assuming that vortices creates a dynamic pressure that is lower in the vortex core regions, vortical coherent structures can thus be identified through the instantaneous total pressure field $p_{tot} = p + p_{dynamic}$ with p the static pressure and $p_{dynamic} = \rho \mathbf{u}^T \mathbf{u}/2$ the dynamic pressure, or thanks to cavitation processes [12] that deal with the formation of vapor cavities in liquids due to rapid changes of pressure. Using the previous properties (i) to (iii) that characterize coherent vortical structures, the vorticity can be related to the pressure field, which allows to link the coherent features identification to the search of local minima of pressure:

$$\frac{\partial \mathbf{u}}{\partial t} + \boldsymbol{\omega} \times \mathbf{u} = -\frac{1}{\rho} \nabla p_{tot} \,. \tag{2.18}$$

This equation refers to the equilibrium between the centrifugal effects and the pressure gradient for a fluid particle close to a vortex. Assuming the definition of physical coherence (iii) and under the local Galilean invariance property, the ratio between the second and the first terms on the left side in Eq. 2.18 can be approximated as $\tau\omega$ where τ is the vortex characteristic turnover time scale defined as $\tau = l^2/\nu_e$ and ω the vorticity concentration as the modulus of the rotational. Therefore, the previous equation may be reduced to the following form

$$\boldsymbol{\omega} \times \mathbf{u} = -\frac{1}{\rho} \nabla p_{tot} \,, \tag{2.19}$$

that can also be obtained thanks to Eq. 2.18 under stationary flow condition.

Hence, in order to counterbalance the centrifugal effects, the dynamic pressure decreases inside a vortex tube in accordance to Bernoulli's principle. This criterion has been proved being better than the previous vorticity modulus as showed Comte et al. [41] and Robinson [165] with iso-surfaces of pressure while detecting coherent features in a turbulent boundary layer.

However, the use of this criterion may sometimes be problematic as Kida and Miura discussed [105]. Indeed, a minimum of pressure is not a necessary and sufficient condition for the presence of a vortex [96]. This minimum of pressure can be generated by an instationary instability without vortices or can be masked by the viscosity in shear zones near the boundary as it cannot distinguish between pure shearing motions and the swirling motion of a vortex. Moreover, the pressure is an intensive variable which only enables to identify the most intense vortices and fails while attempting to identify others that are disturbed by the dominant structures. As mentioned Dubief et al. [60], it is noticeable that the choice of the pressure threshold is not straightforward as it depends on the dynamic pressure surrounding the local structure. If the concentration of vortical structures is high, this criterion may not detect all the details of the vortical organization. Finally, variations in fluid pressure without the presence of vortices may be due to other factors - for instance Venturi effects that occur when a fluid is flowing through a constricted section - and make the vortex representation through iso-surface of pressure difficult highlighting the limits of this criterion.

The Q-criterion

The Q-criterion proposed by Hunt et al [89] for incompressible flows is based on the second invariant of the velocity gradient tensor $\nabla \mathbf{u}$. This criterion has been chosen in this work as it gathers some properties from both vorticity and minimum of pressure criteria. The Q-criterion is expressed as follows:

$$Q = \frac{1}{2}(||\boldsymbol{\Omega}||_F^2 - ||\boldsymbol{S}||_F^2)\,, \tag{2.20}$$

where $\boldsymbol{\Omega}$ refers to the anti-symmetric rotation rate tensor and $\mathbf{S}$ to the symmetric shear rate tensor of the velocity gradient tensor as

$$\Omega_{ij} = \frac{1}{2}\left(\frac{\partial u_i}{\partial x_j} - \frac{\partial u_j}{\partial x_i}\right) \quad \text{or} \quad \boldsymbol{\Omega} = \frac{1}{2}\left(\nabla \mathbf{u} - \nabla \mathbf{u}^T\right)\,, \tag{2.21}$$

and

$$S_{ij} = \frac{1}{2}\left(\frac{\partial u_i}{\partial x_j} + \frac{\partial u_j}{\partial x_i}\right) \quad \text{or} \quad \mathbf{S} = \frac{1}{2}\left(\nabla \mathbf{u} + \nabla \mathbf{u}^T\right)\,. \tag{2.22}$$

Hence, this criterion enables to measure a local equilibrium between two different types of flows: a rigid rotation and a pure deformation flow that are presented in Fig. 2.7. The competition between the rotation and the strain rate allows to interpret positive values of Q-criterion as a local excess of rotation and then to the presence of a vortical structure. Negative values are therefore associated to shear zones where energy dissipation is the predominant phenomenon. Iso-surfaces of the Q-criterion associated with a positive threshold enables thus to represent the vortex envelopes. Here again, the choice of the threshold has to be carefully determined. Moreover, shear zones as boundary layers are associated to negative values of Q-criterion.

Assuming the definition (ii), the Q-criterion can directly be linked to the vorticity modulus ω as

$$Q = \frac{1}{4}(\omega^2 - 2||\mathbf{S}||_F^2)\,. \tag{2.23}$$

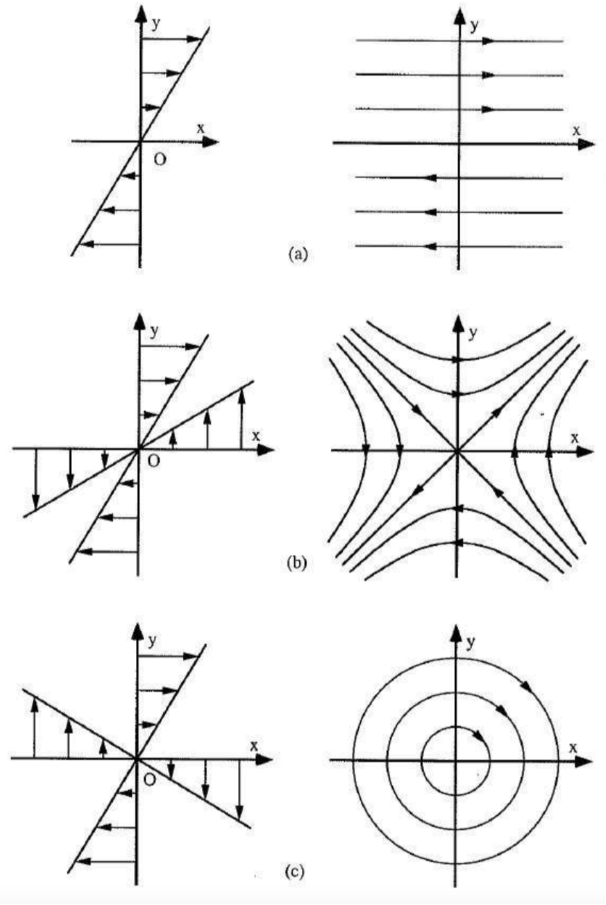

FIGURE 2.7: Flow configurations from [88] with the velocity fields (left) and the streamlines (right): (a) shear flow, (b) pure deformation and (c) solid rotation

This formulation expresses that in a vortex core, the Q-criterion is expected to be positive as the vorticity increases. Moreover, as Dubief et al. [60] explained, it can also be related to the Laplacian of the pressure field for inviscid and incompressible flows as follows:

$$Q = \frac{1}{2\rho}\nabla^2 p \,. \tag{2.24}$$

Hence, maxima of pressure occur for negative Q-criterion values while minima of pressure refer to positive values of the identifier. Jeong and Hussain [96] stated that a minimum of pressure does not necessary implies a region of positive values of Q-criterion, however $Q > 0$ is a necessary condition to a low-pressure tube [60]. Moreover, large negative values of the Q-criterion can also be associated to negative curvatures of the pressure with the presence of a local maximum and large positive values of Q-criterion can be associated to positive curvatures of the pressure leading to the presence of a local minimum. More details about the curvature effects are developed in Chapter 4.

The Δ criterion

Vortical structures can also be defined by considering the eigenvalues of the velocity gradient tensor $\nabla \mathbf{u}$. Indeed, Dallmann [49], Vollmers et al. [201] and Chong et al. [37] showed that complex eigenvalues of $\nabla \mathbf{u}$, noted λ_k, refer to spiraling streamline patterns. Fluid regions where eigenvalues may be complex imply local rotation of $\boldsymbol{\omega}$ and can then be characterized through the inviscid vorticity equation presented hereafter:

$$\frac{D\boldsymbol{\omega}}{Dt} = \boldsymbol{\omega}.\nabla \mathbf{u}\,. \tag{2.25}$$

The eigenvalues of velocity gradient tensor are governed by the characteristic equation defined as

$$\lambda^3 - P\lambda^2 + Q\lambda - R = 0\,, \tag{2.26}$$

where Q refers to the second invariant of the velocity tensor $\nabla \mathbf{u}$ and P, R to the first and third invariants defined with $G = \nabla \mathbf{u}$ as follows:

$$P = \mathrm{tr}\,(G)\,, \quad Q = \frac{1}{2}\left(\mathrm{tr}\,(G)^2 - \mathrm{tr}(G^2)\right), \quad R = \det\,(G)\ , \tag{2.27}$$

where $P = 0$ for incompressible flows.

Equation. 2.26 can have either three real eigenvalues or one real associated with two complex conjugated ones. Moreover, complex eigenvalues are associated to a local rotation rate and also to spiralling streamlines, indicating the presence of a vortex. Those values are linked to a positive value of the discriminant Δ, see Eq. 2.28. Considering incompressible flows, positive values of the Δ criterion can then be expressed through the Cardan method for cubic equations as follows:

$$\Delta = \left(\frac{Q}{3}\right)^3 + \left(\frac{R}{2}\right)^2\ . \tag{2.28}$$

Iso-surfaces of positive values of the discriminant indicate the presence of a vortex with an extremum of Δ in the center of its core.

The λ_2 criterion

This criterion proposed by Jeong and Hussain [96] is based on the search of a minimum of pressure across the vortex. Hence, it enables to link the pressure minima to vortices. This criterion comes from the vorticity transport and the strain-rate transport equations that can be derived by taking the gradient of the Navier-Stokes equations and then decomposing it into symmetric and antisymmetric parts. Using the same previous notation, the symmetric part can be written as follows:

$$\frac{DS_{ij}}{Dt} - \nu\frac{\partial^2 S_{ij}}{\partial x_k^2} + \Omega_{ik}\Omega_{kj} + S_{ik}S_{kj} = -\frac{1}{\rho}\frac{\partial^2 p}{\partial x_i \partial x_j}\,, \tag{2.29}$$

where the right-hand side term $\frac{\partial^2 p}{\partial x_i \partial x_j}$ refers to the Hessian of the pressure and contains informations on the pressure extrema. Indeed, the study of the eigenvalues of this matrix enables to determine if there is an extremum or a node of pressure at a given location. Hence, as Eq. 2.29 shows, the minima of pressure in a plane across a vortex appear when two eigenvalues of the tensor $\nabla\nabla p$ are positive [109].

The λ_2 criterion for incompressible flows can be built by removing the unsteady irrotational straining $\frac{DS_{ij}}{Dt}$ and the viscous effects $\nu\frac{\partial^2 S_{ij}}{\partial x_k^2}$ from the above equation leading to a vortex presence when two eigenvalues of the tensor $\mathbf{S^2} + \mathbf{\Omega^2}$ are negative. Since this tensor is symmetric, it possesses only real eigenvalues that can be ordered in the following form:

$$\lambda_1 \geq \lambda_2 > \lambda_3 \tag{2.30}$$

Then, the vortex-identification criterion can be defined as $\lambda_2 < 0$ for incompressible flows. As for the Q-criterion, the chosen value for the threshold appears to be the key main parameter in order to identify coherent features. Moreover, in two-dimensional flows, these two criteria are analytically equivalent [44]. Finally, the λ_2 criterion has been extended with different thresholds in order to correctly capture vortices in the presence of strong shear that can occur in boundary layer or near walls [97].

2.4 Limitations and introduction to new identification approaches

2.4.1 Vortex identifiers limitations

Recently, various limitations of the previous identification criteria have been pointed out and some new general requirements have been formulated such as the validity for compressible and variable-density flows, non-local properties, the determination of the local intensity of the swirling motion and so on... A review is beyond the scope of this thesis but Václav [109] proposed a complete overview of those limitations with the presentation of several variations of these classical criteria.

In the context of this work, the limitation that may strongly be highlighted deals with the use of these criteria with highly-resolved turbulent simulations. As presented in the introduction, due to the constant increase of the computational resources, the quantity of data generated by numerical simulations has become so large that it has drastically complicated the visualization of coherent features from fully turbulent flows using these criteria. For instance, while the Q-criterion successfully extracts the largest vortices in laminar flows or in LES with coarse meshes, its fails at identifying the large scale dynamics in very refined simulations. As Guedot presented in this thesis [81], this criterion is no more sufficient to extract large-scales from well-refined simulations as shows Fig. 2.8. Here, the large-scale coherent features, that can distinctly be seen on the first left column, are hidden by the smallest scales as the mesh resolution increases.

This issue comes from the scaling of the Q-criterion, which is larger for small vortices than for energy carrying eddies in an isotropic homogeneous turbulence. This can be shown using a simple vortex theory such as the Lamb Oseen vortex. In this case, the velocity in the circumferential direction θ is defined as $u_\theta(r,t) = \Gamma/(2\pi r)\left(1 - \exp(-r^2/r_c^2)\right)$ where Γ is the circulation and r_c the radius of the vortex core. The maximum of the Q-criterion is found at the center of the vortex as the shear component vanishes with $Q_{max} \sim \Gamma^2/r_c^4$. The enstrophy $\mathcal{E}$, i.e. the integral of the squared vorticity, for this vortex is equal to $\Gamma^2/(2\pi r_c^2)$. In the inertial range of homogeneous isotropic turbulence, enstrophy scales as $k^{1/3}$, which implies that the Q-criterion maximum scales as $k^{7/3}$. With this scaling, small vortices have higher values of Q-criterion than large scales. Then, in highly-resolved LES, the small vortices might completely mask large vortices when plotting Q-criterion iso-surfaces.

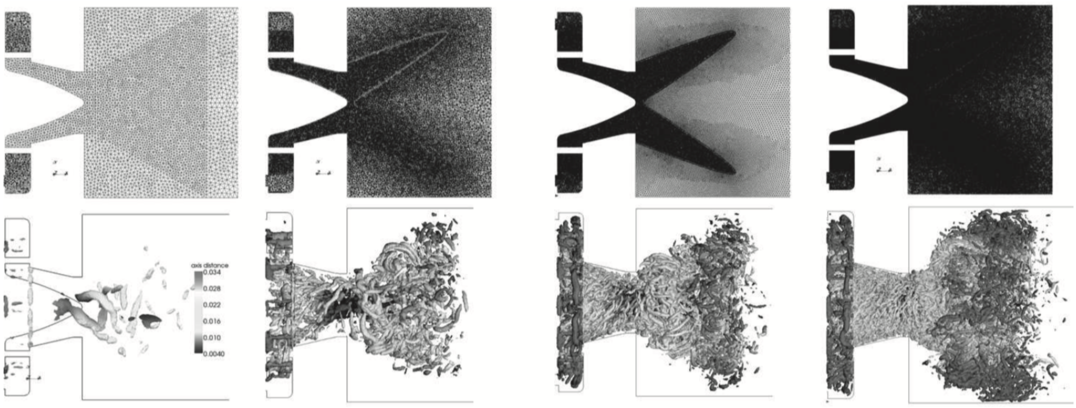

FIGURE 2.8: Q-criterion iso-contour $Q = 0.32 \times 10^8 s^{-2}$ on 4 meshes 1.7 million cells (first column), 14 million cells (second columns), 41 million cells (third column) and 110 million cells (fourth column) from Guedot thesis. [81]

As a consequence, classical vortex identifiers can no more be used in such refined simulations without relevant processing procedure. Hence, the study of large-scale features through vortex identifier in well-resolved turbulent flows has to be performed once the dataset has been reduced thanks to performant extraction tools.

2.4.2 Extraction tools for large amount of data

Besides the large amount of data generated by highly-resolved simulations, it is mandatory to efficiently analyze this huge mass of information and to select the most relevant features. Therefore, some classical post-processing tools in CFD field that attempt to circumvent these issues are here briefly presented:

- **Selective Sampling:** This tool deals with the extraction and the writing on the computer hard-drive of a localized part of the available data. Hence, it is possible to only recover local information such as on a point, a line, a plane or an iso-surface etc ... This method allows to drastically reduced the amount of data that have to be stored. However, this basic extraction tool is not able to circumvent the vortex criterion scaling issue. For instance, iso-surfaces of vorticity from billion-cell DNS of three-dimensional homogeneous isotropic turbulent flow [101] result in extremely noisy and complex pictures of the flow that are hardly exploitable for the analysis of the turbulence dynamics
- **Level-Set:** Level-Set methodologies are powerful numerical methods created in order to provide an implicit and dynamic representation of surfaces [180]. These methods may be applied in various domains of the fluid mechanics, such as spray flows highlighted here with Fig. 2.9, but also in the field of computer assisted animations or for image processing applications. However, this method can only be used for two-phase flows and thus is not applicable to large-scale features representation.
- **High-Order Filter (HOF):** Another method that enables to extract the large-scale features from a flow consists in applying efficient low-pass filters. In that case, the filters require high selectivity to damp the smallest structures while keeping the largest one intact. As presented in Fig. 2.10, Guedot [81] developed during her thesis an unstructured high-order filtering process

FIGURE 2.9: Geometry of the injector and simulated liquid sheet for the Triple Disk Injector on a 1.6 billion tetrahedral cells grid from [135]

that successfully extracts the Precessing Vortex Core [156] (PVC) in a very challenging swirl flow configuration. As the present work strongly refers to the filtering notion, it will be further detailed in Chapter 4.

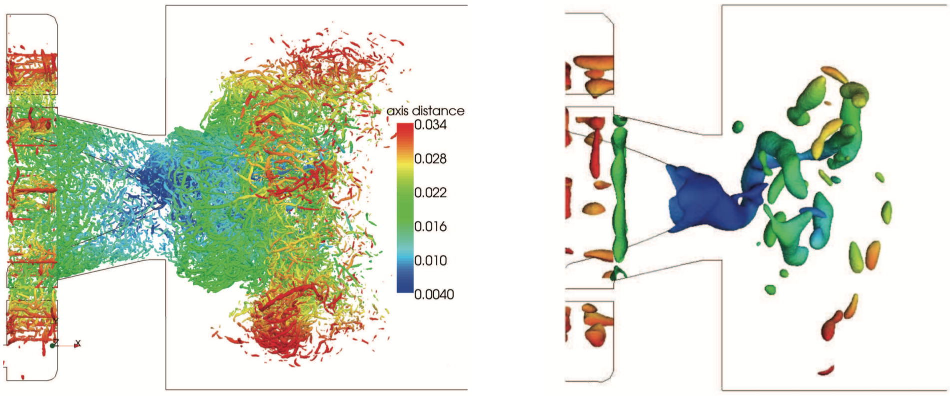

FIGURE 2.10: Unfiltered Q-criterion iso-surface (left) and filtered Q-criterion with the HOF filters (right) coming from the 878 million-cell LES from Guedot Thesis [81]

- **Modal decomposition methods :** The large-scale visualization and extraction may be achieved thanks to the application of modal decomposition methods such as POD [167] or DMD [175]. Such methodologies have been developed and used during this thesis and will be presented in details in Chapter 5.

Finally, the combination of selective sampling and high-order filters or the application of modal decomposition methods can both circumvent vortex identifiers scaling issue and dataset reduction. However, the application of these extraction tools on billion-cell simulations are extremely expensive and therefore cannot be performed in a reasonable way in such simulations. Hence, the main idea of this work is to combine these methods with multi-level approaches that may provide important cost reduction.

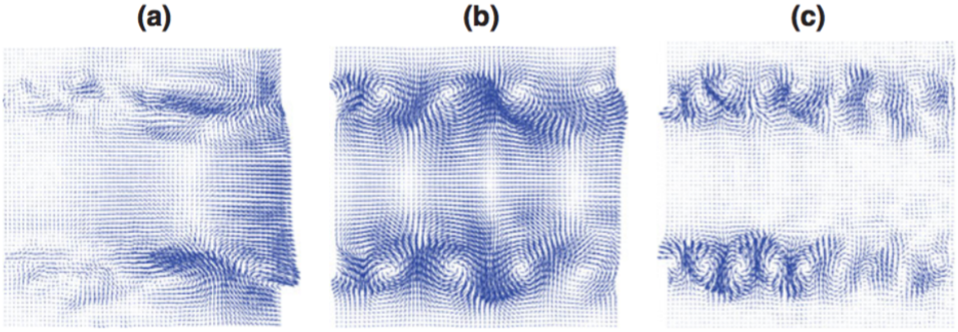

FIGURE 2.11: Selected dynamic modes of a harmonically forced axisymmetric jet from [176]

2.4.3 Multi-level approaches

Since the past decades, interesting new coherent feature processing methods have been developed in order to visualize and to extract large-scale features for highly resolved turbulent LES. Based on a multi-scale filtering approach, Bürger et al. [25] attempt to illustrate basic mechanisms of the inertial range turbulence by showing small structures advected by larger ones, while being sheared and twisted by the previous ones. This procedure is based on several filtering steps of the instantaneous velocity field using a box filter. On the one hand, the instantaneous velocity field is first filtered at scale l_1, then the computation of iso-surfaces of the Q-criterion associated to the threshold $Q > q_1$ enables to delimit the fluid domain $\mathcal{D}_1$. On the other hand, the instantaneous velocity field is filtered again at a different scale $l_2 < l_1$ that refers to another fluid domain $\mathcal{D}_2$ where $Q > q_2$. Using semi-transparent representation of the domains $\mathcal{D}_1$ and $\mathcal{D}_2$, the proposed methodology enables thus to visualize vortices within vortices as Fig. 2.12 shows. The transparent grey features refer to the large-scales vorticity while the green and red features deal with the small-scale vorticity in alignment and off-alignment respectively.

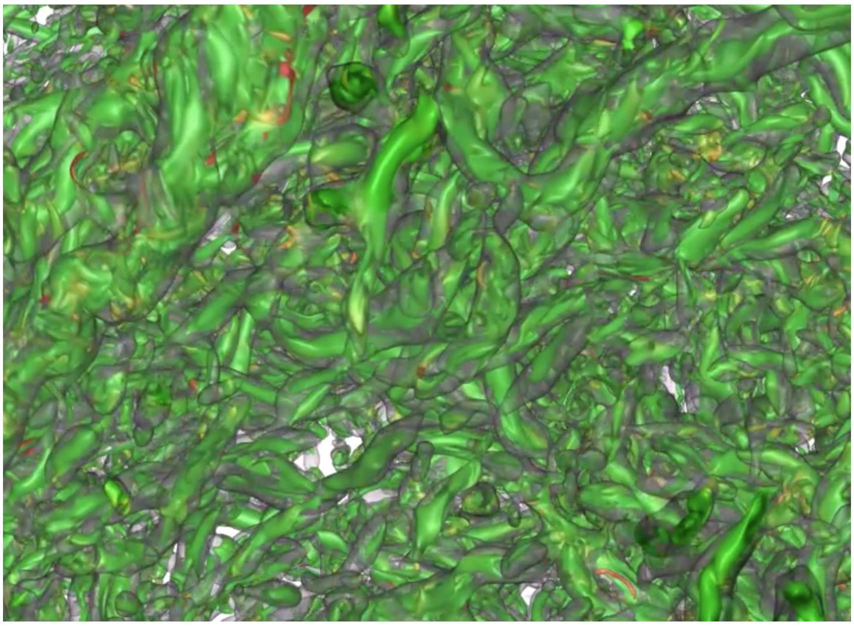

FIGURE 2.12: Vortices within vortices from [25]

However, it is noticeable that the filtering process of this methodology is based on second-order box filters. These filters are not suitable for large-scale extraction of coherent features as they also damp the lowest frequencies present in the flow. This is due to their very low selectivity that produces a very smooth cutoff frequency while sharpness is of paramount importance in that case.

Finally, this work aims at presenting an improvement to these formalisms with the proposal of two multi-level frameworks for the on-the-fly co-processing of highly resolved simulations. On the one hand, the proposed MGHOF framework combines the multi-level approach with velocity-gradient tensor formalism and high-order filters in order to extract and visualize the large-scale features from well-resolved simulations with a drastically reduction of the CPU cost. Thanks to this approach, modal decomposition methods can thus be applied on a reduced dataset leading to the identification of the most dominant dynamically modes in turbulent flows. On the other hand, the second proposed framework, called MR-LES, is also based on the multi-level formalism as it performs several simulations at different scale resolutions simultaneously in order to generate optimized grid for the simulation. Hence, these methodologies attempt to bring deep insights to overcome Big Data issues in highly refined numerical simulations. This manuscript presents in chapter 4, 5 and 6 the development of these new multi-level approaches for the next generation of post-processing tools.

Chapter 3

Governing equations and modeling of turbulent incompressible flows

This third chapter presents the fundamental mathematical background of fluid dynamics. The general concepts and hypothesis of the Navier-Stokes formalism are exposed in a brief introduction. Then, the first main section of this chapter deals with the numerical modeling for turbulent flows. The balance equations for mass, momentum, species and energy are presented, followed by an introduction to the fundamental mechanisms of turbulence such as the Richardson's energy cascade concept and Kolmogorov's hypothesis. Moreover, the most common numerical methods for the simulation of turbulent flows are also presented with a focus on the LES filtered equations and on the sub-grid scale closure models. Finally, the second and last section presents the CFD YALES2 code and some of the main tools and strategies adopted with some highlights on the numerical schemes and solvers used during this thesis.

Contents

3.1 Numerical modeling for the turbulent flows

3.1.1 Equations of conservation

In a continuous medium, the fluid dynamics is governed by the Navier-Stokes equations which can rigorously be deducted from the statistical mechanics and from fundamental principles such as the mass, momentum, species and energy conservation equations. This derivation is not straightforward and can be found in [18, 74] or [86]. All these equations are expressed hereafter using the conservative form and Einstein's notation.

- **The mass conservation** is described through the continuity equation defined as follows:

$$\frac{\partial \rho}{\partial t} + \frac{\partial \rho u_i}{\partial x_i} = 0 \,. \tag{3.1}$$

- **The momentum conservation** is expressed as

$$\frac{\partial \rho u_j}{\partial t} + \frac{\partial \rho u_i u_j}{\partial x_i} = -\frac{\partial p}{\partial x_j} + \frac{\partial \tau_{ij}}{\partial x_i} \,, \tag{3.2}$$

where τ_{ij} refers to the viscous tensor that may be expressed for Newtonian fluids as

$$\tau_{ij} = \mu \left(\frac{\partial u_i}{\partial x_j} + \frac{\partial u_j}{\partial x_i} \right) - \frac{2}{3} \mu \frac{\partial u_k}{\partial x_k} \delta_{ij} \,, \tag{3.3}$$

with μ the dynamic viscosity of the mixture and δ_{ij} the Kronecker symbol.

The addition of the pressure contribution to the viscous stress tensor is used to define the constraint tensor $\boldsymbol{\sigma}$ stress expressed as follows:

$$\sigma_{ij} = \tau_{ij} - p\delta_{ij} \,. \tag{3.4}$$

Then, the strain viscous tensor $\mathbf{S}$ and its deviatoric part $\mathbf{S}^D$ are defined as follows:

$$S_{ij} = \frac{1}{2} \left(\frac{\partial u_i}{\partial x_j} + \frac{\partial u_j}{\partial x_i} \right) \quad \text{and} \quad S_{ij}^D = S_{ij} - \frac{1}{3} S_{kk} \delta_{ij} \,. \tag{3.5}$$

Finally, the previous momentum balance equation 3.2 can thus be written as

$$\frac{\partial \rho u_j}{\partial t} + \frac{\partial \rho u_i u_j}{\partial x_i} = -\frac{\partial p}{\partial x_j} + \frac{\partial}{\partial x_i} \left[2\mu S_{ij}^D \right] \,. \tag{3.6}$$

- **The species conservation** refers to the mass conservation applied to each chemical species and can thus be formulated as

$$\frac{\partial \rho Y_k}{\partial t} + \frac{\partial \rho u_i Y_k}{\partial x_i} = \frac{\partial \mathcal{F}_{k,i}}{\partial x_i} + \dot{\omega}_k \,, \tag{3.7}$$

with Y_k the mass fraction of the species, $\mathcal{F}_{k,i}$ the diffusive flux of the species in the i direction and $\dot{\omega}_k$ the species chemical source term.

- **The energy conservation** may be presented through different expressions depending on the considered variable. Here, the specific sensible enthalpy noted h_s has been chosen as all computations in this thesis have been done under constant pressure assumption. It can be defined through the specific heat capacity C_p as follows:

$$h_s(T) = \int_{T^0}^{T} C_p(\theta) d\theta \,. \tag{3.8}$$

Then, the energy conservation of the mass sensible enthalpy can be written as

$$\frac{\partial \rho h_s}{\partial t} + \frac{\partial \rho u_i h_s}{\partial x_i} = \frac{Dp}{Dt} + \frac{\partial Q_i}{\partial x_i} + \tau_{ij}\frac{\partial u_i}{\partial x_j} + \dot{\mathcal{Q}} + \dot{\omega}_T \,, \tag{3.9}$$

where Q_i refers to the diffusive flux in the i direction, $\dot{\omega}_T$ to the chemical source term, $\dot{\mathcal{Q}}$ to the heat source term and finally the operator $D./Dt = \partial./\partial t + u_i \partial./\partial x_i$ as the particulate derivative. More details can be found in [156].

3.1.2 Introduction to turbulence

3.1.2.1 Laminar versus turbulent flows

In 1883, the pioneer Osborne Reynolds [161] was the first to identify two different states of fluid. Indeed, in flows characterized by low velocities, the small perturbations are immediately damped due to the molecular viscosity which tends to maintain the organized property of the fluid. In that case, the flow is called laminar and is characterized by regular parallel fluid particle trajectories. When the velocity increases, the fluid viscosity and can no longer dissipate these perturbations which are amplified by several instability mechanisms. Hence, the flow evolves from the laminar flow regime to the turbulent state, which is characterized by chaotic, aleatory and intermittent behaviors associated to a large range of temporal scales and 3D spatial structures. However, the same set of equations - the Navier-Stokes model - can be used to describe both laminar and turbulent flow regimes and the transition between these two states can be explained regarding the non-linearity aspects of these equations.

The turbulent behavior of the flows may be quantified by comparing the inertial forces, that tend to disrupt the flow and create new turbulent scales, to the viscous forces that set against the fluid movement and dissipate the structures. The dimensionless Reynolds number enables to quantify the competition between these phenomena and is defined hereafter:

$$Re = \frac{uL}{\nu} \,. \tag{3.10}$$

In this expression, u refers to the characteristic velocity scale of the flow, L to a characteristic length of the configuration and ν represents the kinematic viscosity of the fluid. Hence, small Reynolds numbers are associated to laminar flows while large ones correspond to turbulent flows. The next sub-sections introduce the mathematical background and concepts of turbulent flows and a complete overview of the subject can be found in the seminal book of Pope [157].

3.1.2.2 The Richardson's energy cascade

The energy cascade concept of Richardson can be summarized with the following statement: turbulence is composed of eddies of different sizes. Here, the notion of eddies refers to a coherent turbulent motions localized within a region of size l, that can also contains smallest eddies. The velocity scale associated to these eddies noted $u(l)$ enables to define their turnover timescale as $\tau(l) \equiv l/u(l)$.

The energy cascade infers that the large eddies are unstable and, at the end of their turnover timescales, will break up into various smaller eddies while transferring their energies to them. The same process also happens to these smallest eddies that turn into more smaller ones. Therefore, the successive energy transfer from the largest scales to the smallest ones illustrates the energy cascade concept of Richardson. This process occurs until the molecular viscosity of the fluid becomes stronger than the inertial forces at the smallest scales of the flow, dissipating the kinetic energy. In 1922, Richardson [162], parodying a poem of Jonathan Swift, intrinsically describes the vortex interactions of the turbulence as

> *Big whirls have little whirls*
> *that feed on their velocity,*
> *And little whirls have lesser whirls*
> *and so on to viscosity,*
> *(in the molecular sense).*

Although the dissipation may be seen as the final step of the energy cascade, this dissipation rate is however determined by the first step of the cascade through the energy transfer from the largest eddies. Indeed, these so-called energetic eddies, defined with the characteristic length,velocity and timescale l_0, u_0, τ_0 respectively, have a kinetic energy of order u_0^2 that dissipates at rate τ_0 leading to the estimation of the dissipation rate $\epsilon \equiv u_0^2/\tau_0 = u_0^3/l_0$ that is independent of the kinematic viscosity ν of the fluid.

3.1.2.3 Kolmogorov hypothesis

Although the Richardson's cascade gives some understanding of the turbulent process, some questions remain unanswered such as the size of the smallest eddies that dissipate the kinetic energy but also the evolution of the velocity $u(l)$ and timescale $\tau(l)$ as the eddy characteristic length scale l decreases. The theory advanced by Kolmogorov [111] attempts to answer these questions and is based on three hypotheses that are exposed hereafter using the notation of Pope [157]:

Local isotropy hypothesis: "*At sufficiently high Reynolds number, the small-scale turbulent motions ($l << l_0$) are statistically isotropic.*"

This first hypothesis deals with the isotropy of the small-scale motions and means that, in general directional biases, such as boundary conditions or information about the geometry responsible of the anisotropic behavior of largest eddies, are lost in the energy cascade and do not affect the smallest scales anymore, leading to universal statistics and thus isotropic behavior. The length scale that demarcates the anisotropic and isotropic scales is both noted l_{EI} or l_t, also known as the integral scale, and may be evaluated as $l_{EI} \approx \frac{1}{6} l_0$. The anisotropic range is called the energy-containing range. As the most important processes of the energy cascade are the transfer of energy and the dissipation, this universal state of the smallest scale motions may depend on the rate at which the scales receive energy from the large scales noted $\mathcal{T}_{EI}$ but also on the dissipation rate ϵ through the kinematic viscosity ν that is assumed to be nearly equal $\epsilon \approx \mathcal{T}_{EI}$. This can be stated as follows:

First similarity hypothesis: "*In every turbulent flow at sufficiently high Reynolds number, the statistics of the small-scale motions ($l < l_{EI}$) have an universal form that is uniquely determined by ν and ϵ.*"

Considering the isotropic scales with $l < l_{EI}$, their states are characterized as an universal equilibrium range as their timescales $\tau(l) = l/u(l)$ are small in comparison to $\tau_0 = l_0/u(l_0)$. Indeed, the smallest eddies can quickly be adapted to maintain the dynamics equilibrium with the energy-transfer rate $\mathcal{T}_{EI}$ coming from the largest eddies. The Kolmogorov scales that characterize the smallest dissipative eddies can thus be defined by only using the dissipation rate ϵ and the kinematic viscosity ν as

$$\begin{aligned} \eta_K &\equiv (\nu^3/\epsilon)^{1/4}\,, \\ u_K &\equiv (\epsilon\nu)^{1/4}\,, \\ \tau_K &\equiv (\nu/\epsilon)^{1/2}\,. \end{aligned} \tag{3.11}$$

The Reynolds number based on the Kolmogorov scales can be defined as being equal to unity as at this scale, the inertial motions forces are balanced by the molecular viscous effects.

$$Re_K = \frac{\eta_K u_K}{\nu} \approx 1\,. \tag{3.12}$$

Moreover, the dissipation rate can thus be reformulated using the Kolmogorov scales [157] as

$$\epsilon = \frac{\nu u_K^2}{\eta_K^2} = \frac{\nu}{\tau_K^2}\,, \tag{3.13}$$

with $(u_K/\eta_K) = 1/\tau_K$ a good approximation of the velocity gradients for dissipative eddies.

When the Reynolds number increases, the ratio η_K/l_0 becomes smaller and some range of scales l are small compared to the largest eddies l_0 and very large compared to the Kolmogorov scale η_K, therefore very little affected by the dissipative effects. The state of these scales is characterized as follows:

Second similarity hypothesis: "*In every turbulent flow at sufficiently high Reynolds number, the statistics of the motions of scale l in the range $l_0 >> l >> \eta_K$ have a universal form that is uniquely determined by ϵ independent of ν.*"

Here, the length scale l_{DI}, also noted l_d, is introduced to split the universal equilibrium range $l < l_{EI}$ into two sub-ranges that are the inertial sub-range for $l_{EI} > l > l_{DI}$ and the dissipation range $l < l_{DI}$. This new scale, also known as the Taylor scale, can be evaluated as $l_{DI} = 60\eta_K$. Then, in the inertial subrange, the motions are characterized by inertial forces with negligible viscous effects when in the dissipation range they are characterized by preponderant viscous effects.

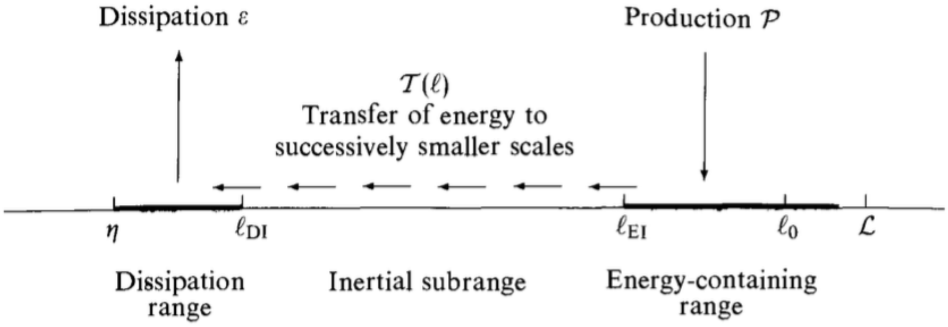

FIGURE 3.1: Energy cascade at very high Reynolds number from [157]

Finally, all the previously presented concepts can be found in Fig. 3.1.

3.1.2.4 Statistical description of the turbulence

As the turbulence is an unsteady, chaotical and random phenomenon, the deterministic behavior of the Navier-Stokes equations may appear unsuitable for modeling it. These characteristics can easily be explained through the systematic presence of perturbations on the boundary conditions for turbulent flows. Indeed, the roughness of the wall materials, impurities, inhomogeneous temperature in the fluid and many others effects may be factors that locally disrupt the flow. Moreover, the Navier-Stokes equations reveals to be very sensitive to these perturbations and the non-linearity of these equations may conduct, for very similar initial conditions, to very different solutions. Hence, small perturbations in the flow may have huge effects and consequences especially for high Reynolds number flow fields. In other words, the Navier-Stokes equations lead to stable solutions for laminar flows but may lead to unstable solutions for turbulent flows.

Because of the random behavior of the flow variables that have to be computed, represented here by φ, it is not possible to build a mathematical model allowing to predict them. Therefore, a numerical model has to provide a statistical description of φ through the prediction of its Probability Density Function (PDF) [34] noted $\mathcal{P}$. The probability of the random variable φ being lower or equal to φ_1, noted $\mathbb{P}(\varphi \leq \varphi_1)$, is defined as follows:

$$\mathbb{P}(\varphi \leq \varphi_1) = \int_{-\infty}^{\varphi_1} \mathcal{P}(x)dx \,. \tag{3.14}$$

Moreover, the PDF $\mathcal{P}$ of a variable φ is perfectly determined if all statistic moments are known. The statistic moment of order q can be defined as

$$\mathcal{M}_q(\varphi) = \langle \varphi^q \rangle = \int_{-\infty}^{+\infty} x^q \mathcal{P}(x)dx \,. \tag{3.15}$$

The first order moment corresponds to the average value of the random variable:

$$\langle \varphi \rangle = \int_{-\infty}^{+\infty} x \mathcal{P}(x)dx \,. \tag{3.16}$$

Hence, the fluctuations of φ, noted φ', refers to the deviation from the average and is written as

$$\varphi' = \varphi - \langle \varphi \rangle \quad \text{with} \quad \langle \varphi' \rangle = 0 \,. \tag{3.17}$$

In this decomposition, called Reynolds average, the fluctuation part φ' refers to the turbulent motions. It can also be interesting to know the statistical moments of the fluctuation φ', also called centered statistical moments:

$$\mu_q(\varphi) = \langle \varphi'^q \rangle = \int_{-\infty}^{+\infty} (x - \langle \varphi \rangle)^q \mathcal{P}(x)dx \,. \tag{3.18}$$

The centered moment of zero-th order μ_0 is equal to unity and the one of first order μ_1 equal to zero. The variance of φ can also be seen as the centered second-order moment and is expressed as follows:

$$\mathrm{var}(\varphi) = \mu_2(\varphi) = \langle \varphi'^2 \rangle = \int_{-\infty}^{+\infty} (x - \langle \varphi \rangle)^2 \mathcal{P}(x) dx \,. \tag{3.19}$$

The Root Mean Square (RMS) of φ, as the square root of the variance, is more widely used in the LES context.

Applying the Reynolds decomposition on the momentum balance equation 3.2 leads to the Reynolds Averaged Navier-Stokes Equations (RANS) as

$$\frac{\partial \langle u_i \rangle}{\partial t} + \frac{\partial}{\partial x_j}(\langle u_i u_j \rangle) + \frac{\partial}{\partial x_j}(\langle u_i' u_j' \rangle) = -\frac{1}{\rho}\frac{\partial \langle p \rangle}{\partial x_i} + \nu \frac{\partial^2 \langle u_i \rangle}{\partial x_j^2} \,, \tag{3.20}$$

using the incompressible constraint that can also be expressed for the averaged and fluctuating parts as $\nabla \cdot \langle \mathbf{u} \rangle = 0$ and $\nabla \cdot \mathbf{u}' = 0$, and with the following properties detailed in Chassaing [34]

$$\begin{aligned} &\langle \mathbf{u}.\nabla \mathbf{u} \rangle = \langle \mathbf{u} \rangle.\nabla \langle \mathbf{u} \rangle + \langle \mathbf{u}'.\nabla \mathbf{u} \rangle \,, \\ &\langle \mathbf{u}'.\nabla \mathbf{u} \rangle \equiv \langle \mathbf{u}'.\nabla \mathbf{u}' \rangle \,, \\ &\langle \mathbf{u}'.\nabla \mathbf{u}' \rangle = \langle \nabla \cdot (\mathbf{u}' \otimes \mathbf{u}') \rangle \,. \end{aligned} \tag{3.21}$$

This equation models the dynamics of the averaged motions and possesses the same contribution as the instantaneous momentum balance plus an extra term that refers to the centered second-order moment of the velocity $\nabla \cdot (\langle \mathbf{u}' \otimes \mathbf{u}' \rangle)$ also known as the Reynolds tensor.

Hence, the momentum balance of the velocity fluctuating part can be expressed by taking the difference between the instantaneous momentum balance in Eq. 3.2 with the averaged one in Eq. 3.20 as

$$\frac{\partial u_i'}{\partial t} + \frac{\partial}{\partial x_j}(u_i u_j - \langle u_i u_j \rangle) - \frac{\partial}{\partial x_j}(\langle u_i' u_j' \rangle) = -\frac{1}{\rho}\frac{\partial p'}{\partial x_i} + \nu \frac{\partial^2 u_i'}{\partial x_j^2} \,. \tag{3.22}$$

From this equation, the next section will develop the turbulent kinetic energy balance equation.

3.1.2.5 Kinetic energy balance equation

For incompressible non reactive flows, the energetic properties of the fluid can be resumed through the local kinetic energy as

$$\mathcal{K} = \frac{1}{2}\mathbf{u}.\mathbf{u} \,. \tag{3.23}$$

Applying the Reynolds decomposition of the velocity field, this energy can thus be expressed as $\langle \mathcal{K} \rangle = K + \langle k_t \rangle$ with

$$K = \frac{1}{2}\langle \mathbf{u} \rangle.\langle \mathbf{u} \rangle \,, \quad \langle k_t \rangle = \frac{1}{2}\langle \mathbf{u}'.\mathbf{u}' \rangle \,, \quad k_t = \frac{1}{2}\mathbf{u}'.\mathbf{u}' \,, \tag{3.24}$$

where K refers to the average of the kinetic energy, $\langle k_t \rangle$ to the turbulent kinetic energy of the averaged flow and k_t the turbulent kinetic energy of the instantaneous velocity field.

The transport equation of the averaged turbulent kinetic energy $\langle k_t \rangle$ can therefore be deduced from Eq. 3.22 and can be written as follow:

$$\underbrace{\frac{\partial \langle k_t \rangle}{\partial t} + \langle u_l \rangle \frac{\partial \langle k_t \rangle}{\partial x_l}}_{A} = \underbrace{-\langle u'_i u'_l \rangle \frac{\partial \langle u_i \rangle}{\partial x_l}}_{P} - \underbrace{\frac{\partial}{\partial x_l}\left(\frac{1}{2}\langle u'_i u'_j u'_l \rangle + \frac{1}{\rho}\langle u'_l p' \rangle\right)}_{D^T} - \underbrace{\nu \langle \frac{\partial u'_i}{\partial x_l}\frac{\partial u'_i}{\partial x_l} \rangle}_{\epsilon} + \underbrace{\nu \frac{\partial^2 \langle k_t \rangle}{\partial x_l^2}}_{D^\nu}, \tag{3.25}$$

where A refers to the advection terms, P to the production term, D^T to the turbulent diffusion, ϵ to the dissipation associated to the molecular viscosity and finally D^ν to the viscous diffusion. Moreover, D^T and D^ν may be seen as a spatial redistribution of the kinetic energy between the different parts of the fluid.

In the case of Homogeneous Isotropic Turbulent flows (HIT), the averaged turbulent kinetic energy balance equation in Eq. 3.25 can be simplified as follows:

$$\frac{\partial \langle k_t \rangle}{\partial t} = -\underbrace{\nu \langle \frac{\partial u'_i}{\partial x_l}\frac{\partial u'_i}{\partial x_l} \rangle}_{\epsilon}. \tag{3.26}$$

More details concerning the definitions of the homogeneity and isotropy properties can be found in the literature as the one of Taylor [189], Craya [43] or Lesieur [118].

3.1.2.6 Spectral view of the energy cascade

The analysis of the spectral view of the Richardson's energy cascade deals with the determination of the turbulent kinetic energy distribution among the different sizes of eddies. Some mathematical tools can be used in order to estimate this distribution. Indeed, the turbulent kinetic energy contained in the eddy of characteristic length r can be achieved through the introduction of the Reynolds tensor that indicates how much the velocity fluctuations are correlated for points separated by the distance r:

$$R_{ij}(\mathbf{r}, \mathbf{x}, t) = \langle u'_i(\mathbf{x}, t) u'_j(\mathbf{x} + \mathbf{r}, t) \rangle. \tag{3.27}$$

Under homogeneous and isotropic assumptions and considering the wavenumber k that refers to the length scale l defined as $k = 2\pi/l$, the Fourier transform of this tensor can be expressed as

$$\Phi_{ij}(\mathbf{k}, t) = \frac{1}{(2\pi)^3} \int_{\mathbb{R}^3} e^{-i\mathbf{k}.\mathbf{r}} R_{ij}(\mathbf{r}, t) d\mathbf{r}, \tag{3.28}$$

and corresponds to the contribution of the wavenumber k to the turbulent kinetic energy.

In order to avoid directional considerations but also to only consider scalar wavenumber k, the turbulent kinetic energy spectrum is defined by integrating the trace of the $\Phi_{ij}(k, t)$ tensor on the k radius sphere in the Fourier space as

$$\mathcal{E}(k, t) = \int_{\mathbb{R}^3} \frac{1}{2} \Phi_{ii}(\mathbf{k}, t) \delta(|\mathbf{k}| - k) d\mathbf{k}. \tag{3.29}$$

Then, the term $\mathcal{E}(k,t)dk$ corresponds to the energetic contribution of the scales that have a wave-number modulus included into the range $k \leq |\mathbf{k}| \leq k+dk$. The production of the turbulent kinetic energy is maximal in $k = 2\pi/l_t$ with l_t the integral scale. The previous property coming fom the Kolmogorov theory can be applied on this integral scale leading to the following relations:

$$Re_t = \frac{l_t u_t}{\nu}\,, \quad l_t = \frac{u_t^3}{\epsilon}\,, \quad \frac{l_t}{\eta_K} = \mathcal{O}\left(Re_t^{3/4}\right)\,. \tag{3.30}$$

Moreover, in the inertial range, the energy spectrum is defined by the following relation

$$\mathcal{E}(k) = C\epsilon^{2/3}k^{-5/3}\,, \tag{3.31}$$

where C is an universal constant.

The turbulent kinetic energy is damped into thermal energy in the dissipation range as Fig. 3.2 shows. The previous definition of the energy spectrum presented in Eq. 3.29 associated to the momentum balance equation in Eq. 3.2 enables to establish the evolution of the turbulent kinetic energy in the Fourier space [85] as

$$\frac{\partial \mathcal{E}(k,t)}{\partial t} = \mathcal{P}(k,t) - \frac{\partial}{\partial k}\mathcal{T}(k,t) - 2\nu k^2 \mathcal{E}(k,t)\,, \tag{3.32}$$

with the energy production at the largest scale for the first term on the left, the energy transfer rate from the largest to the smallest scales for the second term and finally the viscous dissipation that can be expressed as a function of the energy spectrum $\mathcal{E}$.

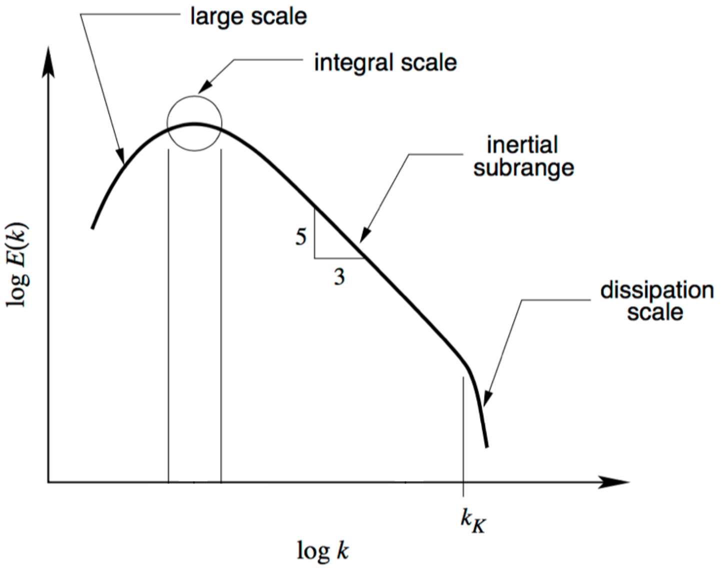

FIGURE 3.2: Turbulent kinetic energy spectrum inspired from [136]

Batchelor [10] defined in 1953 the integral scale for HIT flows l_t based on the integration of the energy spectrum $\mathcal{E}(k)$ as:

$$\frac{3}{2}u_t^2 = \int_0^\infty \mathcal{E}(k,t)dk\,, \tag{3.33}$$

and

$$l_t = \frac{\pi}{2u_t^2}\int_0^{\infty}\frac{\mathcal{E}(k,t)}{k}dk\,. \tag{3.34}$$

Finally, once the main turbulent concepts have been introduced, the next section focuses on the different computation approaches for turbulent flows.

3.1.3 RANS, LES and DNS approaches for turbulent flows

As previously mentioned, the Navier-Stokes equations enable to represent both laminar and turbulent flows dynamics. The resolution of these equations can be achieved thanks to various numerical methods. The three different classical approaches developed to perform CFD of turbulent flows appearing in Fig. 3.3 are briefly summarized as follow:

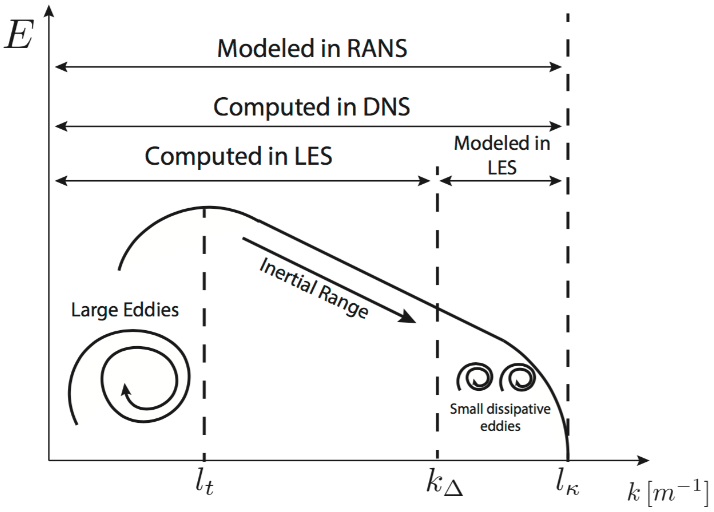

FIGURE 3.3: Illustration of the turbulent energetic spectrum along the energetic cascade from [95]. The solved and modeled scales are given for RANS, LES and DNS formalisms

- **Direct Numerical Simulation (DNS):** The DNS approach consists in directly solving the discretized form of the Navier-Stokes equations under the assumption that all spatial turbulent structures are well resolved, guarantying that the discretized terms are as close as possible to the continuous terms. In that case, there are only discretization errors and no modeling errors. However, this approach appears to be extremely costly for highly turbulent flows, even for non-reacting flows, and therefore it is generally only possible to perform such simulations for academics studies without limited computational resources. As DNS cannot systematically be applied, other formalisms have to be chosen by adding physical models that avoid to resolve all the spatial scales of the turbulence and thus decreasing the CPU cost of the simulation.
- **Reynolds Averaged Navier-Stokes (RANS):** This approach deals with the solving of the Navier-Stokes equations through the application of a time-average operator. Hence, this formalism enables to access to the stationary fields only as it computes the mean flow field while completely modeling the fluctuating parts of the flow. Therefore, none of the scales of the turbulent spectrum are resolved. Moreover, because of the non-linearity of the Navier-Stokes equations, unresolved

terms appear in the time-averaged equations and thus their closures necessitate turbulence models. The RANS approach is very widespread and attractive in industries as it does not require refined meshes but also thanks to very short restitution times. Moreover, this approach allows to exploit the geometric symmetries of the configurations and therefore, to only perform 2D simulations and to benefit of the spatial symmetries of the mean flow field which is not the case for other formalisms.

- **Large-Eddy Simulation (LES) :** Finally, the LES formalism can be considered as a trade-off between the high computational cost of the DNS approach and the entire modeling of turbulent scales in the RANS approach. Indeed, it consists in applying a spatial filtering operator on the Navier-Stokes equations in order to resolve only the largest scales of the flow. Some criteria enable to estimate the needed resolution of the LES approach [157, 198]. Contrary to the RANS approach, it does not rely on the computation of a mean flow field but rather on a filtered instantaneous field, where smallest scales have been removed. In that case, unclosed filtered terms, which represent the effects of the smallest scales on the largest one, have to be modeled. Moreover, as these small structures are assumed to be isotropic, universal and dissipative, they are well suited to this modeling. Finally, LES enables to decrease the CPU cost of turbulent flow simulations compared to DNS and can be applied for various industrial complex configurations.

All simulations performed in this work has been done through the LES formalism which is presented more in details hereafter.

3.1.4 Filtered LES equations

The LES formalism implies the scale separation between the resolved and modeled structures through a low-pass filtering operation applied on the Navier-Stokes equations. Considering a scalar $\phi(t, \mathbf{x})$, this filtering process relies on a spatial convolution product that is defined as

$$\overline{\phi}(\mathbf{x}, t) = \int_{\mathbb{R}^3} \phi(\mathbf{y}, t) G_\Delta(\mathbf{y} - \mathbf{x}) d\mathbf{y} \,, \tag{3.35}$$

where $\overline{\phi}$ is the filtered scalar and G_Δ the filtering kernel associated to the filter size Δ. Moreover, the filter operator has to be normalized so that,

$$\int_{\mathbb{R}^3} G_\Delta(\mathbf{x}) d\mathbf{x} = 1 \,, \tag{3.36}$$

and must verify the commutativity property with both spatial and temporal derivation operators [156] as

$$\frac{\partial \overline{\phi}}{\partial t} = \overline{\frac{\partial \phi}{\partial t}} \quad \frac{\partial \overline{\phi}}{\partial x_i} = \overline{\frac{\partial \phi}{\partial x_i}} \,. \tag{3.37}$$

The filtering notion will be further developed in Chapter 4. Then, the ϕ variable may be decomposed into two parts : a first part that involves scales larger than Δ noted $\overline{\phi}$ and a second that refers to the sub-grid fluctuating part, involving scales smaller than Δ noted ϕ'' :

$$\phi(t, \mathbf{x}) = \overline{\phi}(t, \mathbf{x}) + \phi''(t, \mathbf{x}) \,. \tag{3.38}$$

As the flow density may locally varies, the Favre filter, that corresponds to a filter weighted by the density, has also to be introduced as

$$\widetilde{\phi} = \frac{\overline{\rho\phi}}{\overline{\rho}} \,. \tag{3.39}$$

The Favre filtering process can thus be applied onto the equations 3.1, 3.2, 3.7, 3.9 leading to the instantaneous filtered balance equations defined as follows:

- **Filtered mass conservation**

$$\frac{\partial\overline{\rho}}{\partial t} + \frac{\partial\overline{\rho}\widetilde{u}_i}{\partial x_i} = 0 \,. \tag{3.40}$$

- **Filtered momentum conservation**

$$\frac{\partial\overline{\rho}\widetilde{u_j}}{\partial t} + \frac{\partial\overline{\rho}\widetilde{u_i}\widetilde{u_j}}{\partial x_i} = -\frac{\partial}{\partial x_i}\underbrace{\left[\overline{\rho}(\widetilde{u_i u_j} - \widetilde{u_i}\widetilde{u_j})\right]}_{(1)} - \frac{\partial\overline{p}}{\partial x_j} + \frac{\partial\overline{\tau}_{ij}}{\partial x_i} \,. \tag{3.41}$$

- **Filtered species conservation**

$$\frac{\partial\overline{\rho}\widetilde{Y_k}}{\partial t} + \frac{\partial\overline{\rho}\widetilde{u_i}\widetilde{Y_k}}{\partial x_i} = -\frac{\partial}{\partial x_i}\underbrace{\left[\overline{\rho}(\widetilde{u_i Y_k} - \widetilde{u_i}\widetilde{Y_k})\right]}_{(2)} - \frac{\partial}{\partial x_i}\underbrace{(-\overline{\rho V_{k,i} Y_k})}_{(3)} + \underbrace{\overline{\dot{\omega}}_k}_{(4)} \,. \tag{3.42}$$

- **Filtered energy conservation**

$$\frac{\partial\overline{\rho}\widetilde{h_s}}{\partial t} + \frac{\partial\overline{\rho}\widetilde{u_i}\widetilde{h_s}}{\partial x_i} = -\frac{\partial}{\partial x_i}\underbrace{\left[\overline{\rho}(\widetilde{u_i h_s} - \widetilde{u_i}\widetilde{h_s})\right]}_{(5)} + \frac{D\overline{p}}{Dt} + \frac{\partial}{\partial x_i}\underbrace{(-\overline{\rho V_h h_s})}_{(6)} + \underbrace{\overline{\dot{\omega}}_T}_{(7)} \,. \tag{3.43}$$

These filtered conservative equations possess unresolved terms (1)-(7) and each of them have to be closed:

- **The sub-grid Reynolds stress tensor (1)** necessitates the introduction of a turbulent model for the momentum transport of the unresolved velocity fluctuations to reproduce the energy transfer between the resolved and modeled scales. The Boussinesq approach [20], that is further developed in the next sub-section, has been used during this thesis. Hence, the turbulent fluxes are models through a similar expression to the laminar definition 3.3 but in that case using a turbulent viscosity $\mu_t = \overline{\rho}\nu_t$ as

$$\overline{\tau}_{ij} = \mu_t\left(\frac{\partial\widetilde{u}_i}{\partial x_j} + \frac{\partial\widetilde{u}_j}{\partial x_i}\right) - \frac{2}{3}\mu_t\frac{\partial\widetilde{u}_k}{\partial x_k}\delta_{ij} \,. \tag{3.44}$$

  Other models will be presented in the next sub-section.
- **The sub-grid species (2) and enthalpy fluxes (5)** may be modeled in a similar manner as the sub-grid Reynolds stress tensor [140].
- **The filtered laminar diffusive fluxes of species (3) and enthalpy (6)** that are more detailed in the thesis of Bénard [15].
- **The filtered species chemical rate (4) and enthalpy source term (7)**, respectively noted $\overline{\dot{\omega}}_k$ and $\overline{\dot{\omega}}_T$, are the critical points regarding the modeling of the turbulent combustion, more information can be found in [156] or in the thesis of Gruselle [79] and Bénard [15].

3.1.5 Sub-grid scale modeling of turbulence

Based on the fluctuations of the velocity moments, that refer to the accuracy of the statistical flow representation, several turbulent sub-grid scale models exist in the literature. The number of moments taken into account may thus be the first criterion to classify them. Hence, we can segregate these models into two categories : the first-order moment models based on the averaged values and the second-order moment models that also take the second-order moment into account. Moreover, another criterion that deserves to be quoted is the number of additional equations introduced by the different model classes. During this thesis, only first-order algebraic sub-grid-scale models - without additional equation - have been used and thus only this category is presented hereafter.

3.1.5.1 Boussinesq hypothesis

All the closure models for the momentum balance equation are built upon a turbulent viscosity based on the Boussinesq eddy viscosity assumption [20, 21]. Indeed, Boussinesq introduced in 1877 the concept of the turbulent viscosity with a similar relation to the one of Newton for the molecular viscosity constraints. In Eq. 3.41, the filtered viscous tensor $\overline{\tau}_{ij}$ is expressed as

$$\overline{\tau}_{ij} = 2\mu \tilde{S}_{ij}^D \quad \text{with} \quad \tilde{S}_{ij} = \frac{1}{2}\left(\frac{\partial \tilde{u}_i}{\partial x_j} + \frac{\partial \tilde{u}_j}{\partial x_i}\right) . \tag{3.45}$$

As the filtered momentum conservation equation 3.41 showed, the unclosed term $\overline{\rho}(\widetilde{u_i u_j} - \widetilde{u_i}\widetilde{u_j})$ can therefore be modeled in the same way than the viscous tensor using a turbulent viscosity ν_t as

$$\overline{\rho}(\widetilde{u_i u_j} - \widetilde{u_i}\widetilde{u_j}) = 2\mu_t \tilde{S}_{ij}^D . \tag{3.46}$$

Using the new formulation of the unclosed term, the filtered momentum conservation equation 3.41 can thus be expressed using the two different viscosities.

$$\frac{\partial \overline{\rho}\tilde{u}_j}{\partial t} + \frac{\partial \overline{\rho}\tilde{u}_i\tilde{u}_j}{\partial x_i} = -\frac{\partial \overline{p}}{\partial x_j} + \frac{\partial}{\partial x_i}\left[2(\mu + \mu_t)\tilde{S}_{ij}^D\right] . \tag{3.47}$$

Finally, it can be highlighted that, thanks to the Boussinesq assumption, all first order algebraic sub-grid scale models have only to model the turbulent dynamic viscosity μ_t.

3.1.5.2 Smagorinsky model

The LES formalism implies that the largest scales of the flow are computed while the small sub-grid scales are modeled. As these smallest scales tend to have a more isotropic behavior, it may possible to characterize them with an universal relation which is simpler than standard Reynolds stress model. The classical Smagorinsky [184] SGS model based on the Boussinesq eddy viscosity assumption involves the equilibrium between the production and dissipation rate of the kinetic energy at the LES filter size Δ. Hence, turbulence can thus be considered at this scale as a pure dissipative phenomenon. The eddy viscosity is expressed as

$$\nu_t = (C_s\Delta)^2|\tilde{\mathbf{S}}| \quad \text{with} \quad |\tilde{\mathbf{S}}| = \sqrt{2\tilde{S}_{ij}\tilde{S}_{ij}} , \tag{3.48}$$

where C_s is the Smagorinsky constant, Δ is the LES filter size proportional to the grid size Δx and $|\tilde{\mathbf{S}}|$ is the magnitude of the filtered strain-rate tensor.

However, the choice of the constant C_s depends on the flow configuration. Lilly [122] proposed a constant value of $C_s \simeq 0.23$ for homogeneous isotropic turbulence with cutoff in the inertial subrange and $\Delta = \Delta x$. However, this SGS model is also known to cause an excess of dissipation in mean shear flows and to also have some difficulties at predicting the turbulence transition. Finally, very popular for its simplicity, the Smagorinsky SGS model is generally used with a value of C_s in the range [0.1 ;0.23].

3.1.5.3 Dynamic Smagorinsky model

The major drawback of the SGS stress models based on the eddy viscosity assumption is that they cannot model different turbulent configurations, such as shear flows or transitional regimes, with one universal constant parametrization. Therefore, Germano [72] and Lilly [123] proposed an improved version of the previous Smagorinsky model that attempts to overcome this issue. In this approach, the Smagorinsky constant C_s is locally determined through a dynamic procedure. Indeed, the main idea is based on that the sub-grid scales characteristics can be deduced from smallest resolved scales. In order to achieved this idea, another filtering operator noted here $\widehat{\cdot}$ is introduced and the resolved instantaneous velocity field is filtered with a width Δ' larger than Δ. The sub-grid scale stress term $\tau'_{ij} = \overline{\rho}(\widetilde{u_i u_j} - \widetilde{u_i}\widetilde{u_j})$ and the sub-grid scale stress term based on the two times filtered velocity $\tau''_{ij} = \overline{\rho}(\widehat{\widetilde{u_i u_j}} - \widehat{\widetilde{u_i}}\widehat{\widetilde{u_j}})$ may be written according to the Smagorinsky model as:

$$\begin{aligned} \tau'_{ij} &= 2\overline{\rho}(C_s\Delta)^2|\tilde{\mathbf{S}}|.\tilde{S}_{ij} \,, \\ \tau''_{ij} &= 2\overline{\rho}(C_s\Delta')^2|\widehat{\tilde{\mathbf{S}}}|.\widehat{\tilde{S}}_{ij} \,. \end{aligned} \tag{3.49}$$

The resolved turbulent stress between the two filtering sizes Δ' and Δ, called Germano identity, can be expressed by taking the difference between the two previous sub-grid scale stress tensors as

$$L_{ij} = \widehat{\tau'_{ij}} - \tau''_{ij} = \overline{\rho}\left(\widehat{\tilde{u}}_i\widehat{\tilde{u}}_j - \widehat{\tilde{u}_i\tilde{u}_j}\right) \,. \tag{3.50}$$

Combining the previous equations 3.49 and 3.50 and contracting with $\tilde{S}_{ij}$, the Smagorinsky constant can thus be computed from the two filtered velocity fields as follows:

$$L_{ij}\tilde{S}_{ij} = -2\overline{\rho}C_s^2\left(\Delta^2|\tilde{\mathbf{S}}|.\tilde{S}_{ij}\tilde{S}_{ij} - \Delta'^2|\widehat{\tilde{\mathbf{S}}}|.\widehat{\tilde{S}}_{ij}\tilde{S}_{ij}\right) \,. \tag{3.51}$$

Implicitly, this model implies similarity between the SGS stresses at the two different scales Δ and Δ'. Therefore, the sub-grid scales characteristics, through the turbulent viscosity, are based on the same characteristics than those on the range $[\Delta; \Delta']$. However, the quantity in parentheses can have zero values leading to indeterminate or ill-conditioned C_s constant.

The dynamic Smagorinsky model is relevant for a large range of applications but is costly and complex to apply as it requires explicit filtering operators. Moreover, the computation of the local constant values may locally lead to negative values, which implies a negative turbulent viscosity that corresponds to energy transfers from the small structures to the largest ones also called *backscatter* [27]. A specific treatment has to be applied in order to avoid this phenomenon as it may produce numerical problems.

Finally, based on the same multi-level idea, other dynamic procedures have been proposed as the one of Veynante et al. [199] that automatically determines flame wrinkling factors from known resolved fields in large eddy simulations of turbulent premixed combustion. In the same way, chapter 6 presents the Multi-Resolution LES framework (MRLES) that enables to dynamically optimize meshes based on performing several LES simultaneously on different grid levels that communicate through velocity fields exchanges. Thanks to this approach, both modeling and numerical errors can be estimated and then used in order to build a grid quality criterion that locally determine if the grid has to be coarsened or refined.

3.1.5.4 WALE model

The Wall-Adapting Local Eddy-viscosity (WALE) model developed by Nicoud and Ducros [148] proposes to obtain realistic turbulent viscosity near solid walls and to predict accurately the transition to turbulence. Here, the turbulent viscosity is computed thanks to the following relation:

$$\nu_t = (C_\omega^2 \Delta)^2 \frac{(s_{ij}^d s_{ij}^d)^{3/2}}{(\tilde{S}_{ij}\tilde{S}_{ij})^{5/2} + (s_{ij}^d s_{ij}^d)^{5/4}} \,, \tag{3.52}$$

where the constant C_ω is equal to 0.5 and the tensor s^d is defined as

$$s_{ij}^d = \frac{1}{2}(\tilde{h}_{ij} + \tilde{h}_{ji}) - \frac{1}{3}\tilde{h}_{kk}\delta_{ij} \quad \text{with} \quad \tilde{h}_{ij} = \tilde{G}_{ik}\tilde{G}_{kj} \quad \text{and} \quad \tilde{G}_{ij} = \frac{\partial \tilde{u}_i}{\partial x_j} \,. \tag{3.53}$$

This formulation can be compared to the previously presented Smagorinsky formalism. The main advantages are the following:

- The spatial operator can take into account the rotation and strain rates. Hence, all the vortex structures that dissipate kinetic energy are therefore detected by the model.
- The turbulent viscosity tends naturally to zero in near-wall zones.
- The model imposes $\nu_t = 0$ in shear flows, then the transition to turbulence can be faithfully computed with the birth of unstable linear modes.

3.1.5.5 ILES approach

First of all, it is noticeable that in the LES formalism, the use of an artificial viscosity of the same magnitude order or larger than the turbulent viscosity but also the use of numerical schemes that produce high numerical diffusion errors should strongly be avoided. However, the Implicit LES (ILES) concept is based on the assumption that the sub-grid scale models have a dissipative contribution which can be replicated with discretized numerical schemes (ILES) or with numerical schemes with additional artificial dissipation terms in the Monotonicaly Integrated LES formalism (MILES).

Indeed, convective numerical schemes such as low-order or "upwind" schemes generate a significant numerical viscosity in the LES computation. Moreover, the use of the Jameson viscosity [94] leads to second- and fourth-order dissipation terms. The fourth-order contributions operates as a sub-grid scale model [171] as the highest frequencies associated to the smallest scales are damped.

Concerning the turbulence modeling, this approach consists in the use of no turbulence model and is therefore called "NO-MODEL". Even if, this method is particularly attractive and cheap because of its simplicity, it has to be applied with caution as no real control on the dissipation is introduced.

3.2 Presentation of the LES solver YALES2

This section attempts to present the CFD code YALES2 and gives a global overview of all the numerical tools and strategies that have been implemented in order to circumvent the challenges when solving the reactive Navier-Stokes equations on massive meshes.

3.2.1 General presentation and challenges

In this thesis, all numerical simulations have been performed using the finite-volume CFD code YALES2 [145], a low-Mach number Large-Eddy Simulation (LES) and Direct Numerical Simulation (DNS) solver based on unstructured meshes. This code solves the low-Mach number Navier-Stokes equations in two and three dimensions for turbulent reactive flows using a time-staggered projection method for constant [38] or variable density flows [154]. YALES2 enables to manage all type of elements through dual control volumes for the intregration of the transport equation, an example of the control volume is provided in Fig 3.4. Finally, YALES2 is specifically tailored to solve these low-Mach number equations on massively parallel machines with billion-cell meshes [144].

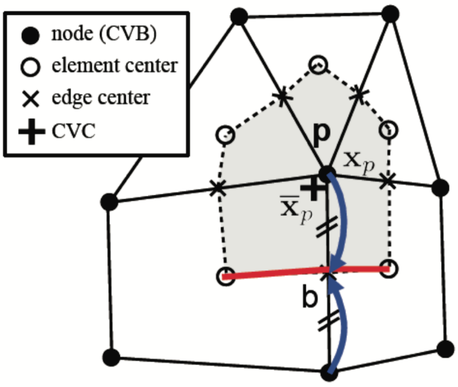

FIGURE 3.4: Control volume based on a mesh node in YALES2: x_p representing the mesh node and $\overline{x}_p$ the barycenter of the control volume

One of the major difficulty when computing turbulent reactive flows, such as combustion in rocket engines, comes from the resolution of very heterogeneous spatial and temporal characteristics scales. Indeed, the reactive Navier-Stokes equations takes into account several physical phenomena - convection, diffusion and reaction - that all are associated to characteristic time and length scales which are not necessary at the same magnitude order.

First, the temporal aspect of this problem may be highlighted through the example of the convective characteristic timescale, which is typically of the order 10^{-5} to 10^{-7} s, comparing to the reaction timescale of order 10^{-9} up to 10^{-12} s for hydrocarbon chemistry.

The Reynolds number represents the ratio between the convective and diffusive characteristic timescales. In turbulent flows - that correspond to high Reynolds number -, as the range of scales of the turbulent spectrum increases, these two timescales are very different and therefore lead to an increase of the cost of the Navier-Stokes equations resolution as the time integration is based on a smaller time step in order to guarantee the accuracy and the stability of the numerical schemes.

Moreover, concerning the spatial characteristic scales, numerical simulations have to ensure some of the following aspects:

- The computational domain has to be able to resolve the largest scales of the flow.
- The mesh has to be fine enough in order to resolve the smallest turbulent scales of the flow for the DNS formalism or until the cutoff frequency for the LES methodology.
- The mesh has to resolve the internal structure of the flame for reactive flows.

However, all these constraints require a large amount of elements in order to represent well all the spatial structures in the flows. Considering a cubic computational domain defined by the edge length L which is discretized by N points in each space direction, the homogeneous cell size can thus be defined as L/N. In the case of an Homogeneous Isotropic Turbulence (HIT), the turbulent scales can reasonably be considered as resolved if the integral scale l_t is smaller than the computational domain characteristic scale L with at least $l_t = L/8$ and if the smallest local mesh size, here $\Delta x = L/N$ is of the same magnitude order as the Kolmogorov scale η_K, which imposes the following relation on the discretization:

$$N \approx \frac{l_t}{\eta_K}\,. \tag{3.54}$$

As previously mentioned, the ratio between the integral length scale and the Kolmogorov scale is approximately the same order as $Re^{3/4}$, the total cell number N_{tot} in the computational domain needed to resolve all the scales therefore satisfies:

$$N_{tot} = N^3 \approx Re^{9/4}\,. \tag{3.55}$$

For instance, a Reynolds number of $10'000$ requires a spatial grid discretization about 10^9 elements. Moreover, it is common in research but also in industrial fields to simulate configurations operating at much higher Reynolds number. Such billion cells numerical simulations may lead to a prohibitive computational cost.

Finally, the multi-species chemistry introduces stiff partial differential system of equations that are not straightforward to solve. Moreover, the large amount of reactive source terms that have to be computed requires in particular exponential operations which are very expensive to compute. Moreover, some configurations necessitate to take into account the resolution of others phenomena such as the injection, atomization, dispersion or the evaporation for two-phase flows or the fluid-solid interactions.

In the next sections, the main numerical strategies and tools of YALES2 that enable to perform billion-cell simulations are presented.

3.2.2 Main tools and strategies

The steadily increase of computational resources supports the development of the CFD field as it enables to improve the fidelity of the numerical simulations by increasing the mesh resolution, the simulated physical time or by adding more physical phenomena in the computation. Here are presented some of the main tools and strategies that have been developed in the CFD code YALES2 in order to perform high-performance computing.

3.2.2.1 Parallel computing

Parallel computing deals with computations in which multiple processing elements are carried out simultaneously [3]. It can be decomposed into several forms as bit-level, instruction-level, data and task parallelism. In high-performance computing, parallelism has been employed for many years in order to solve large problems such as the Navier-Stokes resolution on highly refined grid. It has recently become the dominant paradigm in computer architecture, through the multi-core processors form [6], as the power consumption of computers - associated to the heat release - renewed interest in the recent years. Indeed, Asanovic wisdom has been changed from "power is free, but transistors are expensive" to "power is expensive, but transistors are free". Furthermore, parallelism can be accomplished by splitting complex problems into independent sub-problems that each processing element solves at the same time. The interest in parallel computing lies in its ability to reduce the restitution time, to perform more advanced simulations and also to operate the parallelism on modern processors with multi-core or multi-threading formalisms. Most of the supercomputing machines are distributed-memory machines. There are composed of an ensemble of nodes in which the memory is shared. Moreover, mastering both communication and synchronization between the different sub-tasks is one of the greatest challenge in order to access to good parallel performances. Here are presented two main parallel formalisms, the Message Passing Interface and the Open-Multi-Processing, and Fig. 3.5 highlights their differences in term of parallel architecture and memory distribution.

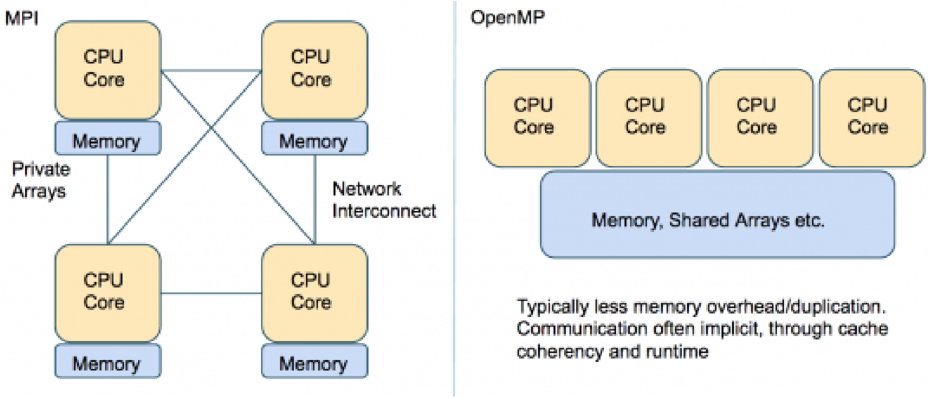

FIGURE 3.5: Node parallelism concepts of MPI and OpenMP from [32]

Message Passing Interface (MPI) : This is a standardized and portable message-passing standard syntax and semantic designed in 1993-1994 by a group of researchers from both academia and industry that defines a library of routines allowing to coordinate processes using the paradigm of the message exchanges. Here, a message is constituted of data packages that transit from the sender process to the receiver one. It also contains the identifier of the sender, the type of the data, the length of the data and the identifier of the receiver process. These exchanged messages are managed by an environment that can be compared to the regular post, phone operator or to electronic mailbox. Moreover, messages are sent to specific addresses and the receiver process has to be able to interpret the addressed messages. The programming model of the message passing formalism can thus be summarized with the following points:

- The program is written in a classical programming language such as Fortran C or C++.
- All variables are private and reside in the local memory of each process.
- Each process eventually execute different parts of the program.
- Data are exchanged between two or more processors through a programmed calls to specific routines.

More information can be found in the following materials [78, 45].

Open-Multi-Processing (OpenMP): This is an Application Programming Interface (API) that supports multi-platform shared memory multi-processing programming and consists of a set of compiler directives, library routines, and environment variables that influence run-time behavior. An OpenMP program is executed by one process that activates light-weight processes also called threads at the entry of a parallel region. Then, each thread executes a task comprised of a group of instructions. During the execution of a task by a thread, a variable can be read and/or updated in memory. It can be defined either in the stack - local memory space - of a thread referring to its private variable or in a shared-memory space accessible by all threads referring as a shared variable. Moreover, an OpenMP program is an alternation of parallel regions and sequential regions that are always executed by the "master" thread, the one whose rank equals zero. A parallel region can be executed by many threads at once by sharing the work contained in these regions. This work-sharing mainly consists in three different methods:

- Executing a loop by dividing up the iterations between the threads (parallel loop).
- Executing many code sections but only one per thread (parallel section).
- Executing many occurrences of the same procedure by different threads (orphaning).

More information can be found in the following materials [48, 92].

3.2.2.2 Two-level domain decomposition and parallelism

Domain decomposition methods are one of the classical approaches in CFD in order to manage this large amount of generated data. It enables to solve a boundary value problem by splitting it into sub-domains where smaller boundary value problems are solved. As these sub-domains are independent, the domain decomposition formalism is suitable for parallel computing as each processor will only solve its own sub-domain boundary value problem. Once each sub-domain problem has been solved, it is mandatory to synchronize each solution of the adjacent sub-domain in order to access to the global solution. This spatial inter-dependance can be taken into account through communications with Message Passing Interface (MPI) instructions between processors which exchange information for each group of cells at the interface. Furthermore, the mesh partitioning into sub-domain has to ensure that the load balancing on each processor is the most homogeneous as possible. In the Eulerian point of view, the most common manner to guarantee this constraint consists in partitioning the mesh into sub-domains with the same quantity of work, that means with the same number of elements or pairs of nodes depending on the problem. In YALES2, this mesh partitioning task is performed thanks to the external libraries METIS [103] and SCOTCH [36] and even this decomposition may appear straightforward on structured meshes, it is generally not the case on unstructured grids.

Moreover, the YALES2 code possesses one particularity with the double domain decomposition formalism [145]. Indeed, each sub-domain obtained through the first level of mesh partitioning is decomposed into several groups of cells. This principle is represented in Fig. 3.6 where the computational domain is split into the processors with black borders but also into smaller groups of elements with the grey borders. The size of the cell groups is defined in agreement with the size of the processors. This double mesh decomposition also enables to optimize the performances of the Poisson solver as the cell groups are used as a coarse mesh for the two-level linear solvers as the deflated PCG [134, 135]. The low frequencies that are more difficult to converge can therefore be solved more efficiently on this coarse level. This solver is based on two different types of communication : i) external communications through MPI instructions that correspond to the first level of partitioning ; ii) internal communications that enable to exchange information between the different cell groups on the same processor. Finally, Fig. 3.6 (right) illustrates this formalism with the data exchanges between the cell groups, the communicators and the boundary conditions.

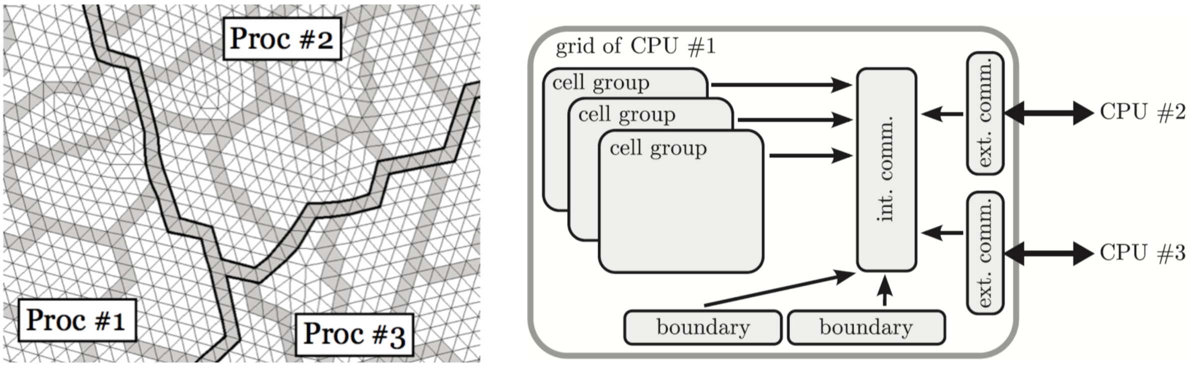

FIGURE 3.6: Representation of the YALES2 double domain decomposition (left) and communication sketch between the communicators and and processors (right)

3.2.2.3 Low-Mach number approach

Depending on the application, the density field can not always be considered as constant. Indeed, several physical factors can lead to density variations in the flow : the compressibility effects, the variations of temperature called thermal expansion and finally the composition variations in fluid mixtures containing components with different molar mass. For compressibility effects, the entire compressible reactive equations presented in section 3.1.1 have to be solved. However, these equations necessitate very small time step, limited by the acoustic Courant Friedrichs Lewy (CFL) criterion, leading to much more expensive CPU costs.

However, since the Mach number M is defined as the ratio between the velocity of the flow u and the one of the sound in the same medium c, the low Mach flow regime is defined for Mach number inferior to 0.3. This regime is very common and can be encountered in various applications. Moreover, Klainerman and Majda [107] show that compressible flows converge to incompressible flows as the Mach number tends to zero. Therefore, a small Mach number as $M << 1$ implies that the pressure in the computational domain becomes rapidly homogeneous. In that case, the acoustic waves propagate much faster than the entropic waves and thus the pressure fluctuations relatively little affect the thermodynamic properties. Hence, as the compressibility effects can be neglected, the thermodynamic pressure can then be considered as constant in space but variable in time. Moreover, the variations of the density ρ are yet only dependent on the dilatation effects due to the temperature and mixture fluctuations. In that case, the incompressible hypothesis can be considered as relevant and can therefore simplify the Navier-Stokes equations with a different treatment concerning their resolution. Finally, this simplification enables to have much larger time step as the limiting acoustic constraint vanishes.

Majda and Sethian [133] proposed an intermediate formalism for the reactive Navier-Stokes equations that is in between the incompressible formulation with constant density and the compressible formulation. These equations can be written as

$$
\begin{aligned}
&\frac{\partial \rho^\star}{\partial t} + \nabla \cdot (\rho^\star \mathbf{u}^\star) = 0\,, \\
&\frac{\partial \rho^\star \mathbf{u}^\star}{\partial t} + \nabla \cdot (\rho^\star \mathbf{u}^\star \otimes \mathbf{u}^\star) = -\frac{1}{M_r^2} \nabla p^\star\,, \\
&\frac{\partial \rho^\star E^\star}{\partial t} + \nabla \cdot (\rho^\star \mathbf{u}^\star E^\star) = -\nabla \cdot (p^\star \mathbf{u}^\star)\,, \\
&p^\star = \rho^\star (\gamma - 1) \left(E^\star - \frac{M_r^2}{2} \mathbf{u}^\star \right)\,,
\end{aligned}
\tag{3.56}
$$

where γ refers to the isentropic coefficient.

Second, the asymptotic development of each dimensionless variables $\varphi^\star = \varphi/\varphi_r$ can be written thanks to Taylor series expansion as

$$
\varphi^\star = \varphi_0^\star + M_r \varphi_1^\star + M_r^2 \varphi_2^\star + \mathcal{O}(M_r^3) \quad \text{with} \quad M_r = \frac{u_r}{c_r}\,, \tag{3.57}
$$

where φ refers to the variables characterizing the system such as the velocity, the pressure, the density, the energy and the index r corresponds to the reference values.

The pressure can therefore be decomposed into two parts: the thermodynamic pressure noted p_0 that is supposed to be constant in space and the dynamic pressure noted p_2 which is variable in space and time. Considering an open system, the thermodynamic pressure p_0 is also considered as constant in space and time and the perfect gas equation may be written as

$$
p_0 = \rho_0 r_0 T_0\,, \tag{3.58}
$$

where r_0 refers to the universal gas constant.

3.2.2.4 Numerical schemes and solvers

First, the CFD code YALES2 features several numerical schemes for the explicit time advancement of the temporal integration: the classical Runge-Kutta schemes of third- and fourth-order are available as well as a more recent one called TFV4A that has been proposed by Kraushaar [112] and that combines both Runge-Kutta and Lax-Wendroff methods. Concerning the spatial integration, second and fourth-order schemes have been implemented. This notion will not be further developed but more information can be found in Vantieghem's thesis [197].

Even if a lot of solvers, dedicated to different physical phenomena, have been implemented in YALES2, only two classical solvers have been used during this thesis for solving the Low Mach Number Navier-Stokes equations:

- The Incompressible solver (ICS): The application domain of this solver is limited to isothermal simulations without chemical reactions and the density is considered as constant.
- The Variable density solver (VDS): Here the variations of pressure, temperature and density due to the acoustic waves are considered as negligible. The temperature and density fields are strongly coupled through Eq. 3.58.

3.2.3 Incompressible constant density solver (ICS)

3.2.3.1 Incompressible Navier-Stokes equations

For incompressible flows, the previously introduced Navier-Stokes equations can be simplified as the fluid density is constant in time and space. The incompressible solver of YALES2 resolves the velocity balance equation written as

$$\begin{aligned} &\nabla \cdot \mathbf{u} = 0\,, \\ &\frac{\partial \mathbf{u}}{\partial t} + \nabla \cdot (\mathbf{u} \otimes \mathbf{u}) = -\frac{1}{\rho}\nabla p + \frac{1}{\rho}\nabla \cdot \boldsymbol{\tau}\,. \end{aligned} \tag{3.59}$$

This solver has been used for the LES of the 3D turbulent plane jet and several other test cases. The previous simplified equation is advanced in time thanks to the modified projection-correction method presented hereafter.

3.2.3.2 Resolution method

The resolution of the Navier-Stokes equations for incompressible flows is based on the projection method proposed by Chorin [38] modified by Kim and Moin [106]. It is noticeable that this formalism resolves the instantaneous velocity field at each time step (associated to integer indices such as n, $n+1$, etc...) when the density, the pressure and other scalar fields are resolved on staggered time step (associated to non integer indices such as $n+1/2$, $n+3/2$, etc...). The main steps of this methodology are presented hereafter:

The classical projection method, that is often used for the simulation of incompressible flows, relies on the Helmholtz-Hodge decomposition under relatively smooth assumption. At each time step, the velocity field can be decomposed into an irrotational part and a solenoidal part as

$$\mathbf{u} = \Pi_i(\mathbf{u}) + \Pi_s(\mathbf{u})\,, \tag{3.60}$$

where $\Pi_i(\mathbf{u})$ refers to irrotational component and $\Pi_s(\mathbf{u})$ to the solenoidal component of instantaneous velocity field with respectively the following properties $\nabla \times \Pi_i(\mathbf{u}) = 0$ and $\nabla \cdot \Pi_s(\mathbf{u}) = 0$. These projection operators are defined as

$$\begin{aligned} \Pi_i &= \nabla \Delta^{-1} \nabla \cdot \,, \\ \Pi_s &= -\nabla \times \Delta^{-1} \nabla \times \,, \end{aligned} \tag{3.61}$$

and some important relationships can be highlighted:

$$\begin{aligned} \Pi_i \Pi_i = \Pi_i \quad \Pi_s \Pi_i = 0 \quad \nabla \cdot \Pi_i = \nabla \cdot \,, \\ \Pi_s \Pi_s = \Pi_s \quad \Pi_i \Pi_s = 0 \quad \nabla \times \Pi_s = \nabla \times \;. \end{aligned} \tag{3.62}$$

The irrotational component derives from a potential scalar and can thus be written as $\Pi_i(\mathbf{u}) = \nabla \varphi$. The application of the divergence operator $\nabla \cdot$ enables to expressed the previous relation as follows:

$$\nabla \cdot \mathbf{u} = \nabla \cdot [\Pi_i(\mathbf{u}) + \Pi_s(\mathbf{u})] = \nabla \cdot \Pi_i(\mathbf{u}) = \nabla^2 \varphi \,. \tag{3.63}$$

Hence, the incompressible Euler equations can thus be projected using these previous operators leading to two projected velocity balance equations:

- The irrotational velocity balance:

$$\Pi_i(\nabla \cdot (\mathbf{u} \otimes \mathbf{u})) = -\frac{1}{\rho} \Pi_i(\nabla p) \,. \tag{3.64}$$

  Applying the divergence operator $\nabla \cdot$ on this incompressible Euler equation enables to link the Q-criterion to the pressure Laplacian as:

$$-\,2Q = -\frac{1}{\rho} \Delta p \,. \tag{3.65}$$

- The solenoidal velocity balance:

$$\frac{\partial \Pi_s(\mathbf{u})}{\partial t} + \Pi_s(\nabla \cdot (\mathbf{u} \otimes \mathbf{u})) = 0 \,. \tag{3.66}$$

  Applying the rotational operator $\nabla \times$ on this equation enables to find the vorticity $\boldsymbol{\omega} = \nabla \times \mathbf{u}$ equation as

$$\frac{\partial \boldsymbol{\omega}}{\partial t} + \mathbf{u} . \nabla \boldsymbol{\omega} = \boldsymbol{\omega} . \nabla \mathbf{u} \,. \tag{3.67}$$

Thanks to this decomposition, the velocity balance equation can therefore be solved in two steps:

1 **Prediction step:** A first estimation of the velocity field for the time $n+1$, noted $\mathbf{u}^\star$, is obtained by advancing the velocity equation without the contribution of the pressure gradient as it does not contribute to the solenoidal part but to the irrotational part of the velocity field.

$$\frac{\mathbf{u}^\star - \mathbf{u}^n}{\Delta t} = -\nabla \cdot (\mathbf{u}^\star \mathbf{u}^n) + \frac{1}{\rho} \nabla \cdot \boldsymbol{\tau}^n \,. \tag{3.68}$$

2 **Correction step:** Once the prediction has been done, leading to $\mathbf{u}^\star$, the velocity field is corrected by taking into account the pressure gradient:

$$\frac{\mathbf{u}^{\mathbf{n+1}} - \mathbf{u}^\star}{\Delta t} = -\frac{1}{\rho} \nabla p^{n+1/2} \,. \tag{3.69}$$

The computation of the corrected velocity, noted here $\mathbf{u}^{n+1}$, necessitates the knowledge of $p^{n+1/2}$ which can be determined by solving the Poisson equation. This equation can be obtained by taking the divergence operator of Eq 3.69 and integrating the zero divergence constraint for $\mathbf{u}^{n+1}$.

$$\nabla \cdot \mathbf{u}^{\star} = \nabla \cdot \Pi_i(\mathbf{u}^{\star}) = \frac{\Delta t}{\rho} \Delta p^{n+1/2} \,. \tag{3.70}$$

However, the advancement of the velocity equation that is implemented in the CFD code YALES2 [13] slightly differs from Chorin's approach:

1 **Prediction step:** In that case, the prediction step is done by considering the contribution of the pressure gradient at the time $n - 1/2$ that is generally a relative good approximation of $p^{n+1/2}$. This approach leads to a better estimation of the predicted velocity $\mathbf{u}^{\star}$ that therefore enables to reduce the numerical errors due to the splitting of the temporal advancement.

$$\frac{\mathbf{u}^{\star} - \mathbf{u}^{n}}{\Delta t} = -\nabla \cdot (\mathbf{u}^{\star} \otimes \mathbf{u}^{n}) - \frac{1}{\rho} \nabla p^{n-1/2} + \frac{1}{\rho} \nabla \cdot \boldsymbol{\tau}^{n} \,. \tag{3.71}$$

2 **Correction step:** Then, the correction step can therefore be written as

$$\frac{\mathbf{u}^{n+1} - \mathbf{u}^{\star}}{\Delta t} = -\frac{1}{\rho} \nabla (p^{n+1/2} - p^{n-1/2}) \,, \tag{3.72}$$

which leads to a Poisson equation of the following form:

$$\Delta (p^{n+1/2} - p^{n-1/2}) = \frac{\rho}{\Delta t} \nabla \cdot \mathbf{u}^{\star} \,. \tag{3.73}$$

Finally, the resolution of the Poisson equation is the key point of the methodology and it necessitates efficient linear solvers in order to guarantee good performances for massively parallel computations. This point will be further developed in the next section.

3.2.4 Poisson equation solving

The Poisson equation for the pressure presented in the previous section are equations that can be expressed on the form

$$\Delta \varphi = RHS \,, \tag{3.74}$$

with RHS meaning right-hand side.

This equation deals with the resolution of a linear system in which the discretized values of the pressure field at each computational nodes in the domain are unknown variables. Therefore, solving this system requires efficient linear solvers as it has to be done for each time step and may represent an important part of the CPU cost of the simulation. Indeed, these solvers are based on iterative numerical methods and the iteration number in order to reach a sufficiently accurate estimation of the solution may be important, depending on the algorithms but also on the characteristics of the discrete Laplacian operator. Moreover, each iteration of the linear solver requires some communications between the processors that can represent a non negligible part of the total simulation time. This proportion can reach 80% if no special considerations are taken into account for the method implementation [135]. Therefore, the optimization of the Poisson equation resolution is one of the major challenges for the simulation of incompressible flows, more detailed information can be found in Malandain's thesis [134]. Finally, several algorithms are available in the CFD code YALES2: The Preconditioned Conjugate Gradient (PCG) [196], the Deflated PCG [147] but also the BICGSTAB scheme [196].

Chapter 4

The Multi-Grid High-Order Filtering framework (MGHOF) for extracting large-scale structures in turbulent flows

The methodology presented here is a geometric Multi-Grid High-Order Filtering (MGHOF) framework for the on-line analysis of high- fidelity simulations. This approach relies on high-order implicit filters and enables the extraction of large-scale features from LES on massive and distributed unstructured grids at a reduced cost. The MGHOF framework is first described and validated, then the methodology is applied to a 3D turbulent jet plane and to the analysis a 3D low-Mach number turbine blade with various mesh sizes, ranging from a few million to a few billion tetrahedra.

Contents

4.1 Introduction

To circumvent the Q-criterion scaling issue, it is mandatory to develop numerical techniques capable of separating the different coherent structures such as spatial low-pass filters. Performing this scale separation is quite challenging as it requires to extract features from a large amount of data distributed across a large number of processors in a parallel environment. Moreover, such a low-pass filter necessitates a good selectivity in order to leave the large scales unaffected while damping all the smallest scales. Performing the scale separation in complex geometries with unstructured grids is also challenging as the stencil of differential operators is generally limited to the closest neighboring control volumes. Finally, in these geometries, the filter kernel degeneracy at the boundaries is also an important issue.

The present geometric multi-grid high-order filtering (MGHOF) framework has been designed to circumvent all these issues and to enable an efficient extraction of large scale features in turbulent flows. It relies on a hierarchy of grids, where the highly-resolved LES data are successively filtered and interpolated on coarser grids. On these coarser grids, the data volume is dramatically reduced. The application of modal decomposition methods such as Proper Orthogonal Decomposition (POD) [183, 17, 131], or Dynamic Mode Decomposition (DMD) [167, 175] becomes tractable on the coarsest grids, as these methods require the storage of large amount of snapshots, which is presently intractable for billion-cell simulations without sub-sampling.

This chapter is organized in five parts. First, the high-order implicit filters are presented and analyzed in terms of CPU cost. The MGHOF framework is then exposed. The validation and the choice of the main parameters of the MGHOF are discussed in a third part. Then, the performances of the MGHOF framework are assessed for a 3D turbulent jet plane, where the large-scale dynamics is exhibited. Finally, this framework is applied to the LES of a low-Mach number turbine blade with meshes up to 2.2 billion cells to highlight its ability to extract the large-scale vortices on-line at a limited CPU cost.

4.2 Presentation of the spatial filtering process

4.2.1 Definition

Considering a scalar function $\phi(\mathbf{x}, t)$ defined on the whole computational domain, the general filtering operation has been introduced by Leonard [116] and is defined as follows:

$$\overline{\phi}(\mathbf{x}, t) = \int_{\Omega} G(\mathbf{r}, \mathbf{x})\phi(\mathbf{x} - \mathbf{r}, t)\mathrm{d}\mathbf{r}\,, \tag{4.1}$$

where Ω refers to the entire flow domain and G the filter function satisfying the following normalized property as

$$\int_{\Omega} G(\mathbf{r}, \mathbf{x})\mathrm{d}\mathbf{r} = 1. \tag{4.2}$$

In the particular case of an homogeneous filter function G, meaning independent of $\mathbf{x}$, on an infinite one dimensional domain, the filtering operation deals with a convolution product defined as

$$\overline{\phi}(x, t) = \int_{-\infty}^{+\infty} G_{\Delta}(r)\phi(x - r, t)dr, \tag{4.3}$$

where G_{Δ} is the convolution kernel associated to a filter size Δ.

The most usual 1D-filters have been summarized by Pope [157] and are presented in Tab 4.1. Here, the Gaussian and box filters have second-order moment defined as $\mathcal{M}_2 = \frac{\Delta^2}{24}$. Other filters have the same value of the transfer function at the characteristic cut-off wavenumber $k_c = 2\pi/\Delta$ dealing with $\widehat{G}(k_c) = \exp(-\pi^2/24)$.

Name	**Filter function**	**Transfert function**
General	$G(r)$	$\widehat{G} \equiv \int_{-\infty}^{\infty} \exp(ikr)G(r)dr$
Box	$\frac{1}{\Delta}H\left(\lvert\frac{1}{2} - \frac{r}{\Delta}\rvert\right)$	$\frac{\sin(\frac{1}{2}k\Delta)}{\frac{1}{2}k\Delta}$
Gaussian	$\left(\frac{6}{\pi\Delta^2}\right)^{1/2} \exp\left(-\frac{6r^2}{\Delta^2}\right)$	$\exp\left(-\frac{k^2\Delta^2}{24}\right)$
Sine Cardinal	$\frac{\sin(\pi r/\Delta)}{\pi r}$	$H(1 - \frac{k}{k_c})$
Cauchy	$\frac{a}{\pi\Delta[(r/\Delta)^2+a^2]}, a = \frac{\pi}{24}$	$\exp(-a\Delta\lvert k\rvert)$
Pao	-	$\exp\left(-\frac{\pi^{2/3}}{24}(\Delta\lvert k\rvert)^{4/3}\right)$

TABLE 4.1: Usual one-dimensional filters in the physical and Fourier space

In the spectral space, the Fourier transform of the filtered data $\overline{\phi}(x)$ noted $\widehat{\overline{\phi}}(k)$ can be expressed as the product of the Gaussian kernel in the Fourier space $\widehat{G}_\Delta(k)$ with the Fourier transform of the data $\widehat{\phi}(k)$:

$$\widehat{\overline{\phi}}(k) = \widehat{G}_\Delta(k)\widehat{\phi}(k). \tag{4.4}$$

Moreover, the convolution kernel $\widehat{G}_\Delta(k)$ enables to represent the damping of each monochromatic wave of the signal as a function of the wave-number k. Figure 4.1 represents the convolution kernels in both physical and Fourier space for the most usual filters, ie the Box, Gaussian and Cardinal Sine filter.

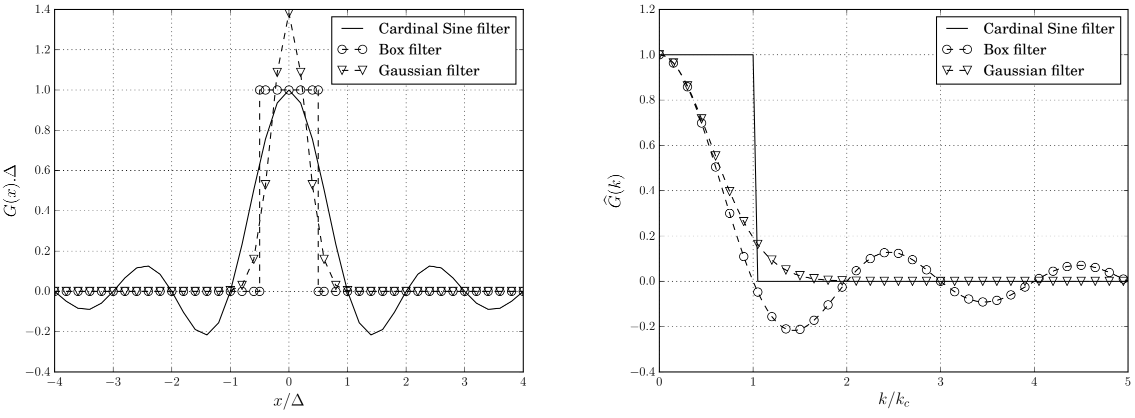

FIGURE 4.1: Most common filters in the physical space (left) and in the Fourier space (right)

Practically, the convolution may be achieved by applying a space discretization of the kernel over the mesh and with classical integration methods. Moreover, the convolution product can also be performed through the Taylor series expansion of the ϕ variable, leading to express the filtered variable $\overline{\phi}$ as a sum of moments [104, 144, 170]:

$$\phi(x,t) = \sum_{j=0}^{\infty} \frac{1}{j!} \frac{\partial^j \phi}{\partial x^j} (y-x,t)^j \,. \tag{4.5}$$

Then, the filtered variable can therefore be written with the following form:

$$\overline{\phi}(x,t) = \int_{-\infty}^{+\infty} \sum_{j=0}^{\infty} \frac{1}{j!} \frac{\partial^j \phi}{\partial x^j} (y-x,t)^j G_\Delta(y-x) dy \,. \tag{4.6}$$

Using the following variable change $z = y - x$, the filtering expression becomes

$$\overline{\phi}(x,t) = \sum_{j=0}^{\infty} \frac{\partial^j \phi}{\partial x^j} \mathcal{M}_j \quad \text{avec} \quad \mathcal{M}_j = \frac{1}{j!} \int_{-\infty}^{\infty} z^j G_\Delta(z) dz \,. \tag{4.7}$$

Then, as Eq 4.7 indicates that the previous Taylor expansion only exists if the kernel G_Δ decreases toward infinity faster than any power of z. Hence, only filters that sufficiently decrease in the physical space can be defined through this expression. For instance, the Taylor series expansion of the Cardinal Sine filter can not be performed through its moments.

Concerning the Gaussian filters, all moments $\mathcal{M}_j$ can be analytically computed and, thanks to the symmetric property, all the odd moments are thus equal to zero as the even moments are defined in the following manner:

$$\mathcal{M}_{2n} = \left(\frac{\Delta^2}{24} \right)^n \frac{1}{n!} \,. \tag{4.8}$$

Finally, the Cardinal Sine filter, as it not sufficiently fast converges toward zero at infinity, can not be defined in the previous usual sense. Moreover, this filter can be seen as the limit, for $n \to \infty$, of filters having their first moments equal to zero and then corresponds to an infinite order filter, also called the ideal low-pass filter.

4.2.2 Relation between selectivity and filter order

The selectivity refers to the ability of spatial low-pass filters to damp the smallest scales while not affecting the largest ones. As the Cardinal Sine filter theoretically leads to a infinite filter order, it has the sharpest transition at the cut-off frequency and therefore the best selectivity. Moreover, Gaussian filters remove signifiant parts of the information before the cut-off frequency and are also not able to completely damp the sub-filter scale information. Those characteristics should absolutely be avoided or minimized when applying filtering procedures for the large-scale extraction.

The design of selective low-pass filters requires a unitary damping function at the neighborhood of the zero frequency allowing to guarantee that the largest flow features associated to the smallest wave-numbers are not affected by the filtering process. This property can be mathematically transposed in term of constraints on the successive derivates of the damping function [200] as

$$\left.\frac{\partial^{2j} G(k)}{\partial k^{2j}}\right|_{k=0} = 0 \quad \text{with} \quad j = 1, 2, ... \tag{4.9}$$

Developing the filtered scalar $\overline{\phi}$ with the moment formulation and then applying the Fourier transform leads to the following expression:

$$\widehat{\overline{\phi}}(k) = \sum_{j=0}^{\infty} (-1)^j k^{2j} \widehat{\phi}(k) \mathcal{M}_{2j} \,. \tag{4.10}$$

Then, taking the ratio between the filtered and unfiltered scalar, the previously introduced damping function in the Fourier space $\widehat{G}$ can thus be written as

$$\widehat{G}(k) = \sum_{j=0}^{\infty} (-1)^j k^{2j} \mathcal{M}_{2j} \,. \tag{4.11}$$

Finally, the successive derivates $\frac{\partial^{2n} \widehat{G}(k)}{\partial k^{2n}}$ can be expressed with the following form:

$$\frac{\partial^{2n} \widehat{G}(k)}{\partial k^{2n}} = (-1)^n (2n)! \mathcal{M}_{2n} + \sum_{j=n+1}^{\infty} \frac{(2j)!}{(2j-2n)!} (-1)^j k^{2j-2n} \mathcal{M}_{2j} \,. \tag{4.12}$$

Moreover, for a zero wave-number $k = 0$:

$$\left.\frac{\partial^{2n} \widehat{G}(k)}{\partial k^{2n}}\right|_{k=0} = (-1)^n (2n)! \mathcal{M}_{2n} \,. \tag{4.13}$$

The previous equation enables to link the successive derivates at $k = 0$ to the moments of the filter and thus highlights the correspondence between the zero values of the $2n$-th moment of the filtering kernel with the zero value of $2n$-th derivates of the Fourier transform of the filtering kernel at the neighborhood of $k = 0$. Hence, selective low-pass filters necessitate a sharp slope near the cut-off frequency allowing to provide an efficient scale separation but also a flat slope at the origin so that to keep the large scales unaffected by the filtering process. As Eq. 4.13 showed, this flatness is directly related to the filter order.

On the one hand, as the first non-zero moment of the Taylor series expansion of the Gaussian filter is the second-order moment, this kernel can thus be defined as a second-order filter and is not ideally suited to perform the large-scale separation. On the other hand, the ideal low-pass filter being of infinite order, therefore has all its derivatives equal to zero for $k = 0$ and allows to perform a perfect scale separation thanks to its discontinuous behavior at the cut-off frequency. High-order filters have a high number of zero derivates for $k = 0$ allowing to keep the largest scales unaffected but also high selectivity behavior at the cut-off frequency. They are thus well suited for the scale separation.

4.2.3 High Order implicit Filter (HOF)

4.2.3.1 Presentation of the High-order filters

The High Order implicit sine Filters (HOF) designed by Raymond and Gardner [160] are considered in this study as they are defined from compact finite-difference operators. A filter of order $2p$ on a one-dimensional domain is obtained by solving the following linear system:

$$[\mathbf{I} + (\beta \mathbf{D})^p]\, \overline{\boldsymbol{\phi}} = \boldsymbol{\phi} \text{ with } \beta = -\epsilon \Delta x^2 \,, \tag{4.14}$$

where $\boldsymbol{\phi}$ and $\overline{\boldsymbol{\phi}}$ respectively represent the unfiltered and filtered variables, Δx the homogeneous mesh size, ϵ a parameter associated to the cut-off wave-number, and $\mathbf{D}$ the second derivative operator defined as

$$(\mathbf{D}\boldsymbol{\phi})_j = \frac{\phi_{j+1} - 2\phi_j + \phi_{j-1}}{\Delta x^2}. \tag{4.15}$$

Considering a monochromatic signal $\phi_k(x) = \mathcal{A} \exp(ikx)$ and defining the cut-off wave-number $k_c = 2\pi/\Delta$, where Δ is the filter width such that the amplitude $\mathcal{A}$ is damped by 50% at k_c, one can write the Fourier transform of ϕ_k and $\overline{\phi}_k$ as

$$\widehat{\phi}_k(k) = \mathcal{A}\delta(k), \tag{4.16}$$

and

$$\widehat{\overline{\phi}}_k(k) = \mathcal{A}\widehat{G}^{2p}(k), \tag{4.17}$$

where $\delta(k)$ is the Dirac function and where the filter kernel $\widehat{G}^{2p}$ is expressed as

$$\widehat{G}^{2p}(k) = \left(1 + \frac{\sin^{2p}(k\Delta x/2)}{\sin^{2p}(k_c \Delta x/2)}\right)^{-1}. \tag{4.18}$$

The maximal attenuation of the Raymond's filters can thus be characterized when the wave number k in Eq. 4.18 tends to the wave number related to the local mesh size defined as $2\pi/\Delta x$:

$$\widehat{G}^{2p}_{max} = \left(1 + \frac{1}{\sin^{2p}(k_c \Delta x/2)}\right)^{-1}. \tag{4.19}$$

In Fig. 4.2, the damping function in the Fourier space of the Raymond filters is compared to a classical Gaussian filter with an adjusted width to have 50% damping at the cut-off frequency. At the order 8 and above, the HOF filters are clearly more selective than the usual Gaussian filter, which is second-order.

The approximated filter kernels in the physical space of the HOF can be computed by filtering a one-dimensional discrete Dirac function, defined as zero everywhere except at the origin where the value is set to $1/\Delta x$,

$$\psi(x) = \begin{cases} 1/\Delta x, & |x| < \Delta x/2 \\ \\ 0, & |x| > \Delta x/2. \end{cases} \tag{4.20}$$

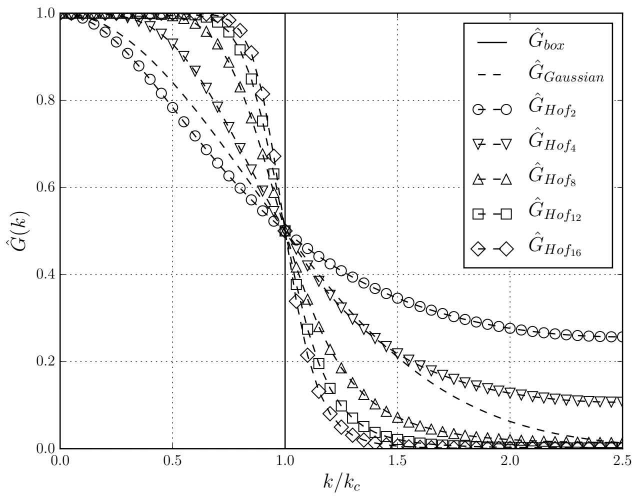

FIGURE 4.2: Comparison of the damping functions in the spectral space for a Gaussian filter and HOF

In Fig. 4.3, the HOF kernels have been compared to the analytic convolution kernel of the Gaussian and cardinal sine filters. It can be noticed that the HOF kernel converges to the cardinal sine kernel as the order increases.

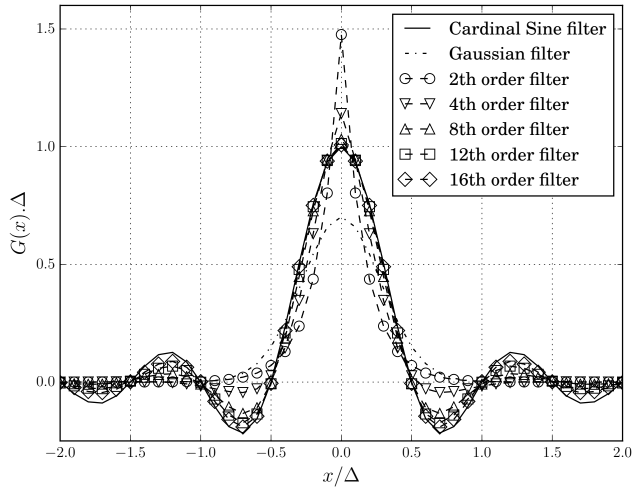

FIGURE 4.3: Comparison of the filter kernel in the physical space for Gaussian and cardinal sine filters and HOF

Moreover, using the Taylor series expansion, the filter kernel $\widehat{G}(k)$ at $k = 0$ can therefore be approximated as

$$\begin{aligned}\widehat{G}^{2p}(k) &= \frac{\widehat{\overline{\mathcal{A}}}(k)}{\widehat{\mathcal{A}}(k)} \\ &= \left(1 + \frac{\sin^{2p}(k\Delta x/2)}{\sin^{2p}(k_c\Delta x/2)}\right)^{-1} \\ &= 1 - k^{2p}\frac{(\Delta x/2)^{2p}}{\sin^{2p}(k_c\Delta x/2)} + o(k^{2p}).\end{aligned} \tag{4.21}$$

Applying a term by term identification with Eq. 4.11 leads to the following form

$$\widehat{G}^{2p}(k) = \mathcal{M}_0 + (-1)^p k^{2p}\mathcal{M}_{2p} + o(k^{2p}), \tag{4.22}$$

with the first moment equal to one ensuring the normalization property of the filter as

$$\mathcal{M}_0 = 1 \quad \text{with} \quad \widehat{G}(0) = 1, \tag{4.23}$$

and

$$\mathcal{M}_{2p} = (-1)^{p+1}\frac{(\Delta x/2)^{2p}}{\sin^{2p}(k_c\Delta x/2)}. \tag{4.24}$$

As the first moment $\mathcal{M}_0$ is equal to 1, the normalization property is guarantied:

$$\mathcal{M}_0 = \int_{-\infty}^{+\infty} G(z)\mathrm{d}z = 1. \tag{4.25}$$

Finally, it is noticeable that the selectivity of the filter increases with the order $2p$ of the filter.

Recently, Guedot et al. [80] adapted those filters to unstructured grids dealing with the resolution of a linear system expressed as $\mathbf{A}\overline{\phi} = \phi$. Here, the matrix $\mathbf{A}$ is defined as $\mathbf{A} = (\mathbf{I} + \mathbf{D}'^p)$ where the matrix $\mathbf{D}'$ consists of a weighted Laplacian operator $(\mathbf{D}'\phi) = (\nabla \cdot \beta\nabla)\phi$. The inversion of this linear system relies on factorization and successive solving of each sub-system [80] and will be briefly detailed below. Both the precision and the performance of this method have been assessed for complex flows in realistic geometries.

4.2.3.2 High-order filters formalism on 3D unstructured grids

Recently, the high-order filters of Raymond have been generalized to 3D unstructured grids with non-uniform grid spacing by Guedot et al. [80] and implemented in the YALES2 CFD code [145]. The proposed methodology attempts to be the most versatile in terms of domain discretization and element type for a finite volume solver using unstructured grid.

First, the second-order derivative operator $\mathbf{D}$ is defined as a node-centered Laplacian operator with periodic boundary conditions. Considering the variable ϕ at the node i, its Laplacian, in the finite volume formalism, deals with the divergence of the gradient, applied to the nodal volume of node i. This operator can therefore be defined as the sum, over the faces of the control volume $\mathcal{V}_i$, of the fluxes equal to $\nabla\phi$ as

$$(\mathbf{D}\phi_i) = \frac{1}{V_i}\sum_{j\in\mathcal{P}_i}\frac{(\phi_j - \phi_i)}{\Delta_{ij}}\mathbf{n}_{ij}.\mathrm{d}\mathbf{A}_{ij}\,, \tag{4.26}$$

where V_i refers to the control volume of the dual mesh element $\mathcal{V}_i$, $\mathcal{N}_i$ is the set of the adjacent nodes of i, $\mathrm{d}\mathbf{A}_{ij}$ is the normal vector of the face of $\mathcal{V}_i$ attributed to the pair (i, j), $\mathbf{n}_{ij}$ is a vector parallel to the direction between the two nodes of the pair (i, j), and Δ_{ij} is the distance between i and j as Fig 4.4 refers.

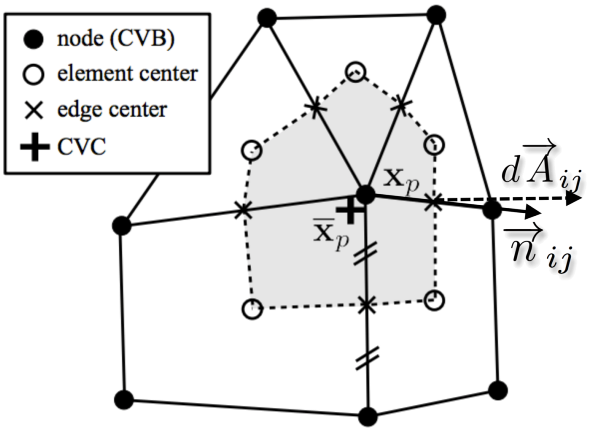

FIGURE 4.4: Node-centered Laplacian computation in YALES2

The discrete conservative properties of the filters are ensured by expressing the β coefficient in a node-centered form and by directly including it in the Laplacian operator itself leading to a modified operator $\mathbf{D}'$ defined as follows:

$$(\mathbf{D}'\phi_i) = (\nabla \cdot \beta \nabla)\phi_i \simeq \frac{1}{V_i} \sum_{j \in \mathcal{N}_i} (\phi_j - \phi_i) \frac{\Delta_{ij}}{(-4)\sin^2(k_c \Delta_{ij}/2)} \mathbf{n}_{ij}.\mathrm{d}\mathbf{A}_{ij}. \tag{4.27}$$

At this point, the high-order filtering operation can thus be written as

$$(\mathbf{I} - \mathbf{D}'^p)\overline{\boldsymbol{\phi}} = \boldsymbol{\phi}\,, \tag{4.28}$$

where $\mathbf{D}'$ is the modified symmetric Laplacian operator with periodic boundary conditions.

Moreover, the computation of the filtered variable necessitates to inverse the following linear system:

$$\mathbf{AX} = \mathbf{b} \quad \text{with} \quad \begin{cases} \mathbf{A} = (\mathbf{I} + \mathbf{D}'^p) \\ \mathbf{X} = \overline{\boldsymbol{\phi}} \\ \mathbf{b} = \boldsymbol{\phi} \end{cases} . \tag{4.29}$$

Here, the matrix $\mathbf{A}$ is $N_n \times N_n$ with N_n referring to the number of nodes of the grid. The performances of the linear system have been verified for complex flows in realistic geometries and the algorithm used for the linear system resolution has been optimized by Malandain et al [135]. However, the convergence of the Preconditioned Conjugate Gradient (PCG) can be improved by replacing the quantity computed by the solver, the filtered variable $\overline{\boldsymbol{\phi}}$, by the difference between the filtered variable and the unfiltered fields as

$$(\mathbf{I} + \mathbf{D}'^p)(\overline{\boldsymbol{\phi}} - \boldsymbol{\phi}) = -\mathbf{D}'^p\boldsymbol{\phi}\,. \tag{4.30}$$

Then, as the filtering operation with those selective low-pass filters does not affect the largest scales of the flow, the variable $\overline{\phi} - \phi$ does not contain any low wave-number components. These low frequencies are the most costly to converge with a PCG algorithm. Finally, the linear system can be expressed as

$$\mathbf{A}\mathbf{X} = \mathbf{b} \quad \text{with} \quad \begin{cases} \mathbf{A} = (\mathbf{I} + \mathbf{D}'^{p}) \\ \mathbf{X} = \overline{\phi} - \phi \\ \mathbf{b} = -\mathbf{D}'^{p}\phi \end{cases} . \tag{4.31}$$

On unstructured grids and for a fixed value of the $\alpha = \Delta/\Delta x$ parameter, the local mesh size Δx is non-homogenous in space leading to a non-homogeneous filter size Δ. In that case, the extraction of coherent structures of a given length can not be correctly achieved as is requires a filter size Δ expressed as the actual physical size of the filter and not as the ratio $\Delta/\Delta x$. However, on meshes with highly heterogeneous mesh size, the filter size Δ may locally becomes smaller than the largest cells leading to troubles in the linear solver convergence. This shortcoming can easily be overcome by limiting the filter size to prevent it from being lower than twice the local mesh size. Moreover, It makes no sense to filter with a filter size smaller than the grid resolution.

4.2.3.3 Factorization of the linear system and real equivalent formulation

For cost reasons that will be developed later, the linear system previously presented has to be factorized in order to be suitable for meshes of several billion cells. Indeed, the solving of the linear system can be improved with better convergence properties and more robustness thanks to the complex factorization of the linear system. This can be achieved by expressing the matrix $\mathbf{A}$ as the product of p complex matrices as

$$\begin{aligned} \mathbf{A} = \mathbf{I} + \mathbf{D}'^{p} &= \prod_{k=1}^{p} \left[\mathbf{D}' - \mathbf{I} \exp\left(\frac{i2k\pi + \pi}{p} \right) \right] \\ &= \prod_{k=1}^{p} (-1) \exp\left(\frac{i2k\pi + \pi}{p} \right) \left[- \exp\left(- \frac{i2k\pi + \pi}{p} \right) \mathbf{D}' + \mathbf{I} \right] \\ &= (-1)^{n}(-1)^{n-1}(-1) \prod_{k=1}^{p} (\alpha_k \mathbf{D}' + \mathbf{I}) = (-1)^{2p} \prod_{k=1}^{p} (\mathbf{I} + \alpha_k \mathbf{D}') \\ &= \prod_{k=1}^{p} (\mathbf{I} + \alpha_k \mathbf{D}') = \prod_{k=1}^{p/2} (\mathbf{I} + \eta_k \mathbf{D}')(\mathbf{I} + \eta_k^{*} \mathbf{D}') \,. \end{aligned} \tag{4.32}$$

with α_k and η_k the real and complex roots of minus one, respectively.

This operation enables to reduce the system order of $2p$ to p second-order systems with sparse matrices easier to inverse. Moreover, each $N \times N$ complex symmetric matrix is then transformed into $2N \times 2N$ real symmetric matrix thanks to real equivalent formulation presented hereafter and are inverted using a PCG algorithm [67]. Hence, p linear systems are inverted instead of one leading to reduce the stencil of the operators for each system. However, matrices are twice larger in both directions.

4.2.3.4 Equivalent real formulation of a complex-valued linear system

Each complex linear system can be expressed with an equivalent real formulation [53]. Considering a complex-valued linear system as

$$\mathbf{C}\boldsymbol{\omega} = \mathbf{d}\,, \tag{4.33}$$

with $\mathbf{C}$ an $m \times n$ known complex matrix, $\mathbf{d}$ is a known complex column vector, and $\boldsymbol{\omega}$ is an unknown complex column vector solution. This system can be expressed by decomposing the previous operators with their real and the imaginary terms as

$$(\mathbf{A} + i\mathbf{B})(\mathbf{x} + i\mathbf{y}) = \mathbf{b} + i\mathbf{c}. \tag{4.34}$$

Then, this formulation gives respectively four possible 2-by-2 block formulations of the previous problem Eq. 4.33 noted from K_1 to K_4:

$$K_1 \text{ formulation} \quad \begin{pmatrix} \mathbf{A} & -\mathbf{B} \\ \mathbf{B} & \mathbf{A} \end{pmatrix} \begin{pmatrix} \mathbf{x} \\ \mathbf{y} \end{pmatrix} = \begin{pmatrix} \mathbf{b} \\ \mathbf{c} \end{pmatrix}, \tag{4.35}$$

$$K_2 \text{ formulation} \quad \begin{pmatrix} \mathbf{A} & \mathbf{B} \\ \mathbf{B} & -\mathbf{A} \end{pmatrix} \begin{pmatrix} \mathbf{x} \\ -\mathbf{y} \end{pmatrix} = \begin{pmatrix} \mathbf{b} \\ \mathbf{c} \end{pmatrix}, \tag{4.36}$$

$$K_3 \text{ formulation} \quad \begin{pmatrix} \mathbf{B} & \mathbf{A} \\ \mathbf{A} & -\mathbf{B} \end{pmatrix} \begin{pmatrix} \mathbf{x} \\ \mathbf{y} \end{pmatrix} = \begin{pmatrix} \mathbf{c} \\ \mathbf{b} \end{pmatrix}, \tag{4.37}$$

$$K_4 \text{ formulation} \quad \begin{pmatrix} \mathbf{B} & -\mathbf{A} \\ \mathbf{A} & \mathbf{B} \end{pmatrix} \begin{pmatrix} \mathbf{x} \\ -\mathbf{y} \end{pmatrix} = \begin{pmatrix} \mathbf{c} \\ \mathbf{b} \end{pmatrix}. \tag{4.38}$$

Here, it is noticeable that the K_4 formulation refers to the same formulation as K_1 with the following form

$$i\mathbf{C}^*\boldsymbol{\omega}^* = i\mathbf{d}^*. \tag{4.39}$$

Similarly, it is straightforward to find the same relation with the K_3 and K_2 formulations. Moreover, Day and Heroux [53] presented the spectral properties of all those configurations and, due to the eigenvalues configuration of Krylov methods, the convergence of the K_1 configuration presents better property than K_2 when applying iterative generalized minimum residual method (GMRES). Finally, if $\mathbf{C}$ is an Hermitian matrix, then K_1 is symmetric and the convergence rate of the real formulation is identical to the one of the initial complex linear system formalism.

Hence, in the case of the HOF filters, assuming the K_1 real matrix formulation for solving the linear system and using the fact that the unknown column vector and right-hand side vector are real-valued, the final equivalent real formulation for the HOF is the following:

$$\begin{pmatrix} Re(\mathbf{I} + \eta_k \mathbf{D}') & -Im(\mathbf{I} + \eta_k \mathbf{D}') \\ Im(\mathbf{I} + \eta_k \mathbf{D}') & Re(\mathbf{I} + \eta_k \mathbf{D}') \end{pmatrix} \begin{pmatrix} Re(\overline{\boldsymbol{\phi}} - \boldsymbol{\phi}) \\ 0 \end{pmatrix} = \begin{pmatrix} Re(-\mathbf{D}'^p \boldsymbol{\phi}) \\ 0 \end{pmatrix}. \tag{4.40}$$

After introducing the resolution of the HOF linear system, some aspects on the filtering cost are then developed.

4.2.4 Modeling the cost of the HOF filters

4.2.4.1 Relationship between the filtering cost and the condition number of the linear system

Applying those filters on fine unstructured LES grids might prove costly as their CPU cost depends non-linearly on various parameters. This cost can be related to the condition number of the matrix $\mathbf{A}$, noted $\kappa(\mathbf{A})$, which is the classical estimator of the convergence speed when solving symmetric positive definite linear systems $\mathbf{Ax} = \mathbf{b}$ with conjugated gradient approaches [76, 196]. This condition number can be expressed with the $\mathcal{L}_2$ norm $||\mathbf{A}||_2$ [196] or using the eigenvalues λ_k of matrix $\mathbf{A}$ [42] as follows:

$$\kappa(\mathbf{A}) = ||\mathbf{A}||_2||\mathbf{A}^{-1}||_2 = \frac{\max|\lambda_k|}{\min|\lambda_k|}. \tag{4.41}$$

In the particular case of the HOF, the condition number of the matrix $\mathbf{A} = \mathbf{I} + \mathbf{D}'^p$ introduced in Eq. 4.14, is expressed by Guedot et al. [80] as:

$$\kappa(\mathbf{A}) = 1 + \frac{1}{\sin^{2p}(k_c \Delta x/2)} = 1 + \frac{1}{\sin^{2p}(\pi \Delta x/\Delta)}. \tag{4.42}$$

This convergence speed estimator thus depends on the filter order $2p$, that has to be large enough to guarantee a high selectivity, but also on the ratio between the filter size Δ and the cell size of the grid Δx. Then, when considering the extraction of large-scale features, the filter size Δ becomes large compared to Δx, leading therefore to a drastically increase of the CPU cost of the filtering process as the condition number scales as $\kappa(\mathbf{A}) \approx \alpha^{2p}$ with $\alpha = \Delta/\Delta x$. Guedot et al. [80] introduced a complex factorization of the linear system, which enables to solve several second-order linear systems instead of one of order $2p$:

$$\mathbf{A}\overline{\phi} = (\mathbf{I} + \mathbf{D}'^p)\overline{\phi} = \prod_{k=1}^{p/2}(\mathbf{I} + \eta_k \mathbf{D}')(\mathbf{I} + \eta_k^* \mathbf{D}')\overline{\phi} = \phi\,, \tag{4.43}$$

with η_k the opposite conjugate complex roots of minus one and η_k^* its conjugate. The eigenvalues of each sub-system $(\mathbf{I} + \eta_k \mathbf{D}')$ can be derived from the analytical expression of the n-dimensional modified Laplacian operator $\mathbf{D}'$ eigenvalues [100] as follows:

$$\lambda_{\eta_k,j} = 1 + \eta_k \frac{\sin^2\left(\frac{j\pi}{N}\right)}{\sin^2\left(\frac{\pi}{\alpha}\right)}. \tag{4.44}$$

Thanks to the complex factorization of the matrix $\mathbf{A}$, the condition number of each sub-system κ_{η_k} can therefore be drastically reduced as only second-order linear systems are solved during the filtering procedure, and the following inequality holds:

$$\kappa_{\eta_k} = \kappa(\mathbf{I} + \eta_k \mathbf{D}') = \frac{\max|\lambda_{\eta_k,j}|}{\min|\lambda_{\eta_k,j}|} << \kappa(\mathbf{A}). \tag{4.45}$$

Equation 4.43 and Eq. 4.44 show that the eigenvalues of each sub-system $\lambda_{\eta_k,j}$ depend on the global filter order $2p$ through the values of the complex roots η_k. Figure 4.5 (left) shows the modulus of the complex eigenvalues $\lambda_{\eta_k,j}$, noted $|\lambda_{\eta_k,j}|$, for the different complex roots η_k with $2p = 12$ and $\alpha = 12$. These complex roots have thus an impact on the condition number of each second order sub-system κ_{η_k} and on the linear system inversion cost. This effect is presented in Fig. 4.5 (right) for various orders with a fixed filter size ratio $\alpha = 12$. It is noticeable that the condition number of the sub-systems increases as the complex roots η_k tend to the complex number value of minus one $\eta_k = -1$. Indeed, this can be explained by the fact that the limit sub-system can be interpreted as an anti-diffusive system which is numerically harder to solve than a diffusive system that would correspond to $\eta_k = 1$.

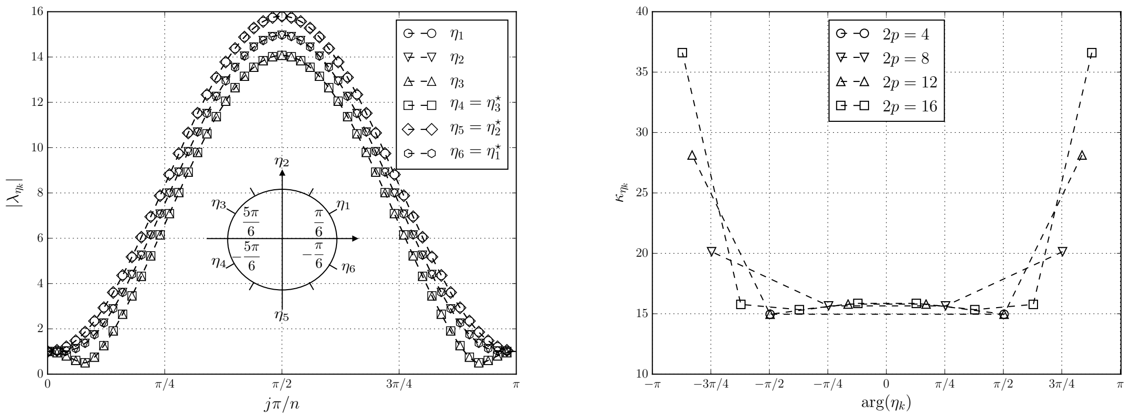

FIGURE 4.5: Eigenvalues modulus $|\lambda_{\eta_k}|$ as a function of the complex roots η_k (left) and condition number κ_{η_k} of each sub-system as a function of η_k (right)

Luenberger [128] demonstrated that for a symmetric definite positive system $\mathbf{Ax} = \mathbf{b}$, the error reduction per iteration using the A-norm, defined as $||\mathbf{x} - \mathbf{x}_n||_{\mathbf{A}} = ||\mathbf{e}_n||_{\mathbf{A}} = \sqrt{\mathbf{e}_n^T \mathbf{A} \mathbf{e}_n}$, is proportional to $\frac{\sqrt{\kappa}-1}{\sqrt{\kappa}+1}$. The same type of error reduction factor at iteration n can be defined based on the residual: $\epsilon_n^{\mathbf{A}} = \frac{||r_n||_{\mathbf{A}}}{||r_0||_{\mathbf{A}}}$. Using the previous result, Van der Vorst [196] stated that the number of iteration N_{iter} so that the residual reduction based on the A-norm falls below a given criterion $\epsilon_{crit}^{\mathbf{A}}$ is given by $N_{iter} \approx -\log(\epsilon_{crit}^{\mathbf{A}})\sqrt{\kappa}$ where κ is the condition number of $\mathbf{A}$.

However, this convergence criterion based on the A-norm is not used in this work as it does not ensure that the residual is sufficiently small everywhere, which can be detrimental to the large-scale feature extraction. Here, the classical residual reduction ϵ_n^∞ based on the infinite norm $\mathcal{L}_\infty$ has been preferred as it enables to guarantee a better accuracy on the computation of the filtered variable $\overline{\phi}$. It is then mandatory to find a relation, similar to the one proposed by Van der Vorst, that links the number of iteration $N_{iter}^{\eta_k}$ to the condition number κ_{η_k} for the $\mathcal{L}_\infty$ convergence criterion. Even if there is no theoretical result on the infinite-norm based convergence criterion, such a relation can be found empirically and is detailed below.

A one-dimensional signal composed of several sine functions with different frequencies is filtered with parameters $\alpha = 12$ and order $2p = 12$. The complex factorization of the linear system imposes the solving of six second-order sub-systems, which correspond to the opposite conjugate of the sixth complex roots of minus one η_k. Figure 4.6 presents the logarithm of the residuals, noted $\log(\epsilon_n^\infty)$ with $\epsilon_n^\infty = \frac{||r_n||_\infty}{||r_0||_\infty}$, against the number of iterations of the conjugated gradient algorithm. From this figure, the linear dependency between the number of iteration for solving one sub-system $N_{iter}^{\eta_k}$ and $\log(\epsilon_{crit}^\infty)$ is observed for several values of the conditions number κ_{η_k} as Tab. 4.2 shows. This linear relation $N_{iter}^{\eta_k} \approx -\beta \log(\epsilon_{crit}^\infty)$ enables to propose a first order approximation of the iteration count as

$$N_{iter}^{\eta_k} = -\gamma \log(\epsilon_{crit}^{\infty}) \kappa_{\eta_k} \,, \tag{4.46}$$

where γ is a constant.

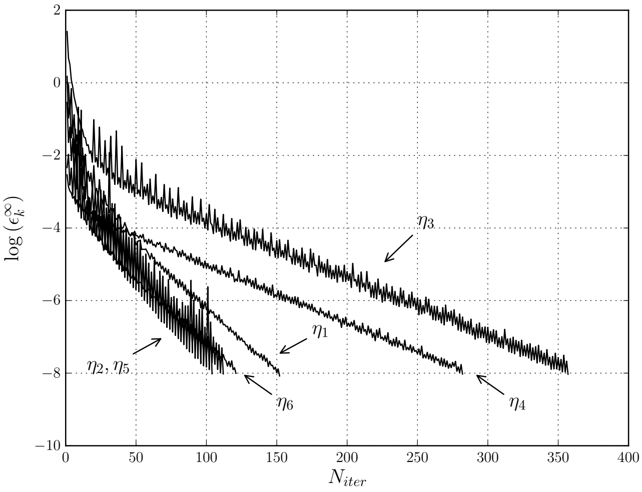

FIGURE 4.6: Residuals logarithm convergence against the iteration count

	η_1	η_2	η_3	$\eta_4 = \eta_3^*$	$\eta_5 = \eta_2^*$	$\eta_6 = \eta_1^*$
$\boldsymbol{\beta}$	3.60×10^{-2}	4.83×10^{-2}	1.58×10^{-2}	1.60×10^{-2}	4.34×10^{-2}	3.59×10^{-2}
$\boldsymbol{\kappa_{\eta_k}}$	15.80	14.96	28.14	28.14	14.96	15.80

TABLE 4.2: Slope β and κ_{η_k} computation for $\alpha = 12$ and $2p = 12$

Finally, under the reasonable assumption that the cost of one iteration of the conjugated gradient algorithm is constant during the computation, it is then clear that the cost of the complex factorization filtering operation is proportional to the sum of the cost from each sub-system through $N_{iter}^{\eta_k}$. The next section further refines the estimation of the filtering cost for the factorized linear system.

4.2.4.2 Estimation of the filtering cost

Even if the complex factorization allows to improve the linear system resolution, the filtering operation still remains expensive for large scales extraction in refined LES. Thus, a precise modeling of the condition number κ_{η_k} is required to estimate their cost and to build a more efficient strategy.

In order to evaluate this cost, a 256^3 homogeneous isotropic turbulence is generated on a Cartesian grid from the synthetic energy spectrum of Pope [157]. Here, l_0 refers to the energetic length scale defined as $l_0 = K^{3/2}/\epsilon$, where K is the turbulent kinetic energy and ϵ is the turbulent kinetic energy dissipation rate as $\epsilon = \nu^3/\eta^4$ with η the Kolmogorov length scale. The model constants β,C_e and C_η are presented in Tab. 4.3 and the relevant physical properties of the turbulent flow in Tab. 4.4 .

Energetic length [m]	l_0	1.5×10^{-3}
Dissipation length [m]	l_d	8×10^{6}
Kinematic viscosity [m^2/s]	ν	1.517×10^{-5}
Model constants	β	5.2
	C_e	$\sqrt{6.78}$
	C_η	0.4

TABLE 4.3: HIT parameters for the Pope synthetic spectrum

Number of grid points	N	256^3
Computational domain size [m]	L	1×10^{-2}
Grid resolution L/N [m]	Δx	3.9×10^{-5}
Integral length [m]	l_t	8.16×10^{-4}
Taylor scale [m]	λ	1.4×10^{-4}
Kolmogorov scale [m]	η_K	8×10^{-6}
Number of integral scales	L/l_t	12.3
Turbulent Reynolds number	Re_t	477
Taylor Reynolds number	Re_λ	84.6
Kinematic viscosity [m^2/s]	ν	1.517×10^{-5}
Turbulent kinetic energy [$\mathrm{m}^2/\mathrm{s}^2$]	K	117.8
Turbulent dissipation rate [$\mathrm{m}^2/\mathrm{s}^3$]	ϵ	8.52×10^{5}

TABLE 4.4: Characteristics of the HIT flow

On a parallel machine with n_c CPU cores, and from the Wall-Clock Time (WCT) or elapsed time of the simulation, one can build a Reduced Computational Time $\mathrm{RCT} = \mathrm{WCT.n_c/n_{cv}}$, where n_{cv} is the number of control volumes of the mesh. With a perfect scalability of the method, this reduced time for a single iteration of a conjugate gradient algorithm should be constant when the mesh size and the number of cores used are modified.

As the RCT of the filtering process is proportional to the number of iterations for solving the factorized linear system, the cost of the global filtering operation, noted $\mathrm{RCT}^{\mathbf{A}_{\Pi_{\mathrm{cplx}}}}$, can therefore be expressed as

$$\mathrm{RCT}^{\mathbf{A}_{\Pi_{\mathrm{cplx}}}} = \sum_{\mathrm{k=1}}^{\mathrm{p/2}} \left[\mathrm{RCT}^{\eta_{\mathrm{k}}} + \mathrm{RCT}^{\eta_{\mathrm{k}}^{\star}}\right] \approx \mathrm{RCT_{iter}} \sum_{\mathrm{k=1}}^{\mathrm{p/2}} \left[\mathrm{N_{iter}^{\eta_k}} + \mathrm{N_{iter}^{\eta_k^{\star}}}\right] \tag{4.47}$$

$$\simeq -\mathrm{RCT_{iter}}\gamma \log(\epsilon_{\mathrm{crit}}^{\infty}) \sum_{\mathrm{k=1}}^{\mathrm{p/2}} \left[\kappa_{\eta_{\mathrm{k}}} + \kappa_{\eta_{\mathrm{k}}^{\star}}\right], \tag{4.48}$$

with $\mathrm{RCT}^{\eta_{\mathrm{k}}}$ the cost for solving one second-order sub-system and $\mathrm{RCT_{iter}}$, the cost for solving one iteration. It can be shown (see 7.2.2) that α the condition number of each sub-system scales as $\kappa_{\eta_k} \approx \alpha^2$ (for α sufficiently large). The analytical sub-system condition numbers are plotted in Fig. 4.7 for a large range of α. Hence, the modeling for the reduced cost of the complex factorization $\mathrm{RCT}^{\mathbf{A}_{\Pi_{\mathrm{cplx}}}}$ can be expressed as

$$\mathrm{RCT}^{\mathbf{A}_{\Pi_{\mathrm{cplx}}}} \propto \mathrm{p}\alpha^2 \,. \tag{4.49}$$

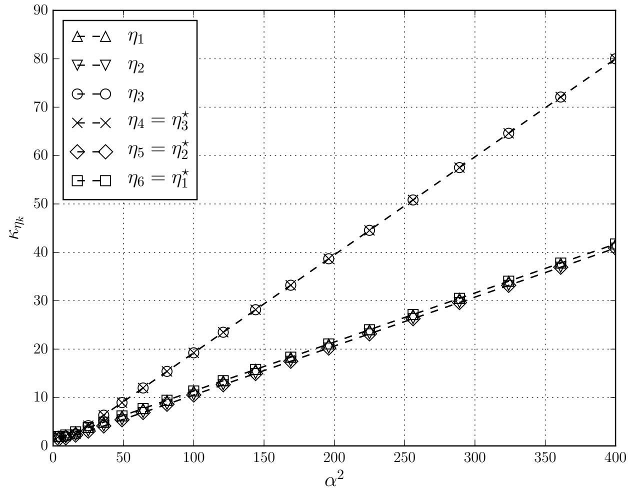

FIGURE 4.7: Analytical condition number of each sub-system as a function of α^2 for $2p = 12$

This scaling is far better than the one of the global system for which $\mathrm{RCT}^{\mathbf{A}} \propto \alpha^{2\mathrm{p}}$. Moreover, these results highlight the linear dependency on the filter order (Fig. 4.8 left) and the quadratic dependency on the filter size ratio (Fig. 4.8 right), all other parameters being fixed. It should be noticed that some parameter combinations are not represented in Fig. 4.8 : for these sets of parameter values, the solving failed even when using the complex factorization. These failures are due to the too stringent values of the condition number κ_{η_k}.

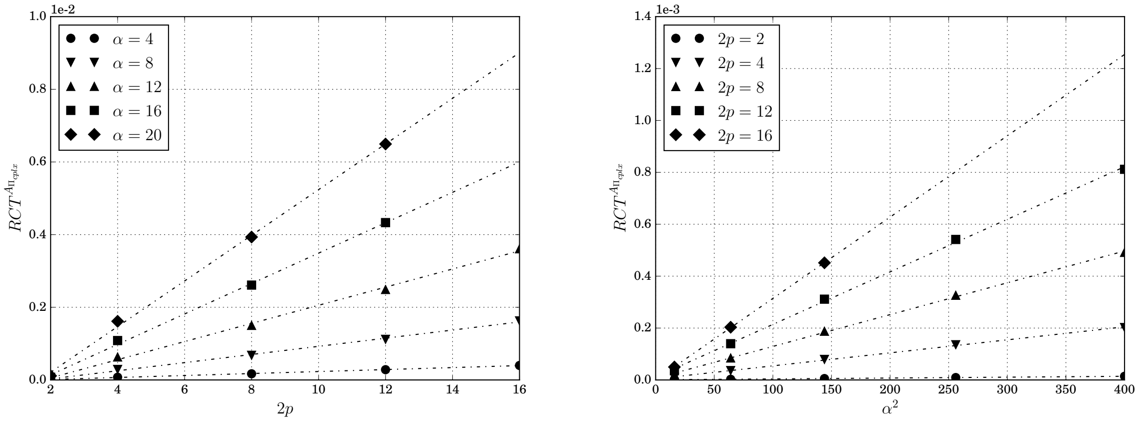

FIGURE 4.8: Evolution of the $\mathrm{RCT}^{\mathbf{A}_{\Pi_{\mathrm{cplx}}}}$ against the filter order $2p$ (left) and filter size parameter α (right)

As a result, the most efficient way to significantly reduce the filtering cost is to propose a framework that enables to decrease the filter size ratio α before applying the filtering procedure. Having a multi-step strategy, where the filtering operation is performed several times with a small α ratio rather than in a single step with a large α ratio, should be more efficient. Those successive filtering operations could be applied on the same fine grid if an sharp cut-off low-pass filter was used, but filtering on a large amount of control volumes still remains expensive. Hence, the cost of the filtering operation can be drastically reduced by transferring the data of interest to intermediate coarser grid levels several times, each time with a smaller dimensionless filter size α. Moreover, the number of control volumes in the intermediate grids is much smaller and the wall clock time needed to perform the filtering on these intermediate grids is greatly reduced.

As an example, Tab. 4.5 shows the variation of the filtering cost for various number of filtering steps with fixed values of $\alpha = \Delta/\Delta x$ = 40 and filter order $2p = 12$. At each step, α is halved, which corresponds to divide Δx by a factor of two keeping the same filter size Δ. The final cost of the filtering operation is noted $\mathrm{RCT_{tot}}$ and is defined as $\mathrm{RCT_{tot}} = \mathrm{n_{step}} \cdot \mathrm{RCT_{step}}$ with n_{step} the number of filtering steps and $\mathrm{RCT_{step}}$ the cost of one step.

Steps	$\Delta/\Delta x$	$\log(\kappa)$	$\mathrm{RCT_{step}}$	$\mathrm{RCT_{tot}}$
1	40	13.264	1.951×10^{-2}	1.951×10^{-2}
2	20	9.668	4.929×10^{-3}	9.857×10^{-3}
3	10	6.120	1.284×10^{-3}	3.852×10^{-3}
4	5	2.770	3.729×10^{-4}	1.492×10^{-3}

TABLE 4.5: Influence of the filtering cost for various intermediate step with $\Delta/\Delta x = 40$ and $2p = 12$

Hence, the cost of the filtering operation can be drastically reduced with a multi-step strategy, which would enable to reduce the filtering cost by an order of magnitude when using three intermediate steps. It should be remarked that this multi-step filtering strategy involves the transfer of data of interest from a grid to a coarser one, which may also have a cost, and this point will be discussed in details hereafter.

4.3 Multi-grid framework

4.3.1 Framework presentation

The multi-grid strategy that has been developed is called the Multi-Grid High-Order Filtering framework (MGHOF). It allows to apply on-the-fly high-order filtering in high-resolution LES at a reasonable cost. As illustrated in Fig. 4.9, the framework relies on two main components: iterative coarsening steps and a final high-order filtering step.

Coarsening step : It is composed of several successive transfers on coarser intermediate grids. Each step combines high-order filtering followed by accurate interpolation onto the coarser grid. The aim is twofold: i) each step allows to decrease the filter size ratio α as the mesh size Δx increases, reducing the CPU cost of the large-scale feature extraction and ii) decreasing the size of the extracted data set. The filtering operation before the interpolation is necessary to avoid any aliasing during the interpolation step.

Filtering step : After having transferred the data of interest onto the coarsest grid, where the large-scale vortices will be analyzed, the filtering process can be performed. On this last level, the grid should have a local mesh size close to the chosen filter size for the large-scale extraction $\Delta \approx \Delta x$.

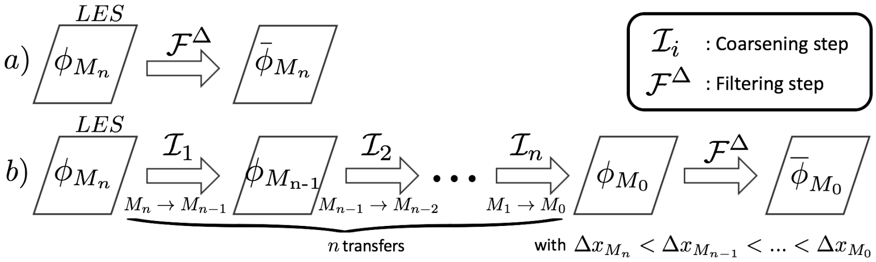

FIGURE 4.9: Presentation of the MGHOF framework : a) The classical filtering procedure and b) the n-steps MGHOF procedure

As stated above, in order to avoid aliasing during the interpolation steps, when the data is transferred from a refined grid to a coarser one, an additional filtering operation has to be performed before interpolation. The filter size has to be large enough to avoid aliasing but small enough to keep the large scales of interest unaffected. This filter size has thus to be related to the local mesh size of the destination grid as $\Delta = \alpha \Delta x$, where α is the filter size ratio, which has to be determined. The complete coarsening step algorithm for transferring data from a fine grid M_f to a coarser one M_c is described hereafter:

Step 1 : Considering the finest grid M_f, the local mesh size of the coarse grid M_c, called Δx_{M_c}, is interpolated onto M_f as $\Delta x_{M_f}^{\mathcal{I}_{M_c}} = \mathcal{I}_{M_c \to M_f}\left[\Delta x_{M_c}\right]$. Transferring from a coarse to a fine grid, there is no need to filter the data to avoid aliasing as the local mesh size field contains only low frequencies that are fully resolved on the fine grid. This local mesh size is defined here as $\Delta x = |V_{node}|^{1/d}$ with V_{node} the control volume around a node and d the number of space dimensions. The accuracy of this approximation depends on the shape of the control volume. It performs well when using dual control volumes in tetrahedral based meshes, which is the case here.

Step 2 : After this first interpolation step, the filter size on M_f, called Δ_{M_f}, is built using the cell size estimation of M_c as $\Delta_{M_f} = \alpha \Delta x_{M_f}^{\mathcal{I}_{M_c}}$. The field of interest ϕ_{M_f} on M_f, can therefore be filtered at this

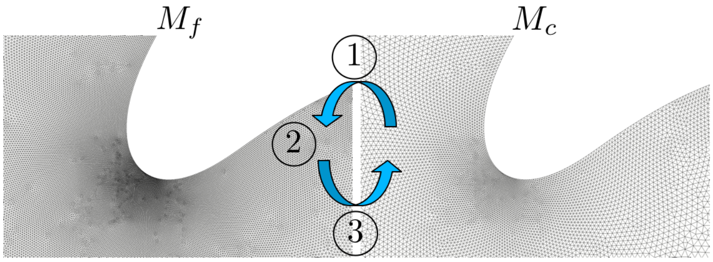

① Interpolate the local mesh size Δx_{M_c} from M_c to M_f

$$\mathcal{I}_{M_c \to M_f}\left[\Delta x_{M_c}\right] = \Delta x_{M_f}^{\mathcal{I}_{M_c}}$$

② Filter the data ϕ_{M_f} $\begin{cases} \Delta_{M_f} = \alpha \Delta x_{M_f}^{\mathcal{I}_{M_c}} \\ \overline{\phi}_{M_f} = \mathcal{F}\left[\phi_{M_f}\right]_{\Delta_{M_f}} \end{cases}$

③ Interpolate the filtered data $\overline{\phi}_{M_f}$ from M_f to M_c

$$\mathcal{I}_{M_f \to M_c}\left[\overline{\phi}_{M_f}\right] = \phi_{M_c}^{\mathcal{I}_{M_f}}$$

FIGURE 4.10: MGHOF framework for large-scales extraction.

filter size leading to $\overline{\phi}_{M_f} = \mathcal{F}\left[\phi_{M_f}\right]_{\Delta_{M_f}}$ with $\alpha \approx 2$ according to the sampling theorem of Nyquist-Shannon.

Step 3 : Once the filtering operation on M_f is done, $\overline{\phi}_{M_f}$ can be interpolated onto M_c as $\phi_{M_c}^{\mathcal{I}_{M_f}} = \mathcal{I}_{M_f \to M_c}\left[\overline{\phi}_{M_f}\right]$.

This procedure can be repeated several times until obtaining a satisfying coarse grid. Two successive grids may have an arbitrary size ratio. However, considering a size ratio of two in each direction, i.e. with a control volume count divided by 8 on the coarser grid, enables to keep small values of the dimensionless filter size $\alpha = \Delta/\Delta x$ and as a result, it ensures good performances of the whole filtering procedure.

4.3.1.1 Grid interpolation method

Each coarsening step requires two interpolations. In the MGHOF, two different interpolation methods have been selected : i) linear interpolation, ii) the high-order interpolation method of Delèze [56, 55]. These two methods are designed for simplicial elements, i.e. triangles in 2D and tetrahedra in 3D. For a given number of dimensions, a simplex is a convex hull with the minimum number of vertices (equal to the number of dimensions plus one). The interpolation kernel of Delèze builds a local finite-element basis in each element based in 3D on 44 continuous and piecewise third-order polynomials, and piecewise rational functions. This basis requires 16 parameters in 3D, i.e. 4 parameters per vertex, which correspond to any data and its gradient. The resulting finite-element representation is $\mathcal{C}^1$ everywhere and $\mathcal{C}^2$ almost everywhere. It is particularly interesting for the present problem as any interpolated scalar and its first derivative are ensured to be continuous across the elements.

Both linear and high-order interpolation methods can only be applied to simplicial elements. These methods are therefore combined to a generic, direct and compact algorithm proposed by Dompierre et al. [93] to subdivide non-tetrahedral elements into tetrahedra in 3D, which does not necessitate neighboring information. This decomposition is based on the use of a unique and constant vertex identifier with a total order relationship that allows splitting quadrilateral faces into triangles in a consistent manner.

4.3.2 Implementation in a massively parallel environment

The MGHOF relies on the filtering and interpolation of a large amount of data across grids with different resolutions. In order to be as generic as possible, it is assumed that the MGHOF grids have their own partitioning and distribution on the MPI ranks within the same MPI communicator, i.e. with the same number of ranks. As such, each rank does not necessarily possess the same part of the computational domain of each grid and therefore, the interpolation process on one rank may require information stored on another rank. This is illustrated in Fig. 4.11 : some parallel copies of mesh blocks have to be performed in order to interpolate the fine grid part of the computational domain stored on processor $\#n$ onto the coarse grid located on processors $\#1$, $\#2$ or $\#3$. This configuration highlights that the interpolation step requires the sending and receiving of a lot of information across the processors. Two choices can be made to perform this data movement : i) to move the coarse grid data, or ii) to move the fine grid data. To minimize the data exchanges and storage requirements, the first choice is the best. Based on this principle, the MGHOF framework only transfers cell groups of the coarse grid from one rank to another as illustrated in Fig. 4.12. In this figure, the MPI data exchanges are two-sided : when a data field is interpolated from the coarse grid to the refined grid, the coarse grid ghost cells have to be populated by the original cells and in the opposite case, the data in the ghost cells have to be copied back to the original cells.

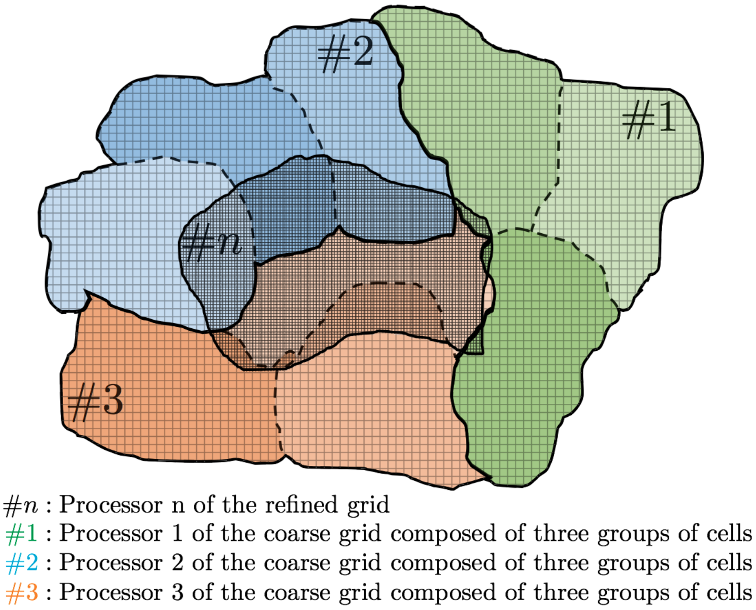

FIGURE 4.11: Mesh partitionning issues between processor n of the refined grid and the coarse grid

The parallelization strategy described below tries to minimize the data duplication and transfers and thus guarantees that the algorithm scales up on massively parallel machines. As shown in Fig. 4.11, all processors are subdivided into cell groups to have a better granularity especially to check if grid blocks overlap or not. Then, only cell groups, whose bounding box intersects with processor $\#n$ bounding box, are sent. All the data transfers are optimized with a packing/unpacking process that enables to minimize the number of messages. The different steps of the implementation are detailed hereafter :

Bounding box intersections and information transfer : The full list of the bounding boxes of all cell

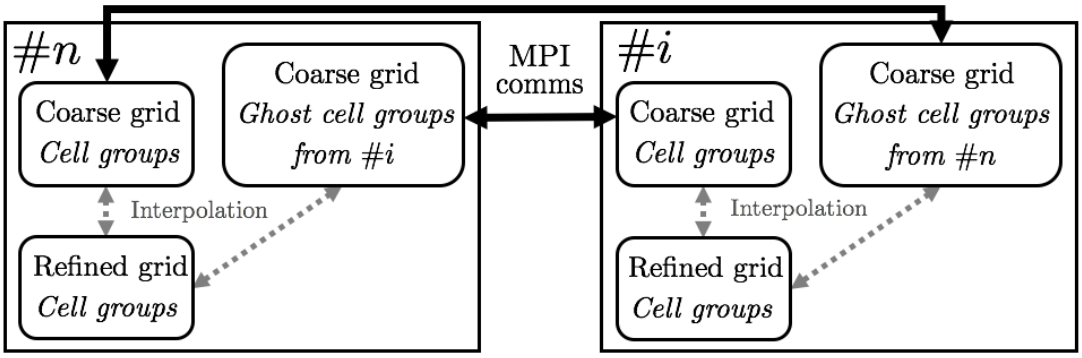

FIGURE 4.12: Data exchanges in the MGHOF framework between two ranks with overlapping coarse and fine grid domains.

groups of the coarse grid is assembled onto all the processors. Then, each processor checks if foreign cell groups intersect with the processor boundaries or not. After this verification, each processor returns to the originating one the list of cell groups they need for the interpolation.

Cell group transfer and data duplication: When the needed information has been returned, each processor successively sends to the other the cell groups they asked for and receives those it needs. The received cell groups are stored as ghost cell groups on the refined grid. All these point-to-point communications are non-blocking and performed simultaneously. The receive operations are posted before the send communications to avoid buffering when possible.

Interpolation step: Here, each processor interpolates the intersecting part between the ghost cell groups and their area of the refined grid. This interpolation step is efficiently performed with a fast grid-to-grid algorithm derived from the vectorized advancing-front vicinity method proposed by Löhner [125].

Reverse cell group transfer and building of the interpolated field: After being interpolated, the ghost cell groups are sent back to their originating processor, and the interpolated field on the coarse grid can be built.

This strategy has been successfully tested up to 2048 cores but it should scale on a larger number of processors as it involves only non-blocking point-to-point communications with a limited number of processors.

4.3.3 Calibration of the MGHOF parameters

This section presents the calibration of the MGHOF framework parameters in a simple configuration. A parametric study is then performed in order to determine the relevant values of three main parameters: filter order $2p$, filter size ratio α, and interpolation order.

4.3.3.1 Numerical experiment

First, a manufactured function ψ defined as a sum of monochromatic sine waves is generated on a fine periodic mesh M_f of size L.

$$\psi(x) = \sum_{k=1}^{N} \sin\left(\frac{2\pi k x}{L}\right) . \tag{4.50}$$

N is chosen so that the fine grid M_f satisfies the sampling theorem of Nyquist-Shannon: the highest frequency is discretized with at least two points per period, and can adequately represent the function ψ in terms of energy in the spectral domain. The function ψ_{M_f} was interpolated with different filtering parameters on a coarser mesh M_c, which cannot correctly represent all these frequencies as $\Delta x_{M_c} \sim 2\Delta x_{M_f}$. So, aliasing occurs unless a filtering operation is performed. This interpolation step is noted $\mathcal{I}_{M_f \to M_c}$ and is applied to the ψ function or to the filtered ψ function noted $\overline{\psi}^{2p}_{\alpha} = \mathcal{F}\left[\psi\right]^{2p}_{\alpha}$ with the filter parameters $2p$ and α. The energy spectrum of the manufactured function $\mathcal{E}_{\psi}(k)$ can be expressed as

$$\mathcal{E}_{\psi}(k) = \widehat{\psi}^{\star,T}(k)\widehat{\psi}(k)\,, \tag{4.51}$$

where $\widehat{\psi}(k)$ is the Fourier transform of ψ and $\widehat{\psi}^{\star,T}(k)$ is its transpose and conjugate, respectively.

The filtering operation in the spectral space is a simple multiplication by the Fourier transform of the filter kernel. As a result, the energy spectrum of the filtered function before interpolation is

$$\mathcal{E}_{\overline{\psi}}(k) = \widehat{G}^2(k)\mathcal{E}_{\psi}(k)\,. \tag{4.52}$$

The important quantity in the MGHOF framework is rather the energy spectrum based on $\widehat{\psi}(k)$ *after it has been interpolated on the coarse mesh*, which is denoted $\mathcal{E}^{\mathcal{I}}_{\overline{\psi}}$. The ratio of this spectrum with the original spectrum $\mathcal{E}_{\psi}$ leads to the energy transfer function defined as

$$\mathcal{T}_{\psi}(k) = \mathcal{E}^{\mathcal{I}}_{\overline{\psi}}(k)/\mathcal{E}_{\psi}(k)\,. \tag{4.53}$$

When $\mathcal{T}_{\psi}$ is less than unity, the combined filtering and interpolation operations damp the signal, while a value larger than unity indicates aliasing. As the Raymond filters were parametrized to have a damping function equal to 50% at the cut-off frequency, the energy spectrum is damped by 25% at the same frequency.

4.3.3.2 Influence of the filter size

First, second-order Raymond filters are considered. This case is interesting because the box and Gaussian filters, that are widely used for data analysis, are also second-order filters. The transfer function for various values of $\alpha = \Delta/\Delta x_{M_c}$, where Δx_{M_c} is the size of the coarse grid, is presented in Fig. 4.13. When no filtering is applied before interpolation, aliasing has a major impact on the transfer function. The amplitude of the under-resolved frequencies may be multiplied by factors exceeding 3.5. When filtering is applied, aliasing effects are removed for the highest values of the filter size ($\alpha > 3$), however the lower frequencies are highly damped. Second-order filters are therefore not suitable for the MGHOF.

4.3.3.3 Influence of the filter order

Figure 4.14 presents the variation of the filter order keeping the dimensionless filter size $\alpha = 2$. The increase of the filter order allows to substantially remove the aliasing and to obtain a selectivity, which becomes comparable to a cardinal sine filter. For a filter order equal to 12, the aliasing is roughly kept under 10%, which guarantees a proper selection of the low frequencies.

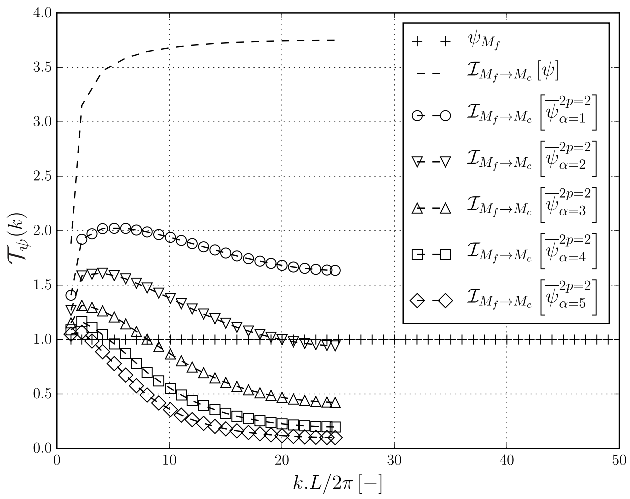

FIGURE 4.13: Influence of the filter size on the energy transfer function with HOF of order 2

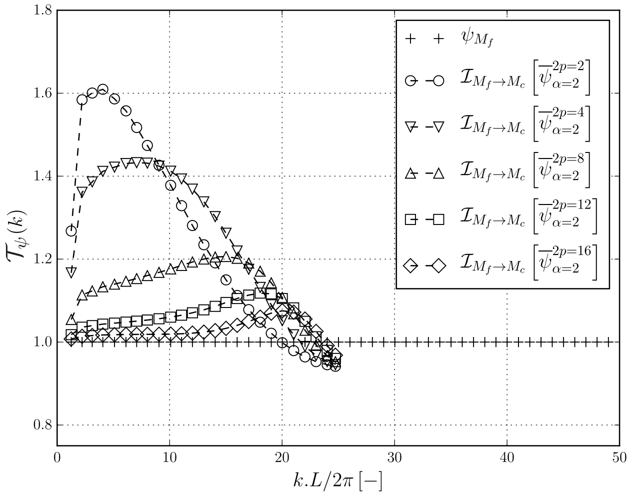

FIGURE 4.14: Influence of the filter order with a filter size $\alpha = 2$

4.3.3.4 Influence of the interpolation order

Finally, the influence of the interpolation method is presented in Fig. 4.15 for a filter order $2p = 12$ and two different filter size ratios. First, considering the filter size $\alpha = 2$, the high-order interpolation seems to be more sensitive to aliasing than linear interpolation. Also, the value of $\alpha = 2.5$ allows to remove all aliasing effects and both interpolation methods give similar results. The optimal value of the filter size seems to be between $\alpha = 2$ and $\alpha = 2.5$.

4.3.3.5 Definition of quality criteria for the HOF

To further investigate the performances of the MGHOF steps, a quality metric Γ_1 is introduced in order to evaluate the amount of frequencies on M_c, which have been damped by less than 90%. Those frequencies, after being filtered and interpolated, are considered as unaltered on M_c. The quantity of

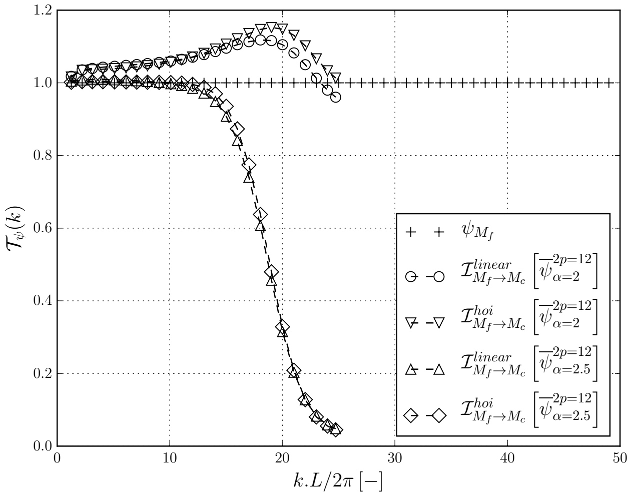

FIGURE 4.15: Influence of the interpolation order with filter size $\alpha = 2$ and $\alpha = 2.5$ and HOF of order 12. High-order interpolation (HOI) is compared to linear interpolation (linear).

unaltered frequencies is then compared to all the frequencies that can be represented on grid M_c according to the Nyquist-Shannon theorem. The quality metric Γ_1 is defined as $\Gamma_1 = k_{c,90\%}/k_{c,M_c}$ where $k_{c,90\%}$ is the cut-off wave-number where the damping rate reaches 90% ie $\widehat{\mathcal{G}}^{2p}(k_{c,90\%}) = 0.9$ and $k_{c,M_f} = 2\pi/2\Delta x_{M_c}$, the cut-off wave-number of the coarse mesh M_c. Γ_1 characterizes the ability of the coarsening step to preserve the frequencies which can be represented on M_c. Table 4.6 shows the variation of Γ_1 with the filter order $2p$ and the filter size ratio α. The percentage of unaltered frequencies increases when the filter order increases but decreases when a larger filter size is used. From these results, it is mandatory to minimize the filter size when using high filter orders.

α	2.0	2.5	3.0	3.5	4.0	4.5	5.0
$n = 2$	0.30	0.25	0.21	0.18	0.16	0.15	0.13
$n = 4$	0.54	0.44	0.37	0.32	0.28	0.25	0.23
$n = 8$	0.72	0.59	0.50	0.43	0.38	0.33	0.30
$n = 12$	0.80	0.65	0.55	0.47	0.41	0.37	0.33
$n = 16$	0.85	0.68	0.57	0.49	0.43	0.39	0.35

TABLE 4.6: Γ_1 metric as a function of the filter order and width

Another quality metric Γ_2 can be introduced in order to quantify more precisely the impact of the interpolation order on the framework. It characterizes the ability of the framework to preserve the largest scales after filtering and interpolation, in other words to quantify the difference between the energy spectrum $\mathcal{E}_\psi$ and $\mathcal{E}^{\mathcal{I}}_{\overline{\psi}}$. For more clarity, the filtered and interpolated function $\mathcal{I}_{M_f\rightarrow M_c}\left[\overline{\psi}^{2p}_{\alpha}\right]$ is here noted ψ_{M_c}. n_c refers to the number of wave numbers smaller than the wave number associated to the filter size $n_c = L/\Delta$ and n_{c,M_c} refers to the number of wave numbers smaller than the one associated to the Nyquist-Shannon limit on M_c $n_{c,M_c} = L/(2\Delta x_{M_c})$. Then, the metric Γ_2 can be defined as

$$\Gamma_2 = \frac{1}{n_c}\sum_{i=1}^{n_c}\left(\frac{n_{c,M_c}}{i}\right)^2 \left|\widehat{\psi}_{M_f}\left(\frac{2\pi i}{L}\right) - \widehat{\psi}_{M_c}\left(\frac{2\pi i}{L}\right)\right|. \tag{4.54}$$

where $\widehat{\psi}_{M_f}$ and $\widehat{\psi}_{M_c}$ are the Fourier transform of ψ_{M_f} and ψ_{M_c}. The weighting factor $(n_{c,M_c}/i)^2$ allows to give more weight to the large scales in the metric calculation as they are the most important for the considered analysis. The results for both interpolation methods are presented in Tab. 4.7 and Tab. 4.8.

α	2.0	2.5	3.0	3.5	4.0	4.5	5.0
$n = 2$	2.33e-02	1.36e-02	8.42e-03	5.18e-03	3.82e-03	2.64e-03	2.12e-03
$n = 4$	1.57e-02	6.69e-03	3.35e-03	1.84e-03	1.43e-03	1.03e-03	9.28e-04
$n = 6$	9.32e-03	2.91e-03	1.32e-03	7.42e-04	3.94e-04	1.45e-04	1.08e-04
$n = 8$	5.37e-03	1.35e-03	6.83e-04	2.28e-04	9.56e-05	4.87e-05	3.52e-05
$n = 10$	3.09e-03	7.38e-04	3.62e-04	1.11e-04	5.23e-05	3.22e-05	2.36e-05
$n = 12$	1.82e-03	4.99e-04	2.13e-04	7.58e-05	4.89e-05	3.16e-05	2.34e-05
$n = 14$	1.12e-03	4.02e-04	1.44e-04	7.26e-05	4.81e-05	3.14e-05	2.33e-05
$n = 16$	7.29e-04	3.56e-04	1.14e-04	7.16e-05	4.78e-05	3.14e-05	2.33e-05

TABLE 4.7: Γ_2 metric for the linear interpolation as a function of the filter order and width

α	2.0	2.5	3.0	3.5	4.0	4.5	5.0
$n = 2$	2.72e-02	1.59e-02	9.84e-03	6.04e-03	4.38e-03	2.97e-03	2.31e-03
$n = 4$	1.78e-02	7.47e-03	3.63e-03	1.93e-03	1.44e-03	1.01e-03	9.03e-04
$n = 6$	1.03e-02	3.05e-03	1.28e-03	6.65e-04	3.28e-04	1.03e-04	7.33e-05
$n = 8$	5.77e-03	1.26e-03	5.48e-04	1.36e-04	3.66e-05	1.09e-05	8.86e-06
$n = 10$	3.17e-03	5.63e-04	2.14e-04	2.97e-05	1.02e-05	5.69e-06	4.03e-06
$n = 12$	1.73e-03	2.89e-04	8.00e-05	1.56e-05	9.97e-06	5.84e-06	4.04e-06
$n = 14$	9.39e-04	1.86e-04	3.93e-05	1.52e-05	9.68e-06	5.93e-06	4.09e-06
$n = 16$	5.08e-04	1.51e-04	2.54e-05	1.47e-05	9.58e-06	6.86e-06	3.93e-06

TABLE 4.8: Γ_2 metric for the high-order interpolation as a function of the filter order and width

The metric Γ_2 allows to highlight and quantify the benefit of using a high-order interpolation method instead of the linear one. For small and medium values of the filter order ($2p \leq 10$) the linear interpolation seems to be more efficient keeping the largest scales unaltered by aliasing and for all filter sizes considered. For higher filter order, the high-order interpolation seems to be better than the linear interpolation whatever the filter size is. This can be explained by the fact that the high-order interpolation seems to be more sensitive to aliasing effects and when those effects are sufficiently removed with adequate filter parameters, the gain of the high-order interpolation method is clear.

4.3.3.6 Choice of the parameter set

From the numerical experiments presented before, a good compromise between selectivity, aliasing and CPU cost is obtained for a filter order 12 ($2p = 12$) and a filter size twice larger than the coarse grid cell size on which the data are interpolated ($\alpha = 2$). These parameters are used at each coarsening step of the MGHOF. The interpolation order does not have a noticeable impact for the chosen parameters and only linear interpolation will be considered. This parameter set is used in all the following sections.

4.4 Applications

4.4.1 Application to the analysis of a turbulent plane jet

In this section, the MGHOF framework is applied to a turbulent plane jet [46] in order to validate the methodology and the chosen parameters on a realistic configuration. The turbulent plane jet features a large range of vortices: Kelvin-Helmholtz vortices are generated close to the inlet slot, which cascade into fully developed turbulence downstream depending on the Reynolds number. The goal of this section is to extract coherent structures of the flow and to compare the cost of the methodology with state-of-the-art visualization techniques based on filtering.

4.4.1.1 Configuration

As the simulation of a turbulent plane jet deals with the spatial growth of coherent vortices, the inflow and outflow boundary conditions have to be set carefully. Slip wall condition have been set on the top and bottom walls while periodic conditions have been imposed in the lateral walls. Moreover, as presented in Fig. 4.16, the dimensions of the computational domain along the three space directions $L_x \times L_y \times L_z$ are expressed from the inlet slot width h as $12.4h \times 12.0h \times 2.9h$.

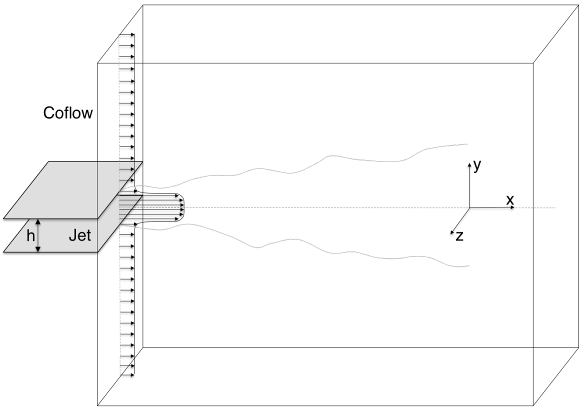

FIGURE 4.16: Turbulent jet plane configuration

The inlet velocity profile is an hyperbolic tangent profile [191] expressed as

$$u_x(x=0,y,z) = \frac{u_j + u_c}{2} + \frac{u_j - u_c}{2} \tanh\left(\frac{h}{4\theta}\left(1 - \frac{2|y|}{h}\right)\right), \tag{4.55}$$

where $u_j = 1.091\, m.s^{-1}$ is the velocity at the jet centerline, $u_c = 0.091\, m.s^{-1}$ is the co-flow velocity, and θ is the momentum thickness which was set to $h/30$. This configuration has been simulated with a Reynolds number defined as $Re_h = \frac{\Delta u h}{\nu} = 66 \times 10^3$ with $\Delta u = u_j - u_c$. Velocity fluctuations with maximum intensity of 5% have been introduced in order to destabilize the flow more rapidly. Large-Eddy Simulation is performed using the dynamic Smagorinsky model [72].

4.4.1.2 Large-scale extraction with the MGHOF

The MGHOF framework may be used in different manners to extract the large coherent structures. However, it will be shown that computing the Q-criterion and then filtering it with the MGHOF may introduce numerical artifacts when the mesh resolution on the final visualization grid is not sufficient. Indeed, the filter kernel of the HOF is close to a cardinal sine function and therefore may introduce negative values when filtering a positive signal. This effect can be illustrated by considering a two-dimensional Gaussian vortex based on the stream function $\psi = u_0 \exp(-(x^2 + y^2)/r_c^2)$ with $2r_c$ the vortex core length. Here, the core length is chosen close to the cut-off frequency of the grid to maximize the numerical artifacts. Then, two different approaches may be chosen to extract the large scales : i) applying directly the MGHOF on Q_u leading to $\overline{Q}_u$, ii) filtering the velocity field noted $\overline{u}$ and then computing the Q-criterion $Q_{\overline{u}}$ from this filtered velocity field. Figure 4.17 shows the raw Q-criterion for this vortex and the differences between these two different approaches. Filtering the Q-criterion ($\overline{Q}_u$) generates several local extrema while decreasing significantly the Q-criterion maximum compared to the alternative method ($Q_{\overline{u}}$). These artifacts are maximized when the mesh is coarse. As a consequence, it is preferable to filter the velocity field during the coarsening steps. However, it may be desirable to filter the Q-criterion on the final mesh to make sure of the scale separation for the visualization or analysis of the flow. The whole strategy is illustrated in Fig. 4.18. As recommended, the velocity field is transferred from the high-fidelity grid to the coarsest grid before computing the Q-criterion and filtering it. This strategy is used to analyze the turbulent plane jet. It will be further adapted for the turbine blade case.

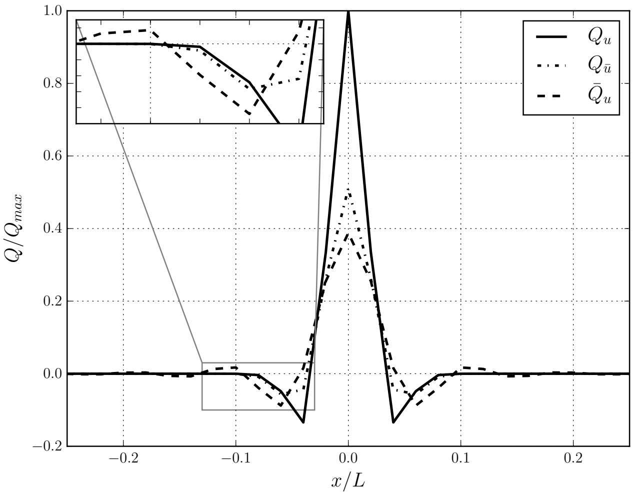

FIGURE 4.17: Q-criterion of a Gaussian vortex for various filtering approaches

4.4.1.3 Application of the framework

An initial coarse grid M_0, with 5 million tetrahedra is first generated. The cell size distribution of this mesh is displayed on Fig.4.19. Applying respectively one and two homogeneous refinement levels on M_0 allows to obtain intermediate grids M_1, with 39 million tetrahedra, and M_2 with 312 million tetrahedra, that are used for the convergence and the computation of the LES. The grid M_2 has therefore a spatial resolution with a cell size close to $\Delta x \approx 0.02h$. The mesh properties are summarized in Tab. 4.9.

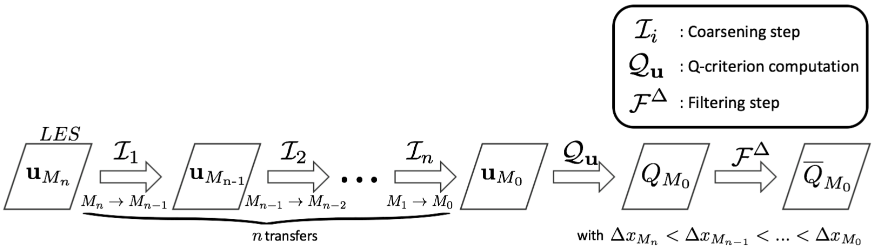

FIGURE 4.18: Principle of the MGHOF framework for the Q-criterion

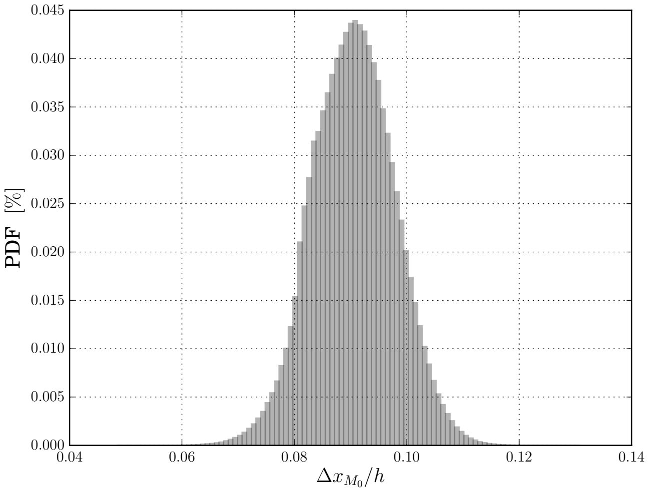

FIGURE 4.19: Normalized local mesh size of M_0: $\Delta x_{M_0}/h$

Mesh	Tetrahedra count ($\times 10^6$)	Average of $\Delta x_M/h$ [-]
M_0	5	9.02×10^{-2}
M_1	39	4.46×10^{-2}
M_2	312	2.23×10^{-2}

TABLE 4.9: Cells count and size for the 3 grids M_0, M_1 and M_2

The ability of the MGHOF framework to identify the coherent flow features is assessed by comparing it to a single high-order filtering procedure. The quality and the accuracy of the large-scale extraction but also the cost of the procedure are the main points of interest. The different considered approaches are presented below:

Classical Filter Operation (CFO): The Q-criterion on the finest mesh M_2, where the LES is performed, has been directly filtered at order $2p = 12$ and with the filter size $\Delta_{0.275h} = 0.275h$. This operation is presented in Fig. 4.20 and is composed of two steps:

$$\begin{cases} \mathcal{Q}_{\mathbf{u}}:\ Q_{M_2} = \mathcal{Q}\left[\boldsymbol{u}_{M_2}\right] \\ \\ \mathcal{F}^{\boldsymbol{\Delta}}:\ \overline{Q}_{M_2} = \mathcal{F}\left[Q_{M_2}\right]^{2p=12}_{\Delta=0.275h}\,. \end{cases} \tag{4.56}$$

FIGURE 4.20: Classical Filtering operation (CFO)

1 Step Multi-Grid Framework (1SMGF): The one-step MGHOF framework is applied to the instantaneous velocity field from M_2 to M_1 with the following parameters $2p = 12$ and $\alpha = 2$. Then, the Q-criterion is computed on M_1, noted Q_{M_1}, using the filtered and interpolated instantaneous velocity field $\boldsymbol{u}_{M_1}$. A last level of filtering, with order $2p = 12$ and filter size $\Delta = 0.275h$, is then applied on Q_{M_1}, i.e. the calculated Q-criterion on M_1. Those operations are presented in Fig. 4.21 and can be summarized as:

$$\begin{cases} \textbf{MGHOF}:\ \boldsymbol{u}_{M_1} = \mathcal{I}_{M_2\to M_1}\left[\overline{\boldsymbol{u}}_{M_2}\right]^{2p=12}_{\alpha=2} \\ \\ \mathcal{Q}_{\mathbf{u}}:\ Q_{M_1} = \mathcal{Q}\left[\boldsymbol{u}_{M_1}\right] \\ \\ \mathcal{F}^{\boldsymbol{\Delta}}:\ \overline{Q}_{M_1} = \mathcal{F}\left[Q_{M_1}\right]^{2p=12}_{\Delta=0.275h}\,. \end{cases} \tag{4.57}$$

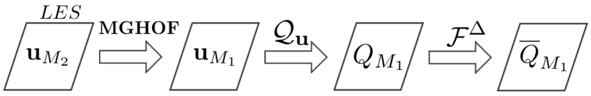

FIGURE 4.21: 1 Step Multi-Grid Framework (1SMGF)

2-Steps Multi-Grid Framework (2SMGF): The two-steps MGHOF framework is applied to the instantaneous velocity field, from M_2 to M_1 a first time and then from M_1 to M_0, with the following parameters $2p = 12$ and $\alpha = 2$. The Q-criterion is then computed on M_0, noted Q_{M_0}, using the filtered and interpolated instantaneous velocity field $\boldsymbol{u}_{M_0}$. A last level of filtering with order $2p = 12$ and filter size $\Delta = 0.275h$ is then applied on Q_{M_0} to compute $\overline{Q}_{M_0}$ (the filtered Q-criterion on M_0). Those operations are presented in Fig. 4.22 and detailed hereafter:

$$\begin{cases} \textbf{MGHOF}:\ \boldsymbol{u}_{M_0} = \mathcal{I}_{M_2\to M_1\to M_0}\left[\overline{\boldsymbol{u}}\right]^{2p=12}_{\alpha=2} \\ \\ \mathcal{Q}_{\mathbf{u}}:\ Q_{M_0} = \mathcal{Q}\left[\boldsymbol{u}_{M_0}\right] \\ \\ \mathcal{F}^{\boldsymbol{\Delta}}:\ \overline{Q}_{M_0} = \mathcal{F}\left[Q_{M_0}\right]^{2p=12}_{\Delta=0.275h}\,. \end{cases} \tag{4.58}$$

4.4.1.4 Results

The following simulations have been performed on the Curie super-computer from CEA in France on 512 processors. The large-scale extraction results are presented in Fig. 4.23 with a chosen Q-criterion

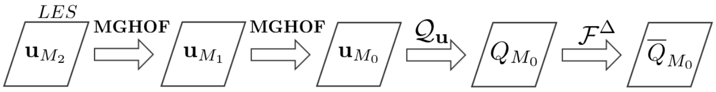

FIGURE 4.22: 2 Steps Multi-Grid Framework (2SMGF)

iso-surface of $Q = 2\,\mathrm{s}^{-2}$. First, the Q-criterion calculated on M_2, noted Q_{M_2} and presented in Fig. 4.23 (a) is compared to the filtered Q-criterion resulting from the three filtering procedures on M_2, M_1 and M_0 respectively noted : $\overline{Q}_{M_2}$ in Fig.4.23 (b), $\overline{Q}_{M_1}$ in Fig. 4.23 (c) and $\overline{Q}_{M_0}$ in Fig. 4.23 (d).

On M_2, the Q-criterion clearly shows an initial region where the Kelvin-Helmholtz vortices are formed, then these coherent structures cascade to small-scale turbulence. The first filtering approach (CFO) allows to damp all the small scales of the flow, especially in the fully turbulent area : this result will be used as a reference for the other methods. The one-step transfer on M_1 (1SMGF) allows to extract Q-criterion iso-surfaces which are very similar to the reference ones : this highlights the ability of the framework to keep the large scales intact after both interpolation and filtering steps. However, the two-steps extraction on M_0 (2SMGF) does not successfully represent all the coherent structures of the flow and noticeably damp the smallest scales : the mesh M_0 is simply too coarse to represent them. The same analysis can also be conducted in Fig. 4.24, which represents a slice of the Q-criterion fields presented in Fig. 4.23.

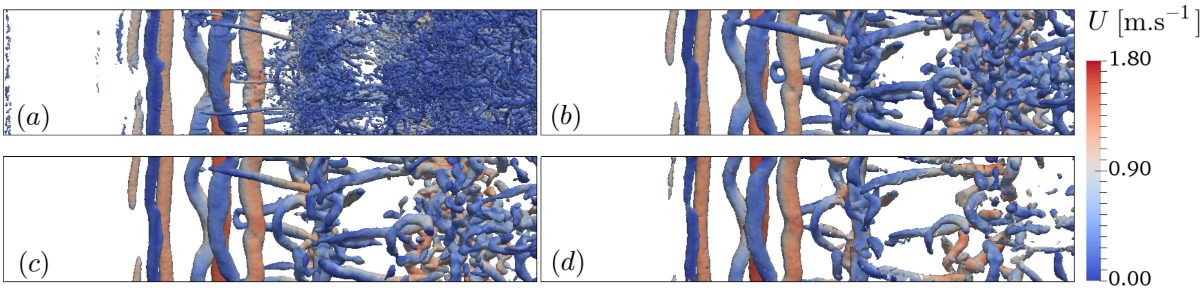

FIGURE 4.23: Q criterion iso-surface ($2s^{-2}$) colored by the instantaneous velocity field on M_2 : (a) Q_{M_2}, (b) $\overline{Q}_{M_2}$, (c) $\overline{Q}_{M_1}$ and (d) $\overline{Q}_{M_0}$

Finally, the performances of all the filtering approaches have been compared by measuring the Reduced Computational Time defined as $\mathrm{RCT} = \mathrm{WCT.n_c/n_{cv}}$, which has been previously introduced. For all the filtering approaches, the convergence criteria, based on the residual infinite norm $||r_k||_\infty = ||\mathbf{A}(\mathbf{x} - \mathbf{x}_k)||$ of the k^{th} iteration, has been set to 1.0×10^{-10}. The Wall-Clock Time of the last filtering step $\mathcal{F}\left[Q_{M_i}\right]^{2p=12}_{\Delta_{0.275h}}$ with $i = 1, ..3$, noted $\mathrm{WCT}_{\mathcal{F}^\Delta}$ and which depends on each filtering approach, is then converted in Reduced Computational Time, noted $\mathrm{RCT}_{\mathcal{F}^\Delta}$, based on the core count of the simulation and the control volumes number of the finest mesh M_2. The RCT of the MGHOF framework, noted $\mathrm{RCT_{MGHOF}}$, has also been taken into account in the total cost of the procedure : $\mathrm{RCT_{tot}} = \mathrm{RCT_{MGHOF}} + \mathrm{RCT}_{\mathcal{F}^\Delta}$.

Table 4.10 presents the performances of the three approaches. First, the $\mathrm{RCT}_{\mathcal{F}^\Delta}$ is drastically decreased when applying one or two steps of the MGHOF framework (1SMGF and 2SMGF) compared to the

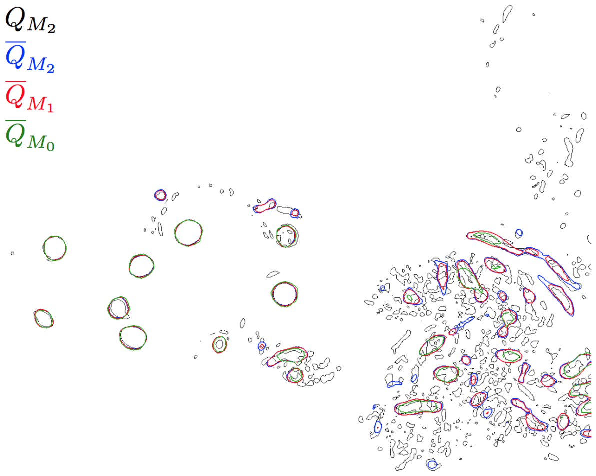

FIGURE 4.24: Comparison of the raw and filtered Q-criterion in a crossing plane

Filtering approach	Final filtering mesh	$\mathrm{WCT}_{\mathcal{F}\Delta}$ $[s]$	$\mathrm{RCT}_{\mathcal{F}\Delta}$ $\left[\frac{s.n_c}{n_{cv}}\right]$	$\mathrm{RCT}_{\mathrm{MGHOF}}$ $\left[\frac{s.n_c}{n_{cv}}\right]$	$\mathrm{RCT}_{\mathrm{tot}}$ $\left[\frac{s.n_c}{n_{cv}}\right]$
CFO	M_2	570.8	9.32×10^{-4}	0	9.32×10^{-4}
1SMGF	M_1	6.5	1.05×10^{-5}	2.78×10^{-4}	2.88×10^{-4}
2SMGF	M_0	0.3	6.04×10^{-7}	2.96×10^{-4}	2.96×10^{-4}

TABLE 4.10: Performance of the filtering approaches

classical filtering operation (CFO). Indeed, the final filtering operation is accelerated as the grid contains respectively 8 and 64 less tetrahedra on M_1 and on M_0. Moreover the filter width when compared to the grid size, $\Delta_{0.275h}/\Delta x$, decreases by a factor 2 and 4, respectively. However, the cost of the MGHOF framework has to be added to the cost of the filtering operation in order to evaluate the gain of the methodology in this configuration. For the CFO approach, the cost of the $\mathrm{RCT}_{\mathrm{MGHOF}}$ is equal to zero as no intermediate grid has been used. Moreover, the total Reduced Computational Time $\mathrm{RCT}_{\mathrm{tot}}$ for both 1SMGF and 2SMGF approaches have been decreased by a factor 3 compared to the CFO approach. The $\mathrm{RCT}_{\mathrm{tot}}$ of the 2SMGF is higher than the one of 1SMGF as the cost of the MGHOF framework $\mathrm{RCT}_{\mathrm{MGHOF}}$ increases. This is due to the selected filter size $\Delta = 0.275h$ which is too close to the local mesh size of M_1 in order to gain more efficiency by adding another intermediate coarse grid. Thus, for this filter width and mesh size, the 2SMGF has a higher cost than the 1SMGF, which appears to be the best approach in terms of cost but also in terms of large-scale resolution.

4.4.1.5 Conclusion for the turbulent plane jet

As a conclusion, the MGHOF framework allows to identify accurately the Kelvin-Helmholtz vortices and the turbulent large scales of the turbulent plane jet with a CPU cost that has been largely decreased, compared to the direct filtering approach. In this configuration, the best filtering strategy is 1SMGF, which is cheaper and more accurate than the 2SMGF. It enables the extraction of the coherent structures on a medium size grid to facilitate the visualization and the post-processing. In this particular case, the potential of the method is not fully exploited as the local mesh size is spatially homogeneous. The next section presents the MGHOF application in a billion-cell LES with highly heterogeneous cell sizes.

4.4.2 Application of the MGHOF to the massively parallel LES of a turbine blade

The MGHOF framework is here applied to the LES of the turbulent flow around a low-Mach number turbine blade from the AITEB2 European project [61]. Identifying the coherent structures in such a complex configuration is quite challenging as it requires to extract on-the-fly features among a broad range of scales and from a very large amount of data.

4.4.2.1 Description of the blade

The T7.2 blade has been experimentally studied by Helge Ladisch [113] and is operated at a Reynolds number of 150,000 based on the chord length and the outlet velocity. At the inlet, the velocity consists of a constant flow with $u_x = 20.4\,\mathrm{m.s}^{-1}$ and $u_y = 15.4\,\mathrm{m.s}^{-1}$ plus homogeneous isotropic turbulence with an intensity of 5.6%. In the experiment, the blade is liquid cooled while the incoming flow is hot. These temperature fluctuations are taken into account in the simulation by transporting a reduced temperature Z, which is equal to 1 at the inlet and 0 at the blade wall. Density and viscosity are computed from this reduced temperature using the ideal gas law and the Sutherland model, respectively. The dynamic Smagorinsky model [72] is chosen to model sub-grid transport. Wall-resolved LES with no-slip walls is considered here. As a result, the meshes have to be fine enough to capture the turbine blade boundary layer.

The main geometrical parameters are presented in Fig. 4.25: D_{max} refers to the maximal blade thickness, C to the chord length, C_{ax} to the axial chord length, P is the pitch distance (blade spacing), Γ to the pitch angle, D_{TE}/P to the trailing edge thickness, and P/C to the pitch to chord ratio.

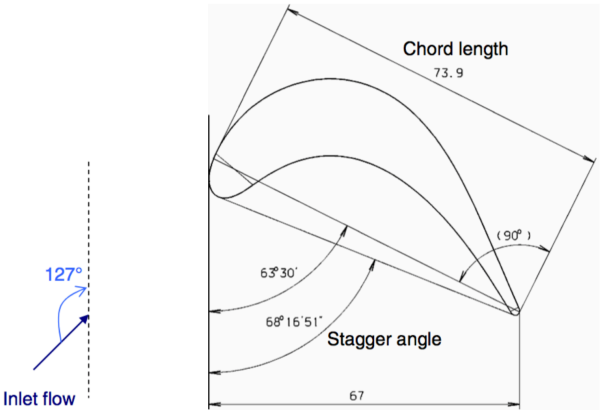

Parameters	Unity	Values
D_{max}	mm	16.53
C	mm	73.93
C_{ax}	mm	67
Γ	°	63.5
D_{TE}/P	[-]	0.035
P/C	[-]	0.772

FIGURE 4.25: Geometrical parameters of the T7.2 blade

An original coarse mesh with 35 million cells, called M_0, is presented in Fig. 4.26. One and two levels of homogeneous grid refinement are then applied on M_0 in order to build M_1 and M_2 with 280 million and 2.2 billion tetrahedra respectively. The LES is performed on M_2 while M_1 and M_0 are intermediate coarser grids used for the large-scale extraction via the MGHOF framework. Moreover, some LES have also been performed on M_0 and M_1 to assess the mesh convergence. Table 4.11 presents the main properties of the grids.

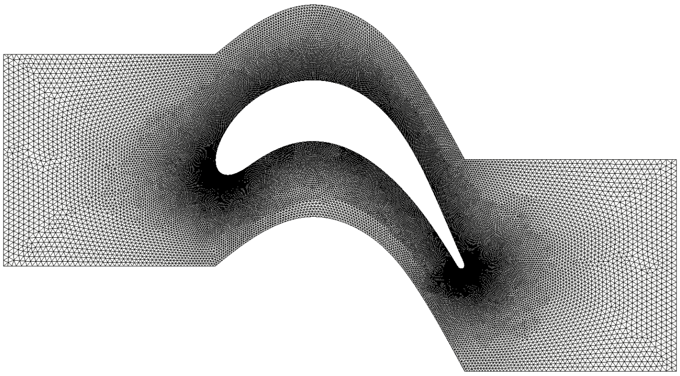

FIGURE 4.26: T7.2 mesh M_0 with 35M cells mesh

Mesh	Tetrahedra count ($\times 10^6$)	Minimum Δx_M [μm]	Maximum $\boldsymbol{y}^+$[-]
M_0	35	30	≈ 19
M_1	280	15	≈ 12
M_2	2200	7.5	≈ 7

TABLE 4.11: Different meshes used for the MGHOF framework

To assess the grid resolution, Fig. 4.27 presents the profiles of mean $\boldsymbol{y}^+$ for the three different grids with s the curvilinear coordinate. On the finest grid, the first grid point is in the viscous sub-layer. The Nusselt number for the finest grid is also presented. Two different methods are used to compute the local Nusselt number based on the chord : i) based on the resolved temperature gradient, ii) based on the total flux at the wall (or residual). The second therefore includes any sub-grid contribution of the models but also from the Dirichlet boundary condition on the temperature. The fact that the two Nusselt number profiles are close and agree well with the experimental data indicates that heat exchanges are well resolved for this mesh resolution.

In this type of configuration, the large amount of data but also the mesh size heterogeneity may lead to a drastic increase of the cost of the filtering process. Indeed, the local mesh size Δx has to be very fine at the leading and trailing edges in order to capture all the flow features while Δx is much bigger in areas far from the blade. As the filtering cost has a quadratic dependency on $\alpha = \Delta/\Delta x$, the smallest local mesh size on the computational domain will therefore be very stringent concerning the convergence and the cost of the filtering process.

4.4.2.2 Large-scale extraction with the MGHOF framework in complex geometry

Before presenting the large-scale extraction strategy, an important aspect has to be taken into account in this configuration : the influence of the blade curvature on the Q-criterion computation and its impact on the visualization of coherent structures.

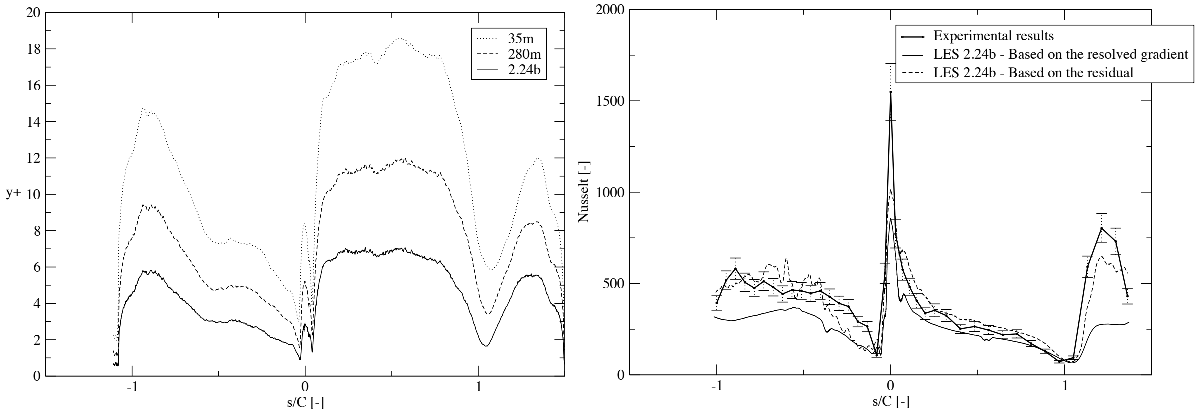

FIGURE 4.27: Mesh resolution based on $\boldsymbol{y}^+$ for the three different grids (left) and Nusselt number on the finer mesh (right)

Curvature effects have a direct impact on the mean velocity field that can disturb the visualization of coherent features when using the Q-criterion as vortex identifier. Figure 4.28 (left) presents the Q-criterion based on the mean velocity field on the mesh M_2 noted $Q_{\langle u_{M_2}\rangle}$ with $\langle . \rangle$ denoting the temporal averaging. Artificial negative Q-criterion values are produced by the curvature on the leading and trailing edges. Layers of positive and negative values are also present at the suction side of the blade. Those artifacts may therefore prevent the extraction of coherent vortices in these regions. An analytic derivation is proposed to quantify this error.

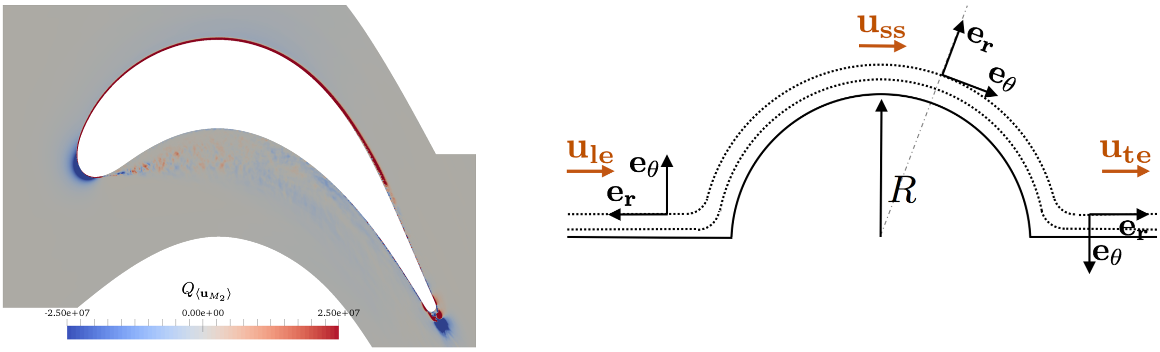

FIGURE 4.28: $Q_{\langle \boldsymbol{u}_{M_2}\rangle}$ field on the M_2 mesh (left) and notations for the estimation of the blade curvature effect on the Q-criterion (left)

First, at the leading edge (LE) and at the trailing edge (TE), due to the presence of stagnation points, the streamlines may approximately derive from a quadratic stream function $\Gamma(x, y) = \frac{a}{2}(y^2 - x^2)$ where a is a non-zero real number, which depends on the local profile curvature. The velocity field denoted $\boldsymbol{u}_{LE}$ and $\boldsymbol{u}_{TE}$, respectively, can then be expressed in local Cartesian coordinates as $\boldsymbol{u}(x, y) = \frac{\partial \Gamma}{\partial y}\boldsymbol{e}_x - \frac{\partial \Gamma}{\partial x}\boldsymbol{e}_y$. With this hypothesis, it is straightforward to express the Q-criterion as $Q = -a^2$. Thus, the Q-criterion is always negative, which is consistent with the negative Q-criterion zones observed on the leading and trailing edges of the blade.

Second, the flow along the suction side (SS) is parallel to the blade and can be represented in local polar coordinates by the following velocity field $\boldsymbol{u}_{SS}(r,\theta) = U(r)\boldsymbol{e}_\theta$ as shown in Fig. 4.28 (right). Following the same methodology, it is found that $Q = U/r \times U'(r)$. This expression explains what is observed on the suction side in Fig. 4.28. The axial velocity profile reaches a maximum at the boundary layer limit and thus the Q-criterion is positive inside the boundary layer and negative outside. These mean values of the Q-criterion due to the blade curvature are able to affect the large-scale vortex extraction and visualization in these area. To avoid this effect, the mean part of the Q-criterion field is substracted from the instantaneous field on M_0. Moreover, some nodes of the mesh can not be interpolated in concave area - for instance under the suction side of the blade - as they are not located in any of the elements of the source grid. These particular points can being interpolated with the "closest node" method interpolation.

As previously presented, the MGHOF framework is applied during the LES computation of the 3D turbulent blade on the 2.2 billion cell mesh M_2 with the following parameters $\alpha = 2$ and $2p = 12$. This on-the-fly co-processing methodology is applied to the instantaneous scalar field z and velocity field $\mathbf{u}$ on M_2. Once the data has been transferred from M_2 to the last coarsening level M_0 leading to $\boldsymbol{u}_{M_0}$ as refers Eq. 4.59, the instantaneous Q-criterion can thus be computed on M_0 using this filtered and interpolated field $\boldsymbol{u}_{M_0}$:

$$\begin{cases} \textbf{MGHOF}: \ \boldsymbol{u}_{M_0} = \mathcal{I}_{M_2\to M_1\to M_0}\left[\overline{\boldsymbol{u}}^{2p=12}_{\alpha=2}\right] \\ \mathcal{Q}_{\mathbf{u}}: \ Q_{\boldsymbol{u}_{M_0}} = \mathcal{Q}\left[\boldsymbol{u}_{M_0}\right]. \end{cases} \quad \begin{cases} \textbf{MGHOF}: \ \langle\boldsymbol{u}_{M_0}\rangle = \mathcal{I}_{M_2\to M_1\to M_0}\left[\overline{\langle\boldsymbol{u}\rangle}^{2p=12}_{\alpha=2}\right] \\ \mathcal{Q}_{\mathbf{u}}: \ Q_{\langle\boldsymbol{u}_{M_0}\rangle} = \mathcal{Q}\left[\langle\boldsymbol{u}_{M_0}\rangle\right]. \end{cases} \tag{4.59}$$

The same procedure is applied to the mean velocity field of M_2 denoted $\langle\boldsymbol{u}\rangle$. Then, the two final Q-criterion fields are substracted in order to remove the curvature effects on the mean flow field, as previously discussed: $Q_{\boldsymbol{u}_{M_0}-\langle\boldsymbol{u}_{M_0}\rangle} = Q_{\boldsymbol{u}_{M_0}} - Q_{\langle\boldsymbol{u}_{M_0}\rangle}$. The full methodology is represented in Fig. 4.29.

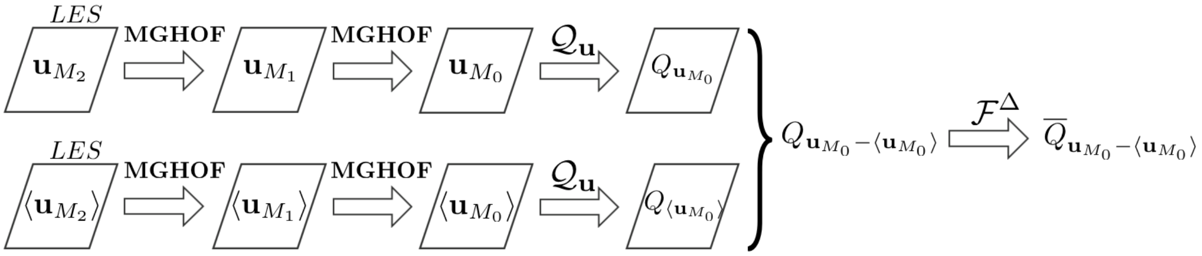

FIGURE 4.29: MGHOF framework for the T7.2 blade applied to the velocity field $\mathbf{u}$

Finally, the last filtering level, here denoted $\mathcal{F}^{\boldsymbol{\Delta}}$, can then be applied to $Q_{\boldsymbol{u}_{M_0}-\langle\boldsymbol{u}_{M_0}\rangle}$ leading to $\overline{Q}_{\boldsymbol{u}_{M_0}-\langle\boldsymbol{u}_{M_0}\rangle}$ defined as

$$\mathcal{F}^{\boldsymbol{\Delta}}: Q_{\boldsymbol{u}_{M_0}-\langle\boldsymbol{u}_{M_0}\rangle} \to \overline{Q}_{\boldsymbol{u}_{M_0}-\langle\boldsymbol{u}_{M_0}\rangle} = \mathcal{F}\left[Q_{\boldsymbol{u}_{M_0}-\langle\boldsymbol{u}_{M_0}\rangle}\right]^{2p=12}_{\boldsymbol{\Delta}}. \tag{4.60}$$

4.4.2.3 Results

The MGHOF framework is here applied to instantaneous and mean velocity fields from the M_2 mesh. This mesh features 2.2 billion cells and has refined boundary layers. This case is therefore very challenging for the large-scale feature extraction.

A few parameters have to be defined for the MGHOF. First, the filter size Δ, that has to be imposed for the last filtering level, denoted $\mathcal{F}^{\boldsymbol{\Delta}}$, has been set up to $\Delta = 0.75\,\mathrm{mm}$, i.e. roughly one tenth of the chord. The aim is to characterize the large-scale vortices close to the boundary layer. Second, this formalism has been applied 50 times during a flow-through time of the simulation using a constant time sampling equal to $\Delta T = 0.05\,\mathrm{ms}$. Finally, this simulation has been performed with 2048 processors of the Curie super-computer. Applying the MGHOF co-processing framework with those parameters only increases the simulation cost of 5%, which is reasonable.

Before performing the large-scale dynamics extraction, Figs. 4.30 and 4.31 present the comparison of the instantaneous non-dimensional temperature and velocity fields computed on the LES grid M_2 to the filtered and interpolated fields of the same data on M_0. It can be noticed that the extracted fields on M_0 contain all the large-scale features of M_2 but they are slightly smoother due to the filtering. Only the highest frequencies corresponding to the smallest scales of the flow that can not be represented on M_0 have been damped.

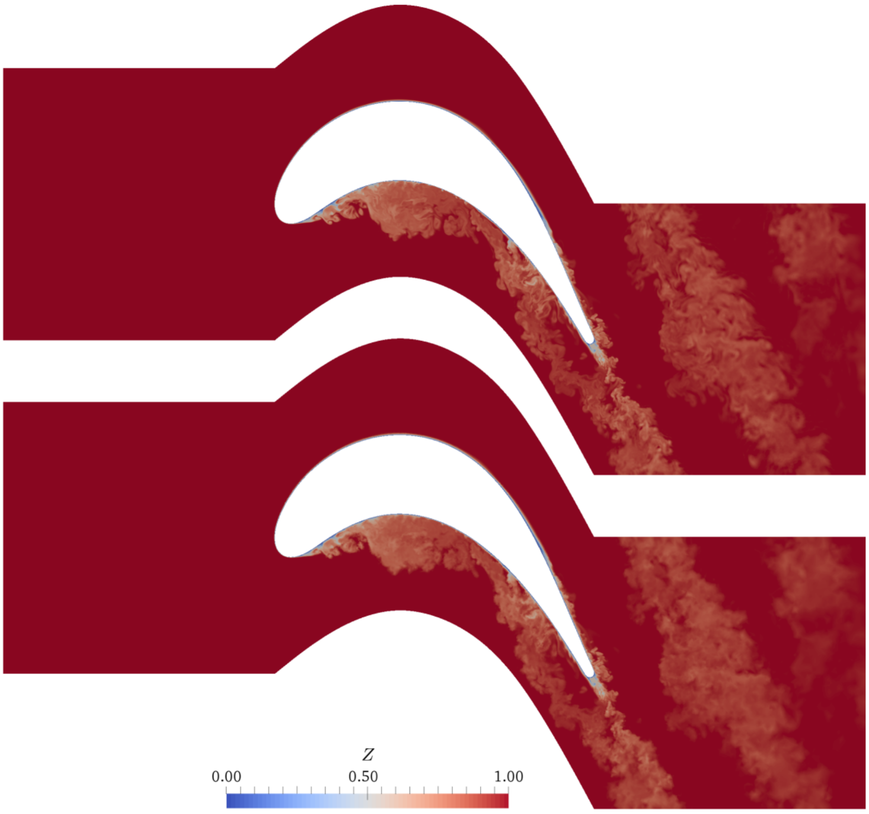

FIGURE 4.30: Comparison between the instantaneous field of the non-dimensional temperature z on M_2 (top) and z_{M_0}on M_0 (bottom)

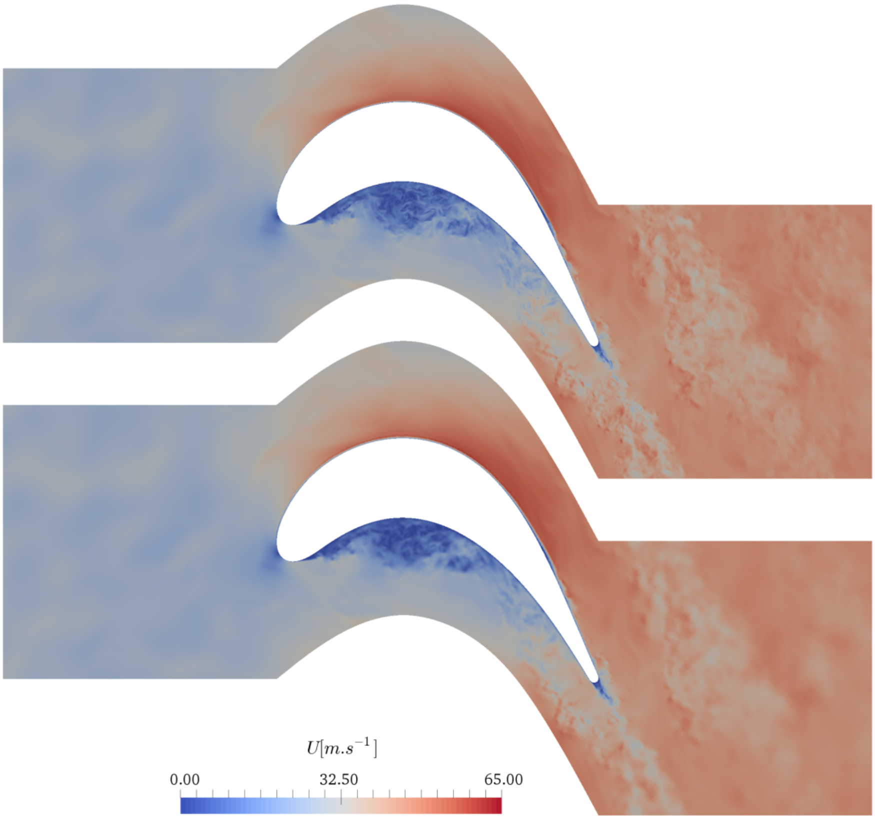

FIGURE 4.31: Comparison between the instantaneous velocity magnitude field $\mathbf{u}$ on M_2 (top) and $\mathbf{u}_{\mathbf{M_0}}$on M_0 (bottom)

The large-scale vortex extraction is presented in Figs. 4.32 and 4.33. On the one hand, the figure on top shows the unfiltered Q-criterion values on the fine grid M_2 previously introduced as $\mathcal{Q}_{\mathbf{u}_{M_2}}$. Here, due to the high level of turbulence, the large vortices are masked by the smallest ones. On the other hand, as shown in the bottom figure, the two steps of the on-the-fly MGHOF framework from M_2 to M_1 and from M_1 to M_0 allows to overcome the Q-criterion scaling issue by removing the smallest vortices of the flow. Indeed, in the recirculation zone at the pressure side and in the wake, the unresolved scales on M_0 disappear due to the filtering. At the leading edge and above the suction side, where large vortices coming from the free-stream turbulence interact with the blade, the largest scales from M_2 are unaffected thanks to the high selectivity of the filters. The wake is also more visible with the MGHOF as all small turbulent scales are removed.

In order to illustrate the performances of the MGHOF framework, the cost of the previous classical filtering operation (CFO) presented in Section 4.4 is compared to the application of the one- and two-steps MGHOF framework, respectively noted 1SMGF and 2SMGF. For the T7.2 blade application, the CFO consists in performing the filtering directly on the 2.2 billion-cell mesh M_2, while 1SMGF refers to the transfer from M_2 to M_1 and 2SMGF from M_2 to M_1 then from M_1 to M_0 before filtering. As previously mentioned, the reduced computational time is noted $\mathrm{RCT}_{\mathcal{F}\Delta}$ for the final filtering step and $\mathrm{RCT}_{\mathrm{MGHOF}}$ for the MGHOF data coarsening. The total cost of the procedure is defined as $\mathrm{RCT}_{\mathrm{tot}} = \mathrm{RCT}_{\mathrm{MGHOF}} + \mathrm{RCT}_{\mathcal{F}\Delta}$. The CPU comparison between these approaches can be found in Tab. 4.12.

Filtering approach	Final filtering mesh	$\mathrm{WCT}_{\mathcal{F}\Delta}$ $[s]$	$\mathrm{RCT}_{\mathcal{F}\Delta}$ $\left[\frac{s.n_c}{n_{cv}}\right]$	$\mathrm{RCT}_{\mathrm{MGHOF}}$ $\left[\frac{s.n_c}{n_{cv}}\right]$	$\mathrm{RCT}_{\mathrm{tot}}$ $\left[\frac{s.n_c}{n_{cv}}\right]$
CFO	M_2	11179.15	1.04×10^{-2}	0	1.04×10^{-2}
1SMGF	M_1	6.32	5.88×10^{-6}	1.64×10^{-4}	1.70×10^{-4}
2SMGF	M_0	6.29	5.86×10^{-6}	1.65×10^{-4}	1.71×10^{-4}

TABLE 4.12: Performance of the filtering approaches for the T7.2 configuration

These performances highlight the fact that the 1SMGF and 2SMGF approaches enable to drastically decrease the CPU cost of the filtering process. Indeed, both approaches lead to a speed-up of more than 60 compared to the CFO approach. It may be noted that the final filtering step has a negligible contribution to the total cost when the MGHOF is used. Remarkably, the data coarsening has the same cost for 1SMGF and 2SMGF, which indicates that the data transfer from M_1 to M_0 is negligible compared to the data transfer from M_2 to M_1. For the same total cost, the 2SMGF approach enables a far better data compression rate.

Although the MGHOF framework successfully extracts coherent features from a highly resolved LES, more physical analysis and flow understanding can be gained by combining it with mode decomposition methods that allows to access to more quantitative information about the dynamically important flow structures.

4.5 Conclusions

In this chapter, the Multi-Grid High Order Filtering framework (MGHOF) for on-the-fly co-processing of highly-resolved LES is proposed. This approach enables to extract and identify coherent features from 3D turbulent flows in complex geometries. It transfers the large-scale dynamics onto coarser levels of grid that allows to drastically decrease the amount of data to post-process. Moreover, the successive coarsening steps based on high-order filtering and interpolation allow to overcome the Q-criterion scaling issue which is particularly annoying for the large scales visualization.

The MGHOF framework has been applied in several complex configurations. First, a 3D turbulent planar jet configuration has been considered in order to extract the Kelvin-Helmholtz vortices and the coherent structures of this turbulent flow. Then, the LES of a 3D turbulent low-Mach turbine blade configuration with a mesh of 2.2 billion tetrahedra has been co-processed, allowing to successfully extract, through the Q-criterion, the dynamically dominant features. This methodology opens new processing possibilities that allow to understand more precisely the interactions between coherent structures coming from the free stream turbulence with those created by the blade.

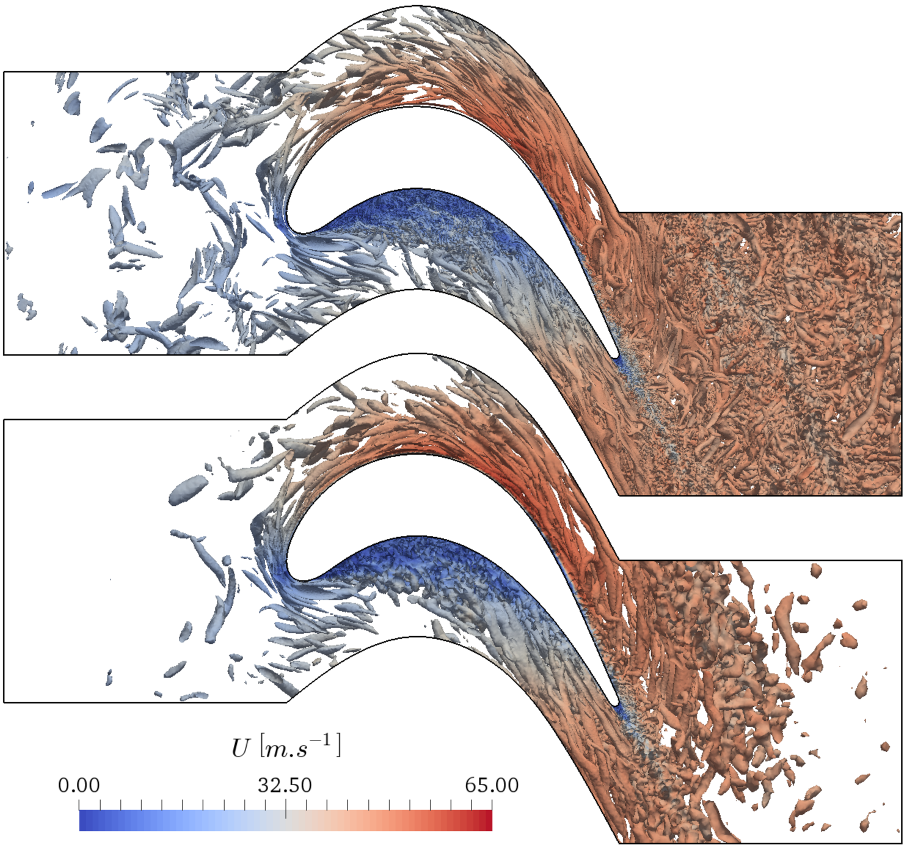

FIGURE 4.32: Side view of the iso-contour of Q-criterion = $2.0 \times 10^6\,\mathrm{s}^{-2}$ for $\mathcal{Q}_{\mathbf{u}_{M_2}}$ (top) and $Q_{\boldsymbol{u}_{M_0}-\langle \boldsymbol{u}_{M_0}\rangle}$ (bottom)

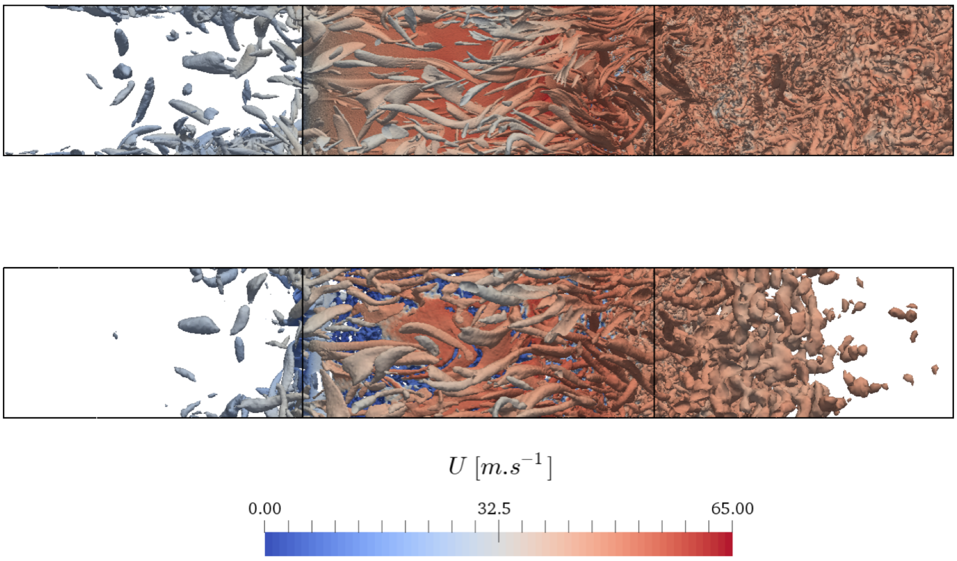

FIGURE 4.33: Top view of the iso-contour of Q-criterion = $2.0\times10^6\,\mathrm{s}^{-2}$ for $\mathcal{Q}_{\mathbf{u}_{M_2}}$ (top) and $Q_{\boldsymbol{u}_{M_0}-\langle \boldsymbol{u}_{M_0}\rangle}$ (bottom)

Chapter 5

Application of the MGHOF framework to modal decomposition methods

This chapter introduces modal decomposition methods such as Proper Orthogonal decomposition (POD) and Dynamic Mode Decomposition (DMD). These approaches enable to identify and to extract the most dominant features from both laminar and turbulent flows. This chapter first presents the main theoretical concepts and mathematical background of the modal approximation methods. Then, the DMD formalism is developed in detail with the presentation of an analytical formulation for solving the minimization problem related to DMD modes amplitudes. Finally, once the methodology has been validated on a laminar 2D cylinder configuration, the modal analysis of the billion-cell LES of a 3D turbulent blade is achieved by applying both the MGHOF framework and the DMD formalism.

Contents

5.1 Introduction

Despite the complexity of turbulence processes, turbulent flows can be pragmatically studied through approaches that reduce the flow dynamics to a reasonable number of parameters thanks to the existence of organized fluid elements. Hence, building reduced order models for unsteady turbulent configurations can be achieved by identifying and selecting the most dominant modes that usually refer to coherent features. The flow dynamics can be reconstructed by superposing selected modes associated to their own coefficients that characterize their temporal evolution. Modal extraction methods for coherent structures from both experiments and numerical simulations have have made considerable progress in the recent decades. Some of the most famous modal decomposition formalisms are mentioned : The Proper Orthogonal Decomposition (POD) modes [183, 17, 131], the global stability analysis [7, 8] and the balanced modes (BOD) [141, 166] have provided useful and interesting insights concerning the flow dynamics. More recently, Rowley and Schmid proposed a most efficient feature extraction method called the Dynamic Mode Decomposition (DMD) [167, 175] with several more advanced variations as the optimized DMD [35] based on combinatory search of the most relevant modes, Low-rank DMD and sparse DMD [99] and the sparsity-promoting DMD [98].

POD and DMD methodologies are both snapshot-based post-processing algorithms that can be applied on collected data from both experiments or numerical simulations and enable to build a low-rank subset of modes that approximates the dynamical system [5]. Indeed, the spectral analysis first extracts the dynamic information while identifying certain modes that are considered having dominant behaviors in the flow. On the one hand, the spatial orthogonality constraint assumed for the POD formalism enables to decompose the flow onto a spatial orthogonal set of modes that contains multi-frequency components and that maximizes the energy content representation of the flow. On the other hand, the DMD approach derived from the linear Koopman analysis [115, 137] and is based on non-orthogonal monochromatic modes to capture the most dominant features in the flow.

Furthermore, identifying the most important frequencies in flows may not alway straightforwardly be achieved through the application of the POD formalism as computed modes are associated to multi-frequency phenomena contrary to the DMD approach that deals with monochromatic modes. Due to the spatial orthogonality property, however, the temporal behavior of the POD modes can simply be computed by projecting the dataset onto the subset of modes which is not the case with the DMD approach where a minimization problem has to be solved. Finally, even if the identification of the dominant coherent features is usually straightforward for canonical simple laminar configurations, it becomes very challenging for highly turbulent flows, where all the resolved frequencies are exited by the background noise and where perturbations from transient and multiple basic modes are strongly present.

In this chapter, the main theoretical concepts of the modal approximation methods will first be introduced with a brief highlight on the particular case of the POD methodology and its shortcomings. In a second time, the mathematical background of the implemented DMD algorithms in the CFD code YALES2 will be presented in details with some aspects about the modes selection criteria. Finally, two applications of the DMD formalism are exposed : First, the classical 2D laminar cylinder is developed in order to validate the implemented algorithms. Second, a very challenging configuration where the DMD formalism is combined with the large-scales extraction MGHOF framework in order to identify the dominant features of the billion-cell LES of the T7.2 configuration.

5.2 Presentation of the modal decomposition methods

5.2.1 Approximation method

Both POD and DMD methodologies are related to approximation methods [164] that deal with the following problem: Considering a vector real function $\mathbf{f}$ that has a temporal and space dependency as $\mathbf{f}(\mathbf{x}, t)$, this function can be approximated by a finite sum of a product of univariate functions such as

$$\mathbf{f}(\mathbf{x}, t) \approx \sum_{k=1}^{n} a_k(t)\boldsymbol{\phi}_k(\mathbf{x})\,. \tag{5.1}$$

As the number of terms n of the sum converges to infinity, this relation tends to more accurately approximate the $\mathbf{f}$ function. However, this decomposition is not unique and thus, it is mandatory to find the best one for a specific norm choice and with a constant number of modes n. In the CFD field, the $\mathcal{L}_2$ norm is generally chosen as it corresponds to flows with finite kinetic energy as $\mathcal{L}_2(\mathbf{u}) = ||\mathbf{u}||_2$. Hence, the unicity problematic can be achieved by considering a least square minimization problem that determines the set of coefficients and functions $\{(a_1, \boldsymbol{\phi}_1), ..., (a_n, \boldsymbol{\phi}_n)\}$ in the following manner:

$$\min_{\boldsymbol{\Phi},\mathbf{a}} \sum_{i=1}^{n_t} ||\mathbf{f}(\mathbf{x}, t_i) - \sum_{k=1}^{n} a_k(t_i)\boldsymbol{\phi}_k(\mathbf{x})||_2^2 \quad \text{with} \quad n \leq n_t\,, \tag{5.2}$$

where n_t refers to the temporal discretization of the $\mathbf{f}$ function.

Finally, the solution of this minimization problem is given by the truncated Singular Value Decomposition (SVD) of order n that is developed in the following section.

5.2.2 Introduction to the Singular Value Decomposition (SVD)

The Singular value Decomposition SVD, introduced by Golub [75], is the generalization of the eigen-decomposition for real or complex positive semidefinite normal matrices - positive eigenvalues with $\mathbf{M}^H\mathbf{M} = \mathbf{M}\mathbf{M}^H$ - and enables to factorize them. This method has many useful applications in signal processing, its theorem is formulated as follows:

Theorem : Singular Value Decomposition Considering a real or complex $m \times n$ matrix $\mathbf{M}$, there exists a factorization, called a singular value decomposition of $\mathbf{M}$, that can be expressed as

$$\mathbf{M} = \mathbf{U}\boldsymbol{\Sigma}\mathbf{W}^H\,, \tag{5.3}$$

where

- $\mathbf{U}$ is a $m \times m$, real or complex unitary matrix.
- $\boldsymbol{\Sigma}$ is a rectangular diagonal matrix $m \times n$ with positive semi-definite σ_i on the diagonal with the following properties $\Sigma^T\Sigma = I_n$ and $\Sigma\Sigma^T = I_m$.
- $\mathbf{W}$ is a $n \times n$, real or complex unitary matrix and $\mathbf{W}^H$ its conjugate and transpose matrix, also called Hermitian matrix.

As unitary matrix, $\mathbf{U}$ and $\mathbf{W}$ have the following property:

$$\begin{aligned}\mathbf{U}^H\mathbf{U} &= \mathbf{I}_m\,,\\ \mathbf{W}^H\mathbf{W} &= \mathbf{I}_n\,.\end{aligned} \tag{5.4}$$

Moreover, the SVD can be used in several practical applications in order to compute the pseudo inverse of the $\mathbf{M}$ matrix defined as follows:

$$\mathbf{M}^+ = \mathbf{W}\mathbf{\Sigma}^+\mathbf{U}^H\,, \tag{5.5}$$

where $\mathbf{\Sigma}^+$ is the pseudo inverse of $\mathbf{\Sigma}$ defined as:

$$\mathbf{\Sigma}^+_{ii} = \begin{cases} 1/\mathbf{\Sigma}_{ii} & \text{if} \quad \mathbf{\Sigma}_{ii} \neq 0 \\ 0 & \text{else} \end{cases}\,. \tag{5.6}$$

The singular values of $\mathbf{M}$ and $\mathbf{M}^H$ are the diagonal coefficients σ_i with $i \in \min(m,n)$ of the matrix $\mathbf{\Sigma}$ and the convention for ordering them is the descending order. The rank of the $\mathbf{M}$ matrix is equal to the number of non-zero singular values. As σ_i are non-negative real numbers, then the column vectors of $\mathbf{U}$ and $\mathbf{W}$, $\mathbf{u}_i$ and $\mathbf{w}_i$ respectively, are called the left and right eigenvectors of the singular value σ_i as they satisfied the following property:

$$\mathbf{M}\mathbf{w}_i = \sigma_i\mathbf{u}_i \quad \text{and} \quad \mathbf{M}^H\mathbf{u}_i = \sigma_i\mathbf{w}_i\,. \tag{5.7}$$

Then, the columns of the matrix $\mathbf{U} = \{\mathbf{u}_1, \mathbf{u}_2, ..., \mathbf{u}_m\}$ and $\mathbf{W} = \{\mathbf{w}_1, \mathbf{w}_2, ..., \mathbf{w}_n\}$ but also the rows of the adjoint matrix $\mathbf{U}^H$ and $\mathbf{W}^H$ form orthonormal bases. Those vectors are respectively called the left-singular and right-singular vectors of $\mathbf{M}$ and some properties can be deducted:

- The left-singular vectors of $\mathbf{M}$ are a set of orthonormal eigenvectors of $\mathbf{M}\mathbf{M}^H$.
- The right-singular vectors of $\mathbf{M}$ are a set of orthonormal eigenvectors of $\mathbf{M}^H\mathbf{M}$.
- The non-zero singular values of $\mathbf{M}$ are the square roots of the non-zero eigenvalues of both $\mathbf{M}^H\mathbf{M}$ and $\mathbf{M}\mathbf{M}^H$.

Indeed, as the direct computation of the SVD singular values and left/right eigenvectors is not straightforward, it is more relevant to compute them by solving an equivalent eigenvalue problem on the square matrix $\mathbf{M}^H\mathbf{M}$. The SVD application on this matrix can thus be expressed as

$$\begin{aligned}\mathbf{M}^H\mathbf{M} &= \left(\mathbf{W}\mathbf{\Sigma}\mathbf{U}^H\right)\left(\mathbf{U}\mathbf{\Sigma}\mathbf{W}^H\right)\\ &= \mathbf{W}\mathbf{\Sigma}^2\mathbf{W}^H\,.\end{aligned} \tag{5.8}$$

Moreover, as $\mathbf{M}^H\mathbf{M}$ is hermitian ie $\mathbf{M}^H\mathbf{M} = [\mathbf{M}^H\mathbf{M}]^H$, its diagonalization on an orthogonal basis leads to:

$$\mathbf{M}^H\mathbf{M} = \mathbf{Z}\mathbf{\Lambda}\mathbf{Z}^{-1} = \mathbf{Z}\mathbf{\Lambda}\mathbf{Z}^H\,, \tag{5.9}$$

where $\mathbf{Z}$ is an $n \times n$ unitary matrix.

Finally, Eq. 5.8 and 5.9 imply that $\mathbf{\Sigma}^2 = \mathbf{\Lambda}$ and $\mathbf{W} = \mathbf{Z}$ and the pair $(\mathbf{W}, \mathbf{\Sigma}^2)$ refers to the eigenvalue decomposition of $\mathbf{M}^H\mathbf{M}$. Assuming the same procedure, the pair $(\mathbf{U}, \mathbf{\Sigma}^2)$ also refers to the eigenvalue decomposition of $\mathbf{M}\mathbf{M}^H$.

However, in the case where $m << n$ the $\mathbf{M}^H\mathbf{M}$ eigenvalue problem is drastically less expensive to solve than the $\mathbf{M}\mathbf{M}^H$ eigenvalue problem. Then, these two approaches are strongly related to different SVD versions called the "classical SVD" and the "snapshot SVD" which are presented in the next subsection. Before that, the computation cost of the SVD methodology can in a first time be moderated by applying its reduced version.

Reduced SVD Generally, it is not useful to compute the full SVD. Instead, it is often sufficient but also faster and more efficient for the data storage to compute a reduced version of the SVD. Here, three different approaches of the reduced SVD are briefly presented:

- Thin SVD: $\tilde{\mathbf{M}}_n \equiv \mathbf{U}_n\mathbf{\Sigma}_n\mathbf{W}^H$. The n^{th} first column vectors of the $\mathbf{U}$ matrix, corresponding to all the row vectors of $\mathbf{W}^H$, are computed. Other columns are not taken into account for the thin SVD allowing to drastically decrease the computer cost of the methodology if $n << m$. Then, the dimension of the matrices are defined as $m \times n$ for $\mathbf{U}$, $n \times n$ for $\mathbf{\Sigma}$ and $\mathbf{W}^H$.
- Compact SVD: $\tilde{\mathbf{M}}_r \equiv \mathbf{U}_r\mathbf{\Sigma}_r\mathbf{W}_r^H$. The r^{th} column vectors of the $\mathbf{U}$ matrix, corresponding to the r^{th} row vectors of $\mathbf{W}^H$ associated to non-zero singular values σ_i are computed. However, this is only computationally less expensive compared to the thin SVD if $r << n$. Then, the dimension of the matrices are defined as $m \times r$ for $\mathbf{U}$, $r \times r$ for $\mathbf{\Sigma}$ and for $r \times n$ for $\mathbf{W}^H$.
- Truncated SVD: $\tilde{\mathbf{M}}_r \equiv \mathbf{U}_r\mathbf{\Sigma}_r\mathbf{W}_r^H$. The r^{th} first column vectors of the $\mathbf{U}$ matrix, corresponding to the r^{th} first row vectors of $\mathbf{W}^H$, are computed. However, this is only computationally less expensive compared to the thin SVD if $r << n$. Then, the dimension of the matrices are defined as $m \times r$ for $\mathbf{U}$, $r \times r$ for $\mathbf{\Sigma}$ and for $r \times n$ for $\mathbf{W}^H$.

In this thesis, the truncated SVD formalism enables to approximate the $\mathbf{M}$ matrix with a truncated matrix $\tilde{\mathbf{M}}$ for a specific rank r with $r < \min(n, m)$, this is the low-rank approximation theorem presented as follow:

Theorem: Low-rank approximation The best k-rank approximation $\tilde{\mathbf{M}}_k$ of the matrix $\mathbf{M}$ is given by zeroing out the $m - k$ trailing singular values of $\mathbf{M}$. The minimal error is given by the Euclidean Frobenius norm of the singular values that have been removed by the process as:

$$||\mathbf{M} - \tilde{\mathbf{M}}_k||_F = \sqrt{\mathrm{tr}\left[(\mathbf{M} - \tilde{\mathbf{M}}_\mathrm{k})^\mathrm{H}(\mathbf{M} - \tilde{\mathbf{M}}_\mathrm{k})\right]} = \sqrt{\sigma_{k+1}^2 + ... + \sigma_m^2}\,. \tag{5.10}$$

5.2.3 Snapshot SVD

The SVD formalism is very useful for the spectral analysis of turbulent flows. It allows to decompose the data matrix, noted here $\mathbf{V}$, into spatial modes associated to their amplitudes and temporal dynamics. This matrix can be filled with instantaneous data fields from numerical simulations such as velocity, pressure, vorticity, passive tracers and so on... or from experiments through tomo-PIV, stereo-PIV, LDV, hot-wire signals smoke visualization, Schlieren images and other. The previous SVD decomposition of the real snapshot matrix $\mathbf{V}$ leads to the following form:

$$\mathbf{V} = \mathbf{U}\mathbf{\Sigma}\mathbf{W}^T \,. \tag{5.11}$$

Applying the SVD to a flow field allows to interpret the significance of the previous $\mathbf{U}$, $\mathbf{\Sigma}$ and $\mathbf{W}$ operators. Hence, the $\mathbf{U}$ matrix represents all the modes present in the flow while the $\mathbf{\Sigma}$ matrix refers to the spectrum amplitude of the modes and the $\mathbf{W}$ matrix contains the dynamics of the modes.

The discretized data series are stored into the data matrix $\mathbf{V}$, from initial time t_0 to a final one t_n with a chosen time increment that has to be relevant regarding to the physics of the flow. Given a series of $n+1$ temporal snapshots of a discrete vector field $\mathbf{v}$, the data matrix is filled by columns for each time step Δt which has to be constant in order to guarantee equispaced snapshots. This is the only assumption of the methodology. Two time-shifted $m \times n$ data matrix $\mathbf{V}_1^n$ and $\mathbf{V}_2^{n+1}$ can be formed as

$$\mathbf{V}_1^n = \{\mathbf{v}_1, \mathbf{v}_2, ..., \mathbf{v}_n\} \,, \tag{5.12}$$

and

$$\mathbf{V}_2^{n+1} = \{\mathbf{v}_2, \mathbf{v}_3, ..., \mathbf{v}_{n+1}\} \,, \tag{5.13}$$

with m referring to the number of freedom degrees of the spatial discrete definition of the flow field $\mathbf{v}_i$.

Hence, thanks to these spatial and temporal discretizations, the SVD complexity is thus reduced in term of operators dimension. Moreover, instead of the full SVD decomposition, it is more convenient for computational cost reasons to apply the truncated SVD, noted $\widetilde{\mathbf{V}}_1^n$, and then to build a low-rank representation of the data matrix $\mathbf{V}$. Once again, in that case m refers to the dimension of the discrete vector field and n to the number of temporal snapshots stored. The truncated SVD of the data matrix $\widetilde{\mathbf{V}_1^n}$, is the best n-rank approximation of the matrices $\mathbf{V}_1^n$ and thus of $\mathbf{V}$.

$$\widetilde{\mathbf{V}}_1^n = \mathbf{U}_n\mathbf{\Sigma}_n\mathbf{W}^T \approx \mathbf{V}_1^n \tag{5.14}$$

This methodology for filling the data matrix $\mathbf{V}_1^n$ is called the "snapshot method" introduced by Sirovitch [183] which differs from to the "classical method" introduced by Lumley [129]. In CFD, the "snapshot method" is always preferred as it drastically decreases the storage and the CPU cost of the SVD computation. Indeed, as the number of time sampling is negligible in front of the number of points for the spatial discrete definition of the fields, it is therefore obvious to fill the data matrix by columns for the temporal discretization. On the one hand, the "snapshot method" considers a spatial average over the whole computational domain Ω defined as $\langle . \rangle_{\mathbf{x}} = \int_\Omega .d\mathbf{x}$, on the other hand "classical method" considers a time average over the whole accumulation time period T defined as $\langle . \rangle_t = \int_T .dt$. Hence, with the "snapshot method", the modes do not depend on time, the snapshots are considered as linearly independent. Some sketches illustrating the SVD formalism based on the "snapshot method" are presented hereafter in Fig. 5.1 and Fig.5.2:

Notation: Henceforth, the truncated SVD $\widetilde{\mathbf{V}}_1^n$ is noted for convenience $\mathbf{V}_1^n$ as it simplifies the writing in the further developments.

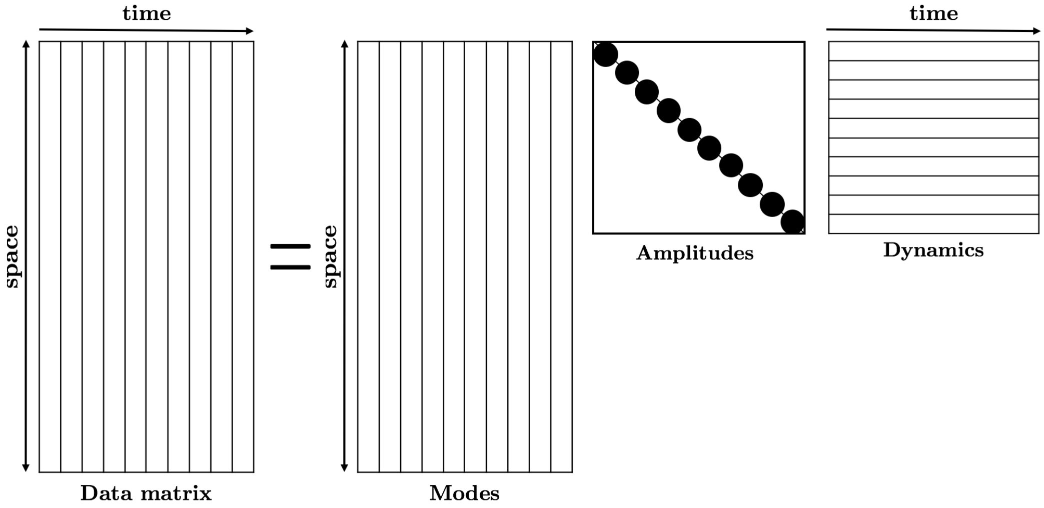

FIGURE 5.1: SVD with snapshot method as spectral analysis approach from [174]

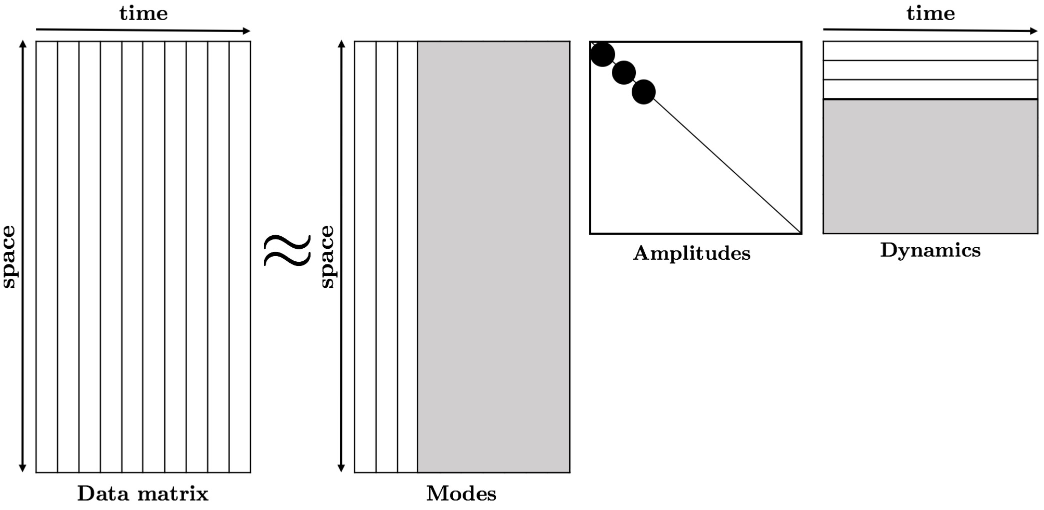

FIGURE 5.2: Truncated SVD with snapshot method as model reduction approach from [174]

Moreover, as the SVD decomposition is not unique, it is mandatory to add an additional constraint on the $\mathbf{U}$ or $\mathbf{W}$ matrices. Hence, each constraint choice produces different modes and associated dynamics. For instance, a spatial orthogonality constraint on the modes decouples the columns of the matrix $\mathbf{U}$ and leads to the well-known Proper Orthogonal Decomposition (POD) method. Similarly, a monochromatic constraint on the mode frequency decouples the columns of the $\mathbf{W}$ matrix and refers to the Dynamic Mode Decomposition (DMD) method. Finally, those two approaches, which are particular constrained versions of the SVD, are further developed in the following sections.

5.2.4 Proper Orthogonal Decomposition (POD)

The Proper Orthogonal Decomposition (POD) or Karhunen-Loève expansion [102, 124] comes from the probability theory and has been historically introduced in the turbulence field by Lumley [129, 130] in order to objectively attempt to extract the coherent features from flows.

The POD allows to determine an orthogonal basis that is optimal in the sense of the energy representation. In other words, this means that it is not possible to find another cardinal basis that better represents the energy contained in the flow. This can be achieved by diagonalizing the matrix $\mathbf{U}$ which represents the spatial uncorrelated POD modes. Through the $\mathbf{\Sigma}$ matrix, the singular values σ_i thus represent the energy content of these modes and the temporal correlation matrix $\mathbf{V}$ refers to their temporal evolution. The spatial orthogonality constraint imposed on the computed modes can be expressed as

$$(\boldsymbol{\phi}_{k_1}, \boldsymbol{\phi}_{k_2}) = \int_{\mathbb{R}} \boldsymbol{\phi}_{k_1}(\mathbf{x}) \boldsymbol{\phi}_{k_2}(\mathbf{x}) d\mathbf{x} = \delta_{k_1,k_2} \,, \tag{5.15}$$

where $(.)$ the canonical scalar product and δ_{k_1,k_2} is the Kronecker symbol.

In the case where the $\boldsymbol{\phi}_k$ functions form an orthonormal basis, the temporal function in Eq. 5.1 $\mathbf{a}(t) = [a_1(t), ..., a_n(t)]^T$ can therefore be computed as a simple projection of the function $\mathbf{f}(\mathbf{x}, t) = \mathbf{V}$ on the orthogonal basis as follows:

$$a_k(t_i) = (\mathbf{v}_i, \boldsymbol{\phi}_k) \quad \text{for} \quad i \in [1, n] \,. \tag{5.16}$$

In that case, assuming that the number of selected modes for the truncated SVD is equal to the number of time sampling snapshots $n_t = n$, the minimization problem in Eq 5.2 can be written by substituting the previous expression of $a_k(t_i)$ which leads to:

$$\min_{\boldsymbol{\phi}} \sum_{i=1}^{n} ||\mathbf{v}_i(\mathbf{x}) - \sum_{k=1}^{n} (\mathbf{v}_i, \boldsymbol{\phi}_k) \boldsymbol{\phi}_k(\mathbf{x})||_2^2 \,. \tag{5.17}$$

Hence, as the POD approach consists in extracting the most energetically dominant modes from the flow, the algorithm searches modes which have the highest contribution in term of the least square mean when projecting them onto the data snapshot matrix $\mathbf{V}_1^n$. This can be mathematically formulated through the following optimization problem:

$$\max_{\mathbf{\Psi}} \frac{\langle (\mathbf{V}_1^n, \mathbf{\Psi})^2 \rangle}{||\mathbf{\Psi}||_2^2} = \frac{\langle (\mathbf{V}_1^n, \mathbf{\Phi})^2 \rangle}{||\mathbf{\Phi}||_2^2} \,, \tag{5.18}$$

with

$$(\boldsymbol{\phi}_k, \boldsymbol{\phi}_k) = ||\boldsymbol{\phi}_k||_2^2 = 1 \,, \tag{5.19}$$

where $(,)$ and $||.||_2$ are the canonical scalar product and the $\mathcal{L}_2$ norm, $\langle . \rangle$ an average operator depending on how the data matrix is filled. It refers to the spatial average $\langle . \rangle_{\mathbf{x}}$ for the "snapshot method" formalism.

Moreover, as the kinetic energy of the mode $\boldsymbol{\phi}_k$ is expressed as (a_k, a_k^*), the POD decomposition guaranties that it is not possible to find another basis that enables to represent more kinetic energy of the flow for a fixed number of modes n.

The major advantages of this approach come from the fact that POD is a non-parametric method that enables sub-domain and local analysis but also because of the relative simplicity of its implementation. Although the POD method seems to be very attractive and elegant while identifying coherent features, some well-known drawbacks have nevertheless to be highlighted:

- The choice of the energy measure for ranking the flow structures is not always the most relevant. Indeed, Noack et al. [149] presented the existence of highly relevant dynamic modes with zero-energy contribution to the flow.
- The averaging process when filling the data matrix for the SVD produces a second-order statistics as a basis for the decomposition, implying the loss of some valuable phase information which can disturb the classification of the modes.
- The spatial orthogonality constraint may be too stringent and also not being always physically relevant because the modes are not monochromatic and due to the loss of the temporal evolution of the dynamics.

Another modal decomposition method also based on the SVD formalism with temporal orthogonality constraint is presented in the next section.

5.3 Dynamic Mode Decomposition (DMD)

5.3.1 Presentation

As previously mentioned, the DMD algorithm guaranties that the computed modes are monochromatic and ranked according to their dynamics. The dynamic modes take the form

$$\mathbf{f}(\mathbf{x},t) = a(t)\boldsymbol{\phi}(\mathbf{x}) \quad \text{with} \quad a(t) = \alpha \exp(i\omega t)\,, \tag{5.20}$$

with $\boldsymbol{\phi}(\mathbf{x})$ a normalized DMD mode, α its amplitude and $\exp(i\omega t)$ its temporal behavior and amplification.

Thanks to the temporal orthogonality constraint of the DMD approach, the matrix $\mathbf{W}^T$, that comes from the SVD decomposition of the matrix $\mathbf{V}_1^n$, can be written as a Vandermonde matrix:

$$\mathbf{W}^T = \begin{bmatrix} 1 & z_1 & z_1^2 & \dots & z_1^{n-1} \\ 1 & z_2 & z_2^2 & \dots & z_2^{n-1} \\ \vdots & \vdots & \vdots & & \vdots \\ 1 & z_n & z_n^2 & \dots & z_n^{n-1} \end{bmatrix}, \tag{5.21}$$

where the $\mathbf{W}^T$ matrix is filled with unknown frequencies $z_k = \exp(i\omega_k \Delta T)$.

5.3.1.1 The Koopman analysis of non-linear dynamical systems

As defined above, the data matrix $\mathbf{V}_1^n$ contains by columns the temporal snapshots of the data field of interest. Under the assumption of an ordered sequence of data separated by a constant time sampling ΔT, in the first approximation then, a linear mapping called the Koopman operator [115, 137] $\mathbf{A}$ links two consecutive snapshots as

$$\mathbf{v}_{i+1} = \mathbf{A}\mathbf{v}_i\,. \tag{5.22}$$

This mapping can be considered as being constant over the whole time sampling range for the DMD application. The sequence of flow field snapshots $\mathbf{v}_i$ can therefore be represented as a Krylov sequence [77, 195]:

$$\mathbf{V}_1^n = \{\mathbf{v_1}, \mathbf{v_2}, ..., \mathbf{v_n}\} = \{\mathbf{v_1}, \mathbf{A}\mathbf{v_1}, ..., \mathbf{A}^{n-1}\mathbf{v_1}\}\,. \tag{5.23}$$

The Koopman operator $\mathbf{A}$ based on $\mathbf{V}_1^n$ contains all the dynamic processes and thus refers to the time-evolution operator of the system, here the Navier-Stokes equations. It is mandatory to extract the dynamic characteristics from this operator as eigenvalues, eigenvectors, energies and mode amplifications.

Assuming a sufficient number of snapshots n in order to capture the dominant features of the underlying physical processes, the last snapshot $\mathbf{v}_{n+1}$ can be considered as dependent on the previous snapshots that are linearly independent. Then, $\mathbf{v}_{n+1}$ can be written as a linear combination as

$$\mathbf{v}_{n+1} = a_1\mathbf{v}_1 + a_2\mathbf{v}_2 + ... + a_n\mathbf{v}_n + \mathbf{r}\,, \tag{5.24}$$

which can also be expressed in the following matrix form

$$\mathbf{v}_{n+1} = \mathbf{V}_1^n\mathbf{a} + \mathbf{r}\,, \tag{5.25}$$

with $\mathbf{a}^T = (a_1, a_2, ..., a_n)$ the vector referring to the linear coefficients and $\mathbf{r}$ the residual vector. Then, Ruhe [169] introduced in the previous relations the $\mathbf{S}$ operator as:

$$\mathbf{A}\mathbf{V}_1^n = \mathbf{V}_2^{n+1} = \mathbf{V}_1^n\mathbf{S} + \mathbf{Eps} \approx \mathbf{V}_1^n\mathbf{S}\,. \tag{5.26}$$

The above formula is thus expressing that the last snapshot can be expressed approximately as a linear combination of all the previous ones. The $m \times n$ residual matrix $\mathbf{Eps} = \{\epsilon_1, \epsilon_2, ..., \epsilon_n\} = \mathbf{r}\mathbf{e}_n^T$ with $\mathbf{e}_n \in \mathcal{R}^n$ as the n^{th} unit vector is the error between the Dynamic Mode Decomposition $\mathbf{V}_1^n\mathbf{S}$ and the data matrix $\mathbf{V}_2^{n+1}$. The matrix $\mathbf{S}$ is defined as as a $n \times n$ companion matrix of the form:

$$\mathbf{S} = \begin{bmatrix} 0 & & & & a_1 \\ 1 & 0 & & & a_2 \\ & \ddots & \ddots & & \vdots \\ & & 1 & 0 & a_{n-1} \\ & & & 1 & a_n \end{bmatrix}\,. \tag{5.27}$$

Moreover, thanks to the structure of the matrix $\mathbf{S}$, it can be decomposed into two distinct parts:

$$\mathbf{S} = \mathbf{S}_0 + \mathbf{E}\,, \tag{5.28}$$

with $\mathbf{S}_0$ is a $n \times n$ companion matrix that represents a time-shift between two successive snapshots as

$$\mathbf{S}_0 = \begin{bmatrix} 0 & & & & 0 \\ 1 & 0 & & & 0 \\ & \ddots & \ddots & & \vdots \\ & & 1 & 0 & 0 \\ & & & 1 & 0 \end{bmatrix}\,. \tag{5.29}$$

This states that the j^{th} column of $\mathbf{V}_2^{n+1}$ is equal to the $j+1^{th}$ column of $\mathbf{V}_1^n$, except for the last one. $\mathbf{E}$ is also $n \times n$ matrix which entries are all zero, except for the last column:

$$\mathbf{E} = \begin{bmatrix} 0 & 0 & \cdots & 0 & a_1 \\ 0 & 0 & \cdots & 0 & a_2 \\ \vdots & & \ddots & \vdots & \vdots \\ 0 & \cdots & \cdots & 0 & a_{N-1} \\ 0 & \cdots & \cdots & 0 & a_N \end{bmatrix} . \tag{5.30}$$

The unknown coefficients are the a_i for $i \in [1, n]$ which are the linear representation of the snapshot $\mathbf{v}_{n+1}$ in term of the previous sample $\mathbf{V}_1^n$. Moreover, the eigenvalues of the $\mathbf{S}$ companion matrix are approximations of the eigenvalues of the Koopman operator $\mathbf{A}$. The matrix $\mathbf{S}$ can therefore be interpreted as the projection of $\mathbf{A}$ on the snapshots base $\mathbf{V}_1^n$.

In order to extract the dynamic characteristics of the Koopman operator $\mathbf{A}$, Greenbaum [77] and Trefethen [195] proposed to applied the Arnoldi method, dealing with a reduction of the matrix $\mathbf{A}$ onto an Hessenberg matrix $\mathbf{H}$, that approximates the eigenvalues of $\mathbf{A}$ thanks to a QR decomposition. This can be achieved by applying successive projections onto Krylov subspaces but in that case, the Koopman operator $\mathbf{A}$ has to be known which is not the case for our applications. In practice, this method is not convenient for stability reason and more details can be found in [175].

Finally, the DMD method allows to estimate the Koopman eigenvalues and modes. Two distinct methods are implemented in the CFD code YALES2. The first one is called "Full Rank", as it based on the assumption that $\mathbf{V}_1^n$ matrix is full-rank. The second is called "Generalized". For both methods, the first step is to compute the Singular Value Decomposition (SVD) of $\mathbf{V}_1^n$.

5.3.1.2 The Full-Rank DMD

The first introduced DMD algorithm deals with a naive approach of the formalism as the matrix $\mathbf{S}$ is not necessarily invertible which can imply an ill-conditioned algorithm. Starting with the data matrices $\mathbf{V}_1^n$ and $\mathbf{V}_2^{n+1}$, the error between those matrices **Eps** can be expressed as:

$$\begin{aligned} \mathbf{Eps} &= \mathbf{V}_2^{n+1} - \mathbf{V}_1^n \mathbf{S} \\ &= \mathbf{V}_2^{n+1} - \mathbf{V}_1^n \left[\mathbf{S}_0 + \mathbf{E}\right] \\ &= -\mathbf{V}_1^n \mathbf{E} + \left[\mathbf{V}_2^{n+1} - \mathbf{V}_1^n \mathbf{S}_0\right] , \end{aligned} \tag{5.31}$$

or, keeping only the last column, which is the only one with non-zero values:

$$\boldsymbol{\epsilon}_n = -\mathbf{V}_1^n \mathbf{E}_{:,n} + \mathbf{v}_{n+1} . \tag{5.32}$$

In this equation, $\boldsymbol{\epsilon}_n$ is equal to zero only if $\mathbf{v}_{n+1}$ is in the image of $\mathbf{V}_1^n$. If not, we can still try to find a vector $\mathbf{E}^\star_{:,n}$ such that $\boldsymbol{\epsilon}_n \perp \mathbf{V}_1^n \mathbf{E}^\star_{:n}$; this will minimize $\boldsymbol{\epsilon}_n$ in the least-square (L2) sense. This vector $\mathbf{E}^\star_{:,n}$ is known as a pseudo solution of the initial problem and can be found by performing the truncated SVD of $\mathbf{V}_1^n$ noted $\mathbf{V}_1^n = \mathbf{U}_n \boldsymbol{\Sigma}_n \mathbf{W}^T$. This pseudo-solution is given by:

$$\begin{aligned} \mathbf{V}_1^n\mathbf{E}^{\star}_{:,n} &\approx \mathbf{v}_{n+1} \\ \mathbf{U}_n\mathbf{\Sigma}_n\mathbf{W}^T\mathbf{E}^{\star}_{:,n} &\approx \mathbf{v}_{n+1} \\ \mathbf{E}^{\star}_{:,n} &\approx \mathbf{W}\mathbf{\Sigma_n}^+\mathbf{U}_n^T\mathbf{v}_{n+1}\,, \end{aligned} \tag{5.33}$$

so that :

$$\mathbf{S} = \mathbf{S}_0 + \mathbf{W}\mathbf{\Sigma_n}^+\mathbf{U_n}^T\left(\mathbf{V}_2^{n+1} - \mathbf{V}_1^n\mathbf{S}_0\right)\,. \tag{5.34}$$

Another solution would have been to compute $\mathbf{S}$ directly as :

$$\mathbf{S} = \mathbf{W}\mathbf{\Sigma_n}^+\mathbf{U_n}^T\mathbf{V}_2^{n+1}\,. \tag{5.35}$$

However, in this case, if $\mathbf{V}_1^n$ has not a maximal rank, then $\mathbf{\Sigma_n}^+\mathbf{\Sigma_n} \neq \mathbf{I}_n$ and $\mathbf{S}$ will not have the form $\mathbf{S} = \mathbf{S}_0 + \mathbf{E}$.

Moreover, the complex eigenvalues $\boldsymbol{\lambda}^T = (\lambda_1, \lambda_2, ..., \lambda_n)$, called the Ritz values, and the right and left eigenvectors of $\mathbf{S}$, $\mathbf{X} = \{\mathbf{x}_1, \mathbf{x}_2, ..., \mathbf{x}_n\}$ and $\mathbf{Y} = \{\mathbf{y}_1, \mathbf{y}_2, ..., \mathbf{y}_n\}$ respectively, are computed with the classical eigenvalues problem defined as :

$$\begin{aligned} \mathbf{S}\mathbf{x}_j &= \lambda_j\mathbf{x}_j\,, \\ \mathbf{y}_j\mathbf{S} &= \lambda_j\mathbf{y}_j\,. \end{aligned} \tag{5.36}$$

As $\mathbf{S}$ is real, eigenvalues are either real or form pairs of complex-conjugates. The vectors $\mathbf{x}_j$ and $\mathbf{y}_j$ are chosen with the following properties :

$$\begin{aligned} \mathbf{x}_j^H\mathbf{x}_j &= 1\,, \\ \mathbf{y}_j\mathbf{y}_j^H &= 1\,, \\ \mathbf{y}_i\mathbf{x}_j &= \delta_{ij}\,. \end{aligned} \tag{5.37}$$

Now, the matrix $\mathbf{\Lambda}$ has to be introduced. This is a $n \times n$ square matrix filled with zero except on the diagonal that contains the eigenvalues λ_i of the $\mathbf{S}$ operator. $\mathbf{\Lambda}$ can therefore be built by projecting the $\mathbf{S}$ operator onto the left and right eigenvectors as Eq 5.36 mentioned.

Finally, the DMD modes $\mathbf{\Phi} = \{\phi_1, \phi_2, ..., \phi_n\}$ are defined as the projection of the data matrix $\mathbf{V}_1^n$ onto the right eigenvectors basis :

$$\phi_j = \mathbf{V}_1^n\mathbf{x}_j\,, \tag{5.38}$$

or in matrix form

$$\mathbf{\Phi} = \mathbf{V}_1^n\mathbf{X}\,, \tag{5.39}$$

and the evolution between two consecutive snapshots is given by

$$\mathbf{V}_2^{n+1}\mathbf{x}_j = \lambda_j\mathbf{V}_1^n\mathbf{x}_j\,. \tag{5.40}$$

Then, using the matrix form $\mathbf{\Lambda}$ for the eigenvalues, a relation between the data matrices $\mathbf{V}_1^n$ and $\mathbf{V}_2^{n+1}$ can be found as follows:

$$\mathbf{V}_2^{n+1}\mathbf{X} = \mathbf{\Lambda}\mathbf{V}_1^n\mathbf{X} \quad \text{i.e} \quad \mathbf{V}_2^{n+1} = \mathbf{V}_1^n\mathbf{X}\mathbf{\Lambda}\mathbf{Y}\,. \tag{5.41}$$

Finally, the $(k+1)^{th}$ with $k \in [1, n-1]$ snapshots of the data matrix $\mathbf{V}_1^n$ can thus be written as a combination of all the DMD modes with their own temporal evolution:

$$\begin{aligned}
\mathbf{v}_{k+1} &= \mathbf{v}_k\mathbf{X}\mathbf{\Lambda}\mathbf{Y} \\
&= [\mathbf{v}_{k-1}\mathbf{X}\mathbf{\Lambda}\mathbf{Y}]\,[\mathbf{X}\mathbf{\Lambda}\mathbf{Y}] \\
&= \mathbf{v}_{k-1}\mathbf{X}\mathbf{\Lambda}^2\mathbf{Y} \\
&= ... \\
&= \mathbf{v}_1\mathbf{X}\mathbf{\Lambda}^k\mathbf{Y} \\
&= \left[\mathbf{e}_1^T\mathbf{V}_1^n\right]\left[\mathbf{X}\mathbf{\Lambda}^k\mathbf{Y}\right] \\
&= [\mathbf{V}_1^n\mathbf{X}]\,\mathbf{\Lambda}^k\left[\mathbf{e}_1^T\mathbf{Y}\right] \\
&= \mathbf{\Phi}\mathbf{\Lambda}^k\mathbf{Y}_{:,\mathbf{1}}\,,
\end{aligned} \tag{5.42}$$

where $\mathbf{e}_1^T$ simply refers to the unit vector in the first direction $\mathbf{e}_1^T = (1, 0, \ldots, 0)$.

Here, $\mathbf{Y}_{:,1}$ represents the first column of $\mathbf{Y}$, which is not the first left eigenvector but rather the first component of every left eignevector. The amplitudes of the modes, noted here $\operatorname{diag}(\mathbf{D}_{\boldsymbol{\alpha}}) = (\alpha_1, \alpha_2, ..., \alpha_\mathrm{n})$ where $\mathbf{D}_{\boldsymbol{\alpha}}$ is a diagonal matrix, are thus contained in the first column of $\mathbf{Y}$:

$$\alpha_j = \mathbf{Y}_{j,1}\,. \tag{5.43}$$

Hence, the reconstruction formulation of a snapshot using the DMD modes can be expressed as

$$\mathbf{v}_{k+1} = \sum_{i=1}^{n} \alpha_i \boldsymbol{\phi}_i \mathbf{\Lambda}_i^k\,. \tag{5.44}$$

Finally, the reconstruction of the "Full-rank" DMD does not guarantee the scaling of the reconstructed data field comparing of the real field. Indeed, as the amplitudes refer to the first components of each eigenvectors $\alpha_i = \mathbf{Y}_{j,1}$, the information about the scaling is lost as each eigenvector has been normalized. Moreover, in this configuration, the sign of the complex amplitude of the mode may therefore not be the right one, as the eigenvectors can have opposite sign. However, the "Generalized" DMD, which also overcome the ill-conditioned problem when $\mathbf{S}$ is not invertible, enables to compute the modes amplitudes keeping the right sign and scaling of the modes that allows to reconstruct the field of interest.

5.3.1.3 The Generalized DMD

Here is presented the generalized DMD algorithm proposed by Schmid [175] based on a modified time shifting operator $\widetilde{\mathbf{S}}$ defined as

$$\widetilde{\mathbf{S}} \equiv \mathbf{U_n}^T\mathbf{V}_2^{n+1}\mathbf{W}\mathbf{\Sigma_n}^{-1}\,, \tag{5.45}$$

which can also be written in the following form when the $\mathbf{V}_1^n$ matrix is full-rank:

$$\widetilde{\mathbf{S}} \equiv \mathbf{U_n}^T \mathbf{V}_2^{n+1} \mathbf{W} \mathbf{\Sigma_n}^{-1} = \mathbf{U_n}^T \mathbf{A} \mathbf{U_n} \,. \tag{5.46}$$

The eigenvalues $\mathrm{diag}(\mathbf{\Lambda}) = (\lambda_1, \lambda_2, ..., \lambda_\mathrm{n})$ and right-eigenvectors $\widetilde{\mathbf{X}} = \{\widetilde{\mathbf{x}}_1, \widetilde{\mathbf{x}}_2, ..., \widetilde{\mathbf{x}}_n\}$ of the time shifting operator $\widetilde{\mathbf{S}}$ can thus be computed by solving the following eigenvalues problem defined as

$$\widetilde{\mathbf{S}} \widetilde{\mathbf{x}}_j = \lambda_j \widetilde{\mathbf{x}}_j \,, \tag{5.47}$$

where $\widetilde{\mathbf{x}}_j$ is normalized such as $\widetilde{\mathbf{x}}_j^H \widetilde{\mathbf{x}}_j = 1$.

The generalized DMD modes $\widetilde{\boldsymbol{\phi}}_j$ of the snapshot sequence are defined as

$$\widetilde{\boldsymbol{\phi}}_j = \mathbf{U_n} \widetilde{\mathbf{x}}_j \,. \tag{5.48}$$

Then, multiplying Eq. (5.45) on the right-hand side by $\mathbf{U_n}^T \mathbf{U_n}$ and $\mathbf{\Sigma_n} \mathbf{W}^T$ gives

$$\widetilde{\mathbf{S}} \mathbf{U_n}^T \mathbf{U_n} \mathbf{\Sigma_n} \mathbf{W}^T = \mathbf{U_n}^T \mathbf{V}_2^{n+1} \mathbf{W} \mathbf{\Sigma_n}^{-1} \mathbf{\Sigma_n} \mathbf{W}^T = \mathbf{U_n}^T \mathbf{V}_2^{n+1} \,, \tag{5.49}$$

and

$$\widetilde{\mathbf{S}} \mathbf{U_n}^T \mathbf{V}_1^n = \mathbf{U_n}^T \mathbf{V}_2^{n+1} \,. \tag{5.50}$$

Multiplying by the eigenvector $\widetilde{\mathbf{x}}_j$ on the left-hand side

$$\widetilde{\mathbf{x}}_j \widetilde{\mathbf{S}} \mathbf{U_n}^T \mathbf{V}_1^n = \lambda_j \widetilde{\mathbf{x}}_j \mathbf{U_n}^T \mathbf{V}_1^n = \widetilde{\mathbf{x}}_j \mathbf{U_n}^T \mathbf{V}_2^{n+1} \,, \tag{5.51}$$

which leads to

$$\widetilde{\boldsymbol{\phi}}_j \mathbf{V}_2^{n+1} = \lambda_j \widetilde{\boldsymbol{\phi}}_j \mathbf{V}_1^n \,. \tag{5.52}$$

In this equation, it is clear that the complex eigenvalue λ_j controls the time evolution of the snapshot sequence. Hence, the $n+1$ snapshot can be expressed as linear combination of DMD modes associated to their amplitudes α_i in the following manner:

$$\widetilde{\mathbf{v}}_{n+1} = \sum_{i=1}^{n} \alpha_i \lambda_i^k \widetilde{\boldsymbol{\phi}}_i(\mathbf{x}) \,. \tag{5.53}$$

This is equivalent to the matrix formulation:

$$\mathbf{V}_1^n = \mathbf{\Phi} \mathbf{D}_{\boldsymbol{\alpha}} \mathbf{V}_\mathrm{and} = [\boldsymbol{\phi}_1 \quad \boldsymbol{\phi}_2 \quad ... \quad \boldsymbol{\phi}_n] \begin{bmatrix} \alpha_1 & & & \\ & \alpha_2 & & \\ & & \ddots & \\ & & & \alpha_n \end{bmatrix} \begin{bmatrix} 1 & \lambda_1 & \cdots & \lambda_1^{n-1} \\ 1 & \lambda_2 & \cdots & \lambda_2^{n-1} \\ \vdots & \vdots & \ddots & \vdots \\ 1 & \lambda_n & \cdots & \lambda_n^{n-1} \end{bmatrix} \tag{5.54}$$

The complex eigenvalues λ_i of the time shifting operator $\widetilde{\mathbf{S}}$ contain all the information concerning the frequencies and growth/decay rates of the modes. With these eigenvalues, the Vandermonde matrix $\mathbf{V}_\mathrm{and}$ can therefore be built and contains all the temporal evolution of the modes dynamics $\boldsymbol{\phi}_i$ in discrete time. At this point, the unknown factors for the reconstruction of the flow field are the complex components of the amplitude vector $\mathrm{diag}(\mathbf{D}_{\boldsymbol{\alpha}}) = \boldsymbol{\alpha} = [\alpha_1 \quad ... \quad \alpha_\mathrm{n}]^\mathrm{T}$ with $\alpha_i \in \mathbb{C}^n$.

5.3.2 Mode selection

The temporal reconstruction can be achieved by trying to minimized the number of modes n that appears in the summation of Eq 5.53. In order to rank and select the modes, several criteria have to be considered. However, this selection can often be seen as a trade-off between the dynamic contribution and the damping behavior of each mode. Even if the the identification and the selection of the dominant flow features is generally straightforward for canonical simple configurations, it becomes more challenging and very difficult in highly turbulent flows where perturbations coming from transient modes and multiple frequencies are strongly present.

Hence, here are presented several criteria with their advantages and shortcomings that enable to identify and select the dominant features for DMD computations :

- **Mode frequency and growth/decay rate :** Those two criteria can directly be computed from the DMD algorithm by considering Eq 5.53 with the following logarithm mapping transformation :

$$\begin{aligned}\mathbf{v}_{k+1} &= \sum_{j=1}^{n} \alpha_j \lambda_j^k \widetilde{\boldsymbol{\phi}}_j(\mathbf{x}) \\ &= \sum_{j=1}^{n} \alpha_j |\lambda_j|^k e^{i\arg(\lambda_j)k} \widetilde{\boldsymbol{\phi}}_j(\mathbf{x}) \\ &= \sum_{j=1}^{n} \alpha_j e^{k\ln|\lambda_j|} e^{i\arg(\lambda_j)k} \widetilde{\boldsymbol{\phi}}_j(\mathbf{x}) \\ &= \sum_{j=1}^{n} \alpha_j e^{k\Delta T \lambda_j^{\ln}} e^{ik\Delta T\omega_j} \widetilde{\boldsymbol{\phi}}_j(\mathbf{x}) \,,\end{aligned} \tag{5.55}$$

  where $\omega_j = \frac{\arg(\lambda_j)}{\Delta T}$ refers to the pulsation and $\lambda_j^{\ln} = \frac{\ln|\lambda_j|}{\Delta T}$ to the amplitude growth/decay rate of the mode $\boldsymbol{\phi}_j$.

  Several aspects can be considered with those criteria. First, the frequency of the modes allows to identify them while the amplitude growth or decay rate enables to verify their convergence. Indeed, a converged mode is characterized by a value of $\lambda_j^{\ln}$ close to zero, this means that the eigenvalue λ_j of the $\mathbf{S}$ operator, called the Ritz eigenvalue, is close to the unit circle. In addition, the sign of $\lambda_j^{\ln}$ enables to determine the temporal stability of the mode. On the one hand, if the sign is negative, the mode is stable and will be damped as the time increases. On the other hand, a positive sign of $\lambda_j^{\ln}$ deals with unstable modes as they will grow exponentially as the time increases. Finally, if $\lambda_j^{\ln} = 0$, then the mode amplitude is constant in time which is often the case for the modes associated to the data mean fields.
- **Norm of the mode :** The modes can be ranked by their norms $||\boldsymbol{\phi}_j||_2$ [167], however this method may not be effective as some modes with a large norm and with a strong damping behavior may be highlighted.

$$||\boldsymbol{\phi}_j||_2 = ||\mathbf{U}_n \mathbf{x}_j||_2 \,. \tag{5.56}$$

- **Mode amplitude :** Contrary to the POD approach, where mode amplitudes are computed through a simple scalar product as seen in Eq 5.16, it is not straightforward to compute them in the DMD formalism as modes do not have the spatial orthogonal property. Then, many different ways have been developed to compute these amplitudes in the DMD formalism, some of them are presented hereafter:

- Projecting the data sequence onto the identified dynamic modes [177] allows to determine their significances. However, this approach does not take into account the growth/decay behavior of the modes. Similarly, the projection of the first snapshot onto the modes may be preferred but modes with a strong damping behavior may still be highlighted.

- Optimized modes amplitude over the whole dataset has been proposed by Jovanovic et al. [99]. This approach allows to guarantee the scaling of the mode for the field reconstruction. However, in that case, transient modes with large amplitude will also be included in the optimization process leading thus to non-negligible amplitudes.

- **Energy contribution:** The computation of the mode energy has been introduced by Tissot et al. [192] and allows to take into account both of the previous main aspects for the mode selection. On the one hand, it integrates the mode contribution over the whole dataset allowing to emphasize the non transient but dynamically dominant modes. On the other hand, it also combines the growth/decay behavior of the mode that is contained into the eigenvalues. Here is presented the development of the mode energy contribution with the assumption that all modes have been normalized such as $||\phi_j||_2 = 1$.

$$\begin{aligned} E_i &= \frac{1}{T}\int_0^T ||\alpha_i \phi_i \lambda_i^{t/\Delta T}||_2^2 dt \\ &= ||\alpha_i \phi_i||_2^2 \frac{1}{T}\int_0^T ||\lambda_i^{t/\Delta T}||_2^2 dt \\ &= |\alpha_i|^2 . ||\phi_i||_2^2 \frac{1}{T}\int_0^T ||e^{t\lambda_i^{\ln}} e^{i\omega_i t}||_2^2 dt \\ &= |\alpha_i|^2 \frac{1}{T}\int_0^T e^{2t\lambda_i^{\ln}} dt \\ &= |\alpha_i|^2 \frac{1}{T}\left[\frac{e^{2t\lambda_i^{\ln}}}{2\lambda_i^{\ln}}\right]_0^T \\ &= |\alpha_i|^2 \left[\frac{e^{2T\lambda_i^{\ln}}-1}{2T\lambda_i^{\ln}}\right] . \end{aligned} \tag{5.57}$$

Finally, the mode energy seems to be the most relevant criterion in order to select the dominant subset of modes. However, this criterion necessitates the computation of the mode amplitudes. The methodology proposed by Jovanovic et al. [99] has been chosen for this computation and is further developed in the next sub-section.

5.3.3 Minimization problem for the computation of the modes amplitude

Due to the temporal orthogonal property of the DMD formalism, the mode amplitude still has to be determined after applying this methodology. In order to find those coefficients presented in Eq 5.54, an optimization problem proposed by Jovanovic et al. [99] using the Frobenius norm $||.||_F$ has to be solved as

$$\underset{\boldsymbol{\alpha}}{\text{minimize}} \; ||\mathbf{V}_1^n - \boldsymbol{\Phi}\mathbf{D}_{\boldsymbol{\alpha}}\mathbf{V}_{\text{and}}||_F^2 \, . \tag{5.58}$$

This minimization problem can be expressed in another form using the SVD decomposition and the definition of $\mathbf{\Phi} = \mathbf{U}_n\widetilde{\mathbf{X}}$. Then it leads to the following convex optimization problem defined as

$$\underset{\boldsymbol{\alpha}}{\text{minimize}}\ J(\boldsymbol{\alpha}) = \underset{\boldsymbol{\alpha}}{\text{minimize}}\ ||\mathbf{\Sigma_n}\mathbf{W}^H - \widetilde{\mathbf{X}}\mathbf{D}_{\boldsymbol{\alpha}}\mathbf{V}_{\text{and}}||_F^2\,. \tag{5.59}$$

This problem is easier to solve because of the reduced dimensions of the matrices. Moreover, the functional $J(\boldsymbol{\alpha})$ may also be written as

$$J(\boldsymbol{\alpha}) = ||\mathbf{A}||_F^2 = \left(\sqrt{\text{tr}(\mathbf{A}^H\mathbf{A})}\right)^2 = \sum_i\sum_j |a_{ij}|^2\,, \tag{5.60}$$

with $\mathbf{A} = \mathbf{\Sigma_n}\mathbf{W}^H - \widetilde{\mathbf{X}}\mathbf{D}_{\boldsymbol{\alpha}}\mathbf{V}_{\text{and}}$ and $a_{ij} = (\mathbf{\Sigma_n}\mathbf{W}^*)_{ij} - (\widetilde{\mathbf{X}}\mathbf{D}_{\boldsymbol{\alpha}}\mathbf{V}_{\text{and}})_{ij} = \sigma_i \mathrm{w_{ji}} - \sum_{\mathrm{k}} \mathrm{x_{ik}}\alpha_{\mathrm{k}}\lambda_{\mathrm{kj}}$.

In order to solve this minimization problem, here is proposed to analytically express the derivative of the functional, noted $\frac{\partial J(\boldsymbol{\alpha})}{\partial \alpha_n}$ with $n \in [1, n]$, and to apply a gradient base descent method.

$$\begin{aligned}
\frac{\partial J(\boldsymbol{\alpha})}{\partial \alpha_n} &= \sum_i\sum_j \frac{\partial}{\partial \alpha_n}\left[|a_{ij}|^2\right] \\
&= \sum_i\sum_j \frac{\partial}{\partial \alpha_n}\left[\mathrm{Re}^2(\mathrm{a_{ij}}) + \mathrm{Im}^2(\mathrm{a_{ij}})\right] \\
&= \sum_i\sum_j \frac{\partial}{\partial \alpha_n}\left[\mathrm{Re}^2\left(\sigma_{\mathrm{i}}\mathrm{w_{ji}} - \sum_{\mathrm{k}}\mathrm{x_{ik}}\alpha_{\mathrm{k}}\lambda_{\mathrm{kj}}\right) + \mathrm{Im}^2\left(\sigma_{\mathrm{i}}\mathrm{w_{ji}} - \sum_{\mathrm{k}}\mathrm{x_{ik}}\alpha_{\mathrm{k}}\lambda_{\mathrm{kj}}\right)\right] \\
&= \sum_i\sum_j \frac{\partial}{\partial \alpha_n}\left[\left(\mathrm{Re}(\sigma_{\mathrm{i}}\mathrm{w_{ji}}) - \sum_{\mathrm{k}}\mathrm{Re}(\mathrm{x_{ik}}\alpha_{\mathrm{k}}\lambda_{\mathrm{kj}})\right)^2 + \left(\mathrm{Im}(\sigma_{\mathrm{i}}\mathrm{w_{ji}}) - \sum_{\mathrm{k}}\mathrm{Im}(\mathrm{x_{ik}}\alpha_{\mathrm{k}}\lambda_{\mathrm{kj}})\right)^2\right] \\
&= \sum_i\sum_j \frac{\partial}{\partial \alpha_n}\left[\left(\sigma_i\mathrm{w_{ji}} - \sum_{\mathrm{k}}\mathrm{Re}(\mathrm{x_{ik}}\alpha_{\mathrm{k}}\lambda_{\mathrm{kj}})\right)^2 + \sum_{\mathrm{k}}\mathrm{Im}^2(\mathrm{x_{ik}}\alpha_{\mathrm{k}}\lambda_{\mathrm{kj}})\right] \quad \text{because} \quad \sigma_i\mathrm{w_{ji}} \in \mathbb{R} \\
&= \sum_i\sum_j \frac{\partial}{\partial \alpha_n}\left[\sigma_i^2\mathrm{w_{ji}^2} - 2\sigma_{\mathrm{i}}\mathrm{w_{ji}}\sum_{\mathrm{k}}\mathrm{Re}(\mathrm{x_{ik}}\alpha_{\mathrm{k}}\lambda_{\mathrm{kj}}) + \sum_{\mathrm{k}}\mathrm{Re}^2(\mathrm{x_{ik}}\alpha_{\mathrm{k}}\lambda_{\mathrm{kj}}) + \sum_{\mathrm{k}}\mathrm{Im}^2(\mathrm{x_{ik}}\alpha_{\mathrm{k}}\lambda_{\mathrm{kj}})\right] \\
&= \sum_i\sum_j \left[-2\sigma_i\mathrm{w_{ji}}\frac{\partial}{\partial \alpha_{\mathrm{n}}}\left[\sum_{\mathrm{k}}\mathrm{Re}(\mathrm{x_{ik}}\alpha_{\mathrm{k}}\lambda_{\mathrm{kj}})\right] + \frac{\partial}{\partial \alpha_{\mathrm{n}}}\left[\sum_{\mathrm{k}}|\mathrm{x_{ik}}\alpha_{\mathrm{k}}\lambda_{\mathrm{kj}}|^2\right]\right]\,.
\end{aligned}$$

Here, the functional derivates for the convex optimization problem are reformulated from the complex vector space to the real vector space:

$$\begin{aligned}
\frac{\partial J(\boldsymbol{\alpha})}{\partial \alpha_n^r} &= \sum_i \sum_j \left[-2\sigma_i \mathrm{w_{ji}} \underbrace{\frac{\partial}{\partial \alpha_n^r}\left[\sum_k \mathrm{Re}(\mathrm{x_{ik}}\alpha_\mathrm{k}\lambda_\mathrm{kj})\right]}_{\mathrm{D_1^r}} + \underbrace{\frac{\partial}{\partial \alpha_n^r}\left[\sum_k |x_{ik}\alpha_k\lambda_{kj}|^2\right]}_{\mathrm{D_2^r}} \right] , \\
\frac{\partial J(\boldsymbol{\alpha})}{\partial \alpha_n^i} &= \sum_i \sum_j \left[-2\sigma_i \mathrm{w_{ji}} \underbrace{\frac{\partial}{\partial \alpha_n^i}\left[\sum_k \mathrm{Re}(\mathrm{x_{ik}}\alpha_\mathrm{k}\lambda_\mathrm{kj})\right]}_{\mathrm{D_1^i}} + \underbrace{\frac{\partial}{\partial \alpha_n^i}\left[\sum_k |x_{ik}\alpha_k\lambda_{kj}|^2\right]}_{\mathrm{D_2^i}} \right] .
\end{aligned} \tag{5.61}$$

Then, the complex number $x_{ik}\alpha_k\lambda_{kj}$ is introduced. This number can be split into real and imaginary parts as:

$$\begin{aligned}
x_{ik}\alpha_k\lambda_{kj} &= (x_{ik}^r + ix_{ik}^i)(\alpha_k^r + i\alpha_k^i)(\lambda_{kj}^r + i\lambda_{kj}^i) \\
&= (x_{ik}^r\alpha_k^r + ix_{ik}^r\alpha_k^i + ix_{ik}^i\alpha_k^r - x_{ik}^i\alpha_k^i)(\lambda_{kj}^r + i\lambda_{kj}^i) \\
&= (x_{ik}^r\alpha_k^r\lambda_{kj}^r - x_{ik}^i\alpha_k^i\lambda_{kj}^r - x_{ik}^r\alpha_k^i\lambda_{kj}^i - x_{ik}^i\alpha_k^r\lambda_{kj}^i) \\
&\quad + i(x_{ik}^r\alpha_k^i\lambda_{kj}^r + x_{ik}^i\alpha_k^r\lambda_{kj}^r + x_{ik}^r\alpha_k^r\lambda_{kj}^i - x_{ik}^i\alpha_k^i\lambda_{kj}^i) ,
\end{aligned}$$

and therefore the real and imaginary parts can be expressed as

$$\begin{aligned}
\mathrm{Re}(\mathrm{x_{ik}}\alpha_\mathrm{k}\lambda_\mathrm{kj}) &= x_{ik}^r\alpha_k^r\lambda_{kj}^r - x_{ik}^i\alpha_k^i\lambda_{kj}^r - x_{ik}^r\alpha_k^i\lambda_{kj}^i - x_{ik}^i\alpha_k^r\lambda_{kj}^i , \\
\mathrm{Im}(\mathrm{x_{ik}}\alpha_\mathrm{k}\lambda_\mathrm{kj}) &= x_{ik}^r\alpha_k^i\lambda_{kj}^r + x_{ik}^i\alpha_k^r\lambda_{kj}^r + x_{ik}^r\alpha_k^r\lambda_{kj}^i - x_{ik}^i\alpha_k^i\lambda_{kj}^i .
\end{aligned} \tag{5.62}$$

Using the previous expression of $x_{ik}\alpha_k\lambda_{kj}$, the second derivatives D_1^r and D_1^i can thus be expressed as follows:

$$\begin{aligned}
D_1^r &= \frac{\partial}{\partial \alpha_n^r}\left[\sum_k \mathrm{Re}(\mathrm{x_{ik}}\alpha_\mathrm{k}\lambda_\mathrm{kj})\right] = \frac{\partial}{\partial \alpha_n^r}\left[\mathrm{Re}(\mathrm{x_{in}}\alpha_\mathrm{n}\lambda_\mathrm{nj})\right] , \\
D_1^i &= \frac{\partial}{\partial \alpha_n^i}\left[\sum_k \mathrm{Re}(\mathrm{x_{ik}}\alpha_\mathrm{k}\lambda_\mathrm{kj})\right] = \frac{\partial}{\partial \alpha_n^i}\left[\mathrm{Re}(\mathrm{x_{in}}\alpha_\mathrm{n}\lambda_\mathrm{nj})\right] .
\end{aligned} \tag{5.63}$$

Using the previous expression of $x_{ik}\alpha_k\lambda_{kj}$, the second derivatives D_2^r and D_2^i can thus be expressed as follows:

$$\begin{aligned}
D_2^r = \frac{\partial}{\partial \alpha_n^r}\left[\sum_k |x_{ik}\alpha_k\lambda_{kj}|^2\right] &= \frac{\partial}{\partial \alpha_n^r}\left[\sum_k \mathrm{Re}^2(\mathrm{x_{ik}}\alpha_\mathrm{k}\lambda_\mathrm{kj}) + \mathrm{Im}^2(\mathrm{x_{ik}}\alpha_\mathrm{k}\lambda_\mathrm{kj})\right] \\
&= 2\mathrm{Re}(\mathrm{x_{in}}\alpha_\mathrm{n}\lambda_\mathrm{nj})\frac{\partial}{\partial \alpha_\mathrm{n}^\mathrm{r}}\left[\mathrm{Re}(\mathrm{x_{in}}\alpha_\mathrm{n}\lambda_\mathrm{nj})\right] \\
&\quad + 2\mathrm{Im}(\mathrm{x_{in}}\alpha_\mathrm{n}\lambda_\mathrm{nj})\frac{\partial}{\partial \alpha_\mathrm{n}^\mathrm{r}}\left[\mathrm{Im}(\mathrm{x_{in}}\alpha_\mathrm{n}\lambda_\mathrm{nj})\right] ,
\end{aligned} \tag{5.64}$$

and

$$
\begin{aligned}
D_2^i = \frac{\partial}{\partial \alpha_n^i}\left[\sum_k |x_{ik}\alpha_k\lambda_{kj}|^2\right] &= \frac{\partial}{\partial \alpha_n^i}\left[\sum_k \mathrm{Re}^2(\mathrm{x_{ik}}\alpha_\mathrm{k}\lambda_\mathrm{kj}) + \mathrm{Im}^2(\mathrm{x_{ik}}\alpha_\mathrm{k}\lambda_\mathrm{kj})\right] \\
&= 2\mathrm{Re}(\mathrm{x_{in}}\alpha_\mathrm{n}\lambda_\mathrm{nj})\frac{\partial}{\partial \alpha_\mathrm{n}^\mathrm{i}}\left[\mathrm{Re}(\mathrm{x_{in}}\alpha_\mathrm{n}\lambda_\mathrm{nj})\right] \\
&+ 2\mathrm{Im}(\mathrm{x_{in}}\alpha_\mathrm{n}\lambda_\mathrm{nj})\frac{\partial}{\partial \alpha_\mathrm{n}^\mathrm{i}}\left[\mathrm{Im}(\mathrm{x_{in}}\alpha_\mathrm{n}\lambda_\mathrm{nj})\right] \ .
\end{aligned}
\tag{5.65}
$$

Hence, the derivates are easily expressed as

$$
\frac{\partial}{\partial \alpha_n^r}\left[\mathrm{Re}(\mathrm{x_{in}}\alpha_\mathrm{n}\lambda_\mathrm{nj})\right] = x_{in}^r\lambda_{nj}^r - x_{in}^i\lambda_{nj}^i = \mathrm{Re}(\mathrm{x_{in}}\lambda_\mathrm{nj})\,, \tag{5.66}
$$

$$
\frac{\partial}{\partial \alpha_n^r}\left[\mathrm{Im}(\mathrm{x_{in}}\alpha_\mathrm{n}\lambda_\mathrm{nj})\right] = x_{in}^i\lambda_{nj}^r + x_{in}^r\lambda_{nj}^i = \mathrm{Im}(\mathrm{x_{in}}\lambda_\mathrm{nj})\,, \tag{5.67}
$$

$$
\frac{\partial}{\partial \alpha_n^i}\left[\mathrm{Re}(\mathrm{x_{in}}\alpha_\mathrm{n}\lambda_\mathrm{nj})\right] = -x_{in}^i\lambda_{nj}^r - x_{in}^r\lambda_{nj}^i = -\mathrm{Im}(\mathrm{x_{in}}\lambda_\mathrm{nj})\,, \tag{5.68}
$$

$$
\frac{\partial}{\partial \alpha_n^i}\left[\mathrm{Im}(\mathrm{x_{in}}\alpha_\mathrm{n}\lambda_\mathrm{nj})\right] = x_{in}^r\lambda_{nj}^r - x_{in}^i\lambda_{nj}^i = \mathrm{Re}(\mathrm{x_{in}}\lambda_\mathrm{nj})\,. \tag{5.69}
$$

Finally, the expressions of the functional derivatives are:

$$
\begin{aligned}
\frac{\partial J(\boldsymbol{\alpha})}{\partial \alpha_n^r} &= \sum_i\sum_j 2\left[\mathrm{Re}\left(\mathrm{x_{in}}\lambda_\mathrm{nj}\right)\left[\mathrm{Re}(\mathrm{x_{in}}\alpha_\mathrm{n}\lambda_\mathrm{nj}) - \sigma_\mathrm{i}\mathrm{w_{ji}}\right] + \mathrm{Im}(\mathrm{x_{in}}\lambda_\mathrm{nj})\mathrm{Im}(\mathrm{x_{in}}\alpha_\mathrm{n}\lambda_\mathrm{nj})\right]\ , \\
\frac{\partial J(\boldsymbol{\alpha})}{\partial \alpha_n^i} &= \sum_i\sum_j 2\left[-\mathrm{Im}\left(\mathrm{x_{in}}\lambda_\mathrm{nj}\right)\left[\mathrm{Re}(\mathrm{x_{in}}\alpha_\mathrm{n}\lambda_\mathrm{nj}) - \sigma_\mathrm{i}\mathrm{w_{ji}}\right] + \mathrm{Re}(\mathrm{x_{in}}\lambda_\mathrm{nj})\mathrm{Im}(\mathrm{x_{in}}\alpha_\mathrm{n}\lambda_\mathrm{nj})\right]\ .
\end{aligned}
\tag{5.70}
$$

Another important criterion that has to be highlighted is the loss function introduced by Jovanovic et al. [98] and which is defined as

$$
\Pi_{loss} := \sqrt{\frac{J(\boldsymbol{\alpha})}{J(\mathbf{0})}} = \frac{||\mathbf{V}_1^n - \mathbf{\Phi}\mathbf{D}_{\boldsymbol{\alpha}}\mathbf{V}_{\mathrm{and}}||_F}{||\mathbf{V}_1^n||_F}. \tag{5.71}
$$

The loss function enables to estimate the quality of the vector solution $\boldsymbol{\alpha}$ of the minimization problem previously introduced.

Finally, the computation of the modes amplitude also enables to reconstruct the field of interest conserving the modes scaling intact [176]. More advanced methodology has been introduced for extracting a subset of dominant modes, Chen et al. [35] introduced a non-convex optimization problem associated to combinatorial search. Moreover, Jovanovic et al. [99, 98] proposed the low rank, sparse and sparsity-promoting DMD and Sayadi et al. [172] a corrected mode amplitude computation method that tries to overcome the selection of dominant but transient features.

5.4 DMD algorithm applications

This section presents the application of the DMD methodology on realistic configurations in order to extract the coherent features from unsteady flows. First, the classical 2D laminar cylinder configuration has been studied with the extraction of the well-known Bénard-von Karman alleys. Second, the challenging 2.2 billion cells LES of the T7.2 configuration, presented in the previous chapter, has been on-the-fly post-processed thanks to the MGHOF framework leading to the generation of hundreds of snapshots that have been analyzed through DMD.

5.4.1 Application to the 2D cylinder flow

This section introduces the dynamics extraction for the classical 2D laminar cylinder configuration thanks to DMD. This test case is ideal as it produces stable and periodic features called the Bénard-von Karman alleys for some values of the Reynolds number.

5.4.1.1 Presentation of the configuration

This configuration is governed by a single dimensionless parameter, the Reynolds number, defined as $Re = u_\infty d/\nu$ with u_∞ the characteristic free-stream velocity scale, d the cylinder diameter and ν the kinematic viscosity of the fluid. When the Reynolds number is below a critical value defined as $Re_c \simeq 46$, the flow field is asymptotically steady and two-dimensional. However, the flow becomes unstable for higher Reynolds numbers through a Poincaré–Andronov–Hopf bifurcation [150] - a critical point where a system's stability turns to a periodic solution - leading to the well-known Bénard-von Karman vortex street. Henry Bénard [14] was the pioneer who studied the experimental aspect of this phenomenon when von Karman [202] was interested in the theoretical considerations. This oscillatory flow is characterized with asymptotically time-periodic and two-dimensional behavior until a Reynolds number value of 188, where the flow becomes turbulent and three-dimensional [9].

Here, the 2D computational domain has been defined with the following geometrical dimensions $L_x \times L_y = 0.6\,\mathrm{m} \times 0.3\,\mathrm{m}$ and with a cylinder width $d = 0.01\,\mathrm{m}$. On the inlet, the initial velocity field has been imposed to $u_x = 0.15\,\mathrm{m.s}^{-1}$ and $u_y = 0.0\,\mathrm{m.s}^{-1}$ leading to a Reynolds number of 99 considering air flow with a kinematic viscosity equal $\nu = 1.517 \times 10^{-5}\,[\mathrm{m}^2.\mathrm{s}^{-1}]$ and a Strouhal number of $St \approx 0.165$ [23]. The LES of this configuration has been performed with 10 processors on an unstructured grid composed of $25'000$ cells as Fig 5.3 presents. Once the flow field convergence is reached, the snapshots have been accumulated through the MGHOF framework with a time sampling defined as $\Delta T = 0.05\,\mathrm{s} \approx \tau/8$ with τ the vortex shedding based on the Strouhal number. Finally, the generalized DMD methodology has been performed on this configuration with the 130 snapshots on 10 processors, corresponding to 8 snapshots per vortex shedding.

5.4.1.2 DMD application on the velocity field

In a first time, the DMD formalism has been applied to the velocity field. As the selection of a subset of DMD dominant features depends both on the eigenvalues and on the mode energy, the graphical representation of those quantities has to be introduced before going further and deeper in the analysis of the DMD results.

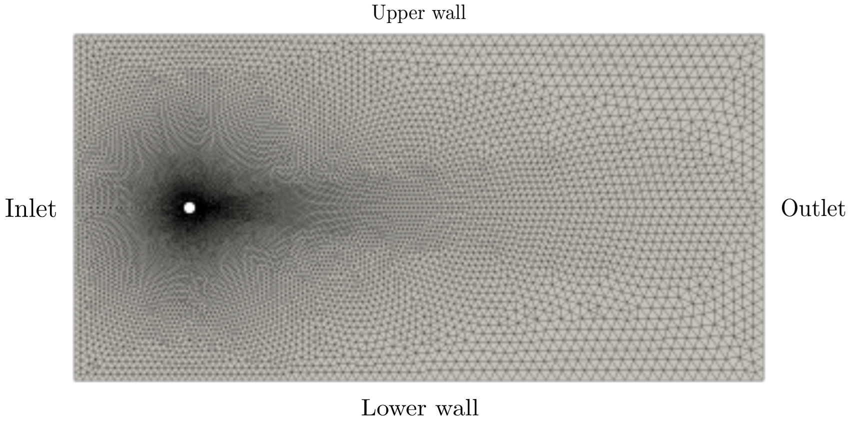

FIGURE 5.3: Sketch of the 2D cylinder configuration

Figure 5.4 presents the location of the mode eigenvalues λ_j relative to the unitary circle. As previously mentioned, the Vandermonde matrix $\mathbf{V}_{\text{and}}$, filled with λ_i^k, contains the temporal evolution of the dynamic mode $\boldsymbol{\phi}_i$, and thus the mode damping for each snapshot. Indeed, the i^{th} mode eigenvalue at the power k, noted λ_i^k, refers to the attenuation of the i^{th} DMD mode $\boldsymbol{\phi}_i$ for the $(k+1)^{th}$ snapshot. As a consequence, Fig. 5.4 (left) shows the mode attenuation for the second snapshot and Fig. 5.4 (right) presents the mode attenuation for the last snapshot n. Stable modes are associated to modulus eigenvalues equal or lower than one as previously explained and conjugate modes can be easily identified thanks to the horizontal axial symmetry.

Considering Fig. 5.4 (left), it is noticeable that some frequencies, colored in red circles, stand apart from the others as they seem to be well converged and thus located on the unit circle. First, the point located at coordinate (1.0, 0.0) refers to the real constant mode and represents the mean flow field. This mode is therefore not damped as the time increases because of its unitary modulus. Others are complex conjugated modes that evolve in time. Moreover, they all seem to be multiples of one lower frequency: they are all harmonics. This can be easily shown with the constant angle between each of them on the unit circle and their frequency.

Looking at Fig. 5.4 (right) allows to quantify the stability and the damping of the DMD modes. Here, it is noticeable that all the red circled modes are still located very close to the unit circle. Therefore, they can be considered as permanent compared to other transient modes. Even if some of them are out the unit circle, they can be considered as quasi-stable and thus relevant for the dynamics of the flow.

Another representation of Fig. 5.4 (left) is presented in Fig. 5.5 which consists in a log-mapped transformation of the mode eigenvalues as $\lambda_j^{\ln} = \frac{\ln \lambda_j}{\Delta T}$. In that case, the x-coordinate represents the pulsation of the mode, noted ω_j, with a vertical symmetry axis. Then, every mode except the constant one, is associated to its conjugate with an opposite frequency. Moreover, unstable modes are here represented by positive value of $\lambda_j^{\ln}$ while most stable modes are located close to the zero x-axis which correspond to

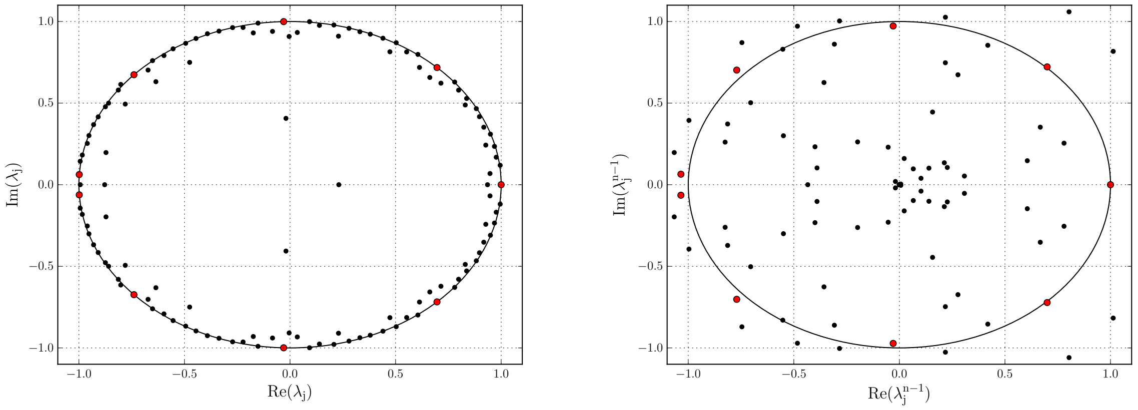

FIGURE 5.4: Eigenvalues λ_j (left) and λ_j^{n-1} (right)

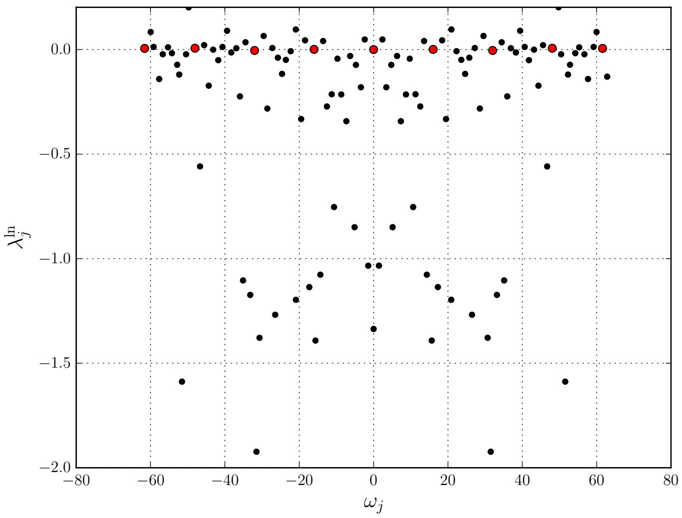

FIGURE 5.5: Log-mapped transformation of the eigenvalues $\lambda_j^{\ln}$

the red circled modes as previously mentioned.

The other relevant criteria when selecting a sub-set of DMD dominant features are the modulus of the mode amplitude, previously obtained by solving the minimization problem, but also the energy of the modes that both combines mode amplitude and convergence. As Fig. 5.6 (left) presents, the modulus of the amplitudes enable to distinguish which modes are the most dynamically relevant features of the flow. However, adding the mode eigenvalues enables to build the integrated energy of each mode which is presented in Fig. 5.6 (right). This criterion is more accurate as it penalizes transient modes that will be strongly damped as the time increases. Then, it is noticeable that the most converged modes, the red circled ones, are also dominant in term of energy that confirms the sub-set selection.

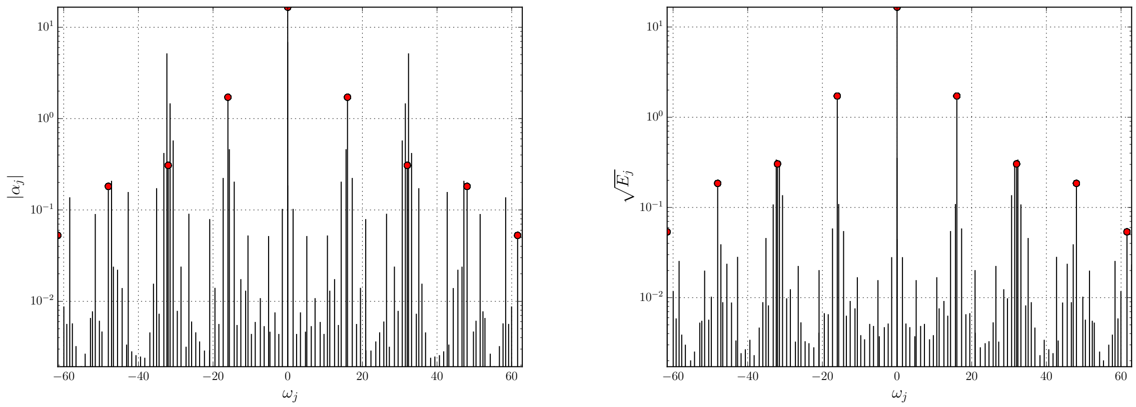

FIGURE 5.6: Mode amplitudes α_j (left) and Mode energy E_j (right)

The spatial selected DMD modes are presented in Fig. 5.7. Here, the frequencies of the selected dominant modes can be compared to experimental results through the Strouhal number defined as

$$St = \frac{d}{\tau U}\,, \tag{5.72}$$

where τ is a period of a vortex shedding.

The experimental Strouhal number for Reynold number case $Re = 100$ is around $St \approx 0.165$ [23]. This value refers to an experimental frequency of $\nu_{exp} \approx 2.48\,[\mathrm{Hz}]$ for the vortex shedding which is very close to the frequency of the mode 31 with $\nu = 2.55\,[\mathrm{Hz}]$. The selected modes 68 and 100 are harmonics of this frequency. However, even if the mode 128 does not have the adequate frequency to be an harmonic, it can be considered has an approximated harmonic o the frequency $\nu = 10.20\,\mathrm{Hz}$ as the time sampling $\Delta T = 0.05\,s$ does not allow to correctly capture frequencies higher than $10\,\mathrm{Hz}$.

Finally, thanks to this sub-set of modes, the instantaneous velocity flow field has been reconstructed by only considering the 4 selected modes with the mean flow. As Fig. 5.8 shows, the reconstructed flow field, noted $\tilde{\mathbf{u}}^{DMD}$, is directly compared to the computed field from the LES, noted $\mathbf{u}^{LES}$, for two different times, respectively $t = 0$ and $t = 19\Delta T$. The reconstructed flow field looks very similar to the LES field and highlights the ability of DMD to identify and extract the dynamics in such simple configuration.

5.4.1.3 DMD application on the scalar

In a second time, DMD has been applied to the scalar field whose boundary conditions have been set to unity at the inlet and to zero on the cylinder wall. First, as previously presented, the selection of the most converged modes can be achieved with Fig. 5.9 and Fig. 5.10. The analysis of the amplitude and the energy of the modes in Fig. 5.11 allows to highlight the same frequencies as the ones on the velocity field. However, one transient mode, characterized with the frequency $\nu = 1.76\,[\mathrm{Hz}]$, seems also to stand apart. Comparing the amplitude and the averaged energy of this mode enables to highlight the penalization due to its transient behavior. The energy of this mode still remains high but despite this value, it has not been selected because of its high damping. The sub-set of relevant modes are presented in Fig. 5.12 and the transient dynamically important mode is presented in Fig. 5.13.

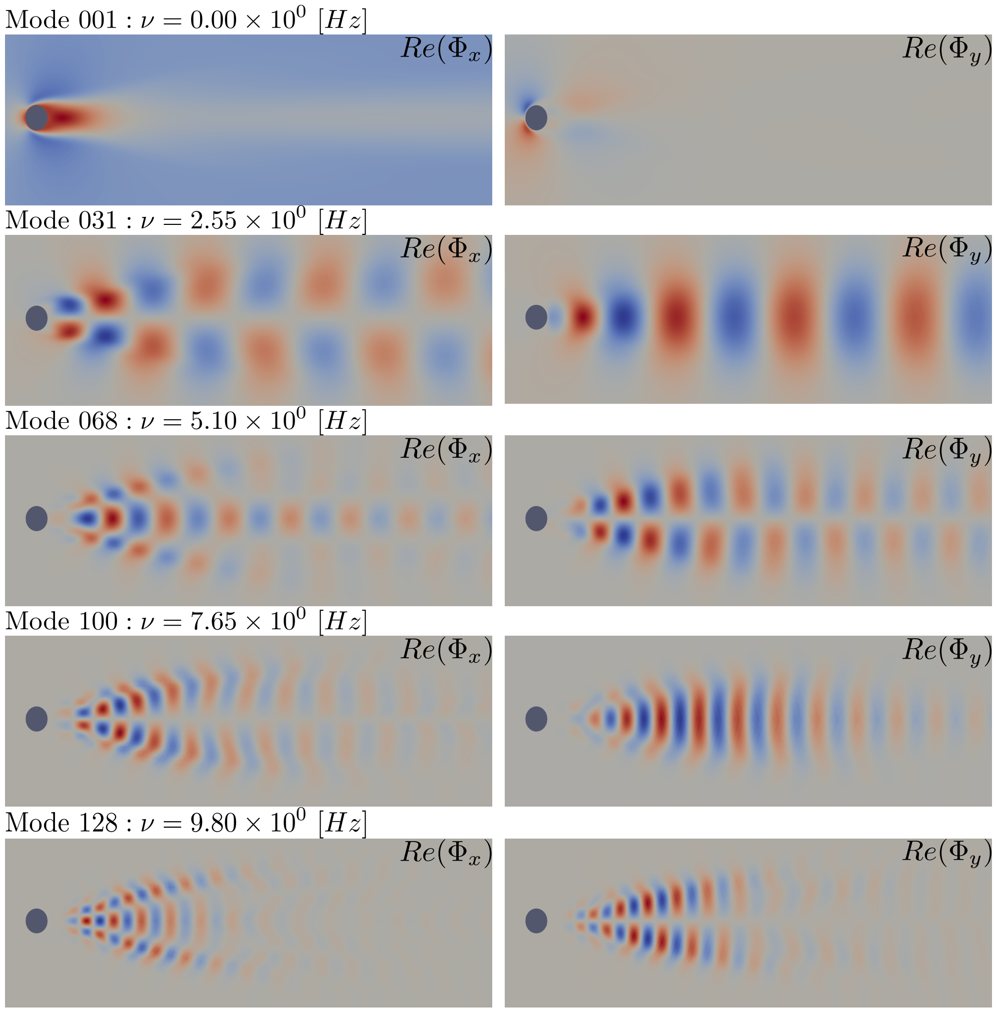

FIGURE 5.7: Dominant DMD modes for the velocity field

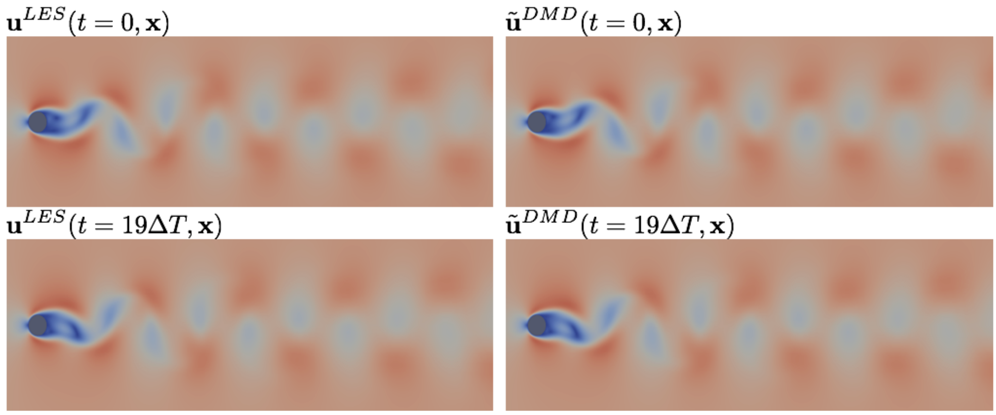

FIGURE 5.8: Reconstruction of the velocity field with four modes and the mean

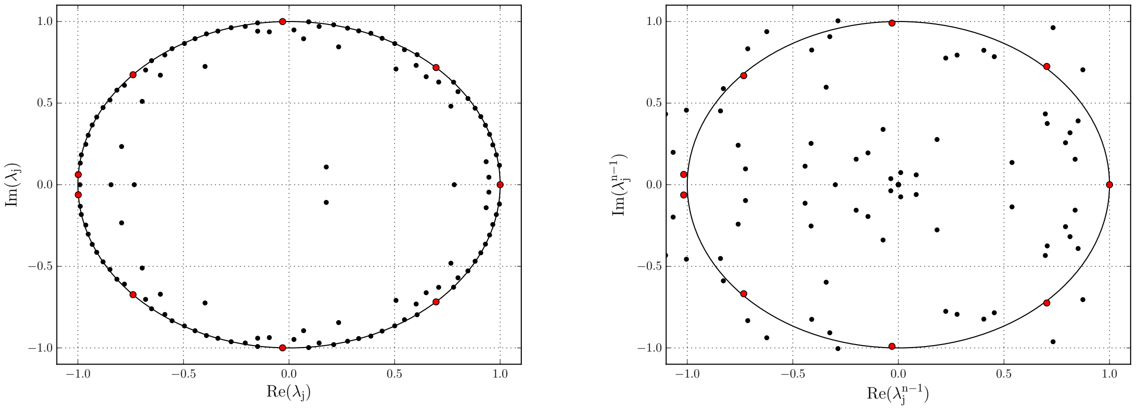

FIGURE 5.9: Eigenvalues λ_j (left) and λ_j^{N-1} (right)

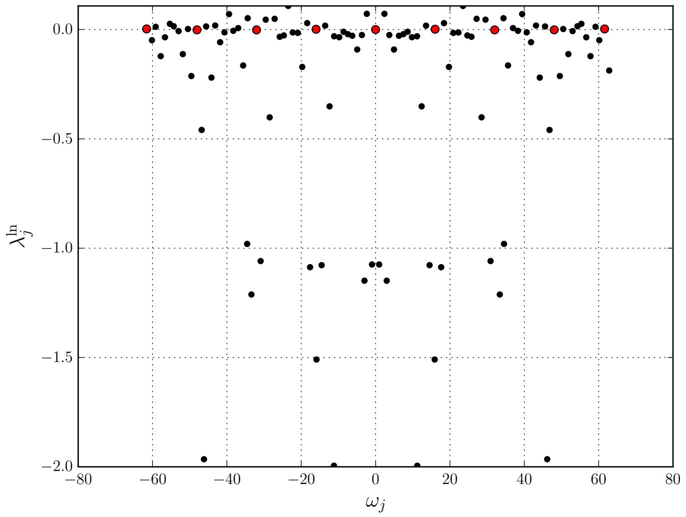

FIGURE 5.10: Log-mapped transformation of the eigenvalues $\lambda_j^{\ln}$

Moreover, the scalar flow field has also been reconstructed using the sub-set of selected DMD modes as Fig. 5.14 shows. Once again, the reconstructed flow field is very close to the one computed.

To conclude, the application of DMD is very efficient to identify and extract coherent flow features. The 2D laminar cylinder is not a challenging configuration for the considered Reynolds number. Indeed, no turbulence is generated and the Bénard-von Karman alleys are periodic features. Moreover, capturing the physics of the flow does not necessitates well refined meshes. In the following sub-section, a much more challenging configuration is considered.

5.4.2 Combining the MGHOF with Dynamic Mode Decomposition

This last section demonstrates that the MGHOF enables to perform advanced analysis of large-scale dynamics from massive high-fidelity simulations.

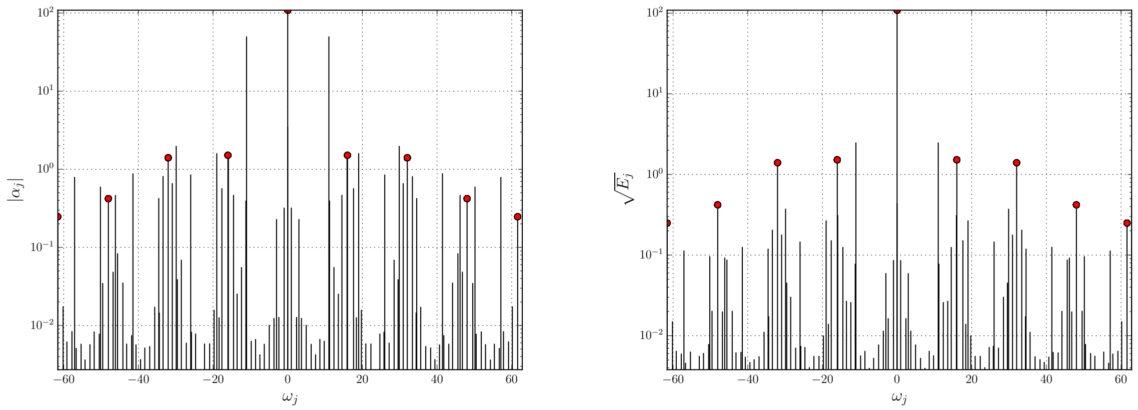

FIGURE 5.11: Mode amplitudes α_j (left) and Mode energy E_j (right)

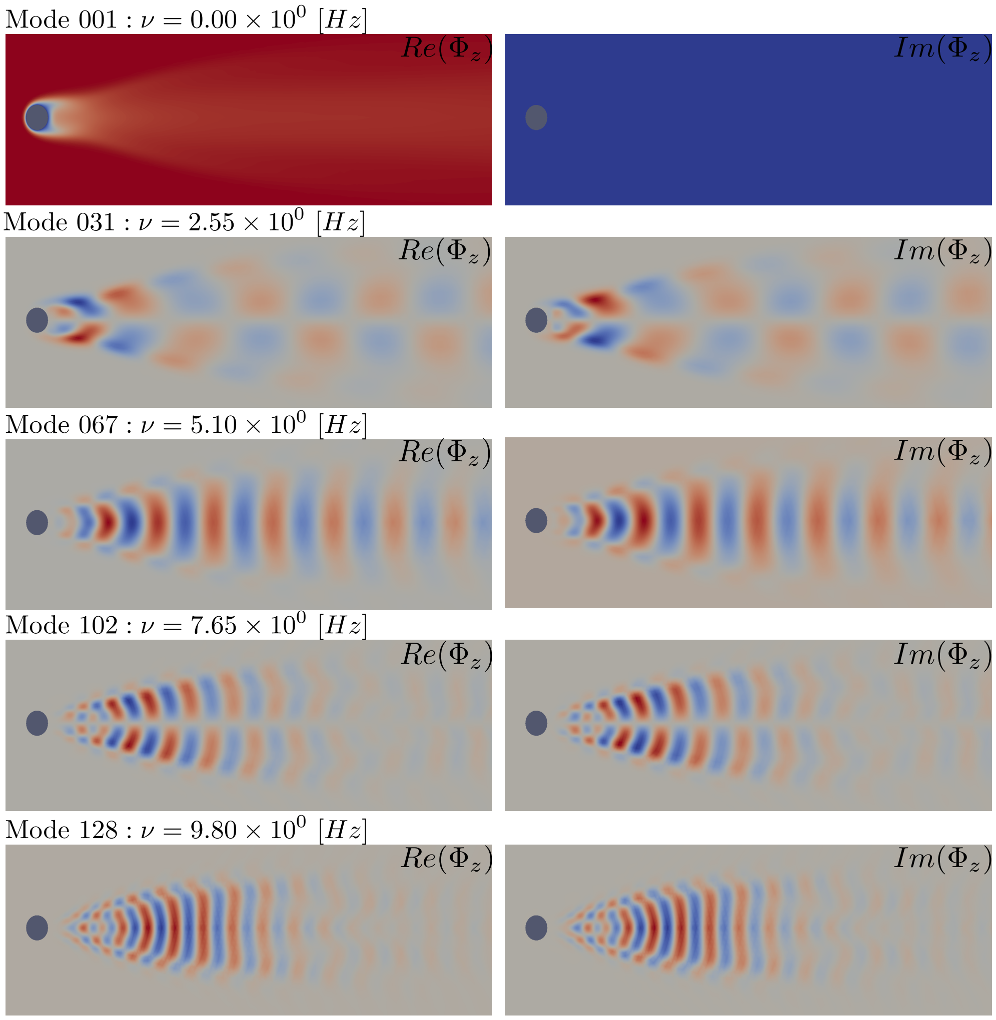

FIGURE 5.12: Dominant DMD modes for the scalar field

In this section, DMD is applied to the LES of the T7.2 blade with the M_2 mesh (2.2 billion elements) through the MGHOF framework, in order to identify the dynamically dominant features of the flow. The

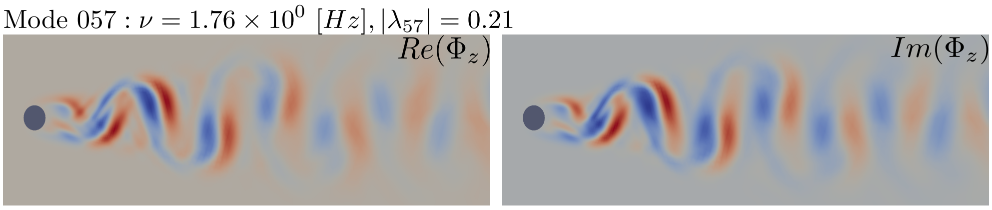

FIGURE 5.13: Dominant unconverged DMD modes for the scalar field

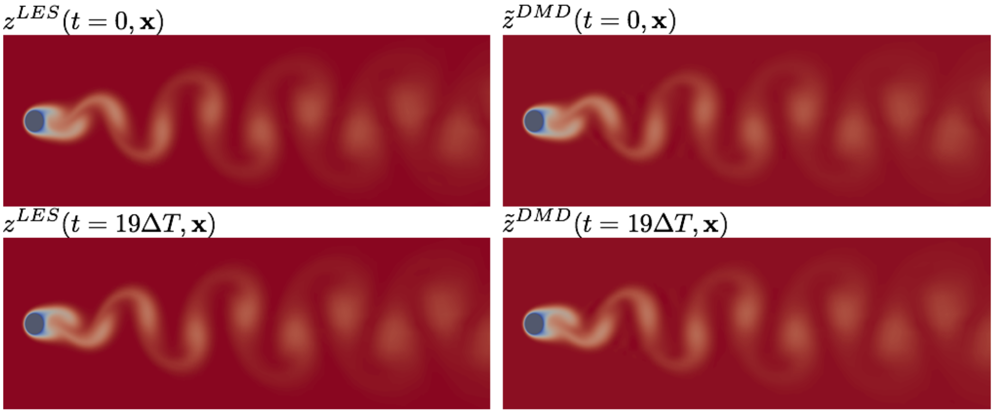

FIGURE 5.14: Reconstruction of the scalar field with four modes and the mean

T7.2 configuration has been previously presented in section 4.4.2.1.

5.4.2.1 Dominant features extraction

Here, the DMD methodology is applied to the passive scalar z_{M_0} and velocity field $\mathbf{u_{M_0}}$ extracted from the LES grid M_2 to M_0 with $n = 200$ snapshots obtained with a constant time sampling $\Delta T = 0.05\,\mathrm{ms}$. These snapshots have been directly generated by applying 200 times the MGHOF framework with the calibrated parameters. The coherent features computed on the mesh with 2.2 billions cells can therefore be analyzed with DMD overcoming the storage issue that would arise if one would apply DMD directly on the fine LES mesh.

In order to assess the quality of the DMD and more particularly its ability to reproduce the flow dynamics, the loss function, previously introduced, is computed. This function enables to estimate the quality of the DMD solution. For $n = 200$ snapshots and $\Delta T = 0.05$ ms, the loss function for the scalar z_{M_0} is $\Pi_{loss} = 0.34\%$. Moreover, by adding twice more snapshots leading to $n = 400$, the loss function for the scalar is slightly reduced to $\Pi_{loss} = 0.12\%$. Concerning the velocity field, the loss function is almost equal to zero for $n = 200$ snapshots and increases when adding more snapshots. Hence, the results presented hereafter have been computed with $n = 200$ snapshots for both scalar and velocity field, which ensures a good approximation of the flow dynamics over the whole sampling time.

Then, the energy of the DMD modes against the pulsation is presented in Fig. 5.15 for the passive scalar (left) and for the velocity (right). Selecting the dominant modes from their energy is very difficult in this type of flow. Indeed, a mode can be dominant during the first snapshots leading to a large energy but not dominant over the whole sampling time. This type of transient mode is not of interest here. The mode energy has to be complemented by an analysis of the mode eigenvalues λ_i and amplitude growth rate $\lambda_j^{\ln} = \frac{\ln|\lambda_j|}{\Delta T}$ presented in Fig. 5.16 and 5.17. If the eigenvalue lies on the unit circle and if the amplitude growth rate is sufficiently large, the mode is not damped and contributes to the dynamics over the full sampling time.

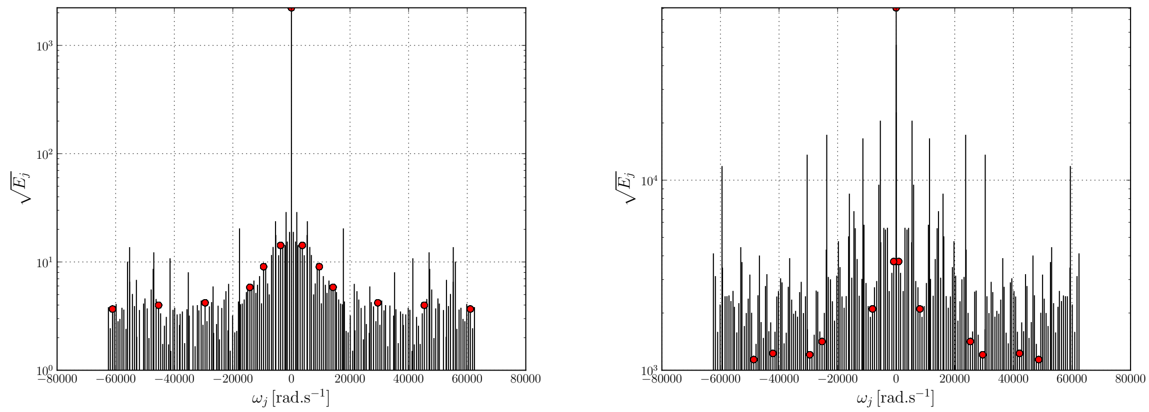

FIGURE 5.15: Energy of the modes for the passive scalar z_{M_0} (left) and the velocity field $\mathbf{u_{M_0}}$ (right)

Based on the three latter criteria, relevant DMD modes have been extracted. These modes are represented with red dots in Figs. 5.15 to 5.17. More advanced DMD methodologies could be applied to select the dominant modes as the optimized DMD [35] based on combinatory search, low-rank DMD and sparse DMD [99] or the sparsity-promoting DMD [98], in order to access to more relevant modes.

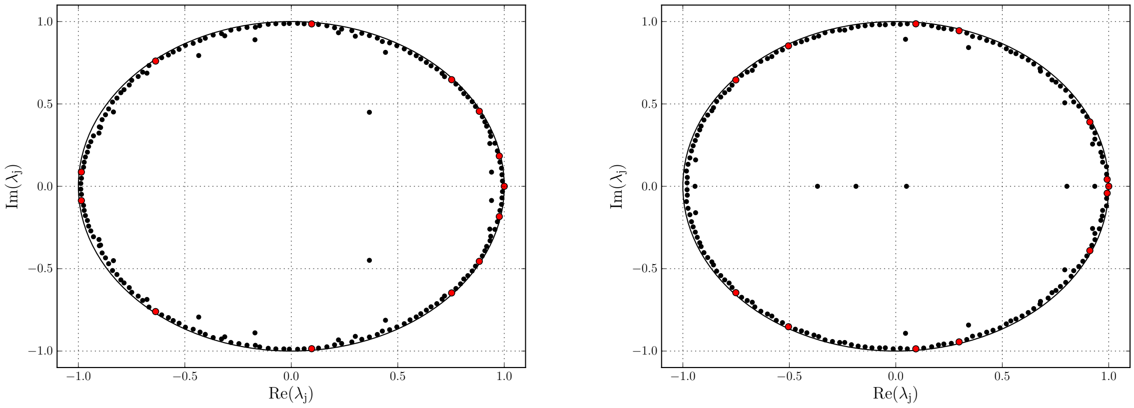

FIGURE 5.16: DMD eigenvalues λ_j for the passive scalar z_{M_0} (left) and the velocity field $\mathbf{u_{M_0}}$ (right)

The real parts of the selected dominant modes for the passive scalar and the velocity fields are presented in Fig. 5.18 and Fig. 5.19 with their detailed properties in Tab. 5.1 and Tab. 5.2. These fields are complemented with 3D visualizations of the modes in Figs. 5.20 to 5.23. For both scalar and velocity

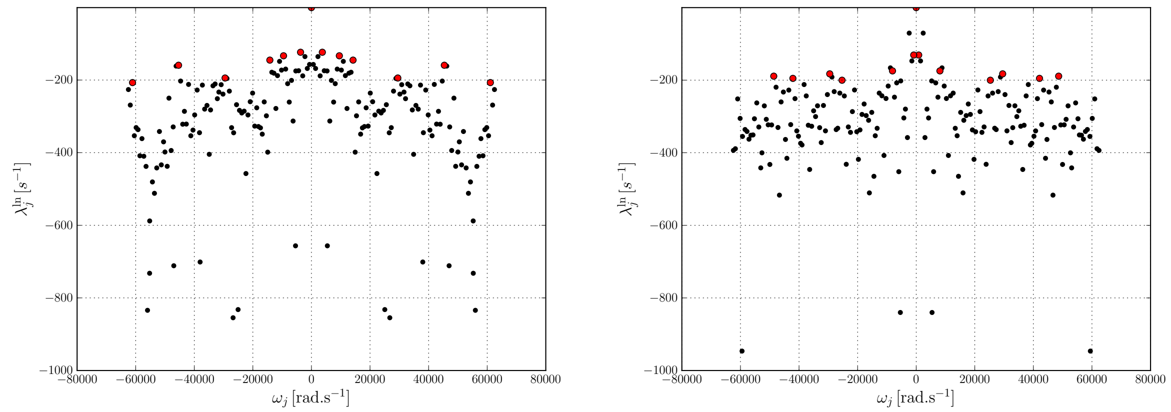

FIGURE 5.17: DMD amplitude growth rate $\lambda_j^{\ln}$ for the passive scalar z_{M_0} (left) and the velocity field $\mathbf{u}_{\mathbf{M}\text{-}\mathbf{0}}$ (right)

Mode	ω_i [rad.s^{-1}]	$\lvert\lambda_i\rvert$ [−]	E_i [−]
ϕ_1	0.0	1.0	2225.17
ϕ_{10}	3.718×10^3	9.94×10^{-1}	14.24
ϕ_{30}	9.527×10^3	9.93×10^{-1}	9.04
ϕ_{44}	1.420×10^4	9.93×10^{-1}	5.84
ϕ_{94}	2.948×10^4	9.90×10^{-1}	4.20
ϕ_{144}	4.537×10^4	9.92×10^{-1}	3.99
ϕ_{196}	6.108×10^4	9.90×10^{-1}	3.68

TABLE 5.1: Properties of the selected DMD modes for the passive scalar z_{M_0}

Mode	ω_i [rad.s^{-1}]	$\lvert\lambda_i\rvert$ [−]	E_i [−]
ϕ_1	0.0	1.0	80694.33
ϕ_2	8.45×10^2	9.93×10^{-1}	3734.18
ϕ_{25}	8.094×10^3	9.91×10^{-1}	2101.21
ϕ_{80}	2.532×10^4	9.90×10^{-1}	1415.55
ϕ_{92}	2.952×10^4	9.91×10^{-1}	1207.12
ϕ_{135}	4.210×10^4	9.90×10^{-1}	1226.53
ϕ_{155}	4.863×10^4	9.91×10^{-1}	1138.00

TABLE 5.2: Properties of the selected DMD modes for the velocity field $\mathbf{u}_{\mathbf{M}_0}$

DMD, the constant mode, noted ϕ_1 and characterized by a frequency equal to zero, represents the mean flow field.

The scalar modes exhibit different types of coherent structures that are mostly located in the boundary layer or in the recirculation zone on the pressure side. These structures depend on the position on the blade: in the laminar boundary layer on the suction side, very elongated structures with a size close to a

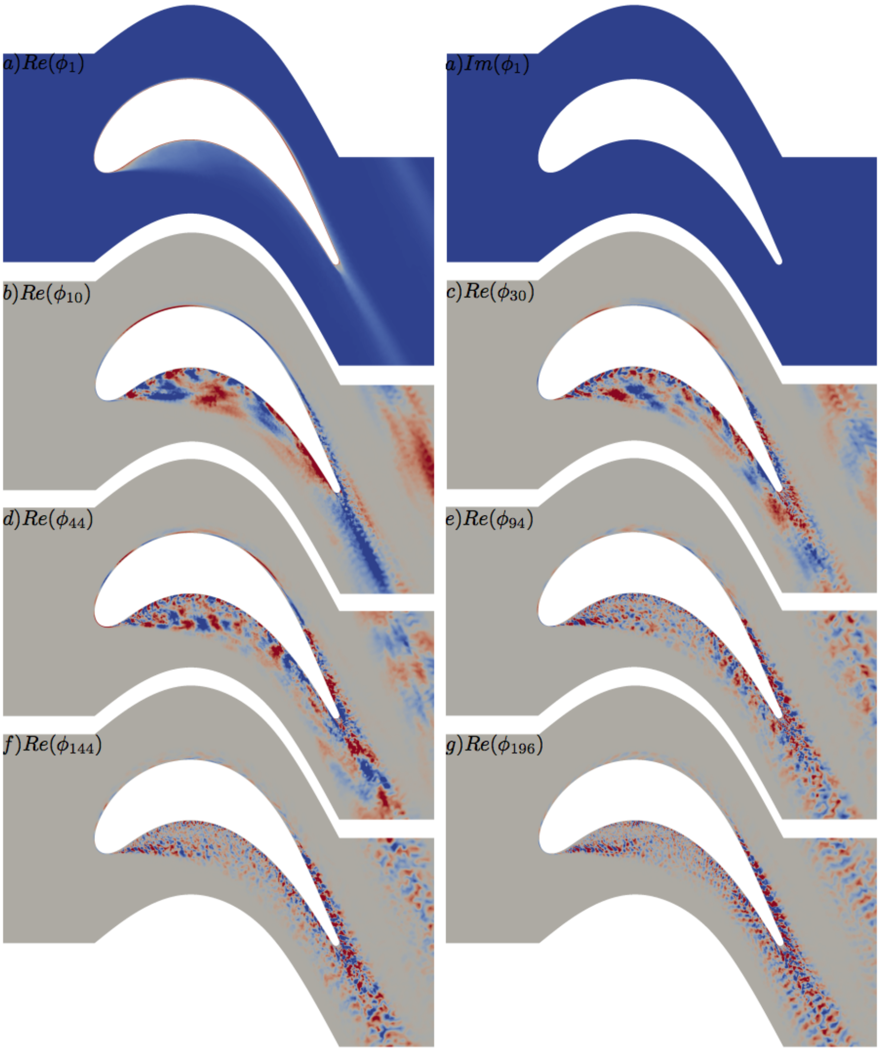

FIGURE 5.18: Constant mode ϕ_1 (first line) and real parts of the next selected DMD modes for the scalar z_{M_0}

mid-chord are present. Other types of elongated structures are present at the trailing edge on both sides. In the recirculation zone on the pressure side, the structures are more isotropic.

The velocity modes are more complex to analyze. In this configuration, homogeneous isotropic turbulence with an intensity of nearly 6% is injected upstream of the blade. Some of the spectral content of this turbulence may interact with the blade. This phenomenon is visible in the upstream content of the different velocity modes, especially those at low frequency. While the recirculation zone on the pressure side has a strong response for the low-frequency modes with large-scale and elongated vortices visible in Fig. 5.22, the wake of the blade responds to higher frequencies. More interestingly, the turbulent boundary layer on the pressure and suction side have also different responses.

When comparing the scalar and velocity modes, it appears that most of the modes are independent, which would suggest that the temperature and velocity fluctuations are decoupled. The only exception is the mode 92 for the velocity, which is very close to the mode 94 for the scalar. This analysis should be supplemented by a study of the cross correlation of these modes, which is out of the scope of the present work.

5.5 Conclusions

The MGHOF framework enables to accumulate a large number of snapshots on coarse grids in order to apply modal decomposition techniques such as POD or DMD. Indeed, the extraction of large scales on coarse grids by removing all the highest flow frequencies overcomes the storage issue of those methodologies. The application of the DMD method successfully identifies the dynamically dominant modes in billion cells LES and enables to better understand the dynamics of the flow. Many other types of analysis would benefit from such accurate and efficient coarsening technique.

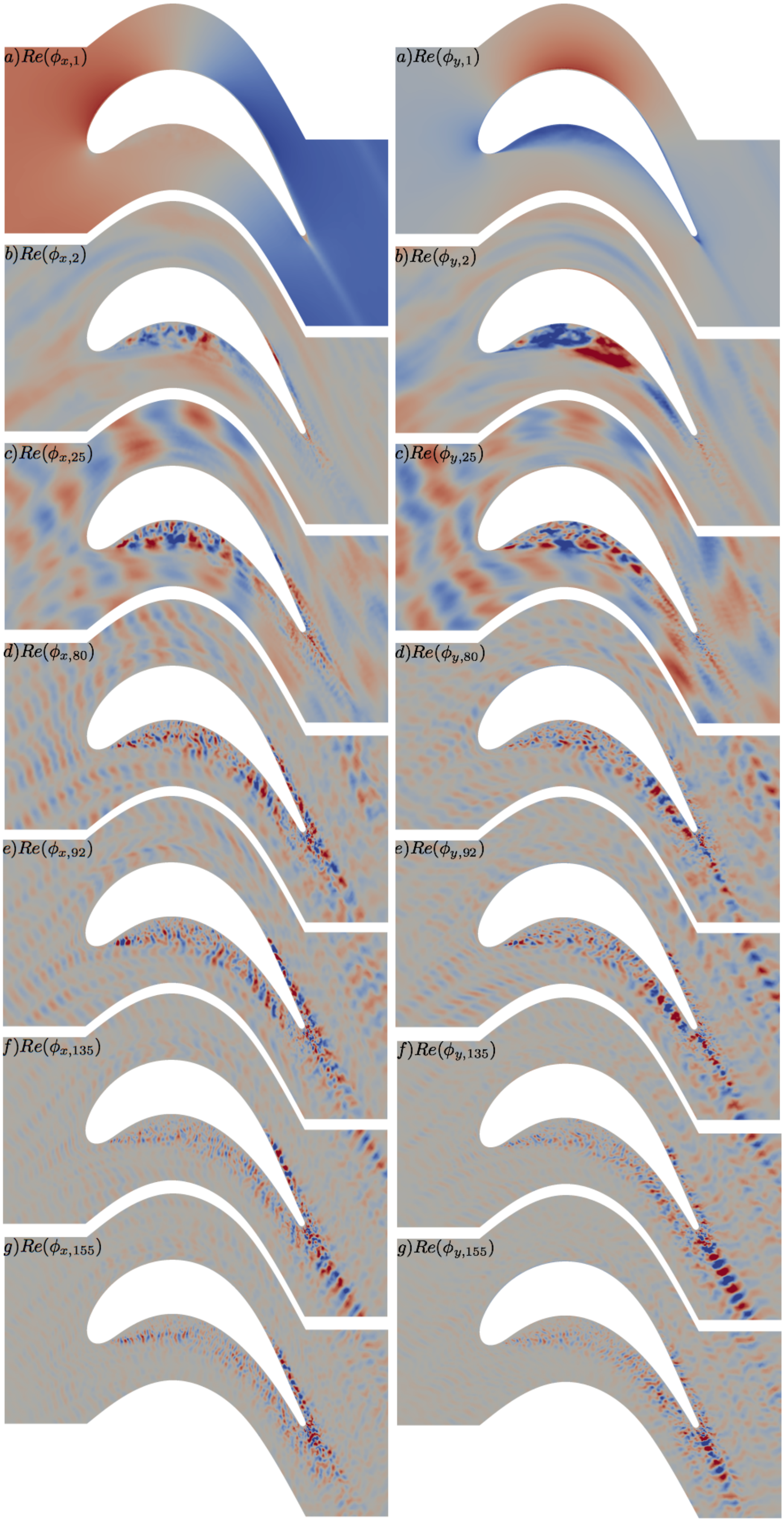

FIGURE 5.19: Real parts of the selected DMD modes for the velocity field $\mathbf{u}_{\mathrm{M}_0}$ with component x of the mode (left) and component y (right)

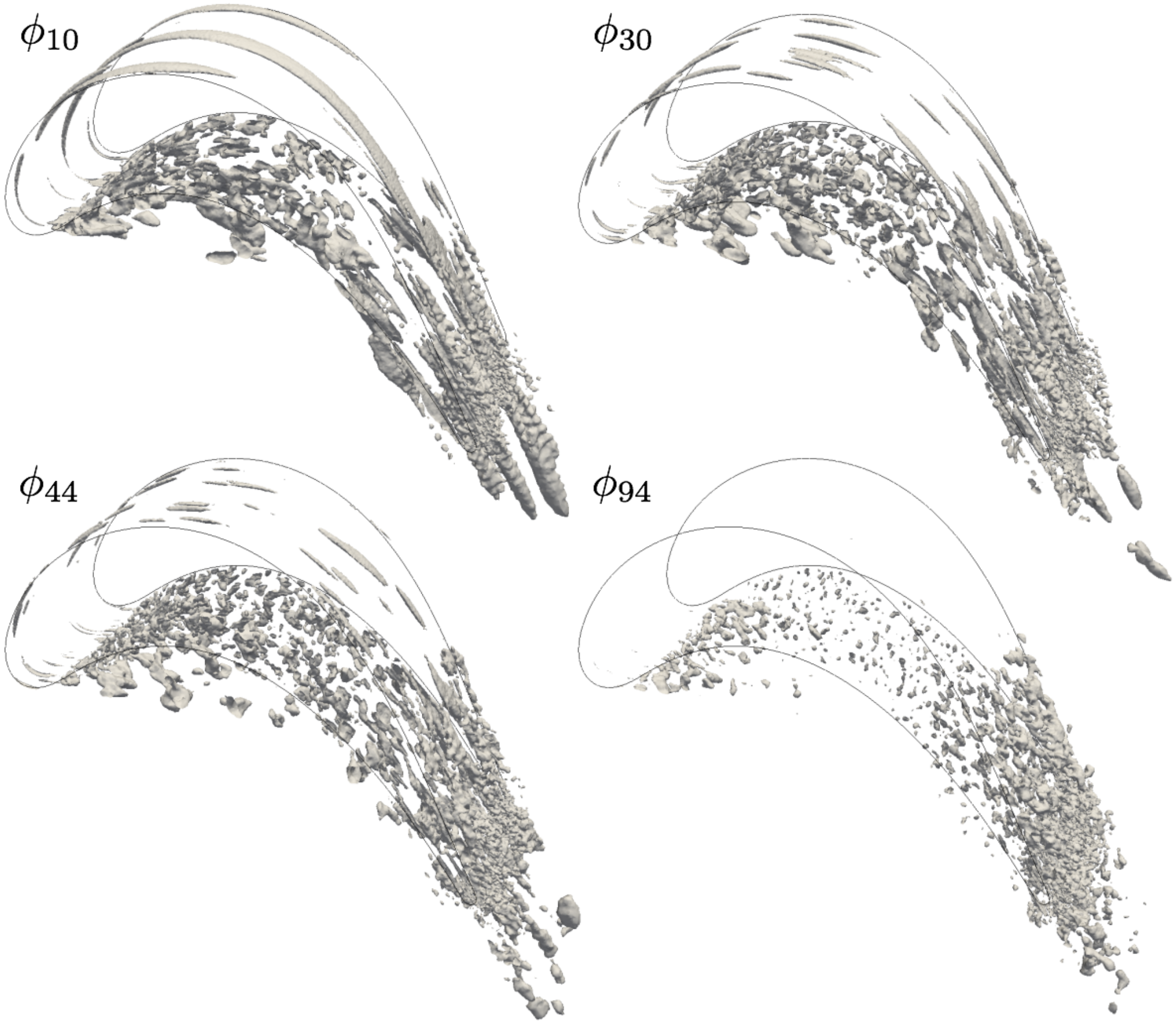

FIGURE 5.20: Iso-contours of the mode modulus for the scalar z_{M_0} (perspective view)

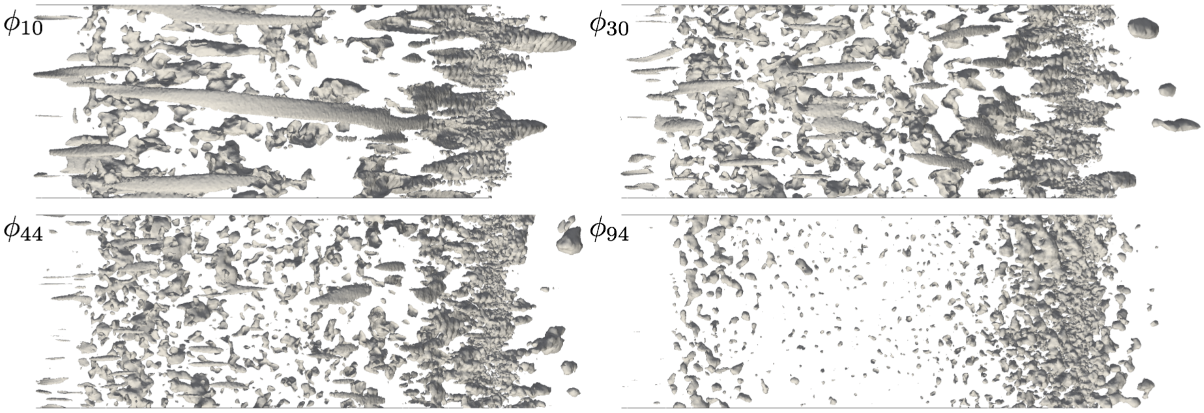

FIGURE 5.21: Iso-contours of the mode modulus for the scalar z_{M_0} (top view)

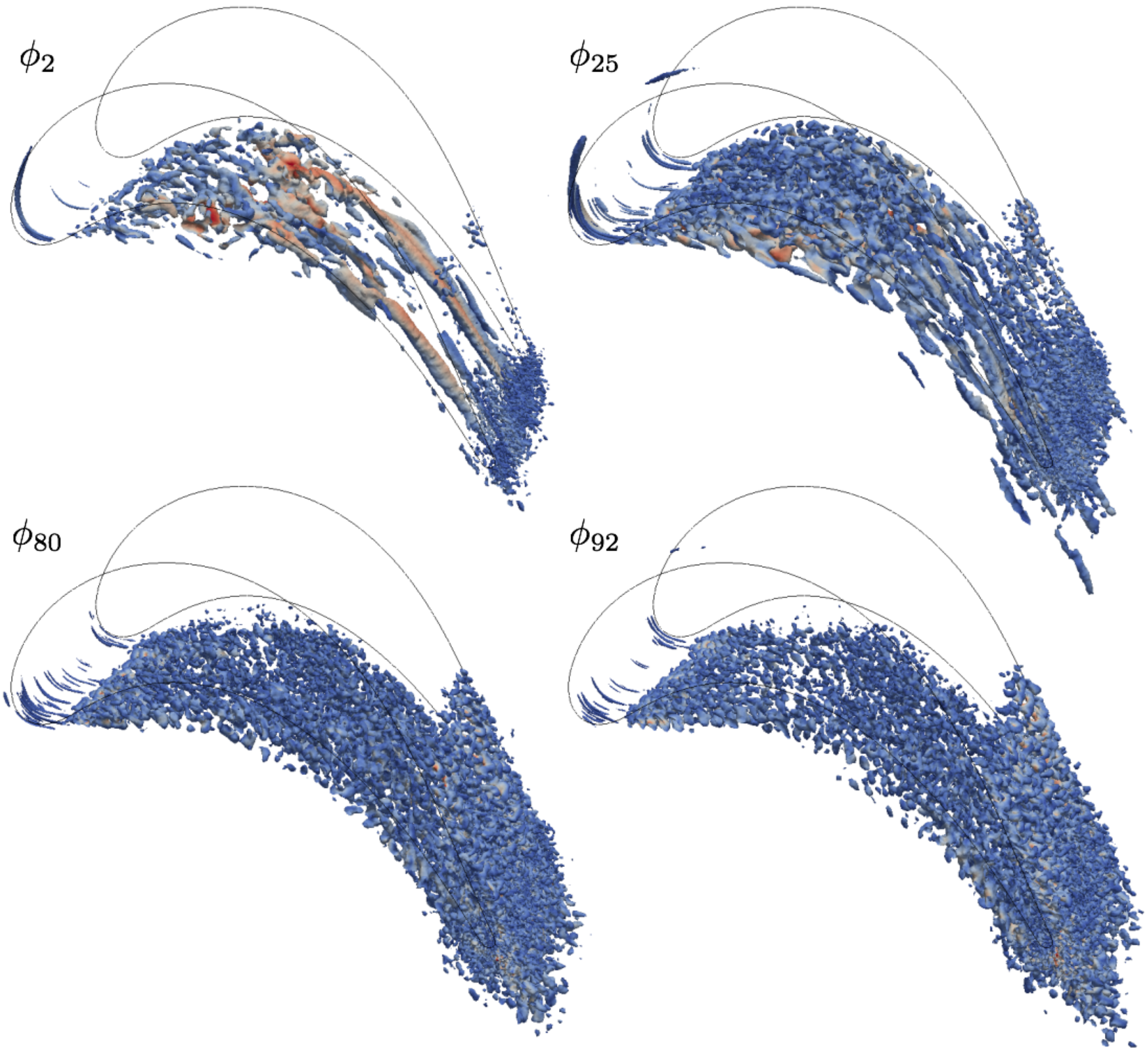

FIGURE 5.22: Iso-contours of Q-criterion for the velocity DMD modes (perspective view)

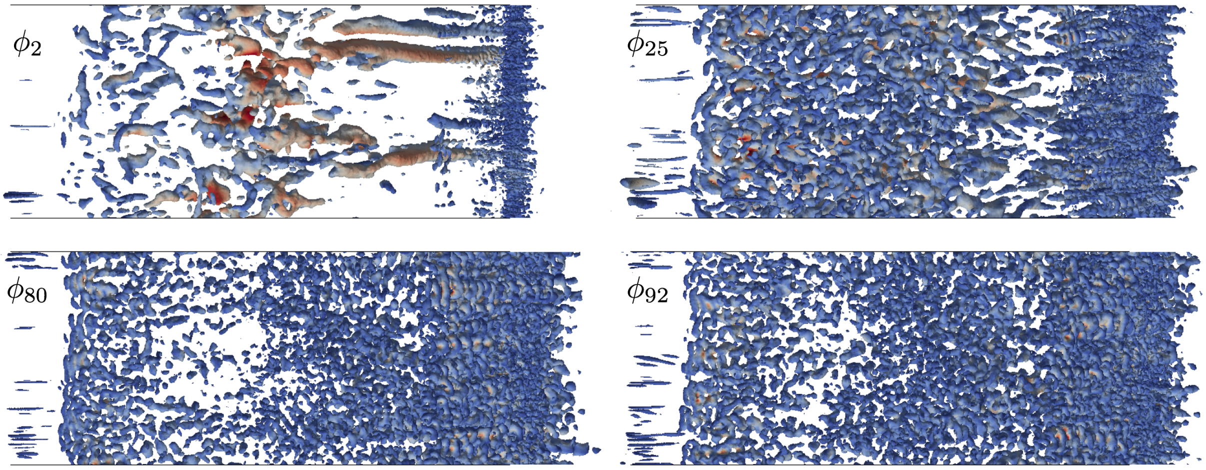

FIGURE 5.23: Iso-contours of Q-criterion for the velocity DMD modes (top view)

Chapter 6

Multiple-Resolution Large-Eddy Simulation framework (MR-LES)

This chapter presents the Multiple-Resolution Large-Eddy Simulation (MR-LES) framework that aims at the on-the-fly generation of optimized meshes based on physical characteristics of the flow. Indeed, mesh quality appears to be one of the major user-dependent parameter while performing LES. Therefore, user-independent LES necessitate to control the quality of the meshes by optimizing them through objective criteria. Hence, the proposed MR-LES methodology is based on the multi-level formalism and deals with evaluation of both numerical and modeling errors through the computation of simultaneous LES at different resolutions. Here, the first section introduces the MR-LES framework with error quantification. Then, a parametric study to both numerical and modeling errors while varying the main user-dependent parameters is performed. Finally, the application of the MR-LES framework on a flow around a 3D turbulent cylinder is presented.

Contents

6.1 Introduction

Due to the steady increase of computational resources that are exploited by modern CFD codes, highly resolved LES with several hundred millions to few billions cells are now commonly performed to simulate realistic systems in complex geometries. However, the analysis of the large amount of data produced by these simulations requires new tools and processing formalisms. As previously mentioned, the classical LES formalism implies a scale separation as the largest scales are resolved while the smallest scales are modeled. This scale separation based on the filtering of the Navier-Stokes equations introduces sub-filter terms that have to be modeled through sub-grid scale (SGS) closures. This filtering results in combined numerical and modeling errors, which both depend on the grid resolution. Their dissociation and segregation is therefore very difficult to achieve. Moreover, as LES tends to DNS - meaning that all the range of turbulent scales are resolved -, the influence of the SGS modeling error becomes negligible while numerical errors decrease. Hence, the mesh convergence appears to be the major issue for numerical simulations. Therefore, it is mandatory to attempt to evaluate the grid quality of the LES computation through several criteria that enable to determine if the grid has to be locally refined or coarsened. Indeed, such indicator would enable to perform LES for complex geometries with adequate and optimized meshes that limit the computational cost of the simulation while guaranteeing the validity of the SGS closures.

From the literature, several studies attempted to characterize the LES accuracy through the uncertainties quantification of the numerical and modeling errors and their combination [188, 28]. Other methods based on the evaluation of the integral length scale [2] or on the Kolmogorov scale [70] from RANS simulations are interesting but strongly depend on the accuracy of the model. Klein et al. [108, 66] proposed a strategy that attempts to evaluate the error contributions with a systematic grid and to model variations through the assumption that numerical and modeling errors scale as a power of the grid spacing. Also, Celik et al. [30, 29] rigorously consider the numerical and modeling errors thanks to the Index of Quality LES_{IQ}. However, this criterion appears to be very expensive and not very suitable to unstructured grids. Moreover, several criteria have been developed only based on one LES computation. These interesting quantities that can be considered are the SGS and molecular viscosity ratio [30], the ratio between the modeled and molecular dissipation [73] or the two points correlations [51]. Bénard et al. [16] proposed two different criteria to assess the quality of the mesh and to adapt it locally. The first criterion minimizes the discretization of the gradient of the mean part of the LES resolved field, whereas the second one ensures explicit resolution of the turbulent scales based on the Pope criterion on the turbulent kinetic energy which considers that the LES is well-resolved when the ratio between the resolved and the total kinetic energy is at least 80%. Daviller et al. [52] have devised a quality criterion based on the kinetic energy dissipation in order to improve the evaluation of pressure losses in aeronautical injection systems. More recently, Toosi et al. [193] derived a mesh quality criterion for anisotropic grid adaptation dedicated to LES. This criterion enables to improve the mesh in wall-bounded flows. Moreover, Alauzet developed optimal mesh adaptation criteria by running several times the same simulations [68].

Hierarchical methods that embed simulations at different resolution levels, also known as multi-resolution mapping methods, have been designed to significantly increase the data access speed. Here, the same idea in the context of Large-Eddy simulations is developed. Indeed, simultaneously performing

LES on several levels of grid with some synchronization process may bring interesting information about the local numerical and modeling errors. This principle is in some sense similar to Germano's model [72], who proposed a dynamic sub-grid scale (SGS) model that enables to dynamically parametrize the coefficient of the eddy viscosity sub-grid-scale stress model. Indeed, this idea is based on a scale similarity between two LES resolutions. While the finest mesh resolution is used to discretize the Navier-Stokes equations, the second one refers to a coarser test filter used to calibrate the SGS model.

Relying on this multi-scale principle, this chapter presents the Multi-Resolution LES (MR-LES) framework that proposes to perform simultaneous LES in parallel to locally measure both modeling and numerical errors. From these error measurements, a grid quality criterion can therefore be built and used to dynamically adapt the mesh during the simulation. This methodology enables to generate adequate and optimized meshes for well-refined LES in complex geometries and thus intents to limit the computational cost of the simulations while minimizing the SGS modeling errors. Hence, this chapter first attempts to define the different errors when comparing several LES at different grid resolutions. Then, the different steps of the MR-LES framework are presented in detail. Once it has been introduced, a parametric analysis of the main parameters of the MR-LES framework is provided using an Homogeneous Isotropic Turbulence configuration driven by a linear forcing term. Finally, the application of the MR-LES framework is validated on a 3D turbulent cylinder configuration with the generation of an optimized mesh through several applications of mesh adaptation algorithms.

6.2 Multi-Resolution LES framework

6.2.1 Error quantification from simultaneous LES at different resolutions

First of all, the proposed framework is based on performing simultaneously several LES at different scales and then to compare their computed fields so that to access to local divergence information. Hence, it is mandatory to estimate and quantify the errors produced by the discretization process on the grid, called numerical errors, and those coming from the SGS models, denoted as modeling errors.

The discretization of a continuous variable ϕ onto two LES grids, M_1 for LES_1 and M_2 for LES_2 associated to their local cell sizes Δx_{M_1} and Δx_{M_2} respectively, leads to the discrete variables $\overline{\phi}^{d_1}_{M_1}$ and $\overline{\phi}^{d_2}_{M_2}$. These variables refer to discrete representations of the filtered LES variables and may thus be written as

$$\begin{aligned} \overline{\phi}^{d_1}_{M_1} &= \overline{\phi}_{M_1} + \Delta x^{p_1}_{M_1} + \mathcal{O}(\Delta x^{p_1+1}_{M_1}) \\ \overline{\phi}^{d_2}_{M_2} &= \overline{\phi}_{M_2} + \Delta x^{p_2}_{M_2} + \mathcal{O}(\Delta x^{p_2+1}_{M_2})\,, \end{aligned} \tag{6.1}$$

where $\overline{\phi}_{M_2}$ and $\overline{\phi}_{M_2}$ are the continuous filtered LES representation of the variable ϕ for LES_1 and LES_2 associated to the LES filter sizes $\Delta_1 \approx \Delta x_{M_1}$ and $\Delta_2 \approx \Delta x_{M_2}$. Their respective exponents p_1 and p_2, that have to be determined, correspond both to the truncation and modeling errors.

Considering an interpolation operator noted $\mathcal{I}$, the transfer of $\overline{\phi}^{d_1}_{M_1}$ from M_1 to M_2 leads to the following quantity $\overline{\phi}^{d_2}_{M_1 \to M_2}$ and can thus be defined as

$$
\begin{aligned}
\overline{\phi}^{d_2}_{M_1 \to M_2} &= \mathcal{I}_{M_1 \to M_2}\left[\overline{\phi}^{d_1}_{M_1}\right] \\
&= \overline{\phi}^{d_1}_{M_1} + \epsilon_{\mathcal{I}} \, ,
\end{aligned}
\tag{6.2}
$$

with $\epsilon_{\mathcal{I}}$ the error due to the transfer from M_1 to M_2 with the Interpolant $\mathcal{I}$.

If the interpolation process is applied through the previously presented MGHOF framework, the interpolation error $\epsilon_{\mathcal{I}}$ can therefore be written as

$$
\epsilon_{\mathcal{I}} = \epsilon_{MGHOF} = \Delta x_{M_2}^{p_{inter}} + \mathcal{O}(\Delta x_{M_2}^{(p_{inter}+1)}) + \epsilon_{\mathcal{F}}(2p, \alpha) \, . \tag{6.3}
$$

This error can be decomposed into two parts: First the filtering error noted $\epsilon_{\mathcal{F}}$, depending on the filter parameters $2p$ and α, and second the interpolation error that depends on the cell size of the LES grid M_2 at power p_{inter} referring to the order of the chosen methodology.

Finally, the difference between the discretized computed field on M_2 and the interpolated field from M_1 to M_2 can thus be expressed in terms of errors:

$$
\begin{aligned}
\overline{\phi}^{d_2}_{M_2} - \overline{\phi}^{d_2}_{M_1 \to M_2} &= \overline{\phi}_{M_2} + \Delta x_{M_2}^{p_2} + \mathcal{O}(\Delta x_{M_2}^{p_2+1}) - \left(\overline{\phi}_{M_1} + \Delta x_{M_1}^{p_1} + \mathcal{O}(\Delta x_{M_1}^{p_1+1}) + \epsilon_{\mathcal{I}}\right) \\
&= \left(\overline{\phi}_{M_2} - \overline{\phi}_{M_1}\right) + \left(\Delta x_{M_2}^{p_2} + \mathcal{O}(\Delta x_{M_2}^{p_2+1}) - \Delta x_{M_1}^{p_1} - \mathcal{O}(\Delta x_{M_1}^{p_1+1})\right) + \epsilon_{\mathcal{I}} \\
&= \epsilon_{\text{modeling}} + \epsilon_{\text{numerical}} + \epsilon_{\mathcal{I}} \, .
\end{aligned}
\tag{6.4}
$$

Assuming that the error due to the transfer from M_1 to M_2 is negligible compared to the numerical and modeling errors, especially when using higher-order interpolation techniques, and assuming both LES exponents being equal such as $p_1 = p_2 = p$, the previous expression can be approximated at order p as

$$
\begin{aligned}
\overline{\phi}^{d_2}_{M_2} - \overline{\phi}^{d_2}_{M_1 \to M_2} &\approx \left(\overline{\phi}_{M_2} - \overline{\phi}_{M_1}\right) + \left(\Delta x_{M_2}^{p} - \Delta x_{M_1}^{p}\right) \\
&\approx \epsilon_{\text{modeling}} + \epsilon_{\text{numerical}} \, .
\end{aligned}
\tag{6.5}
$$

This measure can be very useful when attempting to locally optimize the mesh quality. Indeed, it may give access to relevant information while aiming at refining the grid where the smallest scales are located and coarsening it in other areas, leading to significantly improvements to the reliability of the simulation at a limited CPU cost. Moreover, the comparison of the LES computed fields at different resolutions may also give information concerning the mesh convergence. The following section will further develop this notion through the presentation of the Multi-Resolution LES (MR-LES) framework.

6.2.2 Presentation of the MR-LES framework

For convenient reason, the MR-LES framework is presented here by only considering two LES that run at the same time on different levels of grid. It is noticeable that these grids do not necessarily possess the same mesh partitioning for the same number of processors and parallel environment. Considering a refined LES noted LES_1 and a coarse one LES_2, the two associated grids M_1 and M_2 are characterized by their local cell sizes Δx_{M_1} and Δx_{M_2}, respectively. Here, the refined LES_1 is considered as being the reference one and thus its grid M_1 has to be optimized. Moreover, if M_1 is obtained through one level of homogeneous refinement from M_2, it is noticeable that adding the LES_2 computation - which contains 8 times less elements than LES_1 - will only increase the CPU cost of the simulation by a factor $\frac{1}{16}$. The entire procedure of the MR-LES framework is depicted in Fig 6.1 and is detailed hereafter.

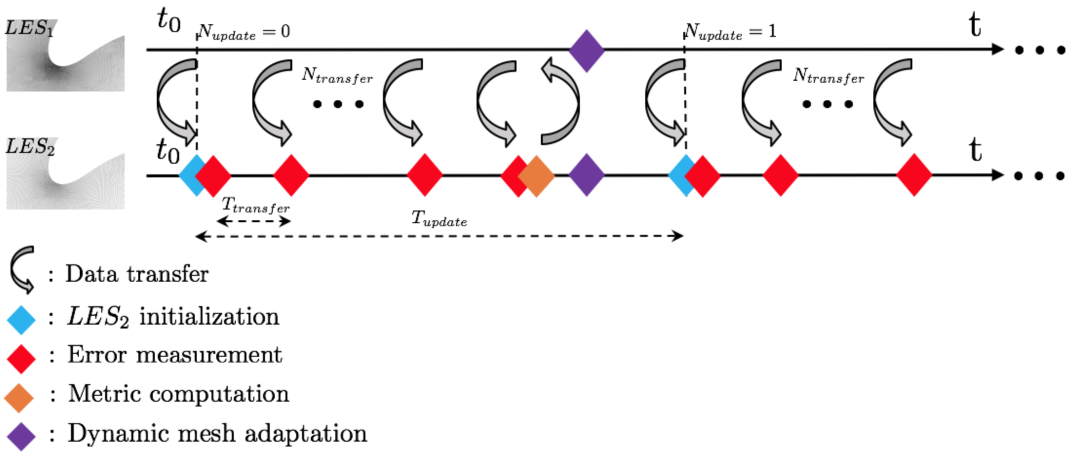

FIGURE 6.1: Sketch of the MR-LES framework algorithm

Velocity field interpolation from the refined LES to the coarse one and building of the error criterion : The first step of the MR-LES framework deals with the interpolation of the velocity field computed on the refined LES_1 onto the coarse LES_2. This operation is based on the previously presented MGHOF framework that combines both high-order filters and a high-order interpolation method. These data exchanges from M_1 to M_2 can thus be summarized as follows :

$$\overline{\mathbf{u}}_{M_1\rightarrow M_2}(t,\mathbf{x}) = \mathcal{I}_{M_1\rightarrow M_2}\left[\mathcal{F}[\mathbf{u}_{M_1}(t,\mathbf{x})]^{2p}_{\alpha}\right] . \tag{6.6}$$

The first time this operation is performed, the velocity field of the coarse LES on M_2, noted $\mathbf{u}_{M_2}$, has to be initialized using this interpolated field such as :

$$\mathbf{u}_{M_2}(t,\mathbf{x}) = \overline{\mathbf{u}}_{M_1\rightarrow M_2}(t,\mathbf{x}) . \tag{6.7}$$

Then, the instantaneous velocity error on M_2, noted $\epsilon_{M_2}(t,\mathbf{x})$, can be built by taking the difference between the velocity field computed on the coarse grid M_2 and the interpolated velocity field coming from the refined one M_1 as

$$\epsilon_{M_2}(t,\mathbf{x}) = |\mathbf{u}_{M_2}(t,\mathbf{x}) - \overline{\mathbf{u}}_{M_1\rightarrow M_2}(t,\mathbf{x})| . \tag{6.8}$$

This interpolation step from M_1 to M_2 followed by the computation of the velocity error is applied several times with a constant time sampling noted $\Delta T_{transfer}$. Then, the error fields $\epsilon_{M_2}(t_k,\mathbf{x})$ for $k \in [1, N_{transfer}]$ are time averaged on M_2 in order to build the mean velocity error defined as :

$$\begin{aligned}\langle\epsilon_{M_2}\rangle_t(\mathbf{x}) &= \frac{1}{T_{transfer}}\sum_{k=1}^{N_{transfer}}\Delta T_{transfer}\epsilon_{M_2}(t_k,\mathbf{x})\\ &= \frac{1}{N_{transfer}}\sum_{k=1}^{N_{transfer}}\epsilon_{M_2}(t_k,\mathbf{x})\,.\end{aligned} \tag{6.9}$$

However, in order to avoid that the coarse LES on M_2 diverges too much from the refined one on M_1, the velocity field on M_2 has to be regularly restarted with another interpolated field coming from LES_1 as previously mentioned with $\mathbf{u}_{M_2} = \overline{\mathbf{u}}_{M_1\to M_2}$. The divergence between the two computations LES_1 and LES_2 through $\langle\epsilon_{M_2}\rangle_t$ is due to the accumulation of both numerical and modeling errors and has to be avoided. Therefore, the update of the coarse LES_2 has to be regularly applied. Hence, the average of all these errors $\langle\epsilon_{M_2}\rangle_t$ enables to compute on M_2 the global mesh quality criterion Qc_{M_2} as:

$$Qc_{M_2}(\mathbf{x}) = \frac{1}{N_{update}}\sum_{k=1}^{N_{update}}\langle\epsilon_{M_2}\rangle_{t_k}(\mathbf{x})\,. \tag{6.10}$$

Finally, the computation of the grid quality criterion Qc_{M_2} requires the application of the MR-LES framework $N = N_{transfer}N_{update}$ times leading to a total time sampling defined as $\Delta T_{MR-LES} = N\Delta T_{transfer}$.

Building of the refinement ratio and of the metric on the coarse LES: As the previous criterion is not fully determined - it possesses an intrinsic degree of freedom through an adjustable parameter referring as the error level -, it therefore needs an additional adjustable parameter to close its intrinsic degree of freedom, namely the error level. This error level has to be constant in the whole computational domain for realistic LES in order to keep an acceptable cell count. The adaptation strategy developed by Bénard et al [16], that enables to control the cell count variation, has been applied on the previously defined Qc grid quality criterion. This formalism allows to evaluate the velocity divergence on the adapted mesh, here of LES_2 noted $Qc_{M_2,a}$, through the computation of Qc on the initial mesh, noted $Qc_{M_2,i}$, thanks to Eq 6.10. This strategy is briefly summarized hereafter:

Considering an isotropic LES mesh with a constant local mesh size Δx, the number of nodes in a volume V can thus be defined as $N = \rho V$ with ρ the local node density. Moreover, the control volume around a node can approximatively be expressed as $\gamma\Delta x^3$ with $\gamma = 1.15$ a constant that refers to the dual volume ratio between a tetrahedron and a cube. The total node number can thus be expressed as $N = V/(\gamma\Delta x^3)$ leading to the local node count density defined as $\rho = 1/(\gamma\Delta x^3)$.

On the initial computational domain $\mathcal{D}$, the total number of nodes noted N_i may be estimated by integrating the initial node count density ρ_i over the whole domain as

$$N_i = \int_{\mathcal{D}}\rho_i dV\,. \tag{6.11}$$

Concerning the number of nodes of the adapted mesh, noted N_a, it may be estimated by using the node count density of the initial mesh ρ_i through the introduction of the local refinement ratio τ defined as the cell size ratio between the initial and adapted meshes $\tau = \Delta x_i/\Delta x_a$:

$$N_a = \int_{\mathcal{D}} \rho_a dV = \int_{\mathcal{D}} \tau^3 \rho_i dV \,. \tag{6.12}$$

Moreover, the node number ratio between the adapted and the initial mesh can thus be expressed as follows:

$$\frac{N_a}{N_i} = \left(\int_{\mathcal{D}} \tau^3 \rho_i dV\right) \left(\int_{\mathcal{D}} \rho_i\right)^{-1} \tag{6.13}$$

$$= \left(\int_{\mathcal{D}} \frac{\tau^3}{\Delta x_i^3} dV\right) \left(\int_{\mathcal{D}} \frac{1}{\Delta x_i^3} dV\right)^{-1} \,. \tag{6.14}$$

Considering the grid quality criterion Qc that aims at homogenizing the averaged velocity error, the local refinement ratio τ may be written as

$$\tau(\mathbf{x}) = \sqrt{Qc_i(\mathbf{x})/Qc_a} \,, \tag{6.15}$$

with Qc_i and Qc_a the evaluation of the velocity divergence on the initial and adapted meshes respectively. The node number ratio can therefore be written as

$$\frac{N_a}{N_i} = \left(\int_{\mathcal{D}} \frac{Qc_i^{3/2}}{\Delta_i^3 Qc_a^{3/2}} dV\right) \left(\int_{\mathcal{D}} \frac{1}{\Delta x_i^3} dV\right)^{-1} \,. \tag{6.16}$$

As the homogeneity of the global velocity error is obtained for a constant value of Qc_a over the full computational domain for a fixed node count ratio N_a/N_i, the quantity $Qc_{M_2,a}$ can be expressed as follows:

$$Qc_a = \left(\frac{N_a}{N_i}\right)^{-\frac{2}{3}} \left(\int_{\mathcal{D}} \frac{Qc_i^{3/2}}{\Delta x_i^3} dV\right)^{2/3} \left(\int_{\mathcal{D}} \frac{1}{\Delta x_i^3} dV\right)^{-2/3} \,. \tag{6.17}$$

However, the mesh adaptation library is a volume algorithm and implicitly necessitates an unity refinement ratio on the boundaries. Therefore, the computed refinement ratio τ differs from the target one. Moreover, it has also to guarantee an additional global constraint referring to the total node count of the adapted mesh such as $N_A \approx N_i$ even if the the initial isotropic mesh assumption is not fulfilled. Therefore, the computation of the local refinement ratio τ is achieved through an iterative process as it needs to be adjusted over the whole computational domain to satisfy these constraints. A rescaling coefficient is then iteratively computed from Eq. 6.14 and is expressed as follows:

$$\alpha = \left(\frac{N_a}{N_i}\right)^{-1} \left(\int_{\mathcal{D}} \frac{\tau^3}{\Delta x_i^3} dV\right) \left(\int_{\mathcal{D}} \frac{1}{\Delta x_i^3} dV\right)^{-1} \,. \tag{6.18}$$

This coefficient enables to link two successive refinement ratio during the iterative method as $\alpha = (\tau_{n+1}/\tau_n)^3$ that converges towards unity. An error tolerance of 1% on the node count is imposed for this configuration.

Moreover, the calculation of the local refinement ratio may imply drastic changes in the local cell size that may be too stringent for the mesh adaptation algorithms. Hence, it has been rescaled in order not to change the size of an edge more than a certain threshold in $\%$ of his initial length, leading to a range of refinement values of $[\tau_{min} = 1/\tau_{max}, \tau_{max}]$. This transform operation still guaranties the conservation of the number of elements obtained by the iterative method.

As this procedure is applied for the coarse LES on M_2, the new target local cell size of the grid $\Delta x_{M_2,a}$ can therefore be expressed as

$$\Delta x_{M_2,a} = \Delta x_{M_2,i} \tau_{M_2} \, . \tag{6.19}$$

Interpolation of the refinement ratio from the coarse LES to the refined one and building of the metric on the refined LES: After being computed on the coarse grid M_2, the refinement ratio τ_{M_2} has to be transferred onto the refined grid M_1 in order to build the new target local cell size $\Delta x_{M_1,a}$ in a similar manner. These operations can be summarized as follows:

$$\overline{\tau}_{M_2 \to M_1} = \mathcal{I}_{M_2 \to M_1} \left[\mathcal{F}[\tau_{M_2}]_{\alpha}^{2p} \right] \tag{6.20}$$

$$\Delta x_{M_1,a} = \Delta x_{M_1,i} \overline{\tau}_{M_2 \to M_1} \, . \tag{6.21}$$

Application of the dynamic grid adaptation on both LES: Once the local target cell sizes, $\Delta x_{M_2,a}$ and $\Delta x_{M_1,a}$ respectively, have been computed on the coarse and refined LES, the mesh adaptation can be applied on both LES levels. Moreover, as these refinement ratios are quite similar, the meshes can be adapted keeping a constant local mesh size ratio before and after the mesh adaptation as

$$\frac{\Delta x_{M_2,i}}{\Delta x_{M_1,i}} \approx \frac{\Delta x_{M_2,a}}{\Delta x_{M_1,a}} \, . \tag{6.22}$$

This property enables to compare, as the time increases, the evolution of the computed error level, and therefore to try to minimize it through successive mesh adaptations.

Finally, the mesh adaptation module used in the YALES2 library is based on the MMG3D library [58, 50], which is a sequential anisotropic mesh adaptation for tetrahedral elements. This module relies on local mesh modifications such as edge flipping, edge collapsing, node relocation, and vertex insertion driven by isotropic or anisotropic metric specifications. The entire procedure of the MR-LES framework can be found in Fig 6.2.

6.3 Parametric study to the numerical and modeling errors

The previously presented MR-LES framework possesses several parameters that have to be tuned in order to build a relevant grid quality criterion. First, one of them refers to the frequency of transfers between the two LES and is characterized by the time sampling period $\Delta T_{transfer}$. Moreover, another characteristic time scale of interest is the frequency of the updates of the coarse LES with new fields

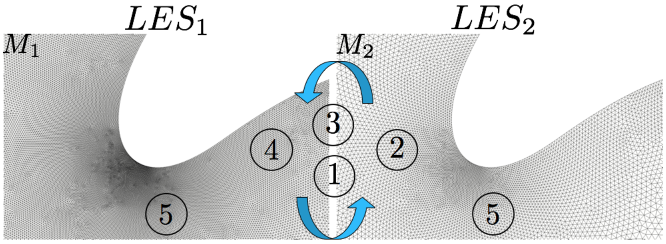

① $N\times$ 1.1 Interpolate the velocity from M_1 to M_2

$$\overline{\mathbf{u}}_{M_1\to M_2} = \mathcal{I}_{M_1\to M_2}\left[\mathcal{F}[\mathbf{u}_{M_1}]_{\alpha}^{2p}\right]$$

1.2 Computation of the local velocity error on M_2

$$\epsilon_{M_2}(t,\mathbf{x}) = |\mathbf{u}(t,\mathbf{x})_{M_2} - \overline{\mathbf{u}}_{M_1\to M_2}(t,\mathbf{x})|$$

② Build the refinement ratio and the target cell size on M_2

$$\epsilon_{M_2}(t,\mathbf{x}) \to \langle\epsilon\rangle_{M_2}(\mathbf{x}) \to Qc_{M_2,i}(\mathbf{x}) \to \tau_{M_2}$$

$$\Delta x_{M_2,a} \propto \Delta x_{M_2,i} \times \tau_{M_2}$$

③ Interpolate the refinement ratio from M_2 to M_1

$$\overline{\tau}_{M_2\to M_1} = \mathcal{I}_{M_2\to M_1}\left[\mathcal{F}[\tau_{M_2}]_{\alpha}^{2p}\right]$$

④ Build target cell size on M_1

$$\Delta x_{M_1,a} \propto \Delta x_{M_1,i} \times \overline{\tau}_{M_2\to M_1}$$

⑤ Dynamic mesh adaptation on both solvers

FIGURE 6.2: MR-LES framework for the cell size optimization

coming from the refined one, previously noted $\Delta T_{update} = N_{transfer}\Delta T_{transfer}$. Thanks to this expression, it can be driven through $N_{transfer}$ that refers to the number of transfers between the LES before update. Finally, the local cell grid ratio between the two LES is considered as being the last main parameter of the MR-LES framework. Indeed, it is mandatory to use adequate meshes in order to compare the computed fields on both levels. For instance, if the secondary LES is too coarse, it can therefore not represent in a sufficiently manner the flow dynamics and thus lead to a grid quality metric Qc that can not be exploited.

6.3.1 Initialization with HIT

As these MR-LES main parameters are very difficult to define a priori, this section presents a parametric study to the numerical and modeling errors. First, an 256^3 homogeneous isotropic turbulence is generated on the reference LES_1, with a Cartesian grid M_1 from the synthetic energy spectrum of Pope [157]. Here, the l_0 and l_d spatial scales refer to the energetic and Taylor length scales, respectively. However, the reference simulation LES_1 has to be well-resolved in order to minimize modeling errors. Hence, the following set of HIT parameters has been chosen in order to resolve almost all turbulent scales leading to consider this reference LES_1 as a DNS rather than a LES. The HIT model constants β, C_e and C_{η_K} are presented in Tab. 6.1 and the relevant physical properties of the turbulent flow in Tab. 6.2.

The energetic length l_0 has been imposed to $l_0 = 2.296 \times 10^{-3}\,\mathrm{m}$ in order to guarantee an integral scale l_t equal to $l_t = 1.25 \times 10^{-3}\,\mathrm{m}$ through the relation $\frac{l_t}{l_0} = \left(\frac{2}{3}\right)^{3/2}$. Indeed, the characteristic length of the computational domain L has to contain a sufficient number of the integral scale for realistic statistical convergence. Moreover, the DNS approach imposes the Kolmogorov scale to be close to the cell size of the grid defined as $\Delta x_{M_1} = 3.9 \times 10^{-5}\,\mathrm{m}$. Therefore it has been set to $\eta_K = 2.0 \times 10^{-5}\,\mathrm{m}$ which leads to the Taylor scale l_d, corresponding to the most dissipative structures, of $l_d = 3.074 \times 10^{-4}\,\mathrm{m}$ through the following expression $l_d \approx \sqrt{10\nu\frac{k_t}{\epsilon}}$.

Energetic length [m]	l_0	2.296×10^{-3}
Dissipation length [m]	l_d	3.074×10^{-4}
Kinematic viscosity [m^2/s]	ν	1.517×10^{-5}
	β	5.2
Model constants	C_e	$\sqrt{6.78}$
	C_{η_K}	0.4

TABLE 6.1: HIT parameters for the Pope synthetic spectrum

Number of grid points	N	256^3
Computational domain size [m]	L	1.0×10^{-2}
Grid resolution L/N [m]	Δx	3.9×10^{-5}
Integral length [m]	l_t	1.25×10^{-3}
Kolmogorov scale [m]	η_K	2.0×10^{-5}
Number of integral scales	L/l_t	8
Turbulent Reynolds number	Re_t	247.97
Taylor Reynolds number	Re_λ	60.99
Kinematic viscosity [m^2/s]	ν	1.517×10^{-5}
Turbulent kinetic energy [$\mathrm{m}^2/\mathrm{s}^2$]	K	13.59
Turbulent dissipation rate [$\mathrm{m}^2/\mathrm{s}^3$]	ϵ	21819

TABLE 6.2: Characteristics of the HIT flow

6.3.2 Introduction to linear forcing

As turbulent scales are dissipated due to viscous effects, it is thus necessary to apply a linear forcing source term noted $\mathbf{f}$ in the momentum balance equation in order to set some of the turbulence properties and then to maintain the vortices production. This imposed volume force is based on the return to the mean velocity field as Schlüter et al. [173] used, which prevents the flow from diverging by adding a source term. A complete overview of the linear forcing volume methods can be found in Laage thesis [54]. Neglecting the body forces, the momentum balance equation can therefore be written as

$$\frac{\partial \mathbf{u}}{\partial t} + \nabla \cdot (\mathbf{u} \otimes \mathbf{u}) = \nabla \cdot (\boldsymbol{\sigma}) + \mathbf{f}\,, \tag{6.23}$$

with

$$\mathbf{f} = A(\mathbf{u} - \langle \mathbf{u} \rangle_{\mathbf{x}})\,, \tag{6.24}$$

and where $\langle . \rangle_{\mathbf{x}}$ refers to the spatial average operator defined as $\langle . \rangle_{\mathbf{x}} = \frac{1}{V} \int .dV$. Moreover, Eq. 6.24 directly refers to the isotropic linear forcing method of Lundgren [132] developed for isotropic turbulent flows in equilibrium. The A parameter is defined as follows:

$$A = \frac{\epsilon}{3u_t^2}\,, \tag{6.25}$$

where u_t refers to the characteristic velocity at the integral scale l_t and is defined as $u_t = \sqrt{\frac{1}{3}\mathbf{u}'\mathbf{u}'}$.

Turbulent Reynolds number	Re_t	247.97
Integral scale [m]	l_t	1.25×10^{-3}
Kinematic viscosity [m^2/s]	ν	1.517×10^{-5}

TABLE 6.3: Input parameters of the linear forcing process

Recalling the previous turbulent expressions $Re_t = \frac{l_t u_t}{\nu}$ and $l_t = \frac{u_t^3}{\epsilon}$, it is then straightforward to expressed the A parameter as follows:

$$A = \frac{\nu Re_t}{3 l_t^2} \,. \tag{6.26}$$

However, one of the major property of homogeneous isotropic turbulence is that the spatial integrated velocity mean field $\langle \mathbf{u} \rangle_{\mathbf{x}}$ is almost equal to zero and thus negligible in front of the instantaneous velocity field $\langle \mathbf{u} \rangle_{\mathbf{x}} \simeq 0 << \mathbf{u}$. As a consequence, the linear forcing term can be approximated as $\mathbf{f} = A(\mathbf{u} - \langle \mathbf{u} \rangle_{\mathbf{x}}) \approx A\mathbf{u}$.

Hence, using the Reynolds averaging decomposition noted $\mathbf{u} = \langle \mathbf{u} \rangle + \mathbf{u}'$ and the averaged turbulent kinetic balance equation, Lundgren [132] expressed this equation with the linear forcing term as:

$$\frac{\partial \langle k_t \rangle}{\partial t} = -\epsilon + 2A\langle k_t \rangle \,, \tag{6.27}$$

with the $\langle k_t \rangle = \frac{1}{2}\langle \mathbf{u}'\mathbf{u}' \rangle$ the statistical averaged turbulent kinetic energy and ϵ the turbulent dissipation rate that is defined as $\epsilon = \nu \langle \frac{\partial u_i'}{\partial x_l} \frac{\partial u_i'}{\partial x_l} \rangle$. It can be noticed that for homogeneous flows, the statistical averaged turbulent kinetic energy $\langle k_t \rangle$ is equivalent through ergodicity assumption to the time averaged of the global turbulent kinetic energy noted K as

$$K = \langle \langle k_t \rangle_{\mathbf{x}} \rangle_t \equiv \langle \langle k_t \rangle_{\mathbf{x}} \rangle \equiv \langle k_t \rangle \quad \text{with} \quad \begin{cases} \langle k_t \rangle_{\mathbf{x}} & = \frac{1}{V} \int k_t dV \\ \langle k_t \rangle_t & = \frac{1}{T} \int_T k_t dt \end{cases} \,. \tag{6.28}$$

Finally, Eq. 6.27 shows that for stationary HIT flows, the variation of the global kinetic energy is zero which leads to an equation that directly links the dissipation to the linear forcing term. Hence, as a source of kinetic energy, the forcing term contributes to maintain the turbulent characteristics of the flow. The dissipation rate can thus be written as follows:

$$\epsilon = 2A\langle k_t \rangle \,. \tag{6.29}$$

Hence, the choice of the linear forcing input parameters have to be in agreement with the previously initialized HIT field. Indeed, using the previous expression of the linear forcing coefficient A, expressed as a function of the turbulent Reynolds number Re_t and the integral scale l_t and kinematic viscosity ν, it has been set to $A = 802.5\,\mathrm{s}^{-1}$. This imposed linear forcing input parameters can be found in Tab. 6.3

Moreover, this turbulent forced flow has to be converged before applying the MR-LES framework. This has been done by simulating $0.05\,\mathrm{s}$ of physical time which correspond to around 80 times the characteristic turn-over time scale of the turbulence. On the one hand, Fig. 6.3 (left) represents the spatial averaged of the turbulent kinetic energy on the computational domain $\langle k_t \rangle_{\mathbf{x}}$ with its temporal average noted as $K \equiv \langle \langle k_t \rangle_{\mathbf{x}} \rangle_t = 29.56\,\mathrm{s}^{-1}$ for the statistical steady state of the flow $t \in [0.015; 0.05]\,\mathrm{s}$. On the other hand, Fig. 6.3 (right) deals with the averaged energy $\mathcal{E}$ and dissipation spectra $\mathcal{D}$ of the flow. These spectra have been computed by averaging the instantaneous spectra each time step $\Delta T = 5.0 \times 10^{-4}\,\mathrm{s}$ for $t \in [0.015; 0.05]\,\mathrm{s}$.

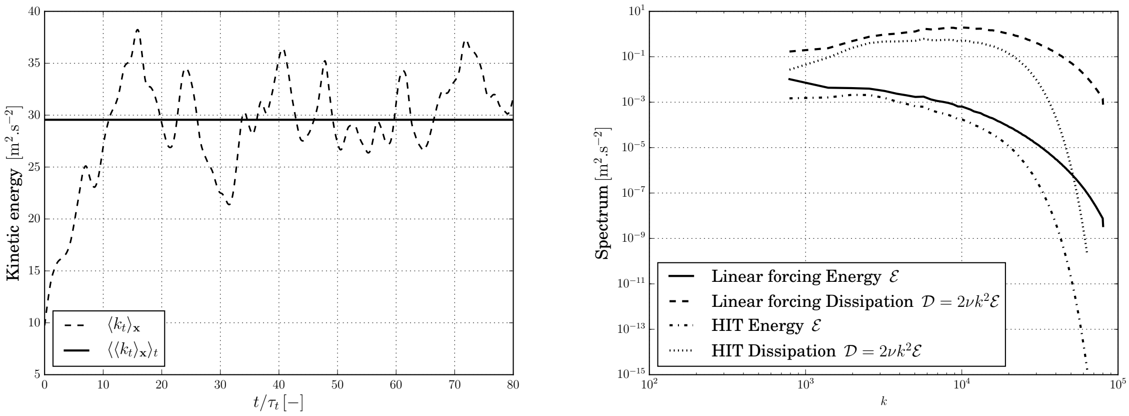

FIGURE 6.3: Characteristics of the converged linearly forced flow with the kinetic energy (left) and the time averaged energy and dissipation spectra (right)

Thus, the characteristics of the converged linearly forced turbulent flow can be computed thanks to the averaged energetic spectrum and the averaged turbulent kinetic energy. First of all, the characteristic integral velocity scale can be deducted from the average turbulent kinetic energy as $K = \frac{3}{2}u_t^2$ leading to $u_t = 4.44\,\mathrm{m.s}^{-1}$. Moreover, this can be validated by considering the following relations of Batchelor [10] for the HIT flows:

$$\frac{3}{2}u_t^2 = \int_0^\infty \mathcal{E}(k,t)dk\,, \tag{6.30}$$

and

$$l_t = \frac{\pi}{2u_t^2}\int_0^\infty \frac{\mathcal{E}(k,t)}{k}dk\,. \tag{6.31}$$

Thanks to the numerical integration method of the energy spectrum, the integral scale is computed to $l_t = 1.318 \times 10^{-3}\,\mathrm{m}$ and the integral velocity scale to $u_t = 4.03\,\mathrm{m.s}^{-1}$. The difference with the previous value comes from the finite temporal discretization of the energy spectrum averaging process.

Once, these variables have been computed, it is straightforward to access to the entire characteristics of the turbulence thanks to the following usual relations:

$$Re_t = \frac{l_t u_t}{\nu},\ \epsilon = 2\langle k_t \rangle A,\ l_0 = l_t\left(\frac{3}{2}\right)^{2/3},\ l_d = \sqrt{\frac{10\nu\langle k_t \rangle}{\epsilon}},\ \eta_K = \left(\frac{\nu^3}{\epsilon}\right)^{1/4} \text{ and } \tau_t = \frac{\langle k_t \rangle}{\epsilon}\,, \tag{6.32}$$

where τ_t refers to the turnover time scale of the integral length. These flow characteristics are summarized in Tab. 6.4.

Linear forcing constant [s^{-1}]	A	802.5
Turbulent kinetic energy [$\mathrm{m}^2/\mathrm{s}^2$]	K	29.56
Integral velocity scale [$\mathrm{m/s}$]	u_t	4.44
Turbulent Reynolds number [-]	Re_t	294.3
Dissipation rate [$\mathrm{m}^2/\mathrm{s}^3$]	ϵ	47438
Largest scale [m]	l_0	1.318×10^{-3}
Integral length [m]	l_t	1.006×10^{-3}
Taylor length [m]	l_d	3.074×10^{-4}
Kolmogorov length [m]	η_K	1.647×10^{-5}
Integral turnover scales [s]	τ_t	6.231×10^{-4}

TABLE 6.4: Characteristics of the linear forcing

Finally, Fig. 6.4 presents the instantaneous velocity field (left) and iso-surface of the Q-criterion colored by the velocity magnitude (right) of the considered HIT.

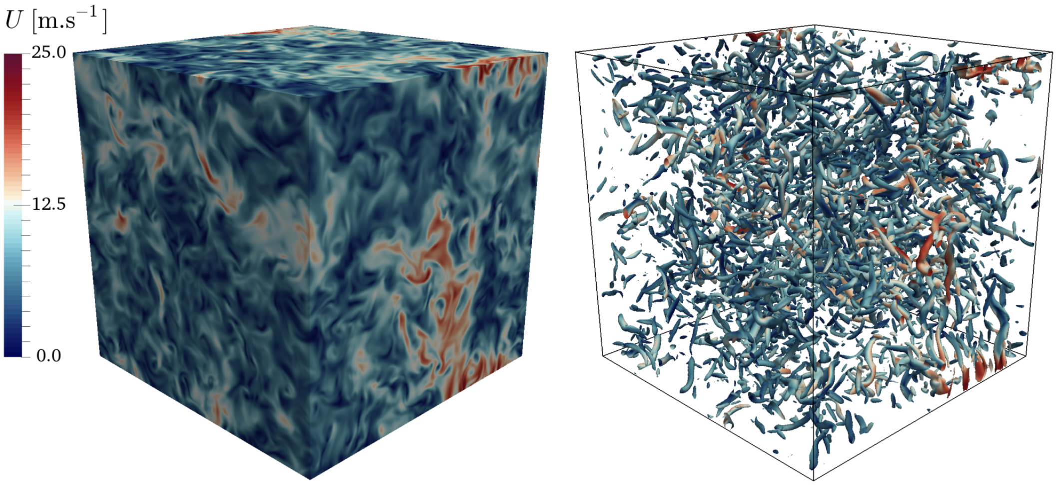

FIGURE 6.4: Instantaneous velocity field (left) and Q-criterion colored by the velocity magnitude of the resulting turbulent flow with the linear forcing source term

6.3.3 Error quantification

At this point, the well-resolved LES_1 is converged and can thus be used for the parametric study of the MR-LES framework. Considering another LES, noted LES_2, on a coarse Cartesian grid M_2 with 64^3, 128^3 or 192^3 elements, the error quantification can be performed through the comparison of computed fields from both LES levels and to measure their divergence. It should be noticed that the same governing equations have to be solved on the two levels to have meaningful comparison. Thus, the linear forcing term also has to be applied with the same previous parameters on the coarse LES_2 in order to guarantee the same flows characteristics on both grid-levels.

Once again, the MR-LES formalism implies that the flow configuration simultaneously runs on both LES grid-levels which communicate through velocity field transfers from the reference LES_1 to the coarse LES_2. Selecting the optimal set of user-dependent parameters $(T_{transfer}, N_{transfer}, \Delta_{x_{M_2}})$ enables to access to a relevant error measurement Qc that characterizes the differences due to their respective spatial discretizations. From these main parameters, several dimensionless numbers can be defined as follows:

- $\frac{T_{update}}{\tau_t}$ as the ratio between the update frequency and the turnover time scale of the most energetic features in the flow also known as the integral length scale. Indeed, the frequency at which the coarse LES is updated $T_{update} = N_{Transfer}T_{transfer}$ has to be carefully chosen. On the one hand, if this frequency is small compared to the integral turnover time scale τ_t, the update will often be applied compared to the characteristic time scale of turbulence leading to a very high CPU cost of the methodology. On the other hand, based on the Shannon-Nyquist sampling theorem, if this frequency is much higher, the interpolation and numerical errors are dominant in the measurement ϵ_{M_2}. Hence, the metric can no longer be applied in order to adapt the grids as it does not spatially represent the modeling errors anymore.
- $\frac{l_t}{\Delta x_{M_2}}$ as the ratio between the integral scale and the local mesh size of the coarse grid M_2. Indeed, the coarse LES has to be fine enough in order to be able to accurately represent the integral length scale of the flow. Then, the local mesh size Δx_{M_2} has to be small enough compared to the integral scale in order to discretize well these structures. However, if Δx_{M_2} tends to the local mesh size of the refined LES, running LES_2 therefore costs as much as the refined LES_1, which leads to very high cost for the proposed methodology. A trade-off between the CPU cost and a sufficient resolution of the coarse LES has to be handled.
- $\alpha = \frac{\Delta x_{M_2}}{\Delta x_{M_1}}$ as the ratio between the local mesh size of the coarse grid M_2 and the refined one M_1. It enables to characterize the level of coarsening for the second LES. If this ratio is close to unity, the cost of simultaneous LES doubles, whereas it becomes negligible as this ratio increases. However, as the coarse LES has to be fine enough to be able to correctly represent the most energetic structures of the flow, this ratio has to be very close to unity. Similarly to the previous dimensionless number, a trade-off between the CPU cost and spatial resolution has to be handled.

Finally, in order to quantify these errors, a kinetic energy based on spatial averaged of the error $\langle\epsilon_{M_2}\rangle_t(\mathbf{x})$ defined in Eq. 6.8 is considered and defined as

$$\langle k_{\langle\epsilon_{M_2}\rangle_t}\rangle_{\mathbf{x}} = \langle\frac{1}{2}\langle\epsilon_{M_2}\rangle_t^2\rangle_{\mathbf{x}} = \frac{1}{V}\sum_{k=1}^{N_{node}}\frac{1}{2}\langle\epsilon_{M_2}\rangle_t^2(\mathbf{x})V_k\,, \tag{6.33}$$

where N_{node} refers in that case to the total number of node of a M_2 grid.

The next sub-section presents the results of the parametric analysis on the 3D Homogeneous Isotropic turbulence configuration.

6.3.4 Results

This parametric study has been performed by considering several set of parameters $(T_{transfer}, N_{transfer})$ associated to various levels of grid resolution for the coarse LES_2. The different ranges of the parameter values can be found in Tab. 6.5 presented hereafter:

First, remarks can be formulated just by taking a look at the ratio between the local cell size of both LES grids, and comparing them with the integral scale of the linearly forced turbulent flow. From Tab. 6.6,

$\mathbf{LES_2}$ **resolution**	$\mathbf{N_{transfer}}$	$\mathbf{T_{transfer}/\tau_t}$
$[64^3, 128^3, 192^3]$	$[1-5]$	$[0.001-0.16]$

TABLE 6.5: Range of the parametric study parameters

it can be noticed that both 192^3 and 128^3 meshes of LES_2 seem to be sufficiently refined in order to accurately represent the integral length scale. This enables to guarantee that these features are well captured with approximately 20 and 13 points per direction in each structure, respectively. However, the 64^3 grid of LES_2 seems to have an insufficient spatial discretization that may not allow to correctly represent the integral length scale with only 6 points per direction within this characteristic scale. This analysis will be further developed with quantified results on the error measurement for various set of parameters.

$\mathbf{LES_2}$ **resolution**	$\mathbf{l_t/\Delta x_{M_2}}$	$\boldsymbol{\alpha} = \mathbf{\Delta x_{M_2}/\Delta x_{M_1}}$
192^3	19.84	1.33
128^3	12.90	2
64^3	6.45	4

TABLE 6.6: Characteristic length scale analysis

As the integral scale corresponds to the most energetic structures in the flow, the influence of the local cell size ratio between the two LES, $\alpha = \Delta x_{M_2}/\Delta x_{M_1}$, may be determined by analyzing its impact on the turbulent kinetic energy while applying the MR-LES framework. Indeed, Fig. 6.5 presents the evolution of the spatial average of the instantaneous turbulent kinetic energy $\langle k_t \rangle_\mathbf{x}$ on both LES levels with different mesh discretizations for LES_2. Here, the MR-LES framework has been applied with the following parameters $N_{transfer} = 1$, $T_{transfer} = 1.0 \times 10^{-4}\,\mathrm{s} \approx 0.16\tau_\mathrm{t}$ and $N_{update} = 5$ without mesh adaptation activation but with only velocity field transfers from the refined LES_1 to the coarse LES_2. Hence, it can clearly be noticed that these interpolations produce discontinuities in the kinetic balance equation on the coarse LES. These discontinuities are due to the imposed velocity field that does not correspond to a physical Navier-Stokes solution on the discretized grid of the coarse LES. Also, the coarser the mesh of the LES_2 is, the more pronounced is the discontinuity. For both curves, the spatial average of the turbulent kinetic energy $\langle k_t \rangle_\mathbf{x}$ is lower than the one on the reference LES_1 as some small scales motions have been removed through both filtering and interpolation steps.

From Fig.6.5, each discontinuity on the turbulent kinetic energy is followed by a strong damping effect resulting from the introduction of high frequencies at the cut-off of the grid due to the imperfect filtering procedure. Hence, it is interesting to characterize this damping effect by a characteristic time scale. In order to achieve this, the integral of the energy spectrum defined as $E(t) = \int_0^{+\infty} \mathcal{E}(k,t)dk$ is introduced and its temporal evolution for the refined LES_2 is expressed as follows:

$$\frac{\mathrm{d}E(t)}{\mathrm{dt}} = \int_0^{+\infty} \frac{\partial \mathcal{E}(k,t)}{\partial t} dk = \int_0^{+\infty} \mathcal{P}(k,t)dk - \int_0^{+\infty} \frac{\partial}{\partial k}\mathcal{T}(k,t)dk - 2\nu \int_0^{+\infty} k^2 \mathcal{E}(k,t)dk\,. \quad (6.34)$$

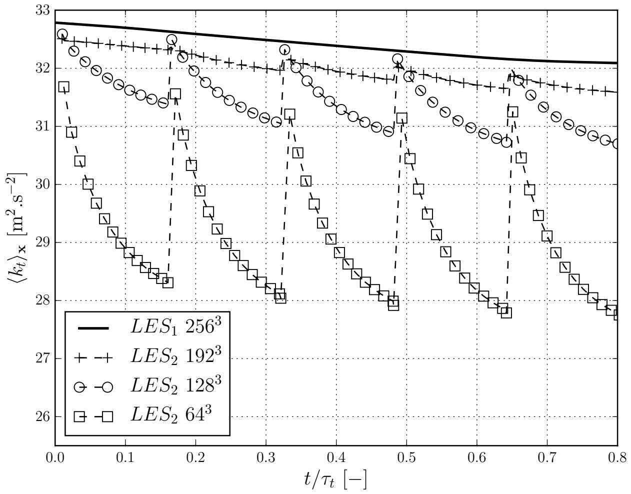

FIGURE 6.5: Evolution of the spatially averaged turbulent kinetic energy on both LES level

However, when the coarse LES_2 is updated by imposing a velocity field, the temporal evolution of the integral of the energy spectrum differs from Eq. 6.34. In that case, an supplementary term defined as $\delta E(t) = \int_0^{+\infty} \delta\mathcal{E}(k,t)dk$ is added to the previous equation. This perturbation refers to the damping term $P(t)$ that is added on the right hand side of Eq. 6.34 leading to the evolution of the perturbed integral energy spectrum on LES_2 defined as

$$\frac{\mathrm{d}}{\mathrm{dt}}\left[E(t) + \delta E(t)\right] = \int_0^{+\infty} \mathcal{P}(k,t)dk - \int_0^{+\infty} \frac{\partial}{\partial k}\mathcal{T}(k,t)dk - 2\nu \int_0^{+\infty} k^2\mathcal{E}(k,t)dk + P(t)\,. \quad (6.35)$$

Under the assumption that this damping term can be modeled through a diffusive effect, the evolution of the perturbation $\delta E(t)$ can therefore be written as follows:

$$\frac{\mathrm{d}\delta E(t)}{\mathrm{dt}} = P(t) = -2(\nu + \nu_t)\int_0^{+\infty} k^2 \delta\mathcal{E}(k,t)dk\,, \quad (6.36)$$

with ν the viscosity of the fluid and ν_t the one due to the turbulent model.

As this perturbation comes from high frequencies at the cut-off of the grid - filters cannot perfectly perform the scale separation before interpolating -, the energetic distribution $\delta\mathcal{E}(k,t)$ of $\delta E(t)$ in the Fourier space can be modeled as a Dirac function located at the cut-off frequency of the LES_2 and defined through its wavenumber $k_{c,M_2} = \pi/\Delta x_{M_2}$. Hence, the previous equation can be simplified as

$$\begin{aligned}\frac{\mathrm{d}\delta E(t)}{\mathrm{dt}} &\approx -2(\nu + \nu_t)\frac{\pi^2}{\Delta x_{M_2}^2}\int_0^{+\infty} \delta\mathcal{E}(k,t)dk\,, \\ &\approx -2(\nu + \nu_t)\frac{\pi^2}{\Delta x_{M_2}^2}\delta E(t)\,.\end{aligned} \quad (6.37)$$

Finally, solving the previous differential equation enables to expressed $\delta E(t)$ through an exponential solution such as

$$\frac{1}{\delta E(t)}\frac{\mathrm{d}\delta E(t)}{\mathrm{dt}} = -2(\nu+\nu_t)\frac{\pi^2}{\Delta x_{M_2}^2}\,, \tag{6.38}$$

where $\tau_{\delta E} = \left[2(\nu+\nu_t)\frac{\pi^2}{\Delta x_{M_2}^2}\right]^{-1}$ is the characteristic time scale of the damping.

As Tab. 6.7 shows the characteristic times $\tau_{\delta E}$ that correspond to the exponential damping after each update of LES_2. It may be seen as a time scale which dissipates the excess energy at the cutoff frequency that has not been damped by the filtering process and thus as a relaxation time to return to an equilibrium state. It is noticeable that it depends on the discretization of the coarse LES. Indeed, as the energy at the cutoff frequency depends on the local cell size, the more refined the LES_2 is, the smaller are the characteristic time scales. These estimated time scales are comparable to those observed in Fig. 6.5 even if the estimation is very crude. Indeed, the response after the update of the turbulence model or of the non-linear terms in the filtered Navier-Stokes equation prevents having a more precise estimate.

LES$_2$ resolution	$\boldsymbol{\tau_{\delta E}}\ [s]$	$\boldsymbol{\tau_{\delta E}/\tau_t}\ [-]$
192^3	6.83×10^{-6}	1.10×10^{-2}
128^3	1.13×10^{-5}	1.81×10^{-2}
64^3	1.68×10^{-5}	2.70×10^{-2}

TABLE 6.7: Characteristic time scales of the exponential decreases in the kinetic energy

The numerical schemes and the turbulence models are thus impacted by this time discontinuity and therefore need some relaxation time in order to return to an TKE equilibrium state. In Fig. 6.6, one step of the MR-LES transfer from LES_1 to LES_2 has been applied at $t = 0$ in order to characterize the return to the equilibrium of the spatial average of the turbulent kinetic energy. Here, it is noticeable that the energetic content of the flow is more impacted when LES_2 gets coarser, due to more pronounced perturbations. The coarse 192^3 LES_2 seems to be relatively unaffected by the imposed velocity field and rapidly gets to its equilibrium state before the effects of the divergence begin to be visible for $t/\tau > 3$. However, even for long time values, the evolution of the averaged kinematic energy is still coherent with the reference one of LES_1. For the 128^3 LES_2, the same remarks can still be formulated with higher perturbations level but the behavior of the curves differs for $t/\tau > 4.5$ and can not be compared anymore. Finally, concerning the coarsest LES_2 with 64^3 elements, here the perturbations are so high that even for short values t/τ, the averaged kinematic energy is totally different compared to the reference flow.

Then, after these few remarks concerning the impact of the update on the kinetic energy, here are presented the results of the sensitive study. Figs. 6.7, 6.8 presents the evolution of the error $\langle k_{\langle\epsilon_{M_2}\rangle_t}\rangle_{\mathbf{x}}$ during the MR-LES applications from LES_1 with 256^3 elements to LES_2 with 192^3 elements. In that case, the local cell sizes on both level are relatively similar which supposes a strong correlation between computed solution fields.

On the one hand, Fig. 6.7 shows the evolution of the error $\langle k_{\langle\epsilon_{M_2}\rangle_t}\rangle_{\mathbf{x}}$ as a function of the time transfer $T_{transfer}$ for different values of transfer number $N_{transfer}$ before updating the LES_2. It is noticeable that the curves have different behaviors depending on the range of values of $T_{transfer}/\tau$. First, for time

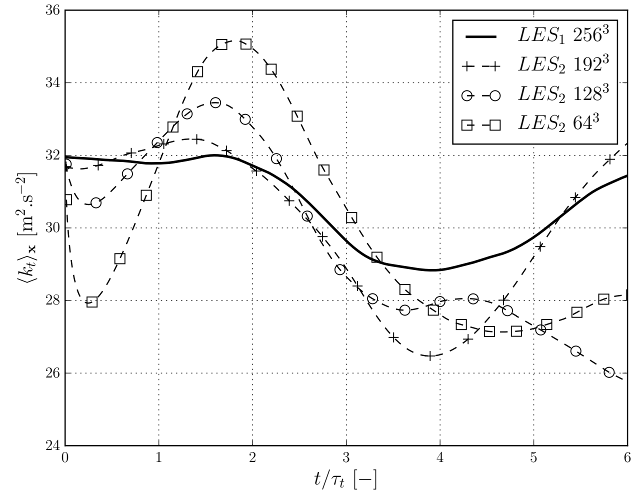

FIGURE 6.6: Off-equilibrium of the average kinetic energy on both LES level

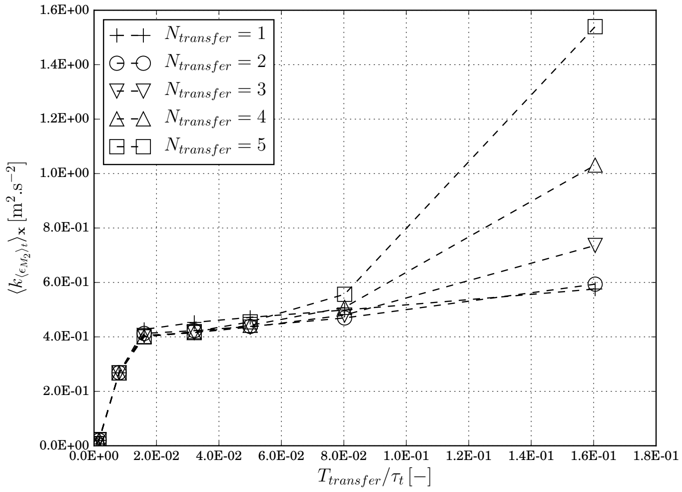

FIGURE 6.7: Measure of the divergence between LES_1 and LES_2 with 192^3 elements with several MR-LES parameters

transfer values defined as $T_{transfer}/\tau > 0.02$, the error $\langle k_{\langle\epsilon_{M_2}\rangle_t}\rangle_{\mathbf{x}}$ growths up as $T_{transfer}$ increases whatever the value of $N_{transfer}$ is. This phenomenon is due to the accumulation of both numerical and modeling errors that make the two computed solutions diverge on both LES levels. Moreover, considering the range of time transfer values with $T_{transfer}/\tau < 0.02$, all curves increase until a certain local maximum before becoming negligible compared to the exponential divergence. Hence, this increase of the error corresponds to an off-equilibrium state that develops after the interpolated field from the reference LES_1 is imposed on the coarse LES_2. Indeed, as previously mentioned, the kinetic balance equation is not guarantied as the imposed velocity field is not a realization in LES_2 as it is disturbed by high frequencies that cannot be resolved on M_2. The coarse LES_2 needs some relaxation time in order to return to an energy equilibrium state, removing some high frequencies that may be produced through the grid transfer. On the other hand, Fig. 6.8 shows the same results as a function of the update

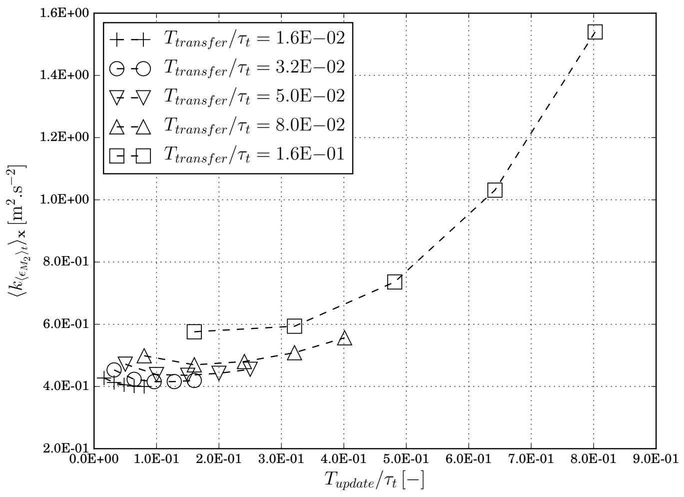

FIGURE 6.8: Measure of the divergence between LES_1 and LES_2 with 192^3 elements with several MR-LES parameters

time between the two LES, $T_{update} = N_{transfer}T_{transfer}$, which enables to represent the evolution of the error. For convenient reasons error measurements corresponding to the smallest ratio $T_{transfer}/\tau$ have been removed. Then, the return to the equilibrium state is here highlighted through the decreasing error until a local minimum that is clearly visible for $T_{update}/\tau \approx 0.15$. Finally, the major remark here concerns the optimal set of parameters in order to minimize the error measurement $\langle k_{\langle\epsilon_{M_2}\rangle_t}\rangle_{\mathbf{x}}$. The values of T_{update}/τ close to unity seem to be not relevant as the error exponentially increases, low values seem to be more appropriate.

Similarly, Figs. 6.9, 6.10 present the same error evolution with a grid discretization of 128^3 for the coarse LES_2. This corresponds to a homogeneous coarsening step compared to the 256^3 LES_1. Once again, the behavior of $\langle k_{\langle\epsilon_{M_2}\rangle_t}\rangle_{\mathbf{x}}$ can be split into two parts as Fig. 6.9 shows. As previously mentioned, the first increase of the error refers to the TKE off-equilibrium state of LES_2 while imposing the interpolated velocity field from LES_1. After that, for higher value of $T_{transfer}$, the divergence between the two LES occurs and takes precedence over the relaxation to a stabilized equilibrium state. Fig. 6.10 shows the same temporal evolutions as the ones seen previously in Fig. 6.8. Here, the local minimum is located for $T_{update}/\tau \approx 0.07$ but is however less prominent. Again, the characteristic time scale of the flow, referring here as the turnover time of the integral scale, has to be sufficiently discretized in time in order to minimize the error. Finally, it is also noticeable that the minimum of the error is higher compared to the 192^3 LES_2 case and has been shifted to smaller values of T_{update}/τ. These remarks corroborate the previous observations.

Finally, Figs. 6.11, 6.12 presents the evolution of the error $\langle k_{\langle\epsilon_{M_2}\rangle_t}\rangle_{\mathbf{x}}$ from LES_1 with 256^3 elements to a coarse LES_2 with only 64^3 elements that corresponds to two homogeneous coarsening steps. Contrarily to the previous configurations, here Fig. 6.11 shows different behaviors concerning the evolution of the error as the time transfer $T_{transfer}$ increases. In that case, the exponential divergence between the two LES occurs for very short time transfers, which leads to the conclusion that the coarse LES_2 is not able to return to a stabilized equilibrium state before the error strongly increases. This phenomenon

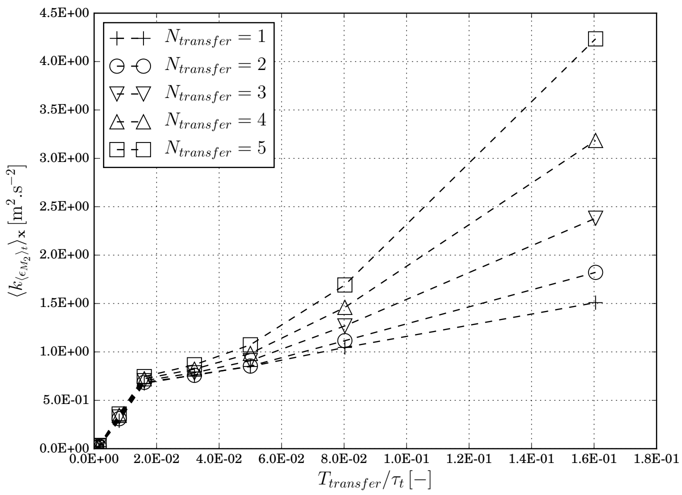

FIGURE 6.9: Measure of the divergence between LES_1 and LES_2 with 128^3 elements with several MR-LES parameters

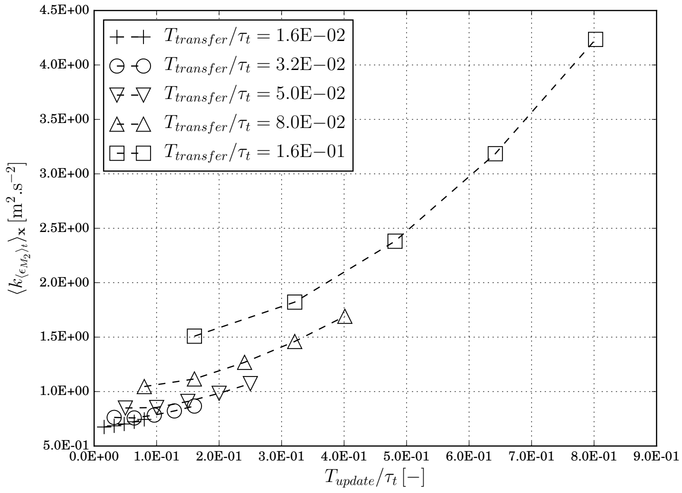

FIGURE 6.10: Measure of the divergence between LES_1 and LES_2 with 128^3 elements with several MR-LES parameters

has already been mentioned for Fig. 6.6 and confirms that 64^3 LES_2 is here too coarse for quantifying numerical and modeling errors before the LES diverge. Hence, as shows Fig. 6.12, no optimal set of parameters can be found in such situation.

These results enable to conclude concerning the evolution of the errors while applying the MR-LES framework and allow to propose a model that is presented hereafter: As Fig. 6.13 illustrates, the evolution of $\langle k_{\langle\epsilon_{M_2}\rangle_t}\rangle_{\mathbf{x}}$ can be decomposed into two parts. The first one deals with an off-equilibrium state due to the instantaneous velocity field coming from LES_1 that is imposed on LES_2. This filtered and interpolated field is not a solution of the filtered Navier-Stokes equations on the grid of the coarse LES_2. Then, this solution does not satisfy locally the TKE equation because of resolved high frequencies at

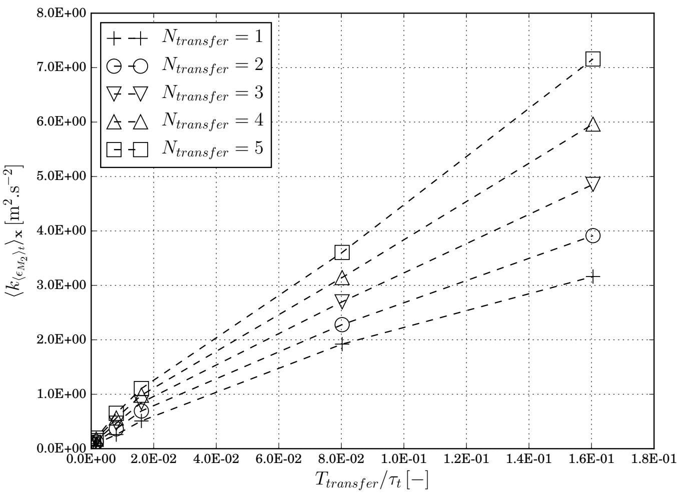

FIGURE 6.11: Measure of the divergence between LES_1 and LES_2 with 64^3 elements with several MR-LES parameters

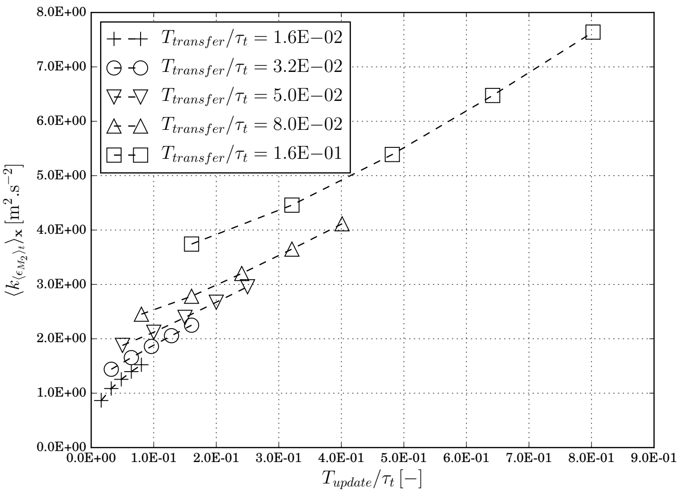

FIGURE 6.12: Measure of the divergence between LES_1 and LES_2 with 64^3 elements with several MR-LES parameters

the cut-off of the grid that have to be dissipated by the numerical scheme or by the fluid viscosity. This off-equilibrium state for the TKE have been previously highlighted in Fig. 6.5 and Fig. 6.6 with discontinuities in the spatial average of the turbulent kinetic energy. This phenomenon is also associated to a relaxation time so that the coarse LES returns to an TKE equilibrium state as Tab. 6.7 showed. The second one deals with the chaotically divergence between the two LES levels that occurs and amplifies as the time increase from an update or synchronization event. Hence, a relevant error quantification for both numerical and modeling error can be seen as a trade-off between the off-equilibrium state of the coarse LES and the exponential divergence between the two-level.

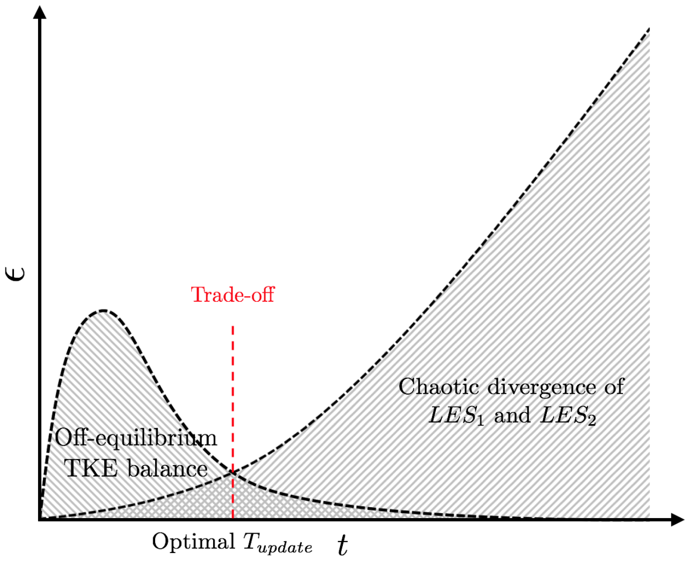

FIGURE 6.13: Analysis of the error evolution as the time between the two LES increases

From the numerical experiments presented before, a good compromise in order to access to a relevant quantification of both numerical and modeling errors is found for update time T_{update} small compared to the characteristic time scale of the most dynamically relevant features in the flow associated to a small local cell size ratio between the LES levels. Decomposing this update time with several transfer $N_{transfer} > 1$ enables to homogenize the error in the off-equilibrium area. Moreover, for cost reason, the cell size ratio α between the grids of both LES has been set to $\alpha = 2$. These rules of thumb enable to guarantee that the divergence between the two levels is not yet dominant and thus to the best possible error measurement between the two grid resolutions.

6.4 MR-LES application to the 3D turbulent cylinder

In this section, the MR-LES framework is applied to the simulation of a turbulent flow around a 3D cylinder in order to validate the methodology on a realistic configuration. It features time-periodic structures called the Bénard-von Karman alleys at the trailing edge of the cylinder. Depending on the Reynolds number, these features may have two or three dimensional behavior. The objective is to build an optimized grid through an objective criterion based on the flow dynamics. Here, the MR-LES framework is combined to mesh adaptation.

6.4.1 Configuration

The computational domain of this configuration is defined with the following dimensions $L_x \times L_y \times L_z = 60d \times 30d \times 5d$ with $d = 1.0 \times 10^{-2}$ m. The behavior of the flow is governed by a single dimensionless parameter which is the Reynolds number based on the cylinder diameter defined as $Re = u_\infty d/\nu$ with u_∞ the characteristic free-stream velocity, d the cylinder diameter and $\nu = 1.517 \times 10^{-5}\,\mathrm{m}^2.\mathrm{s}^{-1}$ the kinematic viscosity of the fluid. This parameter has been set to $10,000$ that approximately leads to a Strouhal number of $St = d/\tau u_\infty \approx 0.2$ as mentioned in [1, 121], where τ refers to the characteristic time scale associated to the coherent feature generation and d/u_∞ to the fluid flow time around the cylinder. Concerning the boundary conditions, a turbulence injection with a fluctuating velocity characteristic scale $u'/u_\infty \approx 0.20$ and the most energetic length-scale $l_e/d = 5$ has been imposed at the inlet. This corresponds to a very high turbulent intensity closed to 20%. Moreover, slip walls and periodic boundary conditions have also been imposed on the y and z plans respectively. A sketch of this configuration can be found in Fig. 6.14.

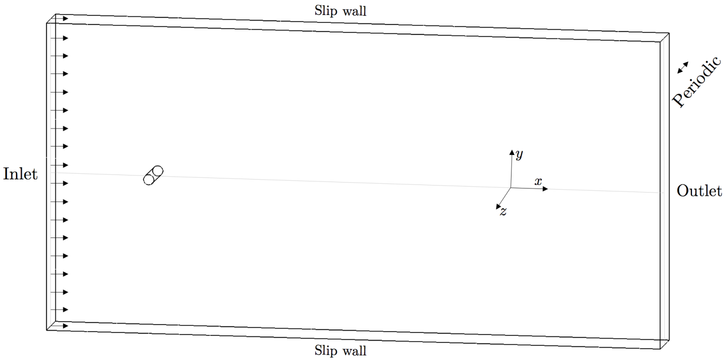

FIGURE 6.14: 3D turbulent cylinder configuration

6.4.2 Parameters of MR-LES

The application of the MR-LES framework necessitates to run simultaneously several LES at different scale resolutions. On the one hand, the coarse LES, noted LES_2, is here associated to the grid M_2 that contains almost 0.5 million elements. The mesh topology of this grid can be found in Fig. 6.15 that presents a slice in the z plane. It is noticeable that this unstructured grid is highly heterogeneous where the smallest elements are located around the cylinder while largest ones are spread out in the rest of the computational domain. This grid has been generated by a commercial meshing software and is very common for such type of geometry. However, as it has not been based on the physical characteristics of the flow, it can therefore certainly be optimized just by moving nodes to relevant areas without adding more elements. On the other hand, the reference or refined LES, noted LES_1, is here associated to the same grid with one level of homogeneous mesh refinement - reducing the edges of the grid M_2 by a factor of two in each direction - that generates the grid M_1 with 4 millions elements.

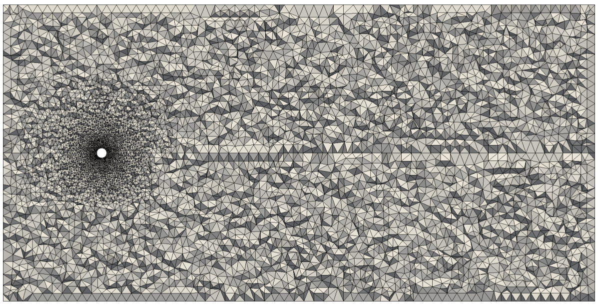

FIGURE 6.15: Crinkle slice in the z plane of the coarse grid M_2^{init}.

Moreover, special attention should be paid to the turbulent injection at the inlet of both LES. Indeed, the MR-LES framework imposes to have exactly the same boundary conditions on each level. This turbulence injection is generated by imposing at the inlet a velocity field plane from a 32^3 HIT box with periodic boundary conditions that moves at the mean flow velocity. The same injection can thus be guaranteed through the application of the same plane for a given moment on both LES levels. Hence, this imposed inlet velocity field is the same on both LES level neglecting the difference due to the interpolation on the inlet boundary condition. Fig. 6.16 presents the magnitude of the instantaneous velocity field computed on the refined LES_1 noted $\mathbf{u}_{M_1}$ (left) and transferred to the coarse LES_2 (right) noted $\mathbf{u}_{M_1 \to M_2}$ with the same imposed turbulent injection at the inlet.

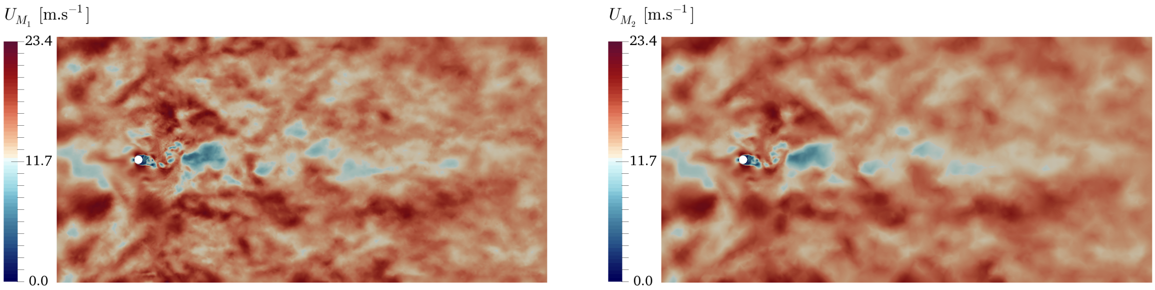

FIGURE 6.16: Instantaneous velocity field on M_1 (left) and interpolated velocity field from LES_1 to LES_2 on M_2 (right) in the z plane of the 3D cylinder case with turbulence injection

As in the previous section for the linearly forced HIT, the MR-LES main parameters have to be chosen carefully by taking into account the characteristic time scale of the flow. Here, an additional characteristic time scale can be introduced as a vortex shedding period, that is more relevant than the turnover time of the integral length scale which is heterogeneous in the computational domain. It can be defined through the definition of the Strouhal number as $\tau = \frac{d}{St.u_\infty} \approx 3.3 \times 10^{-3}$ s. Then, the transfer frequency between the two LES fields has to be small compared to this characteristic time. Moreover, as previously showed in the parametric study, averaging the error before updating the coarse LES - $N_{transfer} > 1$ - enables to homogenize the field. Several updates also need to be applied before applying the mesh adaptation process in order to have a better convergence for the Qc criterion. Finally, the chosen set of parameters can be found in Tab. 6.8.

$\boldsymbol{\alpha}$	$\mathbf{N_{transfer}}$	$\mathbf{T_{transfer}}/\tau$	$\mathbf{N_{update}}$
2	4	0.076	5

TABLE 6.8: Chosen parameters of the MR-LES framework application

The application of the MR-LES framework enables to build the error Qc_{M_2} on the coarse LES_2 that is used in order to compute the local refinement rate τ_{M_2} as previously mentioned. An example of this error can be found in Fig. 6.17. It characterizes the differences between the two instantaneous velocity field on both LES levels with their initial mesh M_1^{ini} and M_2^{ini}. Here, the error is high in the cylinder wake and low in the rest of the computational domain. This field has been directly used to built the objective local cell size and to perform the first mesh adaptation step.

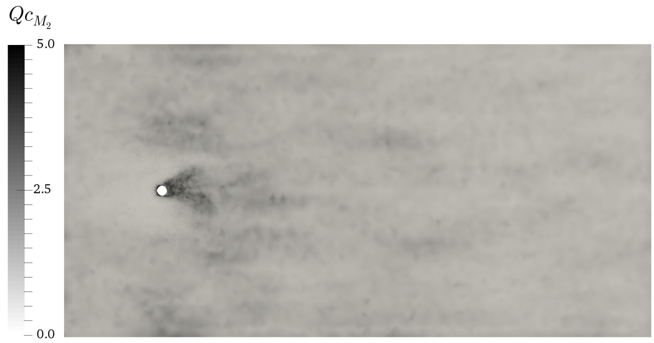

FIGURE 6.17: Qc metric in the z plane computed before the first step of mesh adaptation.

The results of the successive mesh adaptation steps are presented in the next sub-section.

6.4.3 Convergence to an optimized grid

The converge of the MR-LES framework towards an optimized grid with stabilized characteristics has yet to be demonstrated. For this reason, the framework has been applied several times until the adapted mesh metric has been stabilized. Hence, twelve adaptation steps have been performed on both initial meshes M_1^{init} and M_2^{ini} with $3'927'512$ and $490'939$ elements for LES_1 and LES_2, respectively. The characteristics of these twelve adapted meshes are presented in Tab. 6.9 and 6.10. On both grid levels, the conservation of the number of element has been achieved through a threshold constraint set to 1% while applying the mesh adaptation. This constraint has been well respected for the coarse LES_2. However, for the reference LES_1, some differences between the number of elements can be found. Even if these deviations are close to 10% for certain adaptation step, it can be considered as being almost constant without having a significant impact on the ability of the MR-LES framework to optimize the initial grid. These differences come from the mesh adaptation algorithm that has some difficulties to respect the imposed metric due to strong local gradients on the refinement ratio field that introduces errors during the interpolation process of the mesh adaptation.

	M^{adapt_1}	M^{adapt_2}	M^{adapt_3}	M^{adapt_4}	M^{adapt_5}	M^{adapt_6}
Elements $\mathbf{LES_1}$	$4'142'609$	$4'199'983$	$4'361'130$	$4'441'121$	$4'445'060$	$4'452'837$
Elements $\mathbf{LES_2}$	$493'549$	$493'701$	$505'704$	$510'501$	$508'195$	$506'605$

TABLE 6.9: Characteristics of the meshes from adaptation 1 to 6

Furthermore, the convergence of the MR-LES framework can be found in Figs. 6.18, 6.19 that represent the probability density function of the local cell size of the grids of LES_1 and LES_2 through the successive application of mesh adaptation steps. Here, the distribution of the local mesh size converges to

	M^{adapt_7}	M^{adapt_8}	M^{adapt_9}	$M^{adapt_{10}}$	$M^{adapt_{11}}$	$M^{adapt_{12}}$
Elements $\mathbf{LES_1}$	$4'432'940$	$4'412'075$	$4'401'395$	$4'391'917$	$4'376'558$	$4'354'301$
Elements $\mathbf{LES_2}$	$500'838$	$497'824$	$495'033$	$492'723$	$490'795$	$487'745$

TABLE 6.10: Characteristics of the meshes from adaptation 7 to 12

a certain distribution as the number of mesh adaptation steps increases. It is noticeable that the quantity of smallest cells grows up as well as the quantity of the largest cells. Moreover, the extremal values of the local cell size increases as the smallest cells become smaller and the largest ones become larger. As the distribution seems to be almost stabilized for the last mesh adaptation, the MR-LES converges thus to optimal meshes on both LES levels.

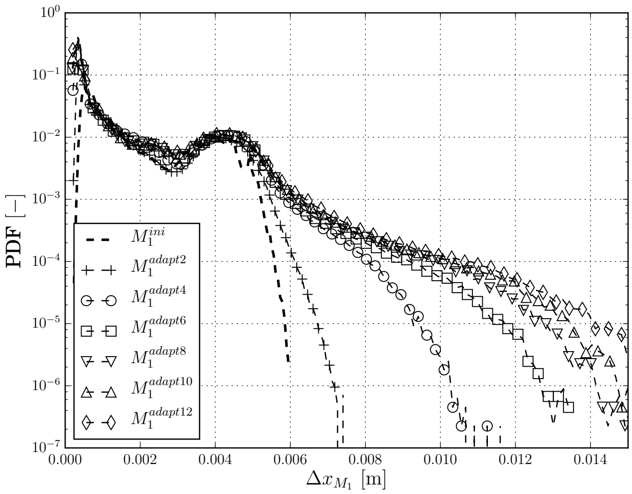

FIGURE 6.18: Probability density function of the local mesh size of the meshes for refined LES_1

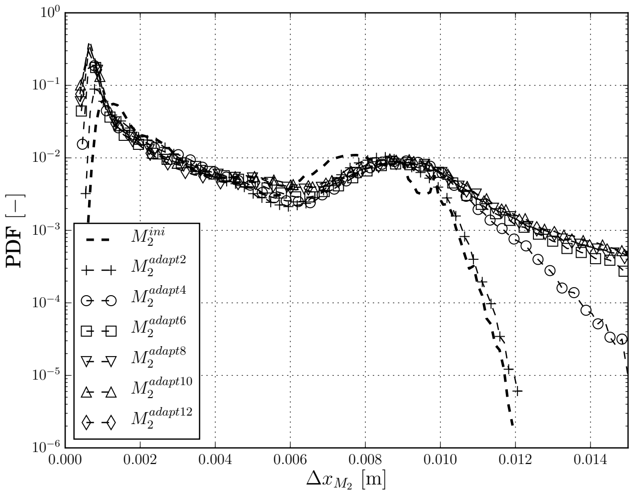

FIGURE 6.19: Probability density function of the local mesh size of the meshes for refined LES_2

6.4.4 Results

All these previously presented mesh adaptation steps have been based on the computation of the error field Qc_{M_2} that has been thereafter used in order to compute the local refinement ratio τ_{M_2}. As this field corresponds to the ratio between the local cell size of the unadapted grid over the adapted one $\tau = \Delta x_i/\Delta x_a$, the target local cell size Δx_a is thus determined and then given as an input to the mesh adaptation algorithm. Furthermore, all these fields enable to characterize and quantify the optimizations applied on the grids, they are presented hereafter in Figs. 6.20, 6.21, 6.22.

First, Fig. 6.20 presents the refinement ratio field associated to mesh adaptation steps $1, 2, 4, 6, 10$ and 12. As expected, this indicator highlights for all steps a high refinement ratio in the wake of the cylinder and a high coarsening rate at the leading edge of the cylinder. The intensity of these processes decrease, with an area that tends to diminish, as the number of applied mesh adaptation grows up. This phenomenon illustrates the convergence of the MR-LES framework. Moreover, other areas of the computational domain are associated to a lower coarsening rate. Furthermore, for the adaptation 1, some spots of high values of refinement ratio can also be identified in the computational domain. As this phenomenon is only visible for the first step of the mesh adaptation, it may be associated to areas where the initial mesh was unadapted and presented some defaults. Finally, it is noticeable that all boundaries are associated to an unitary refinement ratio. This condition has been imposed as the present mesh adaptation algorithm is a volume algorithm and thus do not changes nodes on the boundaries, keeping the ratio $\tau = \Delta x_i/\Delta x_a$ to unity.

Some of the grids generated by the mesh adaptation can be found in Fig. 6.21 that presents optimized meshes associated to adaptation steps $1, 2, 4, 6, 10$ and 12. Here, the evolution of the local cell size is clearly visible with strong coarsening around the cylinder except at the trailing edge and in the wake of the cylinder that concentrates almost the totality of the smallest cells. Also, a positive local mesh size gradient can be shown when the fluid comes closer to the outlet boundary condition. Such local cell size near the outlet may certainly dissipates the smallest scales of the flow. However, this is not important as both injected turbulent structures and vortex shedding of the cylinder have already been dissipated before arriving in this region. Finally, another representation of this local cell size evolution can be highlighted in Fig .6.22.

The quality of the adapted meshes M_1^{adapt} can thus be compared to the quality of the initial one M_1^{ini}. This can be achieved through the comparison of the probability density function of the skewness as Fig. 6.23 shows. Here, the evolution of this function has been plotted for different steps of mesh adaptation. It is noticeable that the initial grid M_1^{ini} - that has been generated by a commercial meshing software - possesses some elements with a poor cell quality that is associated to skewness values higher than 0.8 and 0.95 respectivelly. The maximal value encountered here is about 0.95. However, all adapted meshes possess almost only excellent and good cell quality that correspond to skewness values lower than 0.5 whatever the number of adaptation it concerns. The maximal skewness encountered for these adapted meshes is around 0.6 which is much better compared to the initial mesh.

Once the optimized mesh $M_1^{adapt_{12}}$ has been generated, it is interesting to compare the flow field computed on the initial mesh M_1^{ini} with the one computed on $M_1^{adapt_{12}}$. This comparison is presented in Fig. 6.24 and highlights the effects on the mesh optimization on the flow dynamics captured by the two

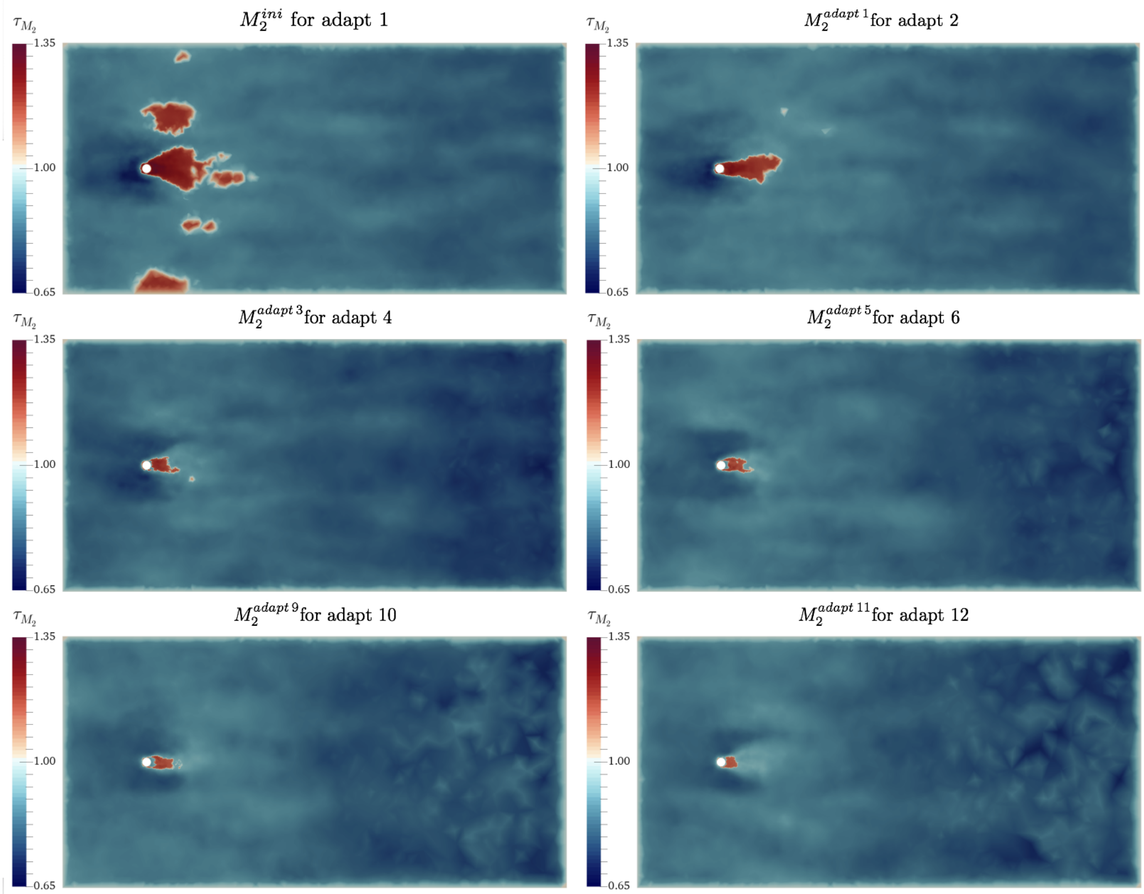

FIGURE 6.20: Several slices in the z plane of the refinement ratio on the coarse LES τ_{M_2} used for the four mesh adaptations

LES. First, both simulations show similar turbulent injection with some slight differences on the smallest scales. However, the dynamics at the trailing edge of the cylinder strongly defers. Moreover, due to the large cell sizes on the optimized mesh near the outlet, the flow is strongly dissipated. Figure 6.25 shows more precisely the difference concerning the interaction between the imposed turbulence injection and the vortex shedding produce by the cylinder. It can be noticed that the adapted grid seems to capture more dynamics and some small structures in the recirculation zone can also be highlighted.

From Fig. 6.26, the mean and root mean square velocity fields computed on M_1^{ini} and $M_1^{adapt_{12}}$ can be compared. These fields appear being highly similar, but it is noticeable that the mean profile in the wake of the cylinder seems to be more stabilized for the optimized grid $M_1^{adapt_{12}}$. Moreover, in the same area, high values of the root mean square field are located in a thiner region compared to M_1^{ini}.

Finally, some consideration has to be furnished concerning the CPU cost while running on this optimized grid. Even if the number of elements is almost constant, the CPU time has been increased by $21.7\,\%$ as the smallest cell size of the optimize grid is smaller than the one on the initial mesh M_1^{ini}. Indeed, the convective time step Δt_{conv} is about 7.47×10^{-6} s on the initial M_1^{ini} grid and about 6.14×10^{-6} s on the $M_1^{adapt_{12}}$.

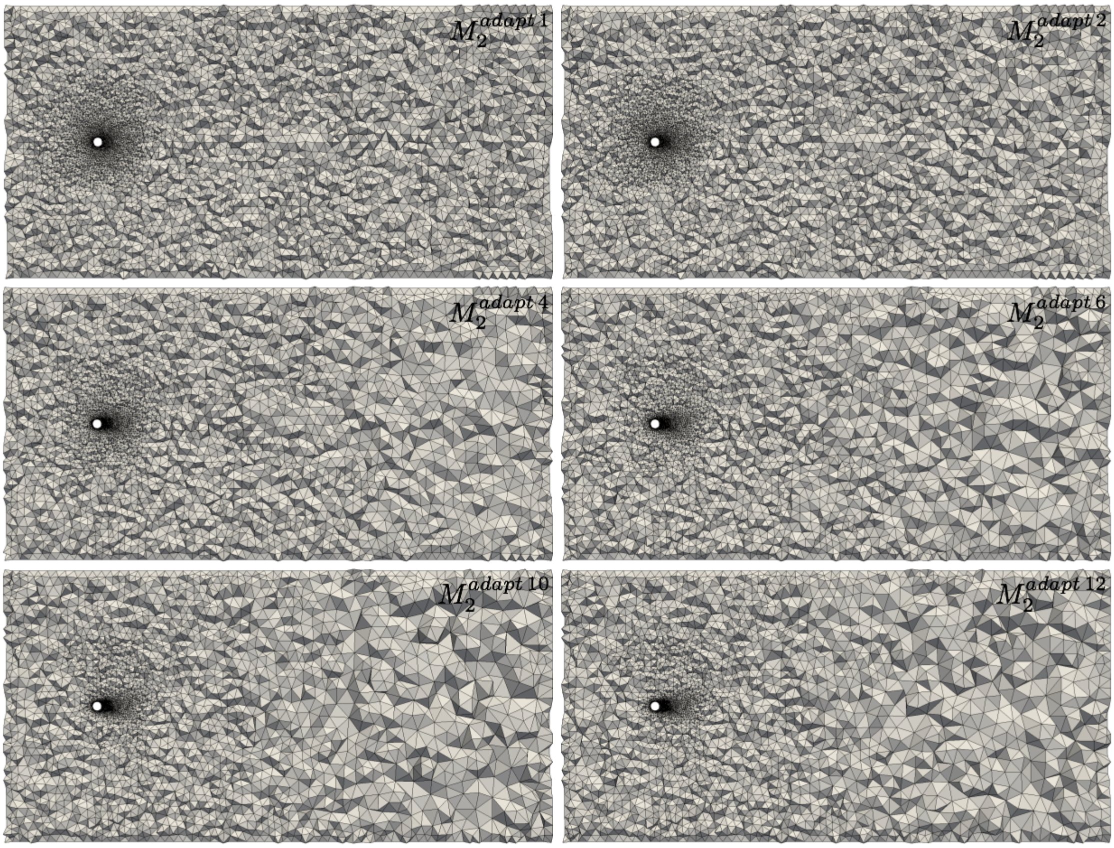

FIGURE 6.21: Several Crinkle slices in the z plane for the four mesh adaptation of the coarse grid M_2

6.5 Conclusions

In this last chapter, the MR-LES framework for processing of LES is proposed. This approach enables to generate optimized grids based on the characteristics of the flow. It uses several LES levels that communicate through transfers of the computed velocity field in order to estimate locally where the LES have to be refined or coarsened. From this error measurement, a metric that refers to a local cell size is built. Then, the application of several steps of mesh adaptation enables to converge to a stabilized and optimized mesh.

The 3D turbulent cylinder has been successfully post-processed thanks to the MR-LES framework application leading to the generation of an optimized grid for this configuration while keeping the number of elements constant. Even if a high turbulent rate has been introduced on the inlet boundary, the framework well reacted by only refining the interesting areas behind the cylinder. The convergence of the methodology has also been highlighted through the stabilization of the probability density function of the local cell size of the adapted meshes. Hence, the converged optimized grid increases the CPU cost of the simulation of $22\,\%$ compared to the initial mesh but enable to capture more physics on the trailing edge of the cylinder and in its wake.

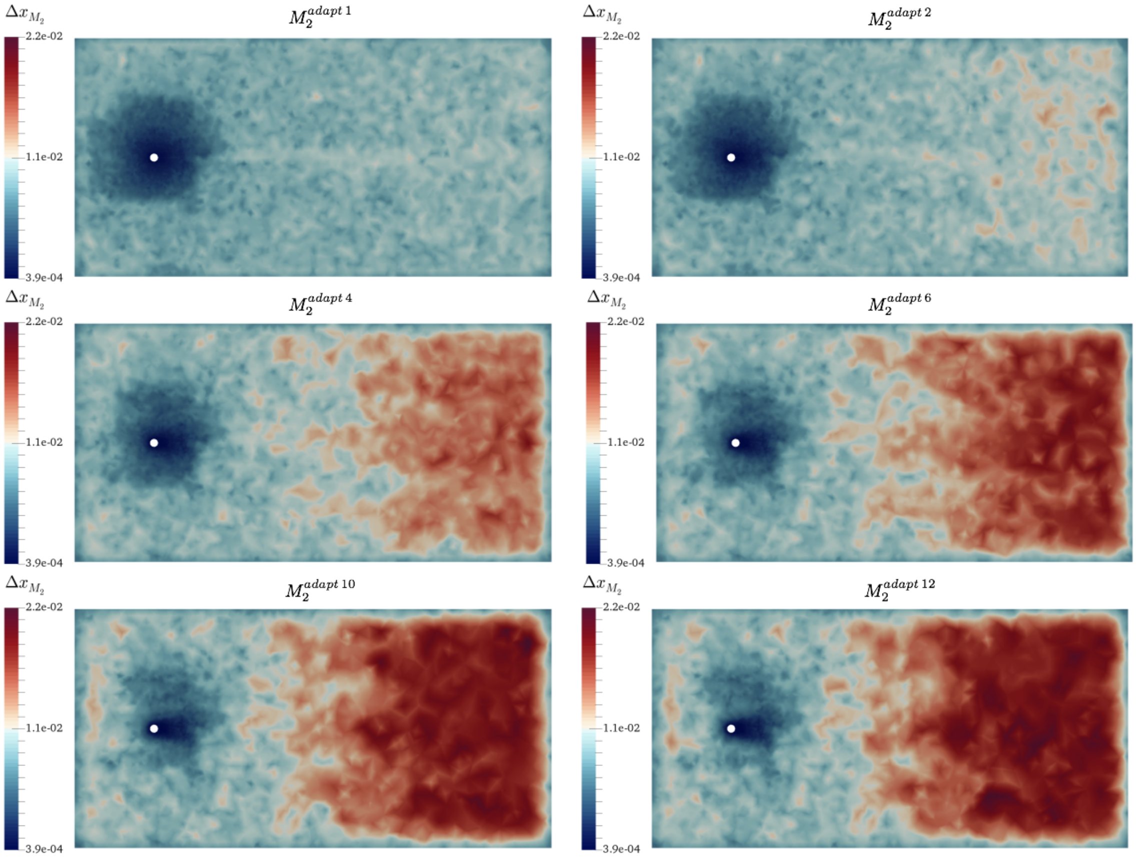

FIGURE 6.22: Slices in the z plane representing the local mesh size on the adapted meshes from the first to the fourth steps of mesh adaptation.

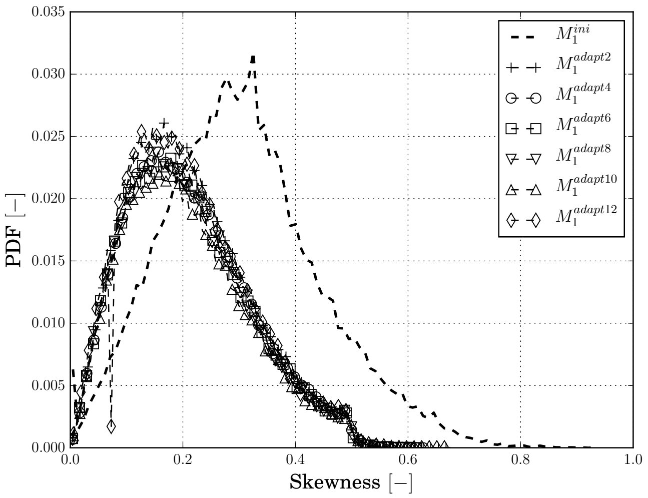

FIGURE 6.23: Probability density function of the skewness for the refined LES_1 through the different mesh adaptation steps.

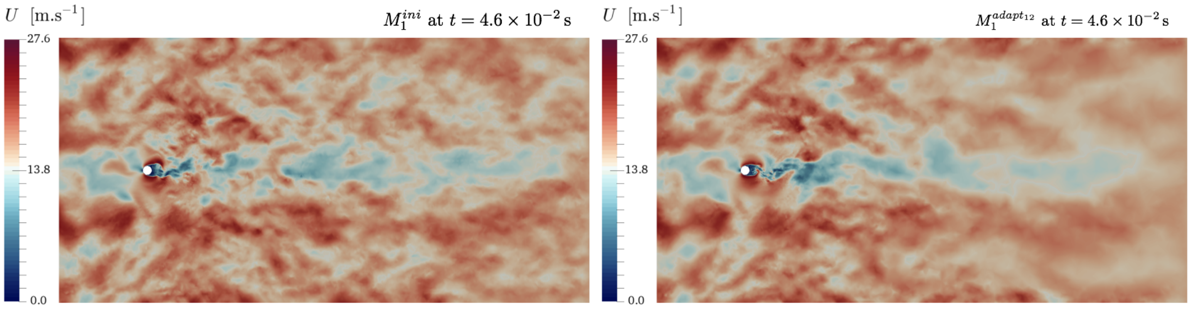

FIGURE 6.24: Comparison of the instantaneous velocity field computed on M_1^{ini} (left) and on $M_1^{adapt_{12}}$ (right) for the $t = 4.6 \times 10^{-2}$ s.

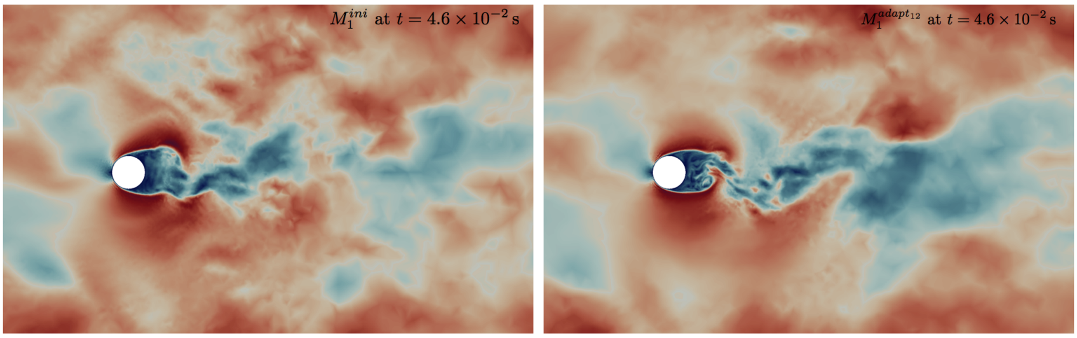

FIGURE 6.25: Comparison of the instantaneous velocity field around the cylinder computed on M_1^{ini} (left) and on $M_1^{adapt_{12}}$ (right) for the $t = 4.6 \times 10^{-2}$ s.

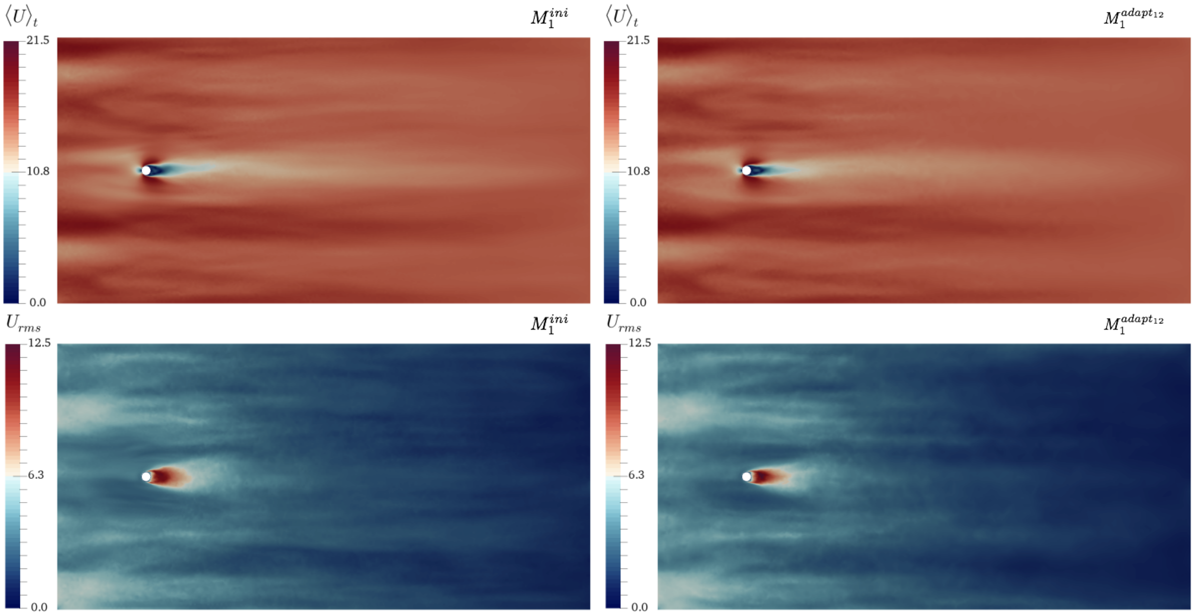

FIGURE 6.26: Comparison of velocity mean and root mean square field on M_1^{ini} (left) and on $M_1^{adapt_{12}}$ (right).

Chapter 7

Conclusions and perspectives

Contents

7.1 Conclusions on multi-level approaches

Modern massively parallel supercomputers are highly hierarchical. On the one hand, the memory hierarchy in computer architecture is separated into different layers - associated to different response times - that can be distinguished by their performances and technologies. On the other hand, the CPU power is shared between hundreds to thousands of nodes, each containing several processors that in turn contain many cores. Therefore, the execution of high-performance numerical simulations with such machines requires the adaptation of CFD codes through the development of new algorithms which can exploit efficiently this hierarchical parallelism. Hence, this thesis aims at developing new multi-level co- and post-processing frameworks for the analysis of high-resolution LES of turbulent flows. In such numerical simulations, the dynamics of the flow is driven by the presence of coherent features that concentrate an important part of the kinetic energy of the flow. However, due to the large amount of generated data, these large-scale vortices are masked by the smallest scales and thus require to be correctly post-processed - that can be achieved through the multi-grid framework - before attempting to access to relevant information. In addition, the second proposed formalism - based on several levels of LES - attempts to answer the question of the simulation dependency on the user mesh generation. In fact, most of the time, mesh generation is mainly based on a topological point a view that is supplemented by the user's knowledge of flow dynamics. However, assuming that the user has a perfect knowledge of this dynamics, he still has to estimate the appropriate local cell size, which is unknown, making the convergence study difficult. This procedure leads to non-optimized meshes for a fixed number of cells and may therefore degrade the quality and the predictability of the simulation. Hence, combined with traditional "Big Data" post-processing tools and methods - such as data partitioning, data ordering and parallel processing -, this thesis work introduces two frameworks based on the multi-level formalism that both attempt to alleviate these classical CFD issues.

7.1.1 Large-scale features extraction framework

The Multi-Grid High-Order Filtering framework (MGHOF) for on-the-fly co-processing of highly-resolved LES has been proposed. This approach enables to extract and identify coherent features from 3D fully turbulent flows in complex geometries. It transfers the large-scale dynamics onto coarser levels of grid that allows to drastically decrease the amount of data to analyze. Moreover, the successive coarsening steps based on high-order filters and interpolation methods enable to overcome the Q-criterion scaling issue - large-scale coherent features are masked by the smallest scales - which is particularly disturbing for the large scales visualization.

First and foremost, a parametric study has been performed in order to find the set of relevant MGHOF parameters that enable to avoid aliasing effects while transferring fields from refined to coarse grids. These parameters have also to ensure that resolved scales on the coarse grids are almost untouched by the filtering operation. Hence, a trade-off between the CPU cost of filters and their selectivity has been made by considering 12^{th}-order Raymond's filters with a filter size equal to twice the local mesh size of the grid as $\Delta = 2\Delta x$. Then, this methodology has been applied in several complex configurations, each time extracting successfully the large-scale features from turbulent flows with a significant CPU cost reduction compared to classical approaches.

The first configuration referred to the LES of a 3D turbulent planar jet that aims at extracting the Kelvin-Helmholtz vortices and coherent structures from the turbulent background noise. Thanks to the MGHOF framework, the Q-criterion computed on a 312 million-cell LES has been successfully transferred onto a 39 million-cell grid reducing the CPU cost by a factor three compared to the classical filtering procedure. This configuration highlighted the ability of the MGHOF framework to extract large-scale features in realistic turbulent flow configurations.

Thereafter, a more challenging 2.2 billion-cell LES of a turbulent low-Mach flow over a 3D turbine blade has been on-the-fly co-processed, allowing to successfully extract on a 35 million-cell grid, through the Q-criterion, the dynamically dominant features. In this configuration, the difficulties encountered referred to the high heterogeneity of the grid cell size and to the curvature effects on the Q-criterion produced by the geometry of the blade. However, an adapted strategy has been set up and the MGHOF framework application successfully extracted the large-scale motions of the flow with CPU cost reduced by a factor 60 compared to the classical filtering procedure. This cost reduction makes accessible the visualization of large coherent features from billion-cell simulations - which was previously not conceivable - and also enables to store hundreds of solutions that can now be analyzed through modal decomposition methods.

Hence, the MGHOF framework accumulated a large number of snapshots for the previous 2.2 billion-cell LES onto a coarse grid with 35 million-cell elements. These solution fields have been successfully analyzed thanks to the DMD modal decomposition method identifying the dynamically dominant modes and thus giving access to more quantitative information about the important flow structures. For instance, this analysis highlighted the presence of very elongated structures with a size close to a mid-chord that are present in the laminar boundary layer on the suction side that are due to the interaction of free-stream turbulence with the blade.

Finally, the MGHOF framework opens new processing possibilities that allow to understand more precisely turbulent complex flows. Many other types of analysis would benefit from such accurate and efficient coarsening multi-level method. This framework has been implemented in a specific module of the CFD code YALES2 as well as the convex optimization of the DMD mode amplitude that has been solved here through the derivation of analytical expressions proposed in this thesis.

7.1.2 Multi-Resolution LES formalism

The Multi-Resolution LES framework (MR-LES) aims at generating adequate and optimized meshes for LES in complex geometries and thus intents to limit the computational cost of the simulations while minimizing the SGS modeling errors. This methodology uses several LES levels that communicate through velocity field transfers from a refined level to a coarse one. Comparing these computed fields enables to measure the divergence between LES levels and thus to estimate where the solution is mesh dependent and where they have to be locally refined or coarsened. Hence, using this metric, the optimization of LES grids can be achieved through the application of several steps of mesh adaptation until the framework converges to grids with a stabilized cell size.

First, a parametric analysis to the main parameters of the MR-LES framework has been provided using an Homogeneous Isotropic Turbulence configuration driven by a linear forcing term. From this numerical study, accessing to a relevant error modeling can be achieved through adequate synchronization time compared to the characteristic time scale of the most dynamically features in the flow and also with a small local cell size ratio between LES levels. These parameters guarantee that the divergence between the two levels is small enough and thus enables to access to the best possible error measurement between the LES-levels.

Then, this methodology has been validated for a turbulent flow over a 3D cylinder. This configuration has been successfully co-processed through the application of the MR-LES framework leading to the generation of an optimized and converged grid keeping the number of elements almost constant. Even if a high turbulent intensity has been imposed at the inlet boundary, the framework well reacted by only refining areas of interest i.e. mainly the wake of the cylinder. The convergence of the methodology has also been highlighted through the stabilization of the probability density function of the local cell size of the adapted meshes. Hence, the converged optimized grid only increases the CPU cost of the simulation by 22% compared to the initial mesh and enables to capture more physics on the trailing edge of the cylinder and in its wake.

7.2 Perspectives

Based on these developed multi-level methodologies, some perspectives and promising new research areas for both turbulence modeling and mesh adaptation improvements are formulated below.

7.2.1 Turbulence analysis with multi-level methods

Multi-level methods open new processing possibilities in the analysis of turbulent flows. First, it could provide important insights into the understanding of the interaction between free-stream turbulence and obstacles such as cylinders, blades and so on... In addition, the MR-LES framework could be applied by considering data exchanges based on other variables of interest than the velocity field. From this new evaluation of local errors between the LES levels, a more adapted and efficient measurement of the grid quality could eventually be built improving the mesh adaptation steps and thus reducing the CPU cost of the methodology. The application of the MR-LES framework on more complex configurations - for instance, LES with several hundred million elements - has yet to be executed but would be very interesting to perform. Furthermore, the application of the MR-LES framework to turbulent reactive flows would also be very challenging. In that case, a relevant criterion allowing to determine where the flame wrinkling or the flame thickness is under-resolved has to be built, this may be achieved by comparing the field of chemical source term between LES levels.

Moreover, the analysis of the cross correlation of DMD modes in turbulent flows has to be further developed. For the previous T7.2 configuration, this could determine if velocity and scalar fluctuations are decoupled or not. Moreover, advanced modal decomposition methods also have to be implemented in order to extract more efficiently the dominant coherent features from highly refined flows. Indeed, it would be interesting to develop criteria that penalize the transient modes of the flow - that contain a high energy content but that are damped very quickly - in order to avoid selecting them in the sub-set of relevant modes. Moreover, a desirable tradeoff between the number of selected modes and the quality of approximation may be achieved through the development of news modal decomposition method formalisms.

7.2.2 Mesh adaptation improvements

Due to the steadily increase of the computational resources and to the improvements of resolution algorithms, the parallel mesh adaptation appears to be an innovative topic that will certainly gain momentum in the coming years. The proposed strategy through the MR-LES framework is a first attempt to an automatic mesh adaptation method, that aims at generating an optimized mesh keeping the number of elements constant. However, some technical advancements still have to be developed before reaching a mature and efficient strategy.

First, the adaptation of surfaces is required in order to modify the mesh on boundary conditions or for two-dimensional computations. In that case, it is mandatory to implement a surface mesh adaptation algorithm that becomes a challenging numerical problem. Furthermore, the interpolation process of data from the initial grid to the adapted one has to be improved in order to avoid numerical errors. This could be achieved through the implementation of the same high-order interpolation methods - linear interpolation is presently used - as the one used in the MGHOF framework. Finally, the application of such formalism can only be profitable if the CPU cost for generating the optimized meshes is inferior compared to the CPU cost while calculating on a more refined mesh and some efforts are still needed to reach this performance objective.

Finally, it would be interesting to determine if the MR-LES framework and more generally mesh adaptation processes always converge to the same final and stabilized mesh for different initial input meshes. In other words, the underlying issue may be formulated as : Does the adaptation process depends on the initial mesh ? If it does not, the numerical simulation could therefore be independent of the user. Moreover, the MR-LES framework could also facilitate the mesh convergence study by taking into account more than two LES levels.

Appendix

Estimation of the Condition number of each filtering sub-system and its scaling This section presents the derivation of the scaling of the condition number of each sub-system previously introduced in chapter 4 as κ_{η_k}. First, the definition of the sub-system eigenvalues is recalled

$$\lambda_{\eta_k,j} = 1 + \eta_k \frac{\sin^2\left(\frac{j\pi}{N}\right)}{\sin^2\left(\frac{\pi}{\alpha}\right)} \,. \tag{7.1}$$

Using the property $|\eta_k| = 1$, the modulus of these eigenvalues are computed as follow :

$$|\lambda_{\eta_k,j}| = \sqrt{1 + 2\mathrm{Re}(\eta_\mathrm{k})\frac{\sin^2\left(\frac{\mathrm{j}\pi}{\mathrm{N}}\right)}{\sin^2\left(\frac{\pi}{\alpha}\right)} + \frac{\sin^4\left(\frac{\mathrm{j}\pi}{\mathrm{N}}\right)}{\sin^4\left(\frac{\pi}{\alpha}\right)}} = \sqrt{A} \,. \tag{7.2}$$

Then the search of extrema of the modulus can be achieved by finding the values for which the gradient is null, i.e. by solving the following equation

$$\frac{\partial}{\partial j}|\lambda_{\eta_k,j}| = 0 \Leftrightarrow \frac{A'}{2\sqrt{A}} = 0 \Leftrightarrow A' = 0 \,, \tag{7.3}$$

with A' expressed as

$$A' = \frac{\partial A}{\partial j} = \frac{4\pi}{N}\frac{\cos\left(\frac{j\pi}{N}\right)\sin\left(\frac{j\pi}{N}\right)}{\sin^2\left(\frac{\pi}{\alpha}\right)}\left[\mathrm{Re}(\eta_\mathrm{k}) + \frac{\sin^2\left(\frac{\mathrm{j}\pi}{\mathrm{N}}\right)}{\sin^2\left(\frac{\pi}{\alpha}\right)}\right] \,. \tag{7.4}$$

Thus, three different cases can be distinguished :

1. $\cos\left(\frac{j\pi}{N}\right) = 0 \Leftrightarrow j_1 = N/2$
2. $\sin\left(\frac{j\pi}{N}\right) = 0 \Leftrightarrow j_2 = \begin{cases} 0 \\ N \end{cases}$
3. $\mathrm{Re}(\eta_\mathrm{k}) + \frac{\sin^2\left(\frac{\mathrm{j}\pi}{\mathrm{N}}\right)}{\sin^2\left(\frac{\pi}{\alpha}\right)} = 0 \Leftrightarrow \begin{cases} \mathrm{Re}(\eta_\mathrm{k}) < 0 \\ j_3 = \frac{N}{\pi}\arcsin\left[\sqrt{-\mathrm{Re}(\eta_\mathrm{k})\sin^2\left(\frac{\pi}{\alpha}\right)}\right] \end{cases}$

The extrema of the modulus can therefore be analytically expressed as

1. $$|\lambda_{\eta_k,j_1}| = \sqrt{1 + \frac{2\mathrm{Re}(\eta_\mathrm{k})}{\sin^2\left(\frac{\pi}{\alpha}\right)} + \frac{1}{\sin^4\left(\frac{\pi}{\alpha}\right)}} \tag{7.5}$$

2. $$|\lambda_{\eta_k,j_2}| = 1 \tag{7.6}$$

3.

$$|\lambda_{\eta_k,j_3}| = \sqrt{1 - \mathrm{Re}^2(\eta_\mathrm{k})} \tag{7.7}$$

The condition number of a linear system is the ratio of the maximum and minimum eigenvalue modulus. The maximum eigenvalue is always the first given above. The minimum eigenvalue can be the second or the third. Thus, two cases have to be distinguished in order to determine the condition number of each sub-system :

- $\mathrm{Re}(\eta_\mathrm{k}) \geq 0 \Rightarrow \kappa_{\eta_\mathrm{k}} = \frac{\sqrt{1+\frac{2\mathrm{Re}(\eta_\mathrm{k})}{\sin^2(\frac{\pi}{\alpha})}+\frac{1}{\sin^4(\frac{\pi}{\alpha})}}}{1} \underset{\alpha\to\infty}{\approx} \frac{\alpha^2}{\pi^2}$
- $\mathrm{Re}(\eta_\mathrm{k}) < 0 \Rightarrow \kappa_{\eta_\mathrm{k}} = \frac{\sqrt{1+\frac{2\mathrm{Re}(\eta_\mathrm{k})}{\sin^2(\frac{\pi}{\alpha})}+\frac{1}{\sin^4(\frac{\pi}{\alpha})}}}{\sqrt{1-\mathrm{Re}^2(\eta_\mathrm{k})}} \underset{\alpha\to\infty}{\approx} \frac{\alpha^2}{\pi^2\sqrt{1-\mathrm{Re}^2(\eta_\mathrm{k})}}$

In both cases, the condition number of each sub-system scales with α^2 for high values of α.

List of Figures

List of Tables

Bibliography

[1] E Achenbach and E Heinecke. On vortex shedding from smooth and rough cylinders in the range of reynolds numbers 6× 10 3 to 5× 10 6. *Journal of fluid mechanics*, 109 :239–251, 1981.

[2] Y Addad, S Benhamadouche, and D Laurence. The negatively buoyant wall-jet : Les results. *International journal of heat and fluid flow*, 25(5) :795–808, 2004.

[3] George S Almasi and Allan Gottlieb. Highly parallel computing. 1988.

[4] RA Antonia, AJ Chambers, D Britz, and LWB Browne. Organized structures in a turbulent plane jet : topology and contribution to momentum and heat transport. *J. Fluid Mech*, 172 :211–229, 1986.

[5] Athanasios C Antoulas, Danny C Sorensen, and Serkan Gugercin. A survey of model reduction methods for large-scale systems. *Contemporary mathematics*, 280 :193–220, 2001.

[6] Krste Asanovic, Rastislav Bodik, James Demmel, Tony Keaveny, Kurt Keutzer, John Kubiatowicz, Nelson Morgan, David Patterson, Koushik Sen, John Wawrzynek, et al. A view of the parallel computing landscape. *Communications of the ACM*, 52(10) :56–67, 2009.

[7] Alexandre Barbagallo, Denis Sipp, and Peter J Schmid. Closed-loop control of an open cavity flow using reduced-order models. *Journal of Fluid Mechanics*, 641 :1–50, 2009.

[8] Alexandre Barbagallo, Denis Sipp, and Peter J Schmid. Input–output measures for model reduction and closed-loop control : application to global modes. *Journal of Fluid Mechanics*, 685 :23–53, 2011.

[9] Dwight Barkley and Ronald D Henderson. Three-dimensional floquet stability analysis of the wake of a circular cylinder. *Journal of Fluid Mechanics*, 322 :215–241, 1996.

[10] George Keith Batchelor. *The theory of homogeneous turbulence*. Cambridge university press, 1953.

[11] George Keith Batchelor. *An introduction to fluid dynamics*. Cambridge university press, 2000.

[12] JF Beaudoin, Olivier Cadot, JL Aider, K Gosse, P Paranthoën, B Hamelin, M Tissier, D Allano, I Mutabazi, M Gonzales, et al. Cavitation as a complementary tool for automotive aerodynamics. *Experiments in fluids*, 37(5) :763–768, 2004.

[13] John B Bell, Phillip Colella, and Harland M Glaz. A second-order projection method for the incompressible navier-stokes equations. *Journal of Computational Physics*, 85(2) :257–283, 1989.

[14] Henry Bénard. *C. R. Acad. Sci.*, 147(839), 1908.

[15] Pierre Bénard. *Analyse et amélioration d'une chambre de combustion centimétrique par simulations aux grandes échelles*. PhD thesis, INSA de Rouen, 2015.

[16] Pierre Benard, Guillaume Balarac, Vincent Moureau, Cecile Dobrzynski, Ghislain Lartigue, and Yves D'Angelo. Mesh adaptation for large-eddy simulations in complex geometries. *International Journal for Numerical Methods in Fluids*, 2015.

[17] Gal Berkooz, Philip Holmes, and John L Lumley. The proper orthogonal decomposition in the analysis of turbulent flows. *Annual review of fluid mechanics*, 25(1) :539–575, 1993.

[18] R Byron Bird, Warren E Stewart, and Edwin N Lightfoot. *Transport phenomena*. John Wiley & Sons, 2007.

[19] JP Bonnet and J Delville. General concepts on structure identification. In *Eddy structure identification*, pages 1–59. Springer, 1996.

[20] Joseph Boussinesq. *Essai sur la théorie des eaux courantes*. Imprimerie nationale, 1877.

[21] Joseph Boussinesq. *Théorie de l'écoulmnent tourbillonnant et tumultuex des liquides dans les lits rectilignes à grande section*, volume 1. Gauthier-Villars, 1897.

[22] P Bradshaw. Possible origin of prandt's mixing-length theory. *Nature*, 249(5453) :135–136, 1974.

[23] M Braza, PHHM Chassaing, and H Ha Minh. Numerical study and physical analysis of the pressure and velocity fields in the near wake of a circular cylinder. *Journal of fluid mechanics*, 165 :79–130, 1986.

[24] Garry L Brown and Anatol Roshko. On density effects and large structure in turbulent mixing layers. *Journal of Fluid Mechanics*, 64(04) :775–816, 1974.

[25] Kai Bürger, Marc Treib, Rüdiger Westermann, Suzanne Werner, Cristian C Lalescu, Alexander Szalay, Charles Meneveau, and Gregory L Eyink. Vortices within vortices : hierarchical nature of vortex tubes in turbulence. *arXiv preprint arXiv :1210.3325*, 2012.

[26] Stephen Butterworth. On the theory of filter amplifiers. *Wireless Engineer*, 7(6) :536–541, 1930.

[27] Daniele Carati, Sandip Ghosal, and Parviz Moin. On the representation of backscatter in dynamic localization models. *Physics of Fluids*, 7(3) :606–616, 1995.

[28] I Celik, M Klein, M Freitag, and J Janicka. Assessment measures for urans/des/les : an overview with applications. *Journal of Turbulence*, (7) :N48, 2006.

[29] I Celik, M Klein, and J Janicka. Assessment measures for engineering les applications. *Journal of fluids engineering*, 131(3) :031102, 2009.

[30] IB Celik, ZN Cehreli, and I Yavuz. Index of resolution quality for large eddy simulations. *Journal of fluids engineering*, 127(5) :949–958, 2005.

[31] NASA Langley Research Center.

[32] The National Energy Research Scientific Computing Center. The difference between the typical pure mpi application targeting inter-node communication and an openmp parallel code targeting on-node parallelism.

[33] Gary J Chandler, Matthew P Juniper, Joseph W Nichols, and Peter J Schmid. Adjoint algorithms for the navier–stokes equations in the low mach number limit. *Journal of Computational Physics*, 231(4) :1900–1916, 2012.

[34] Patrick Chassaing. *Turbulence en mécanique des fluides*. 2000.

[35] Kevin K Chen, Jonathan H Tu, and Clarence W Rowley. Variants of dynamic mode decomposition : boundary condition, koopman, and fourier analyses. *Journal of nonlinear science*, 22(6) :887–915, 2012.

[36] Cédric Chevalier and François Pellegrini. Pt-scotch : A tool for efficient parallel graph ordering. *Parallel computing*, 34(6) :318–331, 2008.

[37] Min S Chong, Anthony E Perry, and Brian J Cantwell. A general classification of three-dimensional flow fields. *Physics of Fluids A : Fluid Dynamics*, 2(5) :765–777, 1990.

[38] Alexandre Joel Chorin. Numerical solution of the navier-stokes equations. *Mathematics of computation*, 22(104) :745–762, 1968.

[39] John M Cimbala, Hassan M Nagib, and Anatol Roshko. Large structure in the far wakes of two-dimensional bluff bodies. *Journal of Fluid Mechanics*, 190 :265–298, 1988.

[40] Donald Coles. Prospects for useful research on coherent structure in turbulent shear flow. *Sadhana*, 4(2) :111–127, 1981.

[41] P Comte, JH Silvestrini, and P Bégou. Streamwise vortices in large-eddy simulations of mixing layers. *European Journal of Mechanics-B/Fluids*, 17(4) :615–637, 1998.

[42] Paul Concus, Gene H Golub, and Dianne P O'Leary. *A generalized conjugate gradient method for the numerical solution of elliptic partial differential equations*. Computer Science Department, School of Humanities and Sciences, Stanford University, 1976.

[43] Antoine Craya. *Contribution à l'analyse de la turbulence associée à des vitesses moyennes*. PhD thesis, Université de Grenoble, 1957.

[44] R Cucitore, M Quadrio, and A Baron. On the effectiveness and limitations of local criteria for the identification of a vortex. *European Journal of Mechanics-B/Fluids*, 18(2) :261–282, 1999.

[45] M. Flé D. Lecas, I. Dupays. Message passing interface (mpi). 2017.

[46] Carlos Bettencourt da Silva and Olivier Métais. On the influence of coherent structures upon interscale interactions in turbulent plane jets. *Journal of Fluid Mechanics*, 473 :103–145, 2002.

[47] da Vinci L. Seated man and water studies. Royal Library, Windsor Castle ; Leoni Volume (12579).

[48] Leonardo Dagum and Ramesh Menon. Openmp : an industry standard api for shared-memory programming. *IEEE computational science and engineering*, 5(1) :46–55, 1998.

[49] U Dalmann. Topological structures of three-dimensional flow separation. *Deutche Forschungs-und Versuchsanstalt fur Luft-und Raumfahrt Report*, (221-82) :A07, 1983.

[50] Charles Dapogny, Cécile Dobrzynski, and Pascal Frey. Three-dimensional adaptive domain remeshing, implicit domain meshing, and applications to free and moving boundary problems. *Journal of Computational Physics*, 262 :358–378, 2014.

[51] Lars Davidson. How to estimate the resolution of an les of recirculating flow. *Quality and Reliability of Large-Eddy Simulations II*, pages 269–286, 2011.

[52] Guillaume Daviller, Maxence Brebion, Pradip Xavier, Gabriel Staffelbach, Jens-Dominik Müller, and Thierry Poinsot. A mesh adaptation strategy to predict pressure losses in les of swirled flows. *Flow, Turbulence and Combustion*, pages 1–26, 2017.

[53] David Day and Michael A Heroux. Solving complex-valued linear systems via equivalent real formulations. *SIAM Journal on Scientific Computing*, 23(2) :480–498, 2001.

[54] Benoit de Laage De Meux. *Modélisation des écoulements turbulents en rotation et en présence de transferts thermiques par approche hybride RANS/LES zonale*. PhD thesis, ISAE-ENSMA Ecole Nationale Supérieure de Mécanique et d'Aérotechique-Poitiers, 2012.

[55] M Délèze, J-J Goël, and B Meyenhofer. Finite elements of c1-class on a tetrahedron. *International Journal for Numerical Methods in Engineering*, 12(5) :787–793, 1978.

[56] Marcel Délèze. *Elements finis tétrahédriques de classe C1 et de dégré deux*. PhD thesis, Faculté des Sciences de l'Université de Fribourg, 1979.

[57] Joël Delville, Laurent Cordier, and Jean-Paul Bonnet. Large-scale-structure identification and control in turbulent shear flows. In *Flow Control*, pages 199–273. Springer, 1998.

[58] Cécile Dobrzynski and Pascal Frey. Anisotropic delaunay mesh adaptation for unsteady simulations. *Proceedings of the 17th international Meshing Roundtable*, pages 177–194, 2008.

[59] Charles R Doering and John D Gibbon. *Applied analysis of the Navier-Stokes equations*, volume 12. Cambridge University Press, 1995.

[60] Yves Dubief and Franck Delcayre. On coherent-vortex identification in turbulence. *Journal of turbulence*, 1(1) :011–011, 2000.

[61] Florent Duchaine, Nicolas Maheu, Vincent Moureau, Guillaume Balarac, and Stéphane Moreau. Large-eddy simulation and conjugate heat transfer around a low-mach turbine blade. *Journal of Turbomachinery*, 136(5) :051015, 2014.

[62] Marie Farge. Wavelet transforms and their applications to turbulence. *Annual review of fluid mechanics*, 24(1) :395–458, 1992.

[63] Marie Farge, Kai Schneider, and Nicholas Kevlahan. Non-gaussianity and coherent vortex simulation for two-dimensional turbulence using an adaptive orthogonal wavelet basis. *Physics of Fluids*, 11(8) :2187–2201, 1999.

[64] HE Fiedler. Coherent structures in turbulent flows. *Progress in Aerospace Sciences*, 25(3) :231–269, 1988.

[65] Joseph Fourier. *Theorie analytique de la chaleur, par M. Fourier*. Chez Firmin Didot, père et fils, 1822.

[66] Martin Freitag and Markus Klein. An improved method to assess the quality of large eddy simulations in the context of implicit filtering. *Journal of Turbulence*, (7) :N40, 2006.

[67] Roland W Freund. Conjugate gradient-type methods for linear systems with complex symmetric coefficient matrices. *SIAM Journal on Scientific and Statistical Computing*, 13(1) :425–448, 1992.

[68] P J Frey and F Alauzet. Anisotropic mesh adaptation for CFD computations. *Computer Methods in Applied Mechanics and Engineering*, 194(48-49) :5068–5082, 2005.

[69] David Galley. *Etude de la stabilisation de flammes turbulentes prévaporisées prémélangées pauvres*. PhD thesis, Châtenay-Malabry, Ecole Centrale de Paris, 2006.

[70] Simon E Gant. Reliability issues of les-related approaches in an industrial context. *Flow, turbulence and combustion*, 84(2) :325–335, 2010.

[71] M Gaster, E Kit, and I Wygnanski. Large-scale structures in a forced turbulent mixing layer. *Journal of Fluid Mechanics*, 150 :23–39, 1985.

[72] Massimo Germano, Ugo Piomelli, Parviz Moin, and William H Cabot. A dynamic subgrid-scale eddy viscosity model. *Physics of Fluids A : Fluid Dynamics*, 3(7) :1760–1765, 1991.

[73] Bernard J Geurts and Jochen Fröhlich. A framework for predicting accuracy limitations in large-eddy simulation. *Physics of fluids*, 14(6) :L41–L44, 2002.

[74] Vincent Giovangigli. Multicomponent flow modeling. *Science China Mathematics*, 55(2) :285–308, 2012.

[75] Gene H Golub and CF Van Loan. Matn ‘z computation, 1990.

[76] Gene H Golub and Charles F Van Loan. *Matrix computations*, volume 3. JHU Press, 2012.

[77] Anne Greenbaum. *Iterative methods for solving linear systems*, volume 17. Siam, 1997.

[78] William Gropp, Ewing Lusk, and Anthony Skjellum. *Using MPI : portable parallel programming with the message-passing interface*, volume 1. MIT press, 1999.

[79] Catherine Gruselle. *Etude du développement d'une flamme soumise à un gradient de concentration : Rôle de la stratification et des EGR*. PhD thesis, INSA de Rouen, 2014.

[80] L Guedot, G Lartigue, and V Moureau. Design of implicit high-order filters on unstructured grids for the identification of large-scale features in large-eddy simulation and application to a swirl burner. *Physics of Fluids (1994-present)*, 27(4) :045107, 2015.

[81] Lola Guedot. *Développement de méthodes numériques pour la caractérisation des grandes structures tourbillonnaires dans les brûleurs aéronautiques : application aux systèmes d'injection multi-points*. PhD thesis, Rouen, INSA, 2015.

[82] Ashwani K Gupta, David G Lilley, and Nick Syred. Swirl flows. *Tunbridge Wells, Kent, England, Abacus Press, 1984, 488 p.*, 1984.

[83] Hermann Haken. *Synergetik-Eine Einführung : Nichtgleichgewichts [übergänge]-Phasenübergänge u. Selbstorganisation in Physik, Chemie u. Biologie*. Springer, 1983.

[84] Francis R Hama. Streaklines in a perturbed shear flow. *The physics of fluids*, 5(6) :644–650, 1962.

[85] JO Hinze. Turbulence mcgraw-hill. *New York*, 218, 1975.

[86] Joseph Hirschfelder, R Byron Bird, and Charles F Curtiss. Molecular theory of gases and liquids. 1964.

[87] Howard Holtz and Cornelius T Leondes. The synthesis of recursive digital filters. *Journal of the ACM (JACM)*, 13(2) :262–280, 1966.

[88] JP Hulin, E Guyon, L Petit, and CD Mitescu. Physical hydrodynamics. *Oxford University Press*, 8 :10–13, 2001.

[89] Julian CR Hunt, Alan A Wray, and Parviz Moin. Eddies, streams, and convergence zones in turbulent flows. 1988.

[90] A KM Fazle Hussain. Role of coherent structures in turbulent shear flows. *Sadhana*, 4(2) :129–175, 1981.

[91] AKM Fazle Hussain. Coherent structures—reality and myth. *The Physics of fluids*, 26(10) :2816–2850, 1983.

[92] P.F. Lavallée J. Chergui. Openmp : Parallélisation multitâches pour machines à mémoire partagée. 2017.

[93] M.G. Vallet J. Dompierre, P. Labb and R. Camarero. How to subdivide pyramids, prisms and hexahedra into tetrahedra. *Rapport CERCA R99-79*, 1999.

[94] Antony Jameson, Wolfgang Schmidt, Eli Turkel, et al. Numerical solutions of the euler equations by finite volume methods using runge-kutta time-stepping schemes. *AIAA paper*, 1259 :1981, 1981.

[95] Thomas Jaravel. *Prediction of pollutants in gas turbines using large eddy simulation.* PhD thesis, 2016.

[96] Jinhee Jeong and Fazle Hussain. On the identification of a vortex. *Journal of fluid mechanics*, 285 :69–94, 1995.

[97] Jinhee Jeong, Fazle Hussain, Wade Schoppa, and John Kim. Coherent structures near the wall in a turbulent channel flow. *Journal of Fluid Mechanics*, 332 :185–214, 1997.

[98] Mihailo R Jovanović, Peter J Schmid, and Joseph W Nichols. Sparsity-promoting dynamic mode decomposition. *Physics of Fluids*, 26(2) :024103, 2014.

[99] MR Jovanovic, PJ Schmid, and JW Nichols. Low-rank and sparse dynamic mode decomposition. *Center for Turbulence Research Annual Research Briefs*, 2012 :139–152, 2012.

[100] Harijs Kalis, Sergejs Rogovs, and Aigars Gedroics. On the mathematical modelling of the diffusion equation with piecewise constant coefficients in a multi-layered domain. *International Journal of Pure and Applied Mathematics*, 81(4) :555–575, 2012.

[101] Yukio Kaneda, Takashi Ishihara, Mitsuo Yokokawa, Ken'ichi Itakura, and Atsuya Uno. Energy dissipation rate and energy spectrum in high resolution direct numerical simulations of turbulence in a periodic box. *Physics of Fluids*, 15(2) :L21–L24, 2003.

[102] Kari Karhunen. Zur spektraltheorie stochastischer prozesse. 1946.

[103] George Karypis and Vipin Kumar. Metis–unstructured graph partitioning and sparse matrix ordering system, version 2.0. 1995.

[104] Fotini V Katopodes, RL Street, and JH Ferziger. Subfilter-scale scalar transport for large-eddy simulation. In *14th Symposium on Boundary Layers and Turbulence*, pages 472–475. American Meteorologic Society Aspen (CO), 2000.

[105] Shigeo Kida and Hideaki Miura. Identification and analysis of vortical structures. *European Journal of Mechanics-B/Fluids*, 17(4) :471–488, 1998.

[106] John Kim and Parviz Moin. Application of a fractional-step method to incompressible navier-stokes equations. *Journal of computational physics*, 59(2) :308–323, 1985.

[107] Sergiu Klainerman and Andrew Majda. Compressible and incompressible fluids. *Communications on Pure and Applied Mathematics*, 35(5) :629–651, 1982.

[108] M Klein. An attempt to assess the quality of large eddy simulations in the context of implicit filtering. *Flow, Turbulence and Combustion*, 75(1) :131–147, 2005.

[109] Václav Kolář. Vortex identification : New requirements and limitations. *International journal of heat and fluid flow*, 28(4) :638–652, 2007.

[110] Andrey Nikolaevich Kolmogorov. Dissipation of energy in locally isotropic turbulence. In *Dokl. Akad. Nauk SSSR*, volume 32, pages 16–18. JSTOR, 1941.

[111] Andrey Nikolaevich Kolmogorov. The local structure of turbulence in incompressible viscous fluid for very large reynolds numbers. In *Dokl. Akad. Nauk SSSR*, volume 30, pages 299–303, 1941.

[112] Matthias Kraushaar. *Application of the compressible and low-Mach number approaches to Large-Eddy Simulation of turbulent flows in aero-engines.* PhD thesis, Institut National Polytechnique de Toulouse-INPT, 2011.

[113] Helge Ladisch, Achmed Schulz, and Hans-Jörg Bauer. Heat transfer measurements on a turbine airfoil with pressure side separation. In *ASME Turbo Expo 2009 : Power for Land, Sea, and Air*, pages 783–793. American Society of Mechanical Engineers, 2009.

[114] MT Landahl. Coherent structures in turbulence and prandtl's mixing length theory (27th ludwig prandtl memorial lecture). *Zeitschrift fur Flugwissenschaften und Weltraumforschung*, 8 :233–242, 1984.

[115] Andrzej Lasota and Michael C Mackey. Chaos, fractals and noise, volume 97 of applied mathematical sciences, 1994.

[116] A Leonard. Energy cascade in large-eddy simulations of turbulent fluid flows. *Advances in geophysics*, 18 :237–248, 1975.

[117] M Lesieur. Turbulence et structures cohérentes dans les fluides. *PITMAN RESEARCH NOTES IN MATHEMATICS SERIES*, pages 207–233, 1998.

[118] Marcel Lesieur. Stochastic and numerical modeling, 1990.

[119] Zinn-Justin J Lesieur M, Comte P. Turbulence and coherent vortices. *Computational Fluid Dynamics*, 1993.

[120] T Leung, N Swaminathan, and PA Davidson. Geometry and interaction of structures in homogeneous isotropic turbulence. *Journal of Fluid Mechanics*, 710 :453–481, 2012.

[121] John H Lienhard. *Synopsis of lift, drag, and vortex frequency data for rigid circular cylinders*, volume 300. Technical Extension Service, Washington State University, 1966.

[122] Douglas K Lilly. On the application of the eddy viscosity concept in the inertial sub-range of turbulence. *National Center for Atmospheric Research*, 123, 1966.

[123] Douglas K Lilly. A proposed modification of the germano subgrid-scale closure method. *Physics of Fluids A : Fluid Dynamics*, 4(3) :633–635, 1992.

[124] Michel Loève. *Probability theory : foundations, random sequences*. van Nostrand Princeton, NJ, 1955.

[125] Rainald Löhner. Robust, vectorized search algorithms for interpolation on unstructured grids. *Journal of computational Physics*, 118(2) :380–387, 1995.

[126] DF Long and REA Arndt. The orthogonal decomposition of pressure fluctuations surrounding a turbulent jet. In *5th Symposium on Turbulent Shear Flows*, pages 4–27, 1985.

[127] O Lucca-Negro and T O'doherty. Vortex breakdown : a review. *Progress in energy and combustion science*, 27(4) :431–481, 2001.

[128] David G Luenberger. *Introduction to linear and nonlinear programming*, volume 28. Addison-Wesley Reading, MA, 1973.

[129] JL Lumley. Similarity and the turbulent energy spectrum. *The Physics of Fluids*, 10(4) :855–858, 1967.

[130] John L Lumley. Coherent structures in turbulence. In *Transition and turbulence*, volume 1, pages 215–242, 1981.

[131] John L Lumley. *Stochastic tools in turbulence*. Courier Corporation, 2007.

[132] TS Lundgren. Linearly forces isotropic turbulence. Technical report, MINNESOTA UNIV MINNEAPOLIS, 2003.

[133] ANDFREW MAJDA and James Sethian. The derivation and numerical solution of the equations for zero mach number combustion. *Combustion science and technology*, 42(3-4) :185–205, 1985.

[134] Mathias Malandain. *Massively parallel simulation of low-Mach number turbulent flows*. PhD thesis, INSA de Rouen, January 2013.

[135] Mathias Malandain, Nicolas Maheu, and Vincent Moureau. Optimization of the deflated conjugate gradient algorithm for the solving of elliptic equations on massively parallel machines. *Journal of Computational Physics*, 238 :32–47, 2013.

[136] JM McDonough. Lectures on turbulence. *Universityof Kentucky*, 2007.

[137] Igor Mezić. Spectral properties of dynamical systems, model reduction and decompositions. *Nonlinear Dynamics*, 41(1) :309–325, 2005.

[138] Alfons Michalke. On spatially growing disturbances in an inviscid shear layer. *Journal of Fluid Mechanics*, 23(03) :521–544, 1965.

[139] John Miles. Strange attractors in fluid dynamics. *Advances in applied mechanics*, 24 :189–214, 1984.

[140] Parviz Moin, Kyle Squires, W Cabot, and Sangsan Lee. A dynamic subgrid-scale model for compressible turbulence and scalar transport. *Physics of Fluids A : Fluid Dynamics*, 3(11) :2746–2757, 1991.

[141] Bruce Moore. Principal component analysis in linear systems : Controllability, observability, and model reduction. *IEEE transactions on automatic control*, 26(1) :17–32, 1981.

[142] Gordon E Moore. Progress in digital integrated electronics [technical literaiture, copyright 1975 ieee. reprinted, with permission. technical digest. international electron devices meeting, ieee, 1975, pp. 11-13.]. *IEEE Solid-State Circuits Society Newsletter*, 20(3), 2006.

[143] Gordon E Moore et al. Cramming more components onto integrated circuits. *Proceedings of the IEEE*, 86(1) :82–85, 1998.

[144] V Moureau, P Domingo, and L Vervisch. From large-eddy simulation to direct numerical simulation of a lean premixed swirl flame : Filtered laminar flame-pdf modeling. *Combustion and Flame*, 158(7) :1340–1357, 2011.

[145] Vincent Moureau, Pascale Domingo, and Luc Vervisch. Design of a massively parallel cfd code for complex geometries. *Comptes Rendus Mécanique*, 339(2) :141–148, 2011.

[146] Tamer Nabil, Waleed Abdel Kareem, Seiichiro Izawa, and Yu Fukunishi. Extraction of coherent vortices from homogeneous turbulence using curvelets and total variation filtering methods. *Computers & Fluids*, 57 :76–86, 2012.

[147] Roy A Nicolaides. Deflation of conjugate gradients with applications to boundary value problems. *SIAM Journal on Numerical Analysis*, 24(2) :355–365, 1987.

[148] Franck Nicoud and Frédéric Ducros. Subgrid-scale stress modelling based on the square of the velocity gradient tensor. *Flow, turbulence and Combustion*, 62(3) :183–200, 1999.

[149] Bernd R Noack, Michael Schlegel, Boye Ahlborn, Gerd Mutschke, Marek Morzyński, and Pierre Comte. A finite-time thermodynamics of unsteady fluid flows. *Journal of Non-Equilibrium Thermodynamics*, 33(2) :103–148, 2008.

[150] Massachusetts Institute of Technology. Hopf bifurcations.

[151] Robert K Otnes and Loren Enochson. *Applied time series analysis : volume 1-basic techniques*. Wiley, 1978.

[152] AE Perry and BD Fairlie. Critical points in flow patterns. *Advances in geophysics*, 18 :299–315, 1975.

[153] Anthony E Perry and Min S Chong. A description of eddying motions and flow patterns using critical-point concepts. *Annual Review of Fluid Mechanics*, 19(1) :125–155, 1987.

[154] Charles D Pierce and Parviz Moin. Progress-variable approach for large-eddy simulation of non-premixed turbulent combustion. *Journal of Fluid Mechanics*, 504 :73–97, 2004.

[155] Henri Poincaré. *Sur les propriétés des fonctions définies par les équations aux différences partielles*. Number 4. Gauthier-Villars, 1879.

[156] Thierry Poinsot and Denis Veynante. *Theoretical and numerical combustion*. RT Edwards, Inc., 2005.

[157] Stephen B Pope. Turbulent flows, 2001.

[158] Ludwig Prandtl. Bericht über untersuchungen zur ausgebildeten turbulenz. *Z. Angew. Math. Mech*, 5(2) :136–139, 1925.

[159] William H Raymond. High-order low-pass implicit tangent filters for use in finite area calculations. *Monthly weather review*, 116(11) :2132–2141, 1988.

[160] William H Raymond and Arthur Garder. A review of recursive and implicit filters. *Monthly weather review*, 119(2) :477–495, 1991.

[161] Osborne Reynolds. An experimental investigation of the circumstances which determine whether the motion of water shall be direct or sinuous, and of the law of resistance in parallel channels. *Proceedings of the royal society of London*, 35(224-226) :84–99, 1883.

[162] LEWIS F Richardson. Weather prediction by numerical process cambridge university press. *CambridgeRichardsonWeather prediction by numerical process1922*, 1922.

[163] Lewis Fry Richardson. *Weather prediction by numerical process*. Cambridge University Press, 2007.

[164] Theodore J Rivlin. *An introduction to the approximation of functions*. Courier Corporation, 2003.

[165] Stephen Kern Robinson. The kinematics of turbulent boundary layer structure. *NASA STI/Recon Technical Report N*, 91, 1991.

[166] Clarence W Rowley. Model reduction for fluids, using balanced proper orthogonal decomposition. *International Journal of Bifurcation and Chaos*, 15(03) :997–1013, 2005.

[167] Clarence W Rowley, Igor Mezić, Shervin Bagheri, Philipp Schlatter, and Dan S Henningson. Spectral analysis of nonlinear flows. *Journal of fluid mechanics*, 641 :115–127, 2009.

[168] David Ruelle and Floris Takens. On the nature of turbulence. *Communications in mathematical physics*, 20(3) :167–192, 1971.

[169] Axel Ruhe. Rational krylov sequence methods for eigenvalue computation. *Linear Algebra and its Applications*, 58 :391–405, 1984.

[170] P Sagaut and R Grohens. Discrete filters for large eddy simulation. *International Journal for Numerical Methods in Fluids*, 31(8) :1195–1220, 1999.

[171] Pierre Sagaut. *Large eddy simulation for incompressible flows : an introduction*. Springer Science & Business Media, 2006.

[172] Taraneh Sayadi, Peter J Schmid, Franck Richecoeur, and Daniel Durox. Parametrized data-driven decomposition for bifurcation analysis, with application to thermo-acoustically unstable systems. *Physics of Fluids*, 27(3) :037102, 2015.

[173] Jörg U Schlüter, Heinz Pitsch, and Parviz Moin. Outflow conditions for integrated large eddy simulation/reynolds-averaged navier-stokes simulations. *AIAA J*, 43(1) :156–164, 2005.

[174] Peter Schmid. Applications of the dynamic mode decomposition. CTR Summer School Tutorial, 2012.

[175] Peter J Schmid. Dynamic mode decomposition of numerical and experimental data. *Journal of Fluid Mechanics*, 656 :5–28, 2010.

[176] Peter J Schmid, L Li, Matthew P Juniper, and O Pust. Applications of the dynamic mode decomposition. *Theoretical and Computational Fluid Dynamics*, 25(1) :249–259, 2011.

[177] Peter J Schmid, Daniele Violato, and Fulvio Scarano. Decomposition of time-resolved tomographic piv. *Experiments in Fluids*, 52(6) :1567–1579, 2012.

[178] Kai Schneider, Marie Farge, Giulio Pellegrino, and Michael M Rogers. Coherent vortex simulation of three-dimensional turbulent mixing layers using orthogonal wavelets. *Journal of Fluid Mechanics*, 534 :39–66, 2005.

[179] Kai Schneider and Oleg V Vasilyev. Wavelet methods in computational fluid dynamics. *Annual Review of Fluid Mechanics*, 42 :473–503, 2010.

[180] James A Sethian. A fast marching level set method for monotonically advancing fronts. *Proceedings of the National Academy of Sciences*, 93(4) :1591–1595, 1996.

[181] Ralph Shapiro. Smoothing, filtering, and boundary effects. *Reviews of geophysics*, 8(2) :359–387, 1970.

[182] Ralph Shapiro. Linear filtering. *Mathematics of computation*, 29(132) :1094–1097, 1975.

[183] Lawrence Sirovich. Turbulence and the dynamics of coherent structures part : coherent structures. *Quarterly of applied mathematics*, 45(3) :561–571, 1987.

[184] Joseph Smagorinsky. General circulation experiments with the primitive equations : I. the basic experiment. *Monthly weather review*, 91(3) :99–164, 1963.

[185] KR Sreenivasan and CJFM Meneveau. The fractal facets of turbulence. *Journal of Fluid Mechanics*, 173 :357–386, 1986.

[186] Roger C Strawn, David N Kenwright, and Jasim Ahmad. Computer visualization of vortex wake systems. *AIAA journal*, 37(4) :511–512, 1999.

[187] Outi Tammisola and Matthew P Juniper. Adjoint sensitivity analysis of hydrodynamic stability in a gas turbine fuel injector. In *ASME Turbo Expo 2015 : Turbine Technical Conference and Exposition*, pages V04AT04A057–V04AT04A057. American Society of Mechanical Engineers, 2015.

[188] XING Tao. A general framework for verification and validation of large eddy simulations. *Journal of Hydrodynamics, Ser. B*, 27(2) :163–175, 2015.

[189] Geoffrey Ingram Taylor. Statistical theory of turbulence. In *Proceedings of the Royal Society of London A : Mathematical, Physical and Engineering Sciences*, volume 151, pages 421–444. The Royal Society, 1935.

[190] R Teman. Infinite dimensional dynamical systems in mechanics andphysics, 1988.

[191] FO Thomas and VW Goldschmidt. Structural characteristics of a developing turbulent planar jet. *Journal of Fluid Mechanics*, 163 :227–256, 1986.

[192] Gilles Tissot, Laurent Cordier, Nicolas Benard, and Bernd R Noack. Model reduction using dynamic mode decomposition. *Comptes Rendus Mécanique*, 342(6) :410–416, 2014.

[193] Siavash Toosi and Johan Larsson. Anisotropic grid-adaptation in large eddy simulations. *Computers & Fluids*, 156 :146–161, 2017.

[194] Albert A Townsend. *The structure of turbulent shear flow*. Cambridge university press, 1980.

[195] Lloyd N Trefethen and David Bau III. *Numerical linear algebra*, volume 50. Siam, 1997.

[196] Henk A Van der Vorst. Parallel iterative solution methods for linear systems arising from discretized pde's. *Special course on parallel computing in CFD*, 2001.

[197] Stijn Vantieghem. Numerical simulations of quasi-static magnetohydrodynamics using an unstructured finite-volume solver : development and applications. *PhD thesis*, 2011.

[198] Luc Vervisch, Pascale Domingo, Guido Lodato, and Denis Veynante. Scalar energy fluctuations in large-eddy simulation of turbulent flames : Statistical budgets and mesh quality criterion. *Combustion and Flame*, 157(4) :778–789, 2010.

[199] Denis Veynante and Vincent Moureau. Analysis of dynamic models for large eddy simulations of turbulent premixed combustion. *Combustion and Flame*, 162(12) :4622–4642, 2015.

[200] Robert Vichnevetsky and John B Bowles. *Fourier analysis of numerical approximations of hyperbolic equations*. SIAM, 1982.

[201] H Vollmers, HP Kreplin, and HU Meier. Separation and vortical-type flow around a prolate spheroid-evaluation of relevant parameters. Technical report, DTIC Document, 1983.

[202] Théodore Von Karman. Uber den mechanismus des flussigkeits-und luftwiderstandes. *Phys. Z.*, pages 49–59, 1912.